

List of Open Literature Papers provided to the NRC Staff at the Meeting on ACR Thermal Hydraulics, February 5-6, 2003, Washington DC

1. File name: "*RC-2491.pdf*"
AECL report RC-2491;
Title: "An Rd-14M Experiment for the Intercomparison and Validation of Computer Codes for Thermalhydraulic Safety Analyses of Heavy Water Reactors".
This report was prepared primarily for the dissemination of information for an IAEA (International Atomic Energy Agency) international study: "Consultancy on Intercomparison and Validation of Computer Codes for Thermalhydraulic Safety Analyses of Heavy Water Reactors."
Experimental data from a RD-14M Large LOCA (loss-of-coolant accident) experiment is provided, along with a detailed description of the RD-14M facility. The information provided in this report is sufficient to prepare an idealization of the facility for simulation with a thermalhydraulics code, including initial and boundary conditions. Code predictions can then be compared to experimental results.
2. File name: "*IAEA TecDoc-1149 May 2000 pp201-212.pdf*"
Paper from IAEA TECDOC-1149;
Title: "Natural Circulation in an Integral CANDU Test Facility".
Over 70 single- and two phase natural circulation experiments have been completed in the RD-14M facility, an integral CANDU thermal hydraulic test loop. The paper describes the RD-14M facility and provides an overview of the impact of key parameters on the results of natural circulation experiments.
3. File name: "*Progress in Nuclear Energy Vol 36 No2 pp 231-233 2000.pdf*"
Paper published in "Progress in Nuclear Energy", Vol. 36 No. 2;
Title: "Clarification of a Recent Comparison of Natural Circulation Flows in "Code Validation and Uncertainties in System Thermal Hudraulics" by F. D'Auria and G. M. Galassi".
4. File name: "*CATHENA Nuclear_Engineering_Design_paper.pdf*"
Paper published in Nuclear Engineering and Design 180 (1998) 113-131;
Title: "CATHENA: A thermalhydraulic code for CANDU analysis"
The paper describes the Canadian algorithm for thermal hydraulic network analysis (CATHENA) transient, thermalhydraulics code developed for the analysis of postulated upset conditions in CANDU reactors. The core of a CANDU reactor consists of a large number of horizontal pressure tubes containing fuel bundles. As a result of the unique design of the CANDU reactor, the CATHENA thermalhydraulic code has been developed with a number of unique modelling capabilities.

5. File name: "*AECL-07664.pdf*"

Title: "Moderator Boiling on the External Surface of a Calandria Tube in a CANDU Reactor During A Loss-Of-Coolant Accident"

The paper describes a simple one-dimensional model developed to analyze the thermal-mechanical behaviour of a fuel channel where a pressure tube creeps circumferentially into contact with its calandria tube. Also described is a series of experiments in which a pressure tube segment is pressurized and heated so that it contacts a surrounding calandria tube segment. Predictions made using the model are compared with the experimental results.

6. File name: "*CFD2K_MTC_Validation.pdf*"

Paper presented at the CFD2k Conference, Montreal, Quebec, June 11-13, 2000;

Title: "Predicted and Measured Flow and Temperature Distributions in a Facility for Simulating In-Reactor Moderator Circulation".

The paper presents validation results of the MODTURC_CLASS code against experimental results obtained at the Moderator Test Facility at the Chalk River Laboratories of AECL.

7. File name: "*21st_CNS_SS_C9Val_paper.pdf*"

Paper presented at the 21st CNS Nuclear Simulation Symposium, Ottawa, September 24-26, 2000;

Title: "Validation of the MODTURC_CLAS Moderator Circulation Code for CANDU 9 Steady-State and Transient Conditions".

8. File name: "*FFC-FCT-103P; AECL-CONF-1198.pdf*"

Paper presented at the 11th International Heat-Transfer Conference, Kyongju, Korea, August 23-28, 1998;

Title: "A Generalized Prediction Method for Critical Heat Flux in CANDU Fuel-Bundle Strings".

9. File name: "*FFC-FCT-235P.pdf*"

Paper presented at the 6th International Conference on CANDU Fuel, Niagara Falls, Ontario, September 26-30, 1999;

Title: "Full Scale Water CHF Testing of the CANFLEX Bundle".

10. File name: "*FFC-FCT-236P; AECL-CONF-1199.pdf*"

Paper presented at the 6th International Conference on CANDU Fuel, Niagara Falls, Ontario, September 26-30, 1999;

Title: "Critical Heat Flux and Pressure Drop for a CANFLEX Bundle String Inside an Axially Non-Uniform Flow Channel".

11. File name: *"FFC-FCT-261P; AECL-CONF-135.pdf"*
Paper presented at the 12th Pacific Basin Nuclear Conference, Seoul, Korea, October 29-
November 2, 2000;
Title: "Introduction of the New Fuel Bundle 'CANFLEX' into an Existing CANDU
Reactor".

12. File name: *"FFC-FCT-270P; AECL-CONF-123.pdf"*
Paper presented at the 15th KAIF/KNS Annual Conference, Seoul, Korea, April 18-20,
2000;
Title: "Demonstration Irradiation of CANFLEX in a CANDU 6 Power Reactor".

13. File name: *"FFC-FCT-273P; AECL-CONF-128.pdf"*
Paper presented at the CNS 21st Annual Conference, Toronto, Ontario, June 11-14, 2000;
Title: "The Dryout-Power Improvement of CANFLEX SEU Bundles in CANDU
Reactors".

14. File name: *"FFC-FCT-311P; AECL-CONF-538.pdf"*
Paper presented at the COG/IAEA 6th Technical Committee Meeting on the Exchange of
Operational Safety Experience of Pressurized Heavy Water Reactors, Trois Rivieres,
Quebec, September 11-15, 2000;
Title: "Increasing CANDU Operating Margins with CANFLEX Fuel".

15. File name: *"FFC-FCT-344P; AECL-CONF-724.pdf"*
Paper presented at the 7th International Conference on CANDU Fuel, Kingston, Ontario,
September 23-27, 2001;
Title: "Dryout Power of a CANFLEX Bundle String With Raised Bearing Pads".

16. File name: *"FFC-FCT-369P; AECL-CONF-1096.pdf"*
Paper presented at the 7th International Conference on CANDU Fuel, Kingston, Ontario,
September 23-27, 2001;
Title: "Status of the Development of CANFLEX 0.9% SEU".

17. File name: *"FFC-FCT-370P; AECL-CONF-1097.pdf"*
Paper presented at the 7th International Conference on CANDU Fuel, Kingston, Ontario,
September 23-27, 2001;
Title: "CANFLEX Mk-IV Qualification Program and Readiness for Implementation".

18. File name: *"AECL-CONF-00660.pdf"*
Title: "A Parallel Virtual Machine Interface for CATHENA".

19. File name: *"AECL-CONF-00782.pdf"*
Title: "CATHENA Validation in Support of Large Break LOCA Analysis".

20. File name: "AECL-CONF-00798.pdf"
Title: "High-Temperature Validation of CATHENA Against a 28-Element Thermal-Chemical Experiment".
21. File name: "AECL-CONF-00804.pdf"
Title: "Validation of Radiation Heat Transfer in CATHENA".
22. File name: "AECL-CONF-00805.pdf"
Title: "Modelling Thermalhydraulic/Thermal-Mechanical Behaviour of a Fuel Channel with Stratified Two-Phase Flow Using CATHENA".
23. File name: "AECL-CONF-00862.pdf"
Title: "Pre- and Post-Test CATHENA Simulations for RD-14M Critical Break Experiments".
24. File name: "AECL-CONF-01130.pdf"
Title: "Post-Test Analysis of the BTF-107 Severe-Fuel-Damage Experiment Using the CATHENA Thermalhydraulics Code".
25. File name: "AECL-CONF-01280.pdf"
Title: "The Solution of Sparse Matrices in CATHENA".
26. File name: "AECL-CONF-01282.pdf"
Title: "Refinement of the Mass Conservation Algorithm Used in CATHENA".
27. File name: "AECL-CONF-01286.pdf"
Title: "Validation of CATHENA MOD-3.5C/Rev 0 for Void-Collapse Water Hammer".

MODERATOR BOILING ON THE EXTERNAL SURFACE
OF A CALANDRIA TUBE IN A CANDU REACTOR
DURING A LOSS-OF-COOLANT ACCIDENT

G.E. Gillespie and R.G. Hoyer

Whiteshell Nuclear Research Establishment
Pinawa, Manitoba, ROE 1LO, Canada

P.D. Thompson

Atomic Energy of Canada Engineering Company
Mississauga, Ontario, Canada

ABSTRACT

Each fuel channel in a CANDU-PHW* reactor consists of a pressure tube inside a calandria tube, with a gap containing insulating gas between them. The calandria tubes are surrounded by cool heavy-water moderator. This water would act as a supplementary heat sink during postulated loss-of-coolant accidents if the primary cooling and emergency coolant injection systems failed to remove the decay heat from the fuel. In such cases, the heat would be transferred radially to the heavy-water moderator and removed by its cooling system.

If a pressure tube were to overheat and deform into contact with its calandria tube, the heat transfer to the moderator would increase. The heat stored in the pressure tube would cause a spike in the heat flux, which might result in film boiling on the outside of the calandria tube. Should film boiling occur, the effectiveness of the moderator as a heat sink might then be reduced.

This paper describes a simple one-dimensional model developed to analyze the thermal-mechanical behaviour of a fuel channel when a pressure tube creeps circumferentially into contact with its calandria tube. Also described is a series of experiments in which a pressure-tube segment is pressurized and heated so that it contacts a surrounding calandria-tube segment. Predictions made using the model are compared with the experimental results.

INTRODUCTION

The CANDU-PHW reactor has a high-pressure primary cooling system and a low-pressure, independently cooled moderator system. The fuel and coolant are separated from the moderator by a fuel channel, which consists of a pressure tube and a calandria tube separated by a gas-filled gap. The zirconium pressure tube is designed to contain the high-pressure heavy-water coolant, and the gas-filled gap is designed to insulate the cool moderator from the hot coolant during normal operation. Figure 1

* Canadian natural-uranium fuelled, heavy-water moderated and cooled reactor
(CANada Deuterium Uranium-Pressurized Heavy Water)

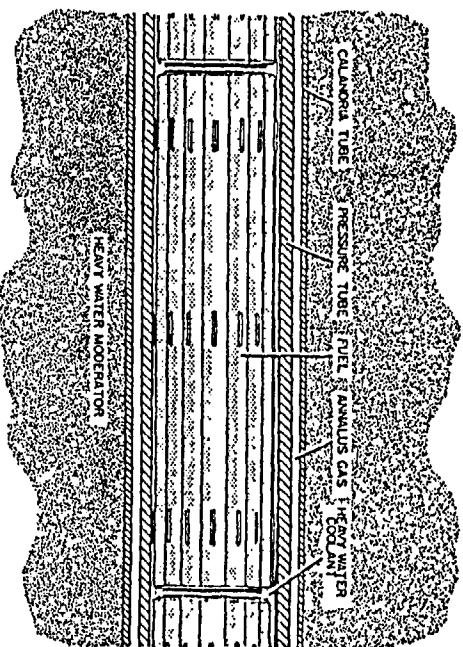


FIGURE 20 FUEL CHANNEL ARRANGEMENT

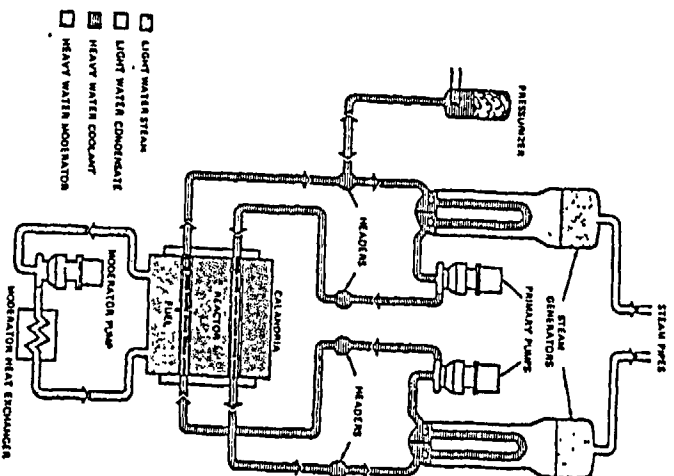


FIGURE 21 Simplified diagram of a CANDU fuel transport system

is a schematic of a CANDU fuel channel, and Figure 2 shows a typical arrangement of fuel channels in the reactor core. In this reactor design, each fuel channel is surrounded by cool heavy-water moderator that can act as a sink for heat generated in the fuel if other means of heat removal fail.

For example, if there were a loss-of-coolant accident (LOCA), and coincident impairment of the emergency coolant injection system, the heat generated in the fuel would be transferred mainly by thermal radiation to the pressure and calandria tubes, and then by boiling heat transfer to the moderator. Because radiation is the principal mode of heat transfer in this case, high temperatures in the fuel and pressure tube would result. At elevated temperatures, the pressure tube may deform into contact with the surrounding calandria tube. If its internal pressure were high, the principal deflection of the pressure tube would be radially outwards, and contact would occur completely around the circumference. If the internal pressure were low, the principal deflection would be downwards, and contact would occur in a strip along the bottom.

The initial contact between the hot pressure tube and the cold calandria tube would result in a "spike" in the heat flux to the moderator. The magnitude of the spike would depend on the pressure-tube temperature at contact and the contact conductance between the pressure and calandria tubes. The magnitude of the spike would determine the boiling regime on the calandria tube surface (either film boiling or nucleate boiling) and, thus, the rate of heat removal.

This paper describes a one-dimensional model developed to analyze the thermal-mechanical behaviour of a fuel channel when a pressure tube creeps radially into contact with its calandria tube. Also described are results of experiments [1] in which a pressure-tube segment is pressurized and heated at a constant rate until it contacts a surrounding calandria-tube segment. Predictions of the one-dimensional model are compared with the experimental results.

ANALYSIS

A coupled, one-dimensional thermal-mechanical computer model, CONTACT, was developed to analyze the fuel channel during and after pressure tube/calandria tube contact. The model predicts the deformation of the pressure tube prior to contact, the transfer of heat to the moderator after contact, and the mechanical deformation of the pressure tube and calandria tube following contact.

The deformation of the pressure tube prior to contact is calculated assuming that deformation is time-dependent (creep). The transverse creep rate in an internally pressurized tube is given by

$$\dot{\epsilon}_t = A \exp\left(\frac{-Q}{RT}\right) \sigma_t^n$$

where $\dot{\epsilon}_t$ is the transverse creep rate
 A is the creep constant
 Q is the creep activation energy
 R is the ideal gas constant
 T is temperature
 σ_t is transverse stress
 n is the stress exponent.

Substituting

$$\dot{\epsilon}_t = \frac{1}{r} \frac{dr}{dt} \quad \text{and} \quad \sigma_t = \frac{Pr}{w}$$

where r is the radius

t is time
P is the internal pressure
w is the wall thickness

and using the fact that the volume is constant, yields the following expression, which can be integrated numerically to obtain the inner radius of the pressure tube at any time t:

$$r = r_o + \int_{t_o}^t A \exp\left(\frac{-Q}{RT}\right) r \left(\frac{Pr^2}{r_o w_o}\right)^n dt$$

where r_o is the original inner radius
 w_o is the original wall thickness.

After contact, the pressure and calandria tubes creep at the same rate. Thus

$$A_c \exp\left(\frac{-Q_c}{RT_c}\right) \left(\frac{P_c r}{w_c}\right)^n = A_p \exp\left(\frac{-Q_p}{RT_p}\right) \left(\frac{(P-P_c)r}{w_p}\right)^n$$

where subscript c refers to the calandria tube, subscript p refers to the pressure tube, and r is the inner radius of the combined pressure/calandria tube.

Using the value of P determined from the above equation, the pressure-tube radius can be determined by numerically integrating

$$r = r_c + \int_{t_o}^t A_p \exp\left(\frac{-Q_p}{RT_p}\right) r \left(\frac{(P-P_c)r^2}{r_o w_o}\right)^n dt$$

Figure 3 is a schematic of the heat-transfer model used to determine the post-contact thermal behaviour. This model predicts the transient heat transfer along a radius through the pressure and calandria tubes. The heat-conduction equation is solved using a one-dimensional finite-element subroutine. The difficulties in

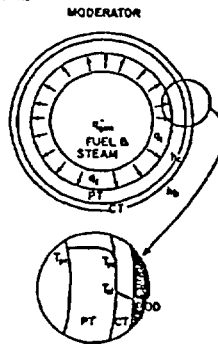


FIGURE 3 SCHEMATIC OF PRESSURE-TUBE/
CALANDRIA-TUBE CONTACT HEAT-
TRANSFER PROBLEM

analyzing the problem lie in specifying the boundary conditions. The boundary condition on the inside surface of the pressure tube is an incident heat flux, which is determined by the heat generated in the fuel due to the decay heat and the reaction between zirconium and steam.

The heat flux at the outside surface of the calandria tube is described by

$$q_o = h_b(T_{co} - T_B)$$

where q_o is the heat flux to the moderator
 h_b is a pool-boiling heat-transfer coefficient
 T_B is the outside temperature of the calandria tube
 T_{co} is the bulk moderator temperature.

The heat-transfer coefficient, h_b , depends on the type of boiling that occurs with the given subcooling, the saturation temperature, the outside surface temperature of the calandria tube, and the heat flux. In the model, h_b is defined for four regimes [1,2]: subcooled, nucleate boiling, transition boiling, and film boiling. The equations were based on experiments by Thibault [3], Rohsenow [4], Bradfield [5], and Dhir and Purohit [6], using large diameter horizontal cylinders.

At the interface between the pressure and calandria tubes, the contact conductance determines the rate at which the heat stored in the pressure tube is transferred to the moderator immediately after contact; thus, it also affects the pool-boiling regime. The contact conductance, h_c , is described by the following relationship:

$$q_c = h_c(T_{po} - T_{ci})$$

where q_c is the heat flux between the tubes
 h_c is the contact conductance
 T_{po} is the temperature of the outer surface of the pressure tube
 T_{ci} is the temperature of the inner surface of the calandria tube.

Correlations have been developed that use the surface parameters (hardness, size and shape of surface asperities), the contact pressure and the type of gas between the tubes to predict the contact conductance [7,8]. However, when these predicted values are used in the model CONTACT, incorrect heat flows are predicted for experiments in which pressure-tube segments are deformed circumferentially into contact with surrounding calandria-tube segments. In this paper, the results of such experiments are compared with predictions from the model, based on assumed values of contact conductance. From these comparisons, an improved value for the contact conductance is obtained.

EXPERIMENTS

The experimental apparatus, shown in Figure 4, consisted of a pressure-tube segment, 1.5 m long, surrounded by a calandria-tube segment, 1.8 m long. Inside the pressure tube was a tubular electric heater, 1.0 m long. The apparatus was mounted inside a water tank with viewing ports in the sides, with the water being heated by submerged steam lines.

The experiments were performed by heating the water to the desired temperature, internally pressurizing the pressure tube, and then heating the pressure tube by applying power to the heater.

In each experiment, cine films (at 80 frames per second) were taken of the outer surface of the calandria tube. The type of boiling was noted visually, and the surface temperature of the calandria tube was monitored by 18 thermocouples spot-welded to the surface. Film boiling left a very distinct oxidized area on the surface.

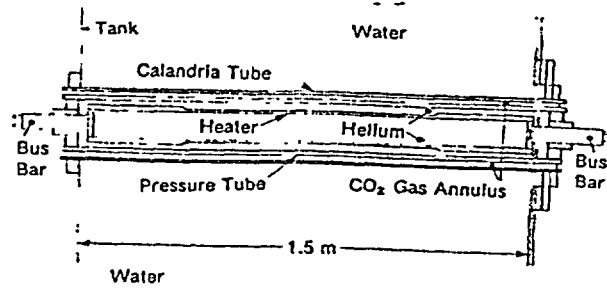


FIGURE 4 EXPERIMENTAL ARRANGEMENT

The experimental conditions and the resulting contact temperatures are listed in Table I. The pressure-tube temperature at contact is a function of the internal pressure of the tube and its heating rate (controlled by the heater power).

TABLE I
Experimental Conditions

Test	Power (kW)	Pressure (MPa)	Water Temperature (°C)	Contact Temperature (°C)
1	66	4	67	750
2	57	4	85	750
3	66	1	74	850
4	66	1	67	850
5	57	2.5	77	750
6	62	4	81	750
7	66	2.5	77	820
8	66	2.5	77	800
9	62	1	80	900
10	62	4	85	750
11	62	2.8	85	820
12	84	1	85	1000
13	28	0.5	71	1070
14	- *	1.1	71	825
15	- *	0.8	71	900
16	54	2.0	99	800

* Power varied to obtain the desired contact temperature.

Figure 5 summarizes the results of the experiments. Each experiment is plotted as a point, with the pressure-tube temperature at contact as the abscissa and the temperature of the pool of water surrounding the calandria tube as the ordinate. The

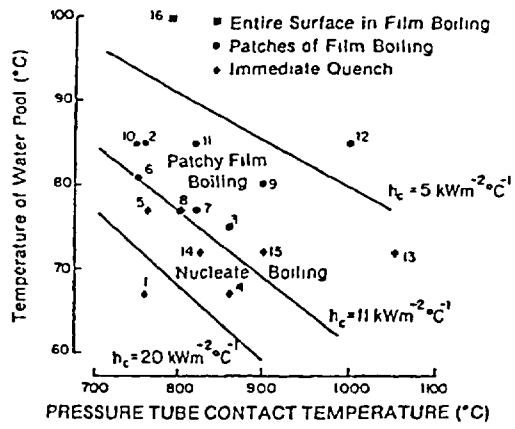


FIGURE 5 SUMMARY OF EXPERIMENTAL RESULTS

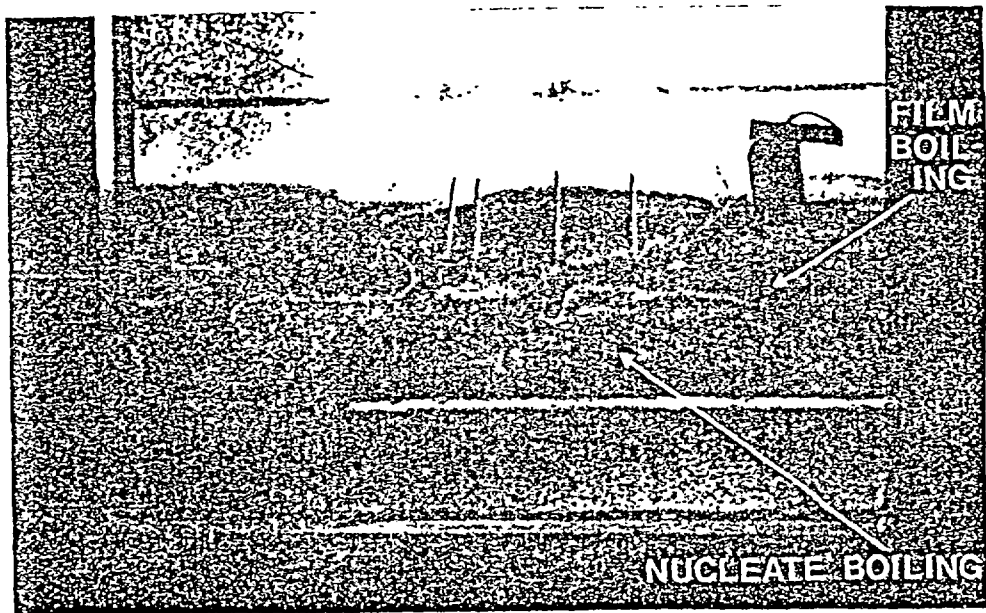


FIGURE 6 BOILING ON CALANDRIA TUBE SURFACE (EXPERIMENT 11)

type of boiling on the calandria-tube surface during the experiment is denoted by the symbols. Also shown in Figure 5 are lines for different assumed contact conductances, showing where the peak heat flux to the moderator at contact, as predicted by the model, equals the critical heat flux. The peak heat flux depends upon the stored energy of the pressure tube and the contact conductance between the pressure tube and calandria tube, while the critical heat flux depends upon the subcooling of the water. Film boiling occurs when the peak heat flux exceeds or equals the critical heat flux; thus, film boiling is predicted for points plotted on the graph above the line if the assumed contact conductance is correct.

In each experiment, the internal pressure was held constant at a value ranging from 0.5 to 4.0 MPa. The results plotted in Figure 5 indicate that, for all of the experiments with an internal pressure of 1 MPa or greater, the maximum local contact conductance was $11 \text{ kW}/(\text{m}^2 \cdot ^\circ\text{C})$ since the type of boiling on the surface was correctly predicted using this value. The patchiness of the film boiling indicates that the contact conductance was less than this maximum for most areas around the circumference. In the experiments performed at pressures of 0.7 and 0.5 MPa, the maximum contact conductance was less than $11 \text{ kW}/(\text{m}^2 \cdot ^\circ\text{C})$, since film boiling would be predicted, and it did not occur. The use of this method to determine the contact conductance assumes that the incident heat flux, determined from the known heater power, and the heat-transfer coefficient at the surface of the calandria tube used in the model, are correct.

In nine of the experiments, film boiling occurred in patches that did not completely cover the area of contact. Figure 6 shows the patches of nucleate and film boiling that occurred in a typical experiment. This behaviour is related to the variation of contact time, temperature, and pressure at a given axial location. The variation of these parameters causes the contact conductance to vary around the circumference.

The patches of film boiling rewet, even when the average incident heat flux is higher than the minimum heat flux required to maintain film boiling. The rewetting is caused by the axial and circumferential conduction of heat through the pressure and calandria tubes from areas of film boiling to areas of nucleate boiling.

To further check the assumptions used to derive the one-dimensional model, an experiment was performed with film boiling completely around the calandria-tube surface. Table 1 lists the conditions used in the experiment (number 16). To obtain this uniform film boiling and the resultant uniform temperatures, the experiment was performed in nearly saturated water. The critical heat flux [9] was a factor of two lower than that of the previous experiments, enabling film boiling to be established over the complete area of contact. The value of subcooling for this experiment was much lower than that expected in the moderator of a CANDU reactor.

Figure 7 shows the temperature of the pressure tube during the experiment in which film boiling occurred completely around the circumference. Figure 8 shows the temperatures obtained from the ring of thermocouples at the axial center of the calandria tube. In the experiment, the power was held constant at 54 kW/m for 250 seconds; then it was increased to 56 kW/m. At 300 seconds, the power was increased to 62 kW/m. At 340 seconds, the internal heater failed and the experiment was terminated. The temperature traces shown in Figures 7 and 8 show that the whole circumference of the calandria tube was surrounded by a steam film and that the behaviour could be reasonably approximated by a one-dimensional model.

Figure 9 compares the average pressure-tube and calandria-tube temperatures obtained during this experiment with the values predicted using the one-dimensional model with a contact conductance of $11 \text{ kW}/(\text{m}^2 \cdot ^\circ\text{C})$ and assuming that the incident heat flux was uniform. The pressure tube heated up very rapidly prior to contact. Contact occurred at 78 seconds, when the pressure-tube temperature was 800°C . The model predicted the heatup very well and the correct contact time and temperature.

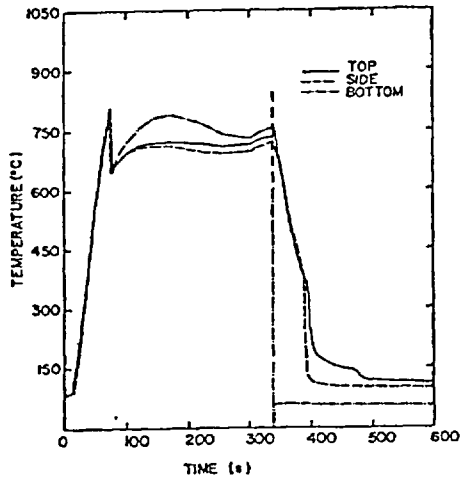


FIGURE 7 TIME VARIATION OF PRESSURE-TUBE TEMPERATURE

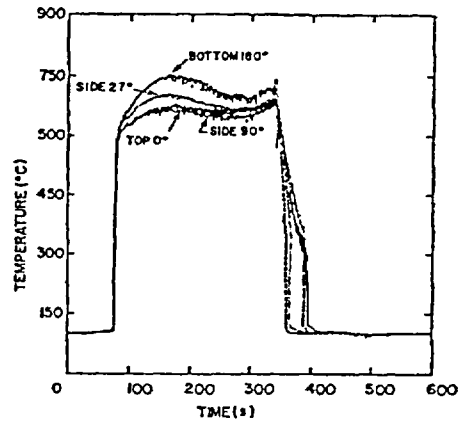


FIGURE 8 TIME VARIATION OF CALANDRIA-TUBE TEMPERATURE

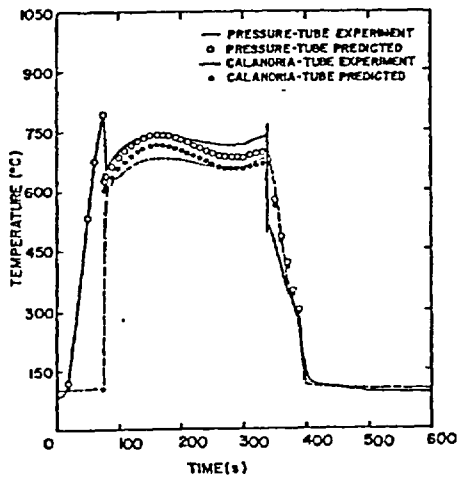


FIGURE 9 COMPARISON OF EXPERIMENTAL RESULTS WITH PREDICTIONS

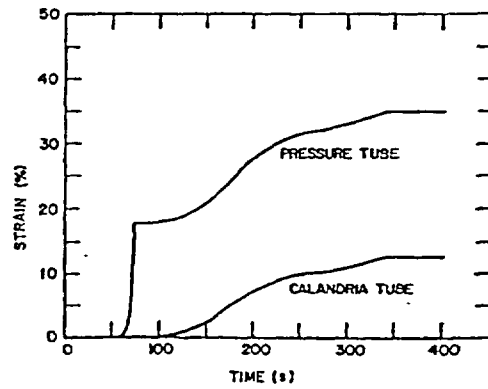


FIGURE 10 PREDICTED STRAIN

Immediately after contact, the pressure-tube temperature fell rapidly and the calandria-tube temperature increased rapidly. Film boiling was established on the surface of the calandria tube. The model predicted this behaviour, but the predicted pressure-tube temperature was lower than that measured and the predicted calandria-tube temperature was greater than that measured, indicating that the assumed value of contact conductance ($11 \text{ kW}/(\text{m}^2 \cdot ^\circ\text{C})$) was higher than the actual value. The temperature of the tubes then slowly increased to a maximum at 165 seconds. This maximum occurred when the heat transmitted through the steam film equalled the heat generated inside the pressure tube. While the calandria tube deformed radially, its surface area increased, whereas the heat flux from its surface depended only on the surface temperature. Therefore, the total heat transferred to the surrounding water increased and the calandria-tube temperature decreased. At 250 seconds, the power was increased to $56 \text{ kW}/\text{m}$, and the rate at which the temperature was falling decreased. At 300 seconds, the power was increased to $62 \text{ kW}/\text{m}$ and the temperatures increased. The model correctly predicted the effects of these power changes. The test was terminated when the heater failed at 340 seconds. Figure 10 shows the strain predicted by the model. The good agreement between the measured and calculated temperatures implies that the strain calculations are reasonably accurate because of the sensitivity of the heat transfer to the surface area. The final deformation of the calandria tube was 15%, close to the calculated value of 13%.

CONCLUSIONS

- (1) The computer model CONTACT gave correct qualitative predictions of the occurrence of film boiling for experiments with an internal pressure $>1 \text{ MPa}$, when a value of $11 \text{ kW}/(\text{m}^2 \cdot ^\circ\text{C})$ was used as the contact conductance.
- (2) The model successfully predicted the behaviour of experiments in which multidimensional effects were not significant. In those in which multidimensional effects were significant, pressure- and calandria-tube temperatures were over-predicted.
- (3) In all of the experiments with subcooling of 14°C or greater, film boiling occurred in patches. These patches eventually rewet because of conduction through the tubes from regions of film boiling to regions of nucleate boiling.
- (4) The purpose of these experiments was not to simulate reactor conditions, but to obtain an understanding of the thermal-mechanical behaviour of a calandria tube as a result of boiling on the external surface. At the expected degree of subcooling in a CANDU reactor, the experiments show that film boiling is unlikely to occur, that heat transfer to the moderator is sufficient to remove the heat generated in the fuel channels and that calandria tubes will not deform.

ACKNOWLEDGEMENT

The financial support of this work by Ontario Hydro is gratefully acknowledged.

REFERENCES

1. G.E. GILLESPIE, "An Experimental Investigation of Heat Transfer from a Reactor Fuel Channel to Surrounding Water", Proceedings of the Canadian Nuclear Society Annual Conference, June 10, 1981.
2. G.E. GILLESPIE, R.G. MOYER, R.S.W. SHEWFELT, "Experiments to Investigate Moderator Boiling when a Pressure Tube Contacts its Calandria Tube", unpublished Report WNRE-401, Whiteshell Nuclear Research Establishment (1980).

. ()

3. J. THIBAUT, "Boiling Heat Transfer Around a Horizontal Cylinder and in Tube Bundles", Ph.D. Thesis, McMaster University, Hamilton Ontario, 1978.
4. W.M. ROSENOW, ed., Developments in Heat Transfer, The MIT Press, Cambridge, Massachusetts, (1964) p. 216.
5. W.S. BRADFIELD, "On the Effect of Subcooling on Wall Superheat in Pool Boiling", Journal of Heat Transfer 89, 269 (1967).
6. V.K. DHIR and G.P. PUROHIT, "Subcooled Film-Boiling Heat Transfer from Spheres", Nuclear Engineering and Design 47, 49 (1978).
7. M.M. YOVANOVICH, "New Contact and Gap Conductance Correlations for Conforming Rough Surfaces", AIAA 16th Thermophysics Conference, AIAA-81-1164, June 1981.
8. M.H. SCHANKULA and D.W. PATTERSON, "A Review of Thermal Contact Conductance Correlations for Pressure Tube-Calandria Tube Contact", Unpublished Report WNRE-155, Whiteshell Nuclear Research Establishment (1982).
9. L.A. BROMLEY, "Heat Transfer in Stable Film Boiling", Chemical Engineering Progress 46, 221 (1950).

Validation of the MODTURC_CLAS Moderator Circulation Code for CANDU 9 Steady-State and Transient Conditions

L.N. Carlucci, V. Agranat*, G.M. Waddington, H.F. Khartabil and J Zhang**

*Atomic Energy of Canada Ltd., Chalk River Laboratories
Chalk River, Ontario, Canada, K0J 1J0*

** Currently with CHAM North America, Toronto, Ontario*

***Atomic Energy of Canada Ltd., Mississauga, Ontario*

1. INTRODUCTION

Knowledge of the moderator flow and temperature distributions within the calandria vessel of a CANDU reactor is particularly important for the safety analysis of certain postulated accident scenarios where the moderator is required to provide a backup heat sink to the emergency core cooling system.

The CFD computer code, MODTURC_CLAS, is employed by the CANDU industry to predict moderator flow and temperature distributions in a range of CANDU moderator designs. It is based on the commercial general-purpose CFD code, TASCflow, developed by AEA Technology Engineering Software Ltd. (formerly Advanced Scientific Computing Ltd.) [1]. The code solves the coupled conservation equations of mass, momentum, thermal energy, turbulence kinetic energy and turbulence energy dissipation rate. Buoyancy effects are modelled using the Boussinesq approximation. The effect of the fuel channels is modelled by using a uniform isotropic porosity to account for the flow-volume reduction, and an empirically based friction-factor correlation to model the distributed hydraulic resistance to the mean flow.

In the recent CANDU 9 design (Figure 1), the moderator is introduced into the calandria vessel through a system of twelve downward-pointing nozzles located symmetrically on both sides of the calandria shell, at about the 10 45 o'clock position. Each nozzle is fitted with fan-shaped, multicompartment diffusers that emit flat, spreading jets of fluid in the reflector region, approximately parallel to the calandria wall. These jets meet at the bottom of the core at approximately the vessel's vertical plane of symmetry (the 6 o'clock position), and turn upward to flow through the core region to remove the heat generated by direct deposition of neutron and gamma energy to the moderator. The hot moderator fluid is removed via four outlet ports, symmetrically located on the vessel wall at approximately the 11:00 o'clock position, passed through external heat exchangers, and returned to the inlet nozzles.

This paper describes the validation of the MODTURC_CLAS code (version 2.2.1a) against data from the Moderator Test Facility (MTF), designed to simulate representative CANDU 9 steady-state and transient moderator flow conditions.

2. MTF SCALING CONSIDERATIONS

To validate the MODTURC_CLAS code, it is desirable to use data from experiments that relate, as far as possible, to the actual geometry and processes occurring within the moderator. The MTF was designed and built to conduct such experiments. It is an integral test facility, having all the key characteristics of a

typical CANDU reactor calandria vessel, with all linear dimensions being ¼ of the corresponding physical values in the CANDU 9 reactor [2].

The scale was arrived at by balancing two competing requirements. It had to be large enough to ensure turbulence throughout the vessel, so that all the governing phenomena in the full-scale reactor calandria play essentially the same role in the reduced scale. At the same time, the size had to be economically viable in terms of capital and operating costs, particularly in aspects related to power and flow requirements, which can increase dramatically with increased scale.

Once the scale was chosen, dimensionless groups, derived by non-dimensionalizing the governing equations, were used to select the appropriate MTF operating conditions to simulate the corresponding full-scale reactor conditions.

The moderator flow and temperature distributions are governed by the following dimensionless groups: dimensionless volumetric heat source,

$$\dot{Q} = \frac{QD}{\rho C_p V \Delta T} \quad (1)$$

Archimedes number, which characterizes the ratio of buoyancy to inertia forces,

$$Ar = \frac{g\beta\Delta TD}{V^2} \quad (2)$$

Reynolds number,

$$Re = \frac{\rho VD}{\mu} \quad (3)$$

and Prandtl number,

$$Pr = \frac{C_p \mu}{\lambda} \quad (4)$$

Q^* and Ar were exactly matched for the MTF and the CANDU 9 calandria vessel, as they were identified to be the primary similarity parameters in the MTF scaling. The thermophysical properties of light water in the MTF and heavy water in the reactor calandria are similar enough to result in close Prandtl numbers similarity. Because of the ¼ length scale chosen for the MTF, it was not possible to achieve Reynolds number similarity. However, as mentioned, the scale was chosen large enough to obtain turbulent flow throughout the MTF vessel (as later confirmed from flow visualization and measurement of turbulence intensities). It can be shown that under such conditions, the relative levels of turbulent mixing in the MTF and reactor calandria, as characterized by the non-dimensional momentum and thermal diffusivities, are virtually independent of the Reynolds number.

To minimize electric power requirements for the calandria tube heaters used to simulate the volumetric neutron and gamma heating in the reactor, the outlet-to-inlet temperature difference ΔT for the MTF was

chosen to be 1/3 the reactor value. This was judged to be large enough to allow for sufficiently accurate temperature measurements, taking into account known measurement instrument errors. With this choice of ΔT , the above equations for Ar and Q^* were used to calculate the total power and inlet flow rate in the MTF.

3. MODTURC_CLAS MODEL

3.1 Phenomena - Modelling Aspects

As mentioned, MODTURC_CLAS solves the time-averaged conservation equations of mass, momentum and energy, coupled with the standard k - ϵ model of turbulence. The following is a brief description of modelling aspects of the key phenomena governing moderator circulation.

3.1.1 Moderator Buoyancy

Moderator buoyancy, resulting from density variations, is accounted for via the gravitational force term in the momentum equation, which acts in the vertical z direction. By redefining the pressure in the momentum equation as the sum of the static pressure and a hydrostatic component based on a reference density:

$$p = p_s + \rho_r g_z z \quad (5)$$

the buoyancy force per unit volume can be expressed as:

$$S_{b,z} = \gamma(\rho - \rho_r)g_z \quad (6)$$

The density difference in the above equation can be expressed in terms of the corresponding temperature difference by introducing the volumetric thermal expansion coefficient calculated from

$$\beta = -\frac{1}{\rho_r} \left(\frac{\partial \rho}{\partial T} \right)_p \cong -\frac{1}{\rho_r} \left(\frac{\rho - \rho_r}{T - T_r} \right) \quad (7)$$

Using the above to substitute for the density difference in Equation (6), the buoyancy force per unit volume becomes:

$$S_{b,z} = -\gamma\beta\rho_r(T - T_r)g_z \quad (8)$$

The above linearization of the buoyancy term, known as the Boussinesq approximation, is used in the MODTURC_CLAS code. MODTURC_CLAS can accommodate either a constant or temperature-dependent thermal expansion coefficient. For the validation work reported herein, a constant value was used.

3.1.2 Turbulence and Inlet Jet Development

To model turbulence effects on moderator inlet jet development as well as on the overall flow in the core and reflector regions, MODTURC_CLAS uses the two-equation k - ϵ model for turbulence, together with wall functions to account for boundary-layer effects near the wall. Turbulent Reynolds stresses and turbulent heat fluxes are then estimated using effective viscosities and thermal conductivities, multiplied by mean velocity and temperature gradients, respectively.

The effective viscosity is defined by:

$$\mu_e = \mu + \mu_t \quad (9)$$

where the turbulent viscosity is calculated from the turbulent kinetic energy and the energy dissipation rate using the relation:

$$\mu_t = c_\mu \rho_r \frac{k^2}{\varepsilon} \quad (10)$$

The effective thermal conductivity is in turn calculated as the sum of molecular and turbulent components from:

$$\lambda_e = \lambda + \lambda_t = C_p \left(\frac{\mu}{Pr} + \frac{\mu_t}{\sigma_t} \right) \quad (11)$$

The $k-\varepsilon$ model works well in flows with one dominant mechanism for generating turbulence. However, it has been established that the model is often deficient in complex flows in which other aspects are introduced, e.g., streamwise curvature (such as the calandria vessel wall), pressure gradients and buoyancy forces. The deficiencies are largely attributed to the formulation's direct relationship between the Reynolds stresses and the mean velocity gradient [3]. As well, because a porous media approach is used to model the effects of the calandria tubes (see below), the $k-\varepsilon$ model, as implemented in MODTURC_CLAS, does not account for any additional turbulence generated by the interaction of the moderator flow with the calandria tubes.

There are a number of empirical constants used in the $k-\varepsilon$ model. The recommended values are listed in the table below [3].

c_μ	$c_{1\varepsilon}$	$c_{2\varepsilon}$
0.09	1.44	1.92

Sensitivity studies have shown that predictions can be quite sensitive to the values of $c_{1\varepsilon}$ and $c_{2\varepsilon}$. For example, a 5% change in either constant can result in a 20% change in the spreading rate of a jet [3]. All analyses reported herein, except some sensitivity cases (see Section 4), were done using these values as defaults.

3.1.3 Interaction with Calandria Tubes

Because of limits to current computing resources, state-of-the art calculations of flows in large tube banks do not involve detailed calculations around individual tubes. Rather, the approach used in MODTURC_CLAS and other codes that model similar problems is to solve the governing partial differential equations over the domain and treat the core region as a porous medium. The latter is characterized by an isotropic porosity, to reflect the average reduction in local fluid volume, and a distributed resistance, to reflect the hydraulic skin friction and drag characteristics of the calandria tube array.

The isotropic porosity in the core region is calculated from:

$$\gamma = 1 - \frac{\pi}{4} \left(\frac{d}{p} \right)^2 \quad (12)$$

The momentum sink per unit volume, to account for pressure losses in the calandria tube bank, is calculated from

$$S_v = -\frac{1}{2} \frac{f}{l_{rom}} \rho_r \gamma^3 \bar{V} V f(\Psi) \quad (13)$$

in the above, the distance between tube rows is calculated from:

$$l_{rom} = p \cos(\alpha) \quad (14)$$

where α is the angle between the flow direction and either the horizontal or vertical component of the flow, whichever is dominant. For in-line flow, α is equal to 0.

The function $f(\Psi)$ is introduced to account for the pressure loss due to flow along the tube axis (i.e., parallel flow), which is lower than in cross-flow.

The cross-flow friction factor for the relatively large pitch-to-diameter ratio typical of CANDU calandria tubes, has been determined from tests on tubes arranged in in-line and staggered arrangements in the Stern two-dimensional moderator test facility [4]. It is given by

$$f = 4.5626 \text{Re}_f^{-0.1655} \quad (15)$$

where Re_f is the Reynolds number based on the tube diameter and free-stream or approach velocity

$$\text{Re}_f = \frac{\rho_r V_f d}{\mu} = \frac{\rho_r \gamma W d}{\mu} \quad (16)$$

3.1.4 Energy Deposition in the Moderator

During normal operation of the reactor, thermal energy is deposited directly into the moderator liquid as the result of the slowing down of neutrons from the fission process, as well as the absorption of gamma rays and beta particles from fission products and various sources. The neutron heating component dominates during normal reactor operation; therefore the local volumetric heat generation rate is approximately proportional to the local neutron flux and, hence, reactor power. During a transient, such as a large LOCA, the neutron component rapidly decreases as the reactor is tripped, and the principal source of heating is from gamma rays due to fission product decay, along with heat transferred from the fuel channels and other components. The heat transferred from the fuel channels may become significant if pressure tube ballooning occurs. The energy deposition from any of the above processes is determined from physics and fuel channel calculations and modelled in MODTURC_CLAS by the specification of a volumetric heat generation rate in the energy equation:

$$S_T = f(Q, x, y, z, t) \quad (17)$$

In the MTF, energy deposition to the moderator fluid is simulated by the direct electrical heating of the calandria tubes, with the heat transferred to the light-water coolant, representing the heavy-water moderator, by a combination of natural and forced convection. The details of the heat transfer process from the individual calandria tube surfaces to the coolant are not modelled; instead, the local deposition of thermal energy from the electric heating is included as a local volumetric heat source (i.e., Equation (17)), the same way as in an operating reactor.

3.2 Boundary Conditions

Boundary conditions are as follows: at the inlets, a uniform fluid velocity, temperature, k and ε are specified; at the outlets, the pressure is given; and at the vessel walls, the no-slip adiabatic conditions are used. The values of k and ε at the inlets are expressed in terms of the inlet turbulence intensity and the eddy length scale, taken as being 0.05 and 0.005 m, respectively.

3.3 Computational Grid and Solution

The computational grid used is the butterfly design grid (see Figure 2). The base grid applied in most simulations comprises $69 \times 82 \times 24 = 135\,792$ nodes, with 69 being the number of cross-sectional planes in the axial direction, and $82 \times 24 = 1968$ being the number of nodes in each cross-sectional plane. The base grid size was chosen based on the results of grid independence tests involving three other nodalizations, two finer than the base grid, and one coarser.

The MODTURC_CLAS equations are solved by iterations until user-specified convergence criteria are satisfied.

4. RESULTS AND DISCUSSION

In all, the MTF was used to carry out five steady-state and two transient integral tests. The steady-state tests covered a range of possible steady-state operating conditions, including isothermal, nominal flow and power for two outlet-to-inlet temperature differences, nominal flow and power with inlet flow asymmetry, and reduced flow and power with inlet flow asymmetry to simulate one-pump operation. The transient tests were designed to simulate, in a stylized way, the main features of two postulated accident scenarios: a large LOCA with LOECC (Loss Of Emergency Core Cooling), and a large LOCA with loss of Class IV power. Measurements during the steady-state tests included local velocities (magnitudes and turbulence intensities) and temperatures throughout the vessel using moveable probes, whereas measurements during the transients were limited to coolant temperatures throughout the vessel using fixed probes.

All of the above tests were simulated and assessed with MODTURC_CLAS. In addition a number of additional simulations of the nominal steady state flow and power test were carried out to investigate sensitivity of flow and temperature predictions to grid spacing; reduction of nozzles flow areas; and changes to the turbulence model constants, hydraulic resistance of the calandria tube bank, and axial variation of the volumetric heating rates.

Figures 3 and 4 compare predicted and measured temperature distributions and velocity vectors in the middle cross-section of the MTF vessel for the steady-state test with nominal flow and power conditions. The figures illustrate the typical patterns of flow and temperature distributions in the MTF core: the fluid

flow is predominantly vertical and the temperature distribution is stratified, i.e., the fluid temperature increases with elevation. The asymmetry in the velocity measurements at the vessel bottom is attributed to a combination of the highly unsteady nature of the turbulent jets and possible geometric misalignments of the inlet nozzles due to manufacturing tolerances. Code predictions do not show this asymmetry because the k - ϵ model accounts for only the mean behaviour of the turbulent flow and not its unsteady nature, and the nozzle geometries on each side of the vessel were assumed symmetric.

Figure 5 shows good agreement between the predicted and measured time-variation of the liquid temperature in the upper part of the core during the stylized large LOCA+LOECC experiment.

In general, the code predictions, particularly the location and magnitude of the maximum temperature, were found to be relatively insensitive to the changes in the parameters investigated, with one exception. Figure 6 shows that better agreement between measured and predicted temperatures in the lower part of the core is obtained when the turbulence model parameter $c_{1\epsilon}$ is decreased by 10% and $c_{2\epsilon}$ is increased by 10%. These results suggest that the use of the default parameters in the k - ϵ model leads to calculated jet entrainments that are too low, and, hence, result in the consistent underprediction of temperatures in the lower part of the vessel. A possible reason is that the interaction of the jets with the calandria tubes, which is not accounted for in the k - ϵ model, could lead to more entrainment of core fluid by the jets.

Overall, results from the validation of MODTURC_CLAS against the MTF data for representative CANDU 9 steady-state and transient conditions indicate good agreement between the code predictions and measurements, specifically

- The measurements and code predictions of velocity and temperature fields confirm the stability of the CANDU 9 moderator system over a wide range of conditions, including significant flow asymmetry resulting from one-pump operation.
- The measurements and code predictions show the temperature to be monotonically increasing from the bottom to the top of the core (Figure 3). In general, there is good agreement between the measured and predicted temperatures. There is a slight tendency to underpredict temperatures at the bottom of the vessel, possibly due to insufficient jet entrainment, as modelled by the code. However, agreement improves near the top, where the maximum temperature is reached. The difference between the predicted and measured maximum temperatures is less than 1°C.
- The measurements and code predictions indicate that the overall flow and temperature patterns are determined primarily by the forced flow induced by the inlet jets, as they flow and entrain core liquid toward the bottom of the vessel, collide, and induce a stable upward flow through the core, assisted by buoyancy forces (Figure 4).
- The measurements and code predictions indicate that the temperature field and, to a lesser extent, the velocity field are largely two-dimensional in the core cross-section, with decreasing axial variation as the top of the core is reached.

5. CONCLUSIONS

- The CFD code, MODTURC_CLAS, has been validated against MTF data representing a range of CANDU 9 nuclear reactor conditions.

- Good quantitative agreement between the code predictions of three-dimensional water temperature distribution in the MTF vessel and the temperature measurements has been obtained for both steady-state and transient simulations.
- The predicted and measured flow and temperature distribution patterns in the MTF vessel have confirmed the stability of the CANDU 9 moderator system.

6. ACKNOWLEDGEMENTS

The authors would like to acknowledge the contributions of A.O. Banas in the initial stage of the project, J.K. Szymanski of Ontario Power Generation for providing details of the resistance model and assistance in running MODTURC_CLAS, and M. Ivanovic of AEA Technology Engineering Software Ltd. for conducting the grid independence tests.

7. NOMENCLATURE

Ar	=	Archimedes Number
C	=	specific heat at constant pressure
d	=	calandria tube diameter
D	=	calandria vessel diameter
f	=	tube bank friction factor
g	=	gravitational constant
l	=	distance between tube rows
k	=	turbulent kinetic energy
p	=	pressure; pitch
Q	=	volumetric heat sources
Pr	=	Prandtl number
Re	=	Reynolds number
S	=	volumetric source term
t	=	time
\vec{V}, V	=	velocity vector and magnitude
z	=	co-ordinate along the vertical direction
α	=	angle
β	=	coefficient of volume expansion
ϵ	=	energy dissipation rate
γ	=	isotropic porosity
λ	=	liquid thermal conductivity
μ	=	liquid dynamic viscosity
σ	=	turbulent Prandtl number
ρ	=	liquid density

Subscripts

b = buoyancy
 e = effective
 fs = free stream
 r = reference
 s = static
 t = turbulent
 V = velocity
 z = vertical z direction
 T = temperature

8. REFERENCES

1. "TASCflow Theory Documentation", Version 2.2, 1993 April, Advanced Scientific Computing Ltd., Waterloo, Ontario, Canada.
2. H F. Khartabil, et al. "Three-Dimensional Moderator Circulation Experimental Program for Validation of CFD Code MODTURC_CLAS," paper in 21st Nuclear Simulation Symposium, Ottawa, Ont , 2000, September 24-26.
3. W. Rodi, "Turbulence Models and Their Application in Hydraulics – A State of the Art Review," University of Karlsruhe Report SFB 80/T/127, 1978 May.
4. G I. Hadaller, R.A Fortman, J.K Szymanski, W.I. Midvidy and D.J. Train, "Frictional Pressure Drop for Staggered and In-Line Tube Banks with Large Pitch to Diameter Ratio", Proceedings of the 17th Annual CNS Symposium on Reactor Dynamics and Plant Control, Kingston, Ontario, Canada, 1992 August.

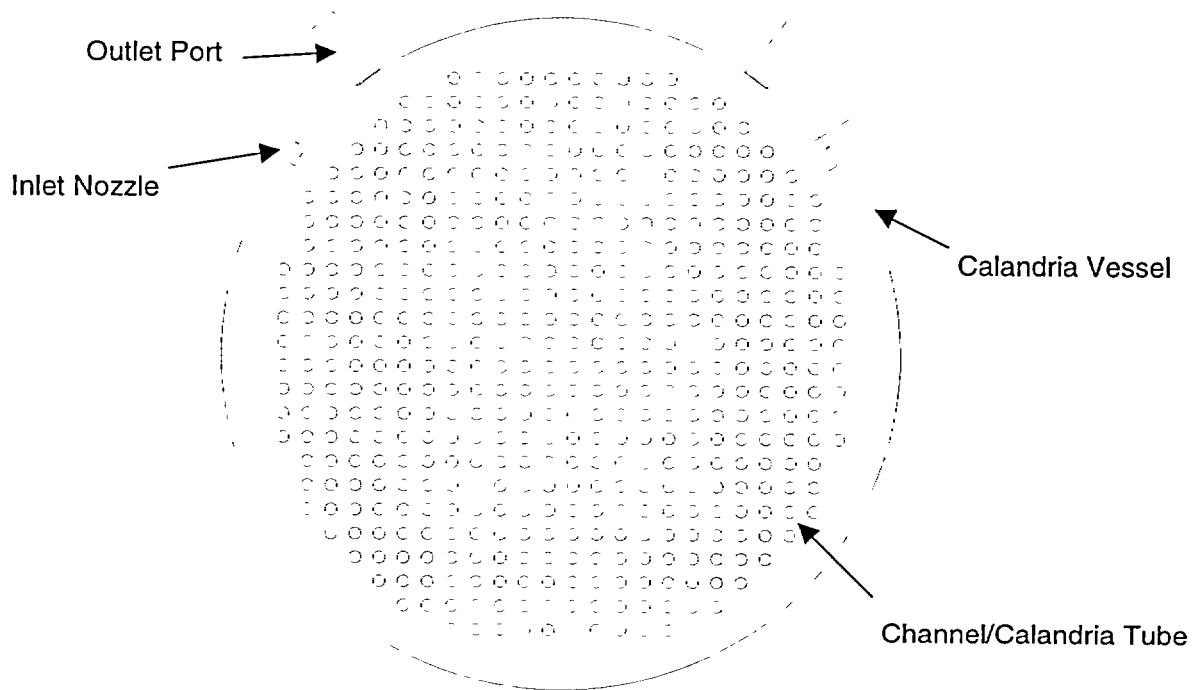


Figure 1: Simplified cross-sectional view of a CANDU 9 calandria vessel

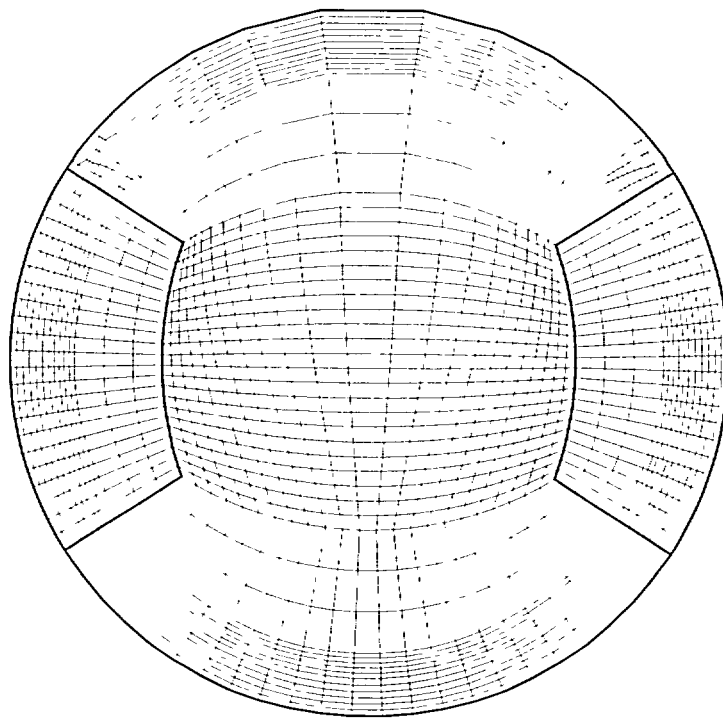


Figure 2: Cross-section of base grid at inlet nozzle plane

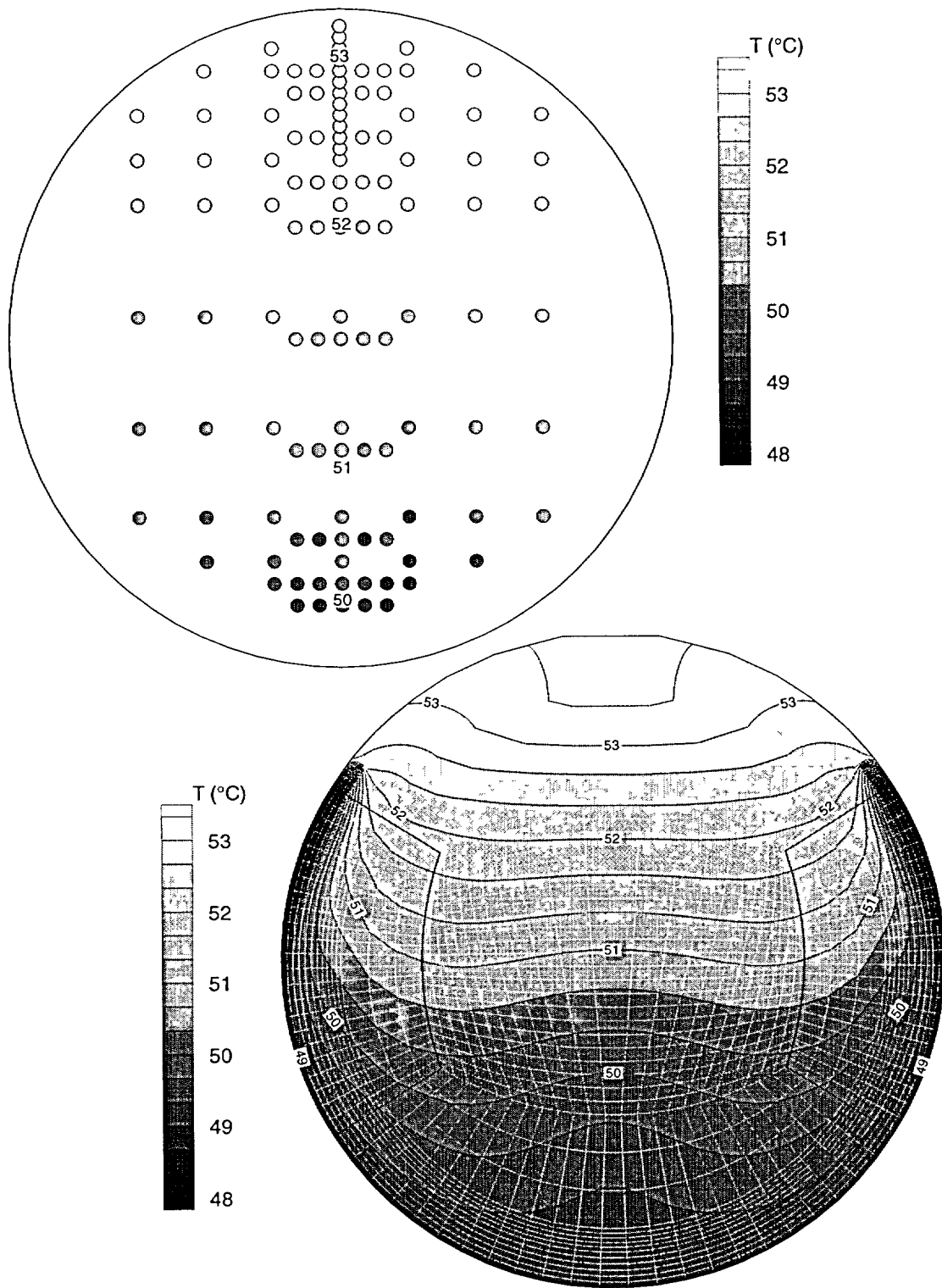


Figure 3: Comparison of predicted (lower) and measured (upper) temperature distributions in middle cross-section for nominal flow and power conditions

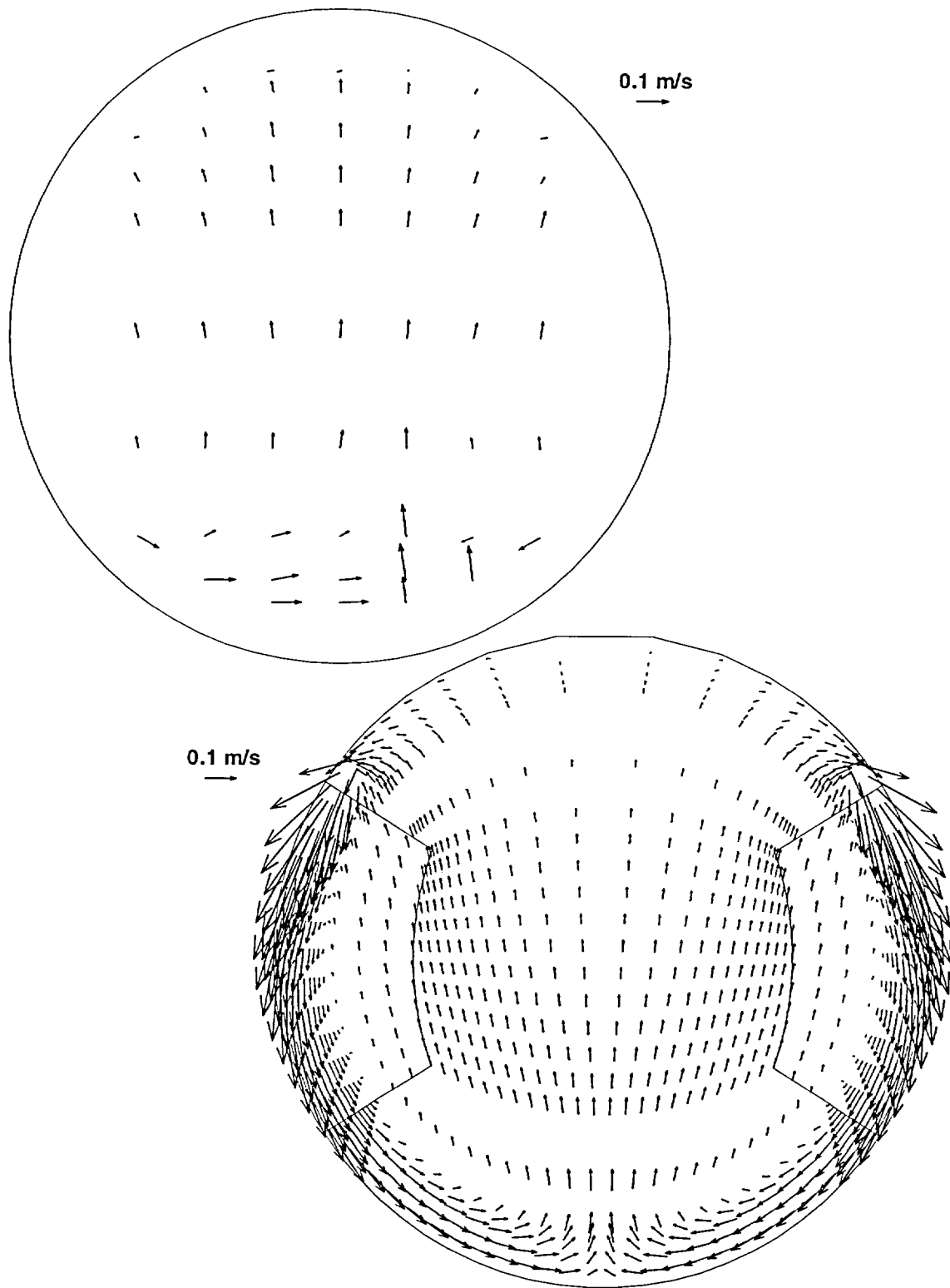


Figure 4: Comparison of predicted (lower) and measured (upper) velocity vectors in middle cross-section for nominal flow and power conditions

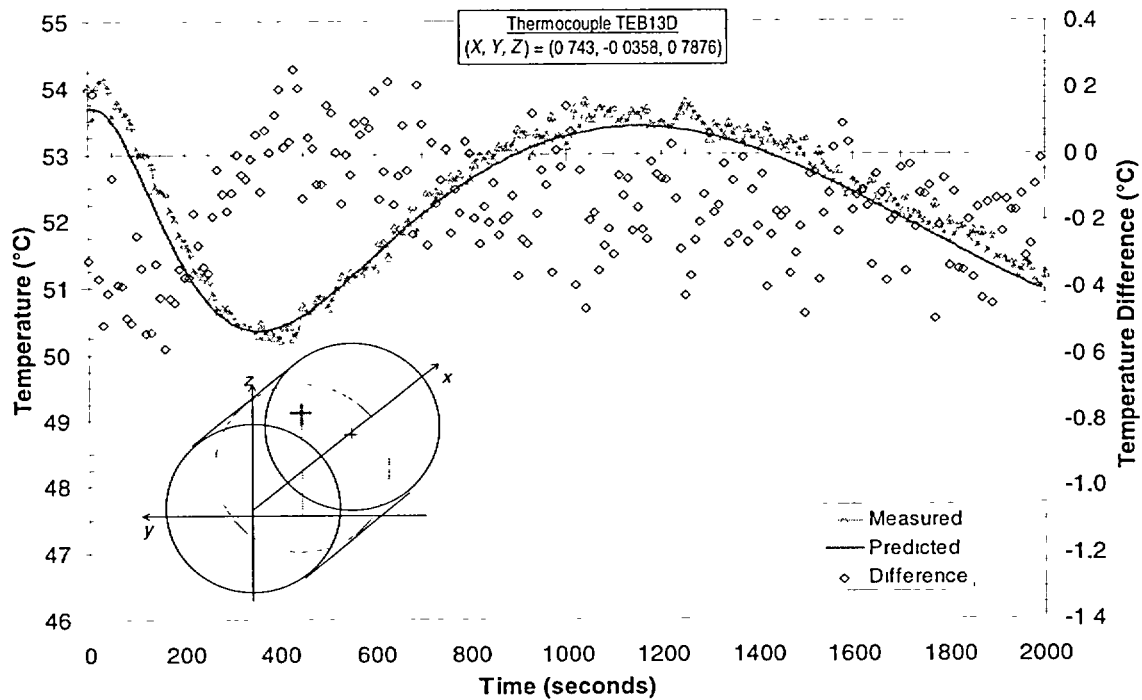


Figure 5: Predicted and Measured (gap thermocouple) Temperatures Near Top of Core for the Stylized Large LOCA+LOECC Transient

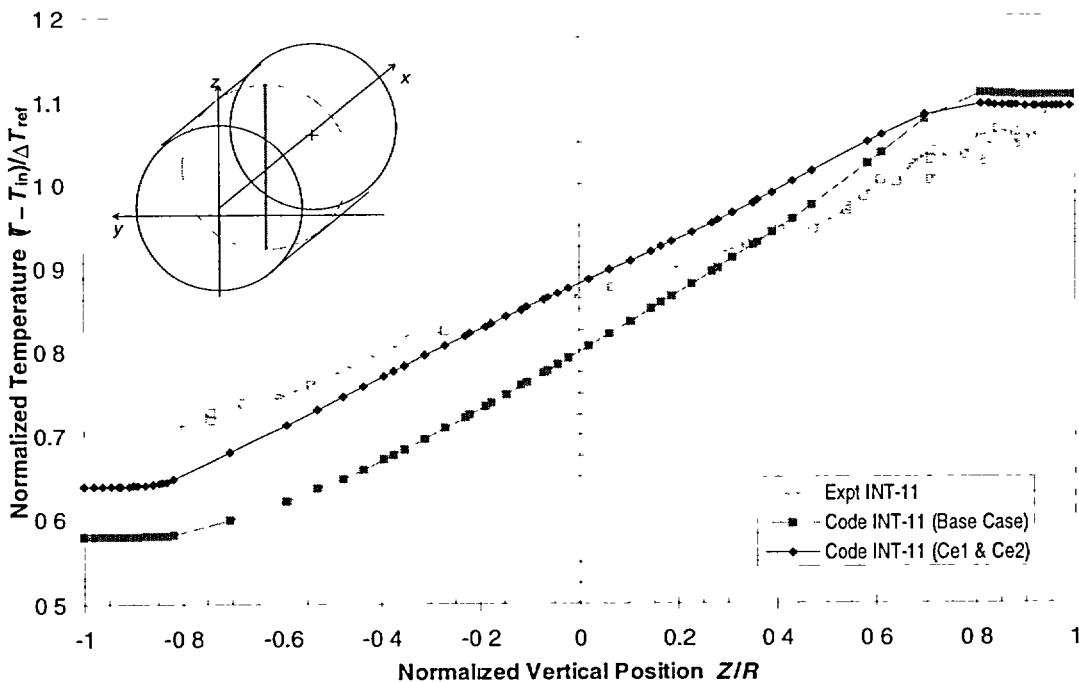


Figure 6. Predicted (Base Case and $0.9c_{1e}$, $1.1c_{2e}$) and Measured Temperatures Along Vertical Centerline for Nominal Flow and Power Test.

A Parallel Virtual Machine Interface for CATHENA

Darryl Dormuth

**Safety Thermalhydraulics Branch
Atomic Energy of Canada Limited, Whiteshell Laboratories
Pinawa, Manitoba R0E 1L0**

Abstract

In pursuit of best-estimate analysis for CANDU® safety and design issues, several computer codes that model such processes as systems thermalhydraulics, fuel behaviour, reactor kinetics, and reactor controllers will be required to interact with each other to facilitate the modelling of integrated effects among reactor systems. It would be cumbersome, in terms of usage, software management, and quality assurance practices, to incorporate all potential numerical models into a single computer code. Instead, a "coupled-code" methodology can be employed that relies on message-passing via computer network protocols to exchange the data among the computer codes. This approach has the advantage of maintaining the computer codes as separate entities which makes their usage, software management and quality assurance easier. In this paper, the coupled-code methodology is applied to the AECL thermalhydraulics code CATHENA (CANadian THERmalhydraulic Network Algorithm) so that it can be used in conjunction with other safety and design codes for better-estimate analyses of reactor behaviour.

**Presented at the 19th Annual Canadian Nuclear Society Conference
1998 October 18-21
Toronto, Ontario**

CANDU® is a registered trademark of Atomic Energy of Canada Limited (AECL).

1. INTRODUCTION

When design engineers need to examine a condition or event that could affect the safety of a reactor, they customarily utilize computer codes to aid in their examination. Often two or more computer codes are needed to analyze such events because the models for the affected physical systems are not contained in a single code. If significant feedback occurs between physical systems that are not modelled by a single code then information (usually in the form of time-dependent boundary conditions) must be exchanged between the codes to capture the feedback behaviour [1,2]. Typically this information is exchanged manually between codes either in an iterative procedure until a converged solution is obtained or in a "start-stop" procedure over small time intervals [3,4]. This form of information exchange has limitations, most notably the time required to do the analysis and the difficulty in capturing rapid feedback among physical systems such as void-reactivity feedback encountered during some postulated events. Automating this information exchange would reduce the analysis time and provide a more efficient way of capturing feedback effects among reactor systems that are modelled by different codes.

One way to automate information exchange between separate codes is to combine them into a single executable [5]. This has the advantage of fast information transfer as all data remains in memory but can require considerable computer resources to load and execute if the original codes are large. Also, the combined-code executable becomes a new code itself and may be subjected to software quality assurance practices and procedures which can add overhead to its development and maintenance. An alternative to this approach is to keep the codes separate and couple them with a computer network through which pertinent data can pass. This approach has the advantage of maintaining the computer codes as separate entities which makes their usage, software management and quality assurance easier but it does require that an interface be built in each code so that the necessary data can be exchanged in a consistent and timely manner [6].

In this paper, the design criteria and implementation of a network interface are described for the system thermalhydraulic code CATHENA which gives it the ability to communicate with a variety of other safety analysis codes. This network interface makes use of a software package called PVM (Parallel Virtual Machine) which is a library of subroutines that performs all the necessary functions for a group of processes, potentially located on different computers, to work as a collective. It is a shareware package maintained and supported by Oak Ridge National Laboratories and is available for UNIX and Microsoft Windows operating systems.

Implementation of the CATHENA network interface is demonstrated with a simulation of a power reduction in a CANDU 6 reactor. For this example, CATHENA is coupled to two other codes - a reactor controller code for Point Lepreau and a point neutron kinetics code. This example was chosen because the controller and point kinetics models reside in the current reference version of CATHENA permitting a direct means of verifying the network interface. Also, once the interface is successfully implemented with these models, the groundwork is laid for connections to other controller models such as those for Gentilly-2 or Wolsong and to other reactor kinetics models such as CERBERUS.

2. DESIGN REQUIREMENTS

To make the network interface as accessible as possible to CATHENA users and to minimize its development and maintenance, several design criteria were considered.

Robustness

The intent of the network interface is to be able to couple CATHENA to many types of analysis codes. In terms of usability and code maintenance it is desirable to have one interface that can handle all the desired connections, such as to

- a) multi-dimensional reactor kinetics codes,
- b) reactor controller codes,
- c) finite-element codes for structural behaviour of pipe components,
- d) fuel behaviour codes, or
- e) aerosol codes for aerosol transport in the primary heat transport system.

One Reference Version

Each reference version of CATHENA must contain all the source for the network interface which means the interface has to be coded so that it works in the same way on all supported CATHENA computer platforms. Also, CATHENA must operate unimpaired if network connections are not specified or network software is absent from the computer being used. It should be noted that if a network connection is requested and network software is absent then an appropriate error message should be provided to the user.

Maintain CATHENA Solution Method

As stated above, the network interface must be robust enough to handle connections to many types of safety analysis codes and be available on supported computer platforms. This requires that a protocol be established between CATHENA and any code connecting to it so that data can be transferred in a correct and consistent manner. As CATHENA is a finite-difference code (in time and space), it steps through the time domain of the problem by executing a main loop of coding for varying sizes of time intervals (commonly referred to as time-steps). CATHENA also has the ability of repeating a time-step if conditions in the thermalhydraulic system dictate that a smaller time interval was needed to capture the dynamics.

Codes that connect to CATHENA must be able to follow CATHENA's time-step solution method. If data are transferred at every CATHENA time-step then any connecting code must allow for varying sizes of time intervals and be able to consider the possibility that a time-step will be repeated. It is also important that data transfers occur at a location in the code that is executed at every time-step. Often there are sections of coding that are not always executed, depending on system conditions, and data transfers in the sections are to be avoided. Based on these requirements, the network interface must provide enough information to a connecting code for it to handle CATHENA's solution method and the data transfers must be at a location within CATHENA where all the pertinent thermalhydraulic data is accessible at every time-step.

Minimize Additional Code Maintenance

CATHENA is written in FORTRAN-77 and to minimize code maintenance effort the network interface should also be written using standard FORTRAN-77 coding practices. The routines used to access the network must be portable to all supported computer platforms which means that if third-party software is used it too must be available on these supported systems.

3. IMPLEMENTATION

The approach taken in implementing the design requirements of the CATHENA interface was to minimize the amount of new internal coding and to maintain the basic processing structure. Although the potential for parallelism exists using the network interface, only sequential operations were considered for the first version. This means that for each data transfer to an external code CATHENA will send its data and wait, the external code will receive the data and perform its calculations for the given time interval, CATHENA will receive the results, and then CATHENA will continue its processing until the next time for a data exchange. By implementing a sequential processing approach initially, new internal coding is minimized and CATHENA's basic processing structure is maintained.

One of the first challenges in building a coupled-code system is determining how start the simulation. Each code must start execution, establish a connection to the other codes in the system, and discover what data is to be exchanged. It was decided for the CATHENA network interface that the user would start CATHENA and then CATHENA would start the external codes. Using this start-up procedure, CATHENA becomes responsible for starting up the other codes and synchronizing communication instead of the user. Information needed to initiate the execution of each remote code would be contained in the CATHENA input file. To keep the interface as robust as possible, the input file would contain three pieces of information to start a remote process:

- 1) The executable file name and location of the remote code. The location would include the network node and the directory on that node where the executable resides.
- 2) The directory on the node where working files will be stored.
- 3) The name of the input file for the remote code. This input file will be contained in the working directory.

The input for the network interface is provided in a similar fashion as for the point kinetics and output models. In the System Control Model section of the input file, the user creates a 'REMOTE PROCESS' model that contains all the appropriate information regarding the start-up and data transmission.

When the remote code is started by CATHENA it will read the two character strings containing the working directory and input file name, call an operating system routine to point to the working directory, and then open the input file and read its contents. Any remote code that is to be coupled to CATHENA through this interface must adhere to this protocol. Each remote code should have some mechanism for determining whether it was

started by a user to be run as an independent process or whether it was started by CATHENA as part of a coupled-code simulation. The PVM software package (discussed below) provides an easy way of testing if a process was started by a user or another process.

Parallel Virtual Machine (PVM) is a software package that enables a collection of heterogeneous computers to be used as a single computational resource [7]. The name Parallel Virtual Machine refers to the virtual parallel computer that is created when a group of computers are networked together with the PVM software. PVM was developed at the Oak Ridge National Laboratories and the University of Tennessee in the late 1980's and early 1990's and is made available as shareware to the scientific community. It employs a message-passing form of distributed processing in which data is exchanged in packets sent across the network and it is available for UNIX and MS-WINDOWS operating systems that use Transfer Control Protocol/Internet Protocol (TCP/IP).

PVM consists of essentially two parts: a background process that runs on each computer in the virtual machine (commonly known as a daemon process) and a library of callable C or FORTRAN routines. Each computer code, such as CATHENA, uses routines from this library to perform such tasks as starting a process on a remote computer node, transmitting and receiving data from other processes, checking the status of the virtual machine, and halting remote processes. A code will communicate with another code by first sending a message to its local PVM Daemon process (PVMD), this PVMD will then send the message to the PVMD on the appropriate remote computer, and that PVMD will pass the message onto the second code. All inter-computer communication is done through the PVMDs using TCP/IP socket protocols.

Once the remote process is started, the next steps are to establish what data are to be transferred, the order in which they are to be sent and received, and the frequency of transmissions. For the first version of the interface it was decided that this information would be contained in the input files of each code. This means that before commencing a simulation the user must verify that the lists between the two codes match so that data are sent and received in the appropriate order and at the appropriate frequency. The use of the PVM message passing routines provides a flexible method of transmitting the data. Each message would contain a set of data that would be structured according to what the user requests in the input file. The user would also specify in the input file the order in which the messages would be transmitted.

The start-up and message-passing form of data transmission described above establishes the basic protocol for the CATHENA network interface. Any code that is to be coupled to CATHENA through this version of the interface must follow the same protocol and it must also include the applicable PVM routines. The PVM routines are also available for some UNIX scripting languages such as PERL so that driver programs could be written around some codes to give them access to the CATHENA interface. It should also be noted that codes can be networked on the same computer through this interface, although PVM and the appropriate networking software must be available.

4. EXAMPLE

To illustrate the capabilities of the CATHENA network interface, a power reduction transient in a CANDU 6 reactor was chosen as an example case. In this transient, the power was reduced from 100% to 77% full power at a rate of 0.5% per second and requires thermalhydraulic, reactor kinetics, and reactor controller models to simulate the event. CATHENA contains a reactor controller model for Point Lepreau (called LEPCON - LEPreau CONToller) developed by New Brunswick Power [8] and a point neutron kinetics model so this event can be simulated by CATHENA itself. By removing the kinetics and controller models from CATHENA and making them into separate stand-alone executables, the event can also be simulated using these two codes coupled to CATHENA through the PVM network interface and the results can be directly compared to those produced by the single CATHENA simulation.

Figure 1 shows how the parallel virtual machine is set up for this example. The removed kinetics model is named POKIN (POint KINetics) and the controller model, LEPCON-S (LEPreau CONTroller Stand-alone). As mentioned in Section 3, the coupled calculations are done in a sequential manner and in Figure 2 the processing order for this simulation is presented. The number of data items in each message are shown over the arrows. No reduction in simulation time was expected from the coupled-code simulation versus the single CATHENA run because no parallelism in the computations was exploited. In fact a slight increase in simulation time was seen because of the overhead in network communications.

Plots of the power transients from the two cases are shown in Figure 3 and indicate a very good comparison between the two simulations. The slight deviations between the two transients are attributable to differences in numerical round-off. This example not only demonstrates that the PVM network interface works for multiple connections it also illustrates a way of verifying that it is functioning correctly.

5. SUMMARY

In this paper, the design and implementation of the PVM network interface for CATHENA were presented. It was shown that using the PVM software package, a network interface can be built to meet the requirements outlined in Section 2. A basic protocol was established that permits the coupling of CATHENA to many types of safety analysis codes. To demonstrate this, an example was provided in Section 4 in which a power reduction in a typical CANDU 6 reactor was modelled with reactor controller and reactor kinetics codes connected to CATHENA through the PVM interface. Future investigations will include coupling CATHENA to a multi-dimensional reactor kinetics code and other reactor controller models.

6. ACKNOWLEDGMENTS

The author would like to express his thanks to Dr. Bruce Hanna and Mr. Marc Lavack for their comments and to New Brunswick Power for their permission to reference the Point Lepreau controller model. This work was partially funded by Hydro Québec, New Brunswick Power and AECL, through the CANDU® Owners Group under WPIR 12, and their support is appreciated.

7. REFERENCES

[1] DeVaal, J., Gauld, J., Klein, M., McDonald, B., Dormuth, D., Whitehouse, D., Lavack, M., Chiang, H-W., and Wilken, B., Parallel Computing Applied to the Modelling of the Complex Interacting Phenomena in Severe Fuel Damage Experiments, presented at the ICHMT International Seminar of Heat Transfer in Severe Reactor Accidents in Cesme, Turkey, 21-26 May 1995.

[2] Tetner, A. et. al., Advances in Parallel Computing for Reactor Analysis and Safety, Communications of the ACM, Vol. 37(4), 1994.

[3] Dormuth, D. and McDonald, B., A Parametric Study of Thermalhydraulic Factors Affecting Pressure Tube Rupture, CANDU Owners Group Report COG-91-307 (Protected), 1993.

[4] Liu, W., McDonald, B., Richards, D., Gold, M., Rouben, B., Barkman, J., Sills, H., Carlucci, L. and Luxat, J., Thermal-Hydraulic Interfacing Code Modules for CANDU Reactors, presented at the OECD/CSNI Workshop on Transient Thermal-Hydraulic and Neutronic Code Requirements, Annapolis MD, November 5-8, 1996.

[5] Carlucci, L., Gauld, J., Richards, D. and Arimescu, V., Coupling Subroutine Version of ELOCA for High-Temperature Fuel Behaviour to CATHENA System Thermalhydraulics Code, presented at the 20th Annual CNS Simulation Symposium, Montreal PQ, 1996.

[6] McDonald, B. Wallace, D. Hanna, B. and Dormuth, D., INTARES - A Concept Code for Integrated Thermalhydraulics and Aerosol Safety Analysis, presented at the CSNI Workshop on Aerosol Behaviour and Thermal-Hydraulics in Fontenay-aux-Roses, France, 26-28 November 1991.

[7] Geist, A., Beguelin, J., Dongarra, J., Jiang, W., Manchek, R., and Sunderam, V., PVM: Parallel Virtual Machine. A User's Guide and Tutorial for Networked Parallel Computing, MIT Press, Cambridge MA, 1994.

[8] Girard, Rene, LEPCON Abstract, Users Manual, and Program Description, New Brunswick Power Report IR-03500-51 Vol. 1,2,3, 1995.

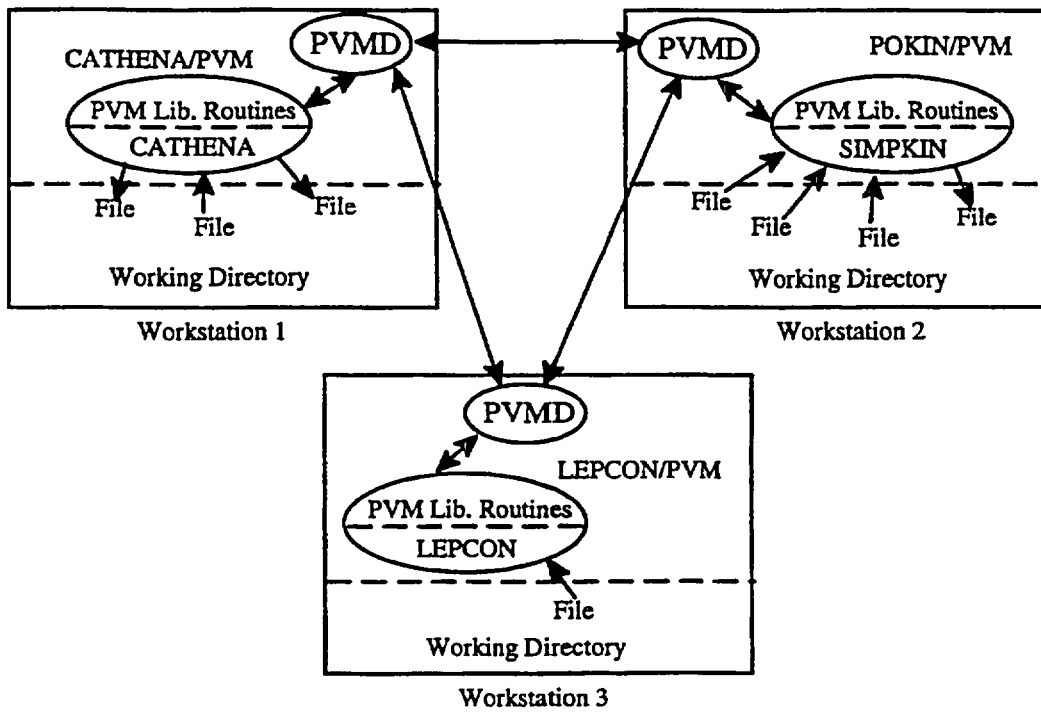


Figure 1: The parallel virtual machine arrangement for power reduction example.

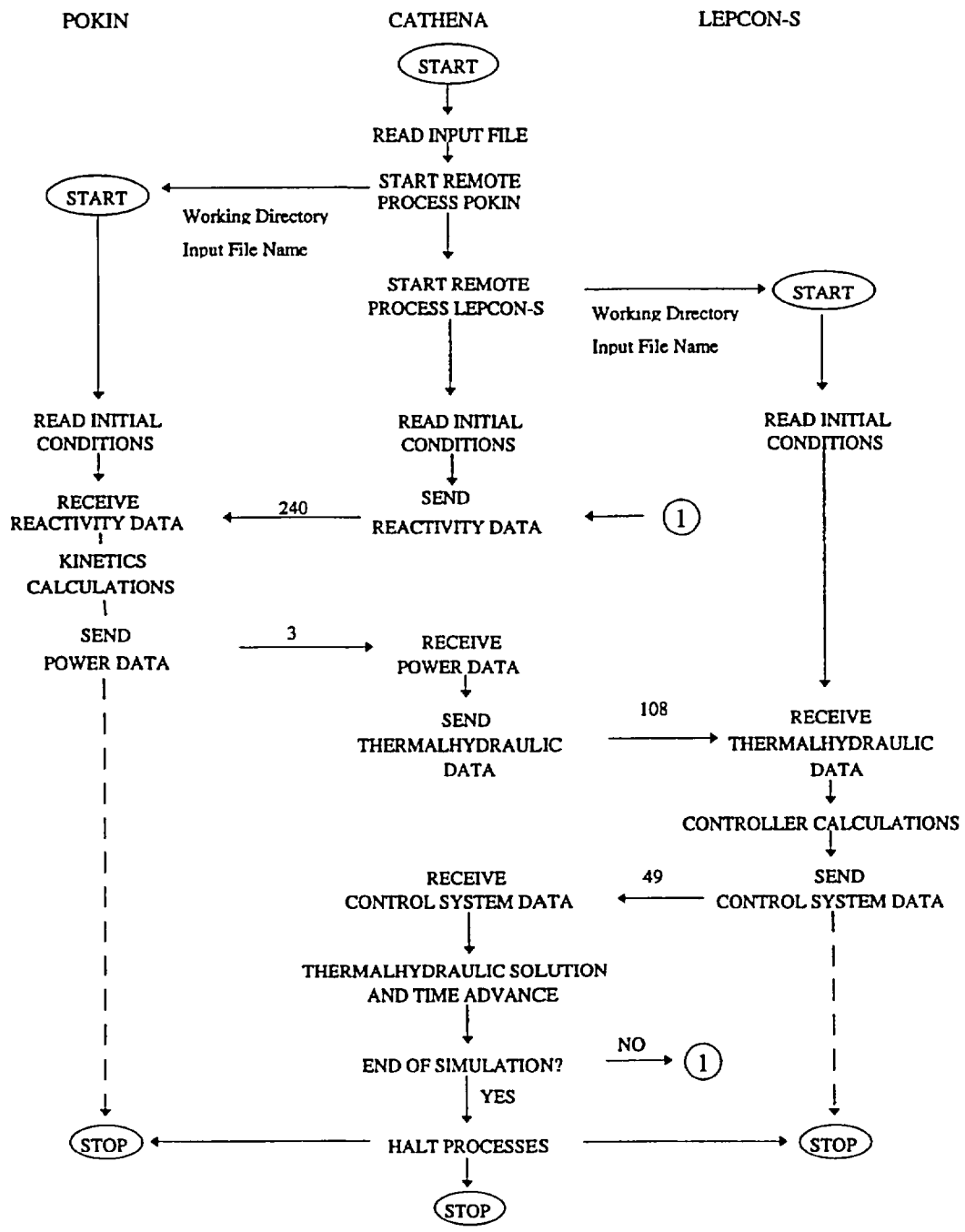


Figure 2: Processing order in example simulation.

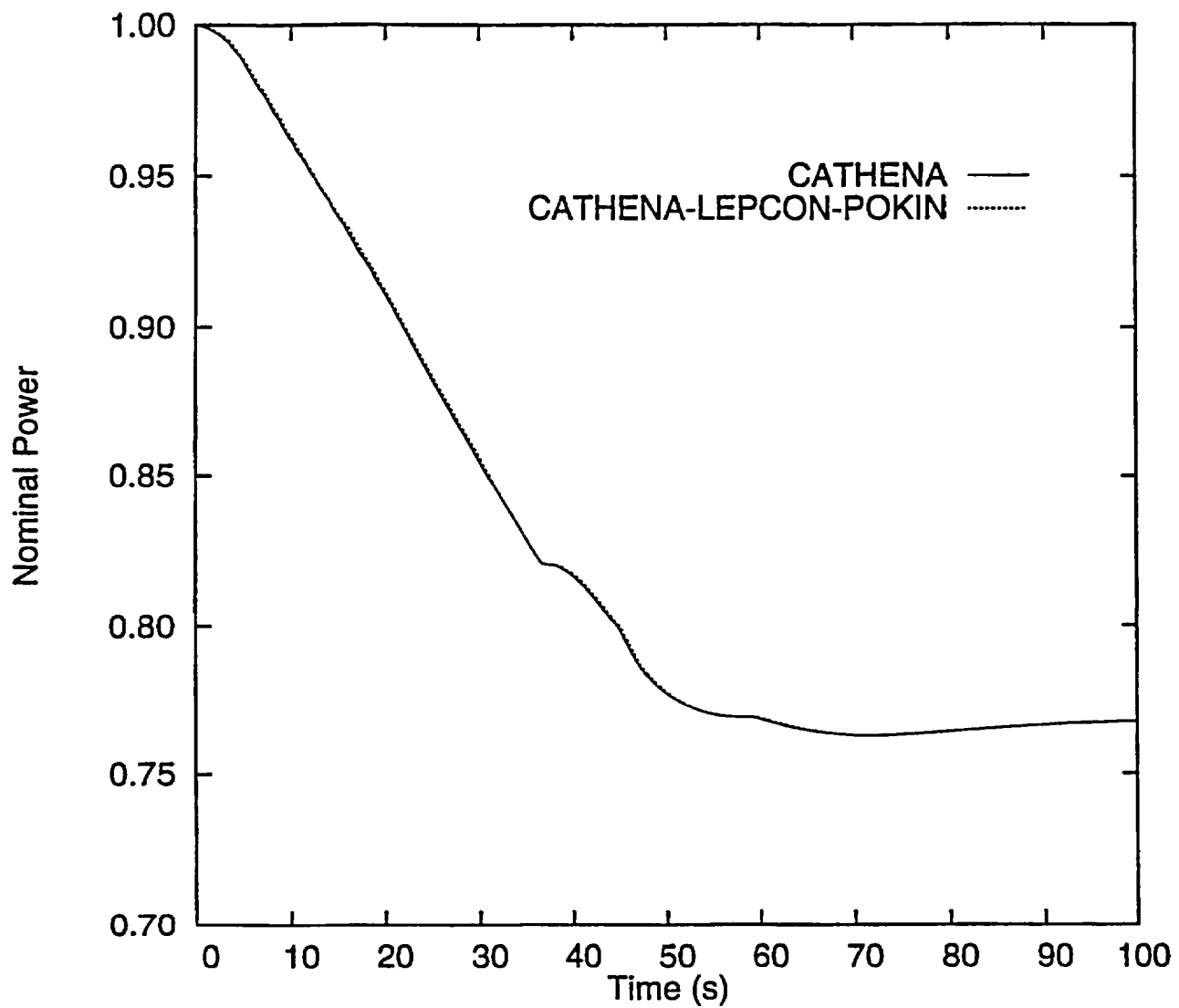


Figure 3: Comparison of power transients between CATHENA and coupled-code simulations.

CATHENA VALIDATION IN SUPPORT OF LARGE BREAK LOCA ANALYSIS

T.G. Beuthe and J.P. Mallory

Atomic Energy of Canada Limited
Whiteshell Laboratories
Pinawa, Manitoba, Canada R0E 1L0

ABSTRACT

An effort is currently underway to improve the validation of the CATHENA thermalhydraulics code for use in CANDU reactor safety analysis and licensing. As part of this work, a series of RD-12, RD-14, and RD-14M simulations were performed to help qualify CATHENA for large break loss-of-coolant accident analysis. This paper discusses modelled and experimental results from large break loss-of-coolant accident tests conducted in the RD-12, RD-14, and RD-14M test facilities and how they are used in the validation process.

1 INTRODUCTION

CATHENA is being validated using the industry wide phenomenology-based matrix approach to code validation [1]. This approach identifies the accident categories for reactor safety analysis, the primary phenomena in each category, and the experimental data that can be used to assess and validate the adequacy of the models in reproducing these phenomena. The information presented in this paper provides an overview of a portion of the work conducted to date in support of the use of CATHENA for large break Loss-Of-Coolant Accident (LOCA) analysis in CANDU[®] reactors. The primary phenomena of interest to large break LOCA analysis are identified by the industry wide phenomenology-based matrix. These include break discharge characteristics, coolant voiding, quench/rewet characteristics, and convective heat transfer. Data from the RD-12, RD-14, and RD-14M integrated test facilities were identified as being appropriate for validating these phenomena. Data from these facilities were also selected to demonstrate that scaling and multiple channel effects are captured by the code. CATHENA MOD-3 5b/Rev 0 simulations of experiments conducted in these facilities were performed on an HP-UX 9000/800 computer.

2 CATHENA

CATHENA (Canadian Algorithm for THERmalhydraulic Network Analysis) is a computer program developed by AECL at Whiteshell Laboratories (WL) primarily for the analysis of postulated LOCA events in CANDU reactors. CATHENA uses a transient, one-dimensional two-fluid representation of two-phase flow in piping networks. In the thermalhydraulic model, the liquid and vapour phases may have different pressures, velocities, and temperatures. The thermalhydraulic model consists of solving six partial differential equations for the conservation of mass, momentum, and energy for each phase. Interface mass, energy, and momentum transfer between the liquid and vapour phases are specified using constitutive relations obtained either from the literature or developed from separate-effects experiments.

The computer program uses a staggered-mesh, one-step, semi-implicit, finite-difference solution method, that is not transit time limited. The extensive wall heat transfer package can account for radial and circumferential

conduction, solid-solid contact, thermal radiation, pressure tube deformation, and the zirconium-steam reaction. The heat transfer package is general and allows the connection of multiple wall surfaces to a single thermalhydraulic node. The CATHENA computer program also includes component models required for complete loop simulations such as pumps, valves, tanks, break discharges, separator models, and an extensive control system modelling capability. A more complete description of the CATHENA thermalhydraulic computer program is provided in [2].

3 FACILITY DESCRIPTIONS

Experiments have been performed in the RD-12, RD-14, and RD-14M experimental facilities to investigate large break loss-of-coolant accidents in CANDU reactors. Tests from these facilities were chosen to demonstrate CATHENA's ability to predict break discharge characteristics, coolant voiding, quench/rewet characteristics, and convective heat transfer for a variety of reactor-like facilities of various scales operated at reactor typical conditions.

3.1 RD-12 Facility

As shown schematically in Figure 1, the RD-12 facility was a small scale pressurized-water loop containing the essential features of a CANDU reactor arranged in a figure-of-eight configuration. It was designed to operate at reactor typical conditions (i.e., pressure, temperature). The test selected had a single channel per pass configuration with each channel containing a 3.9 m-long, 7-element electrically heated bundle or Fuel Element Simulator (FES) in the Test Section. The RD-12 large break blowdown test used in this work was selected to be comparable to an RD-14 test to demonstrate the CATHENA computer code can account for the effects of scale. Of the available RD-12 tests in which the Emergency Core Coolant (ECC) system was used the chosen test had the longest period at full power after break initiation and hence had the highest channel temperatures.

3.2 RD-14 Facility

As shown schematically in Figure 2, the RD-14 facility was also a pressurized-water loop with the essential features similar to the primary heat transport loop of a typical CANDU reactor. This facility was full vertical reactor scale, with full size feeders and channels. It had a single channel per pass configuration with each pass containing a 6-m long, 37-element electrically heated bundle. It was designed to operate at reactor-typical conditions (i.e., pressure, temperature, flowrate, mass flux). The RD-14 large break blowdown test data was selected because the loop was full vertical scale and contained full size feeders and channels (see reference [3] for further details). The RD-14 and RD-12 large break LOCA tests were conducted under similar conditions. They were chosen to demonstrate the code could account for the effects of scale. The tests used in this work were selected to cover the range of break sizes and break locations investigated in the facility. Results from a representative test are shown in this paper.

3.3 RD-14M Facility

As shown schematically in Figure 3, the RD-14M facility is a pressurized-water loop with the essential features similar to the primary heat transport loop of a typical CANDU reactor. The facility is full vertical reactor scale with the channel inlet and outlet feeder piping arrangements designed to represent the Darlington Nuclear Generating Station feeders. The loop has a multiple (5) channel per pass configuration with each channel containing a 6-m long, 7-element electrically heated bundle (see reference [4] for further details). The

RD-14M facility was designed to operate at reactor-typical conditions (i.e., pressure, temperature, mass flux, transit time). The RD-14M large break blowdown test data was selected because the loop was full vertical scale and contained a multiple channel per pass configuration. Comparison of RD-14 and RD-14M test data addresses the issue of multiple channel effects. The RD-14M large break blowdown tests used in this work were also selected to cover the range of break sizes and break locations investigated in the facility. Results from a representative test are shown in this paper.

4 RD-12 IDEALIZATION

The CATHENA idealization used to simulate the RD-12 facility primary-side, secondary-side and ECC systems is shown in Figures 4, 5 and 6 respectively. The idealization had 409 thermalhydraulic nodes, 412 links, 154 wall heat transfer models and 568 fluid-wall heat transfer surfaces.

The primary-side idealization, shown in Figure 4, consisted of the RD-12 primary-side piping connecting the headers, test sections containing the FES, steam generators, and primary pumps. Only the portion of the surge tank line up to the surge tank isolation valve was included, since the surge tank was isolated prior to initiation of the break. The surge tank was modelled as a pressure boundary condition. The heat transfer models in GENHTP (GENERALized Heat Transfer Package) were used to account for the heat transfer from the primary fluid to the pipe walls, from pipe walls to the environment, and from the steam generator tubes to the secondary-side fluid. Pipe radii (inner and outer) were used to define the metal mass and heat transfer area in contact with the primary fluid. Heat losses to the environment were accounted for. The thermal properties used for the piping materials as well as the material in the 7-element fuel element simulators were obtained from CATHENA's internally stored temperature dependent properties or derived from standard references.

The secondary-side idealization of the RD-12 test facility is shown in Figure 5. This idealization included the steam generators and that part of the feedwater line from the thermocouple location measuring feedwater temperature to the steam generator feedwater inlets. Portions of the feedwater line upstream of this location were represented by flow and enthalpy boundary conditions extracted from the experimental data.

The CATHENA idealization of the RD-12 ECC system is shown in Figure 6. System Control models were used to open the ECC isolation valves at the same time as in the experiment. Time-varying pressure boundary conditions, extracted from experimental data, were used to model the high-pressure ECC tank pressure response.

5 RD-12 SIMULATION RESULTS

Once a steady state had been established, a CATHENA simulation of the RD-12 experiment was conducted. Figures 7, 8, 9 and 10 show representative simulated and measured header pressures, ECC flows, and test section outlet void fractions and FES pin temperatures respectively for test B8223.

5.1 RD-12 Primary System Pressure and ECC Flowrate

As shown in Figure 7, Header 1 rapidly depressurizes starting at 10 s (break initiation time) as a result of the break at header 3. The depressurization curves of headers 1, 2, and 4 are similar to each other, whereas the depressurization of header 3 is more rapid, owing to the break at this location. As illustrated in Figures 7 and 8 the simulation results closely follow the experimental results.

The ability to accurately predict header pressures can be used as an indirect validation of the ability of CATHENA to predict break discharge characteristics. Break discharge rates were not measured in the RD-12 facility. However, good agreement between simulated and experimental break discharge rates can be inferred from agreement between simulated and measured system pressures, since system pressure is strongly affected by the discharge rate. In the RD-12 test under examination here, critical saturated, two phase flow, as well as subcritical liquid flow occurred at the break. As illustrated in Figure 7, the modelled header pressures were in agreement with the experimental measurements throughout the transient. Consequently, it may be inferred that the break discharge characteristics were captured by the CATHENA simulation.

5.2 RD-12 Void and FES Temperature

Figure 9 shows the measured and simulated void history at the outlet of Test Section 1 (TS1). For comparative purposes, Figure 10 shows the experimental and modelled outlet top pin FES temperature histories. It should also be noted that although the FES temperature measurements were taken inside the test section, the void fractions were measured downstream in the piping attached to the test section. Thus, the measured void does not necessarily reflect the void occurring in the channel.

As illustrated in Figures 9 and 10, as the system depressurized, voiding occurred in TS1, and the top FES temperature rapidly increased shortly after the break was initiated at 10 s. The FES temperatures reached about 750 °C by 20 s. By 50 s, the FES temperature had reduced to 200 °C as the power to the FES was reduced to decay power, and the FES was cooled by the two-phase flow occurring in the channel. The upper FES began to heat up once again at 90 s under the influence of the decay power and the reduced flow in the channel. ECC entered at the channel inlet at about 180 s and channel refill was completed by 225 s.

Figure 9 shows that the timing for the onset of void in TS1 was well simulated by CATHENA and the void fractions in the initial stages of the blowdown were also captured well. However, the modelled TS1 top pin temperatures exceed the experimental values in the first 150 s of the simulation (see Figure 10). This overestimation results from an underestimation of the film boiling heat transfer rates for some conditions. While this is undesirable, the results are considered conservative. Refilling and final quenching of the channel occurred earlier than in the experiment.

The FES temperature in TS2 (not shown) decreased monotonically after the break was initiated as flowrates through TS2 increased due to the proximity of the broken header downstream (see Figure 1). CATHENA correctly demonstrated that dryout did not occur in TS2 and that the FES remained well cooled despite continued high void at the outlet after ECC entered the channel.

6 RD-14 IDEALIZATION

The CATHENA idealization of the RD-14 facility primary side, secondary side and ECC systems is shown in Figures 11, 12, and 13 respectively. The complete RD-14 idealization had 274 thermalhydraulic nodes, 279 links, 101 wall heat transfer models and 647 fluid-wall heat transfer surfaces.

The primary-side idealization, shown in Figure 11, consisted of the RD-14 primary-side piping connecting the headers, heated sections, steam generators, and primary pumps. Only that portion of the surge tank line up to the surge tank isolation valve was included, since the surge tank was isolated prior to the initiation of the break.

GENHTP models were used to account for the heat transfer from the primary fluid to the pipe walls, from pipe walls to the environment, and from the steam generator tubes to the secondary side fluid. The heat transfer

coefficients applied to the outside of the piping, to simulate heat losses to the environment, were derived from RD-14 heat loss tests. The thermal properties used for the piping materials were obtained from CATHENA's internally stored temperature dependent properties.

The secondary-side idealization of the RD-14 test facility is shown in Figure 12. This idealization included the steam generators up to the steam nozzle and that part of the feedwater line from the thermocouple location measuring the feedwater temperature to the steam generator feedwater inlets. Portions of the feedwater line upstream of this location were represented by flow and enthalpy boundary conditions. The secondary-side steam generator outlet pressures were modelled using pressure boundary conditions obtained from the experimental boiler steam drum pressures.

The CATHENA idealization of the RD-14 ECC system is shown in Figure 13. It included provision for both the high-pressure tank and low-pressure (pumped) injection modes used in the RD-14 facility.

7 RD-14 SIMULATION RESULTS

Initially, steady state conditions were established for each RD-14 CATHENA simulation to ensure that an energy balance between all metal surfaces and the fluid had been obtained. Steady state FES temperatures were used to validate the ability of CATHENA to predict liquid convective heat transfer for a variety of flowrates and powers. Simulation results were compared to the initial 10 s of steady state data taken at the beginning of each test. The results show that CATHENA is able to capture single phase liquid heat transfer with acceptable accuracy.

Once steady states had been established, CATHENA simulations of a number of different RD-14 large inlet and outlet header break tests were conducted. Figures 14, 15, 16, and 17 show simulated and measured header pressures, ECC flows, test section outlet void fractions, and test section outlet pin temperatures for outlet header break test B8711. In all cases, the blowdown and high-pressure ECC injection phases of the test are shown.

7.1 RD-14 Primary System Pressure and ECC Flowrate

As illustrated in Figures 14 and 15 the header pressure for the B8711 test shows rapid depressurization down to the ECC injection pressure after opening the break. The primary pressure continued to decline after the onset of ECC, reaching about 2 MPa(a) by about 45 s. Between 45 and 90 s, the pressure and ECC flowrates stabilized. With the termination of high-pressure ECC between 80 and 90 s and the onset of low-pressure pumped injection, ECC flowrates decreased and the primary pressure declined to less than 1 MPa(a). The CATHENA simulation results show that the header pressures and ECC flowrates were well predicted. While some discrepancies between measured and simulated pressures and ECC flowrates did appear, they tended to be of short duration.

As discussed earlier for the RD-12 simulation, the ability of CATHENA to predict break discharge characteristics may be inferred from its ability to predict header pressures since the primary system pressure is largely impacted by the discharge rate. Break discharge rates were not measured in the RD-14 facility, but the good agreement between experimental and simulated primary system pressures such as those shown in Figure 14 indicate that CATHENA was able to predict the discharge rate. The discharged coolant in the RD-14 tests experienced both critical and subcritical flow at saturated single-phase, two-phase, as well as highly non-equilibrium fluid conditions. Results from the other tests in the CATHENA validation showed that CATHENA correctly captured the effect of break size on break discharge characteristics.

7.2 RD-14 Void and FES Temperature

Figures 16 and 17 show measured and simulated void fractions, and top and bottom FES temperature histories in the middle of TS1 respectively. The void fraction was measured in the piping attached to the heated section, whereas the FES temperatures were taken inside the heated section. Therefore, the void fraction measurements do not necessarily reflect the void fraction behaviour in the test section.

The B8711 experiment was a large outlet header break test in which forward flow increased on break initiation in TS2 (not shown), and void briefly appeared before ECC entered TS2 at about 35 s. Quenching and refilling of TS2 was complete by 40 s. In TS1, forward flow initially continued and rapid voiding occurred at the outlet, as shown in Figure 16. By 30 s the test section was almost completely voided and remained so until ECC began refilling the channel at about 55 s. As shown in Figure 16 the CATHENA simulated void fraction behaviour in TS1 is in acceptable agreement with measured results. The simulated void in the unbroken pass was also well captured. The channel void fraction data shown in Figure 16 was also used to validate the ability of CATHENA to capture coolant voiding. Simulated and experimental channel inlet and outlet pressures, voids, and FES temperatures were examined in the early portion of the blowdown (the first 25 s after the break). Results of this work showed that the CATHENA calculated parameters are in good agreement with the experimental results, leading to the conclusion that CATHENA is able to accurately capture coolant voiding.

Figure 17 shows the simulated and measured top and bottom FES temperature histories at the middle of TS1. In test B8711, no significant temperature excursion was seen in either channel. TS1 showed a small temperature excursion at the initiation of the break which was quickly quenched since the high-quality, high-velocity flow through the channel was sufficient to maintain good cooling. The CATHENA results tend to overestimate the brief temperature excursion at the beginning of the blowdown phase of the experiment. Since CATHENA tends to underestimate the film boiling heat transfer rates, the simulation results did not indicate quenching of the FES until the arrival of ECC later in the test. However, FES temperature excursions were correctly simulated not to occur in TS2.

8 RD-14M IDEALIZATION

The CATHENA idealization of the RD-14M facility primary side, secondary side and ECC systems used to simulate test B9013 is shown in Figures 18, 12, and 19 respectively. The complete RD-14M idealization had 518 thermohydraulic nodes, 532 links, and 178 wall heat transfer models.

The RD-14M primary side idealization consisted of all piping connecting the headers, test sections, steam generators, pumps and surge tank as shown in Figure 18. The volume, length, flow area and elevation change of each CATHENA pipe component resembled, as closely as possible, the RD-14M test facility. The break occurred at inlet header 8.

GENHTP models were used to simulate all solid components in contact with the fluid. They were also used to account for the heat transfer from all solid components in contact with the fluid and the heat transfer from the primary fluid to the pipe walls to the environment, or in the case of the steam generator tubes, to the secondary side. Pipe radii were used in defining the metal mass and heat transfer area in contact with the primary fluid. Heat losses to the environment were also accounted for.

The secondary side model used to simulate the test is shown in Figure 12. The RD-14M and RD-14 secondary side models are identical since the same steam generators were used in both experiments.

The CATHENA idealization of the ECC configuration used in test B9013 is shown in Figure 19. This idealization includes provisions for both the high pressure ECC phase where water is injected from a pressurized tank (CANDU-6 configuration) and the low pressure ECC phase where water is injected using a pump. In the high pressure ECC phase, time varying pressure boundary conditions extracted from experimental data were used to model the high pressure ECC tank since unknown quantities of nitrogen gas were injected into the ECC tank in an attempt to maintain a constant tank pressure.

9 RD-14M SIMULATION RESULTS

Initially, steady state conditions were established for each RD-14M CATHENA simulation to ensure that an energy balance between all metal surfaces and the fluid had been achieved. As with the RD-14 simulations, RD-14M simulations of the steady state were used to help validate CATHENA simulations of convective heat transfer for a variety of flowrates and powers under single phase conditions. The RD-14M results showed that CATHENA is able to simulate single phase liquid heat transfer with acceptable accuracy.

Once steady states had been established, CATHENA simulations of several RD-14M inlet header break experiments with different sized breaks were conducted. Figures 20, through 22 show representative measured and simulated results from one of the inlet header break cases (B9013). All plots show the blowdown phase, the high pressure ECC injection phase and part of the low pressure pumped ECC injection phase.

9.1 RD-14M Primary System Pressure and ECC Flowrate

Figures 20 and 21 show the measured and calculated pressure for header 8 (the broken header) and the corresponding header ECC flowrates respectively. The experimental header pressure shows the rapid depressurization down to the injection pressure within a few seconds after the initiation of the break. The primary pressure continued to decline after the onset of high pressure ECC, reaching about 1.0 MPa(a) by 60 s. With the termination of the high pressure ECC phase and the onset of the low pressure pumped injection at about 225 s, ECC flowrates decline. CATHENA header pressures show good agreement with the experimental results. As illustrated in Figure 21, the distribution of ECC flowrates to each individual header was not as well modelled, but the results were considered acceptable.

As with the RD-12 and RD-14 results, the good agreement between the modelled and experimental RD-14M header pressures indicates that CATHENA simulates the critical and subcritical single-phase and two-phase discharge conditions, at various break sizes, with acceptable accuracy.

9.2 RD-14M Void and FES Temperature

Figures 22 and 23 show measured and calculated void fractions, and FES temperature histories of an upper elevation pin respectively at the outlet of Test Section 13. Void fraction was measured in the piping attached to the test section while the FES temperature measurements were taken within the test section. Therefore, the void fraction measurements do not necessarily reflect the void fraction behaviour in the test section.

As illustrated in Figure 22, rapid and nearly complete voiding of Test Section 13 took place on initiation of the break. Similar results occurred in all test sections in the pass in which the break occurred. Refilling of these test sections occurred from the outlet end. As shown in Figure 23 the FES temperature excursions in the test sections within the broken pass immediately began upon initiation of the break as flow in these channels dropped significantly to very low values. The FES temperatures initially increased quickly and then slowed as

the channel power was reduced to decay levels beginning at about 12 s. Shortly after the onset of the high pressure ECC injection phase, quenching began as ECC water entered these channels.

Test sections in the unbroken pass (no example shown) experienced rapid voiding immediately after the initiation of the break, but only at the outlet end since flow remained forward through these sections during this time. Voiding at the inlet occurred later in the test. No significant temperature excursions were recorded in the unbroken pass as channel flows remained high enough to maintain adequate cooling of the FES. The CATHENA simulation shows similar results.

The CATHENA calculated void fraction behaviour of all the heated sections in both the broken and unbroken pass are in good agreement with the measured results. CATHENA correctly calculated that rapid and near complete voiding at the inlet and outlet test sections in the broken pass occurred upon the initiation of the break. As with the RD-14 results, the RD-14M void fraction data from the broken pass was used to validate the ability of CATHENA to predict coolant voiding. Results showed that CATHENA calculated parameters are in good agreement with the experimental results, leading to the conclusion that CATHENA is able to accurately capture coolant voiding. CATHENA correctly demonstrated that only the outlet of the test sections in the unbroken pass experienced rapid voiding at the break initiation.

In general the FES temperatures also showed acceptable agreement with the measured results. CATHENA indicated that large FES temperature excursions occurred in the test sections in the broken pass immediately after the break. However, peak FES temperatures tended to be overestimated. CATHENA correctly calculated that the FES in the channels in the unbroken pass did not experience any significant temperature excursions after the initiation of the break as sufficient flow through these channels was present to maintain adequate cooling.

As illustrated in Figure 23, the FES temperatures at the outlet of the channels in the broken pass quenched at about the same time as indicated by the void fraction in Figures 22. It should be noted that quenching in some channels may not have been caused by the arrival of ECC water, but rather by a flow generated in the channels at the onset of high pressure ECC injection. Overall, quenching of the channels in the broken pass was in acceptable agreement with the measured results, indicating CATHENA correctly captured the parameters affecting the quench/rewet characteristics.

10 SUMMARY AND CONCLUSIONS

CATHENA is currently being validated using the phenomenology-based validation matrix approach. This approach identified that data from RD-12, RD-14, and RD-14M was suitable for validating a number of primary phenomena of the large break accident category. CATHENA simulations of RD-12, RD-14, and RD-14M tests have helped show that break discharge characteristics, coolant voiding, quench/rewet characteristics, and convective heat transfer phenomena are captured with acceptable accuracy by CATHENA. Use of data from all three facilities have also helped to address scaling and multiple channel effects.

ACKNOWLEDGEMENTS

Construction and operation of the RD-14 and RD-14M facilities was funded by the CANDU Owners Group.

REFERENCES

1. E.O. Moeck, J.C. Luxat, M.A. Petrilli, and P.D. Thompson, "Status of Validation Matrices for CANDU Power Plants", Proceedings of the 18th Annual Conference of the Canadian Nuclear Society, June 8–11, 1997.
2. B.N. Hanna, "CATHENA: A thermalhydraulic code for CANDU analysis", Nuclear Engineering & Design, 180 (1998) 113–131.
3. P.J. Ingham, G.R. McGee, and V.S. Krishnan, "LOCA Assessment Experiments in a Full-Elevation, CANDU-Typical Test Facility", Nuclear Engineering and Design, 122 (1990) 401–412.
4. A.J. Melnyk, P.J. Ingham, and T.V. Murray, "Critical Break Experiments in the RD-14M Thermalhydraulic Test Facility", Proceedings of the 16th Annual CNS Simulation Symposium, St. John, New Brunswick, August 26–27, 1991.

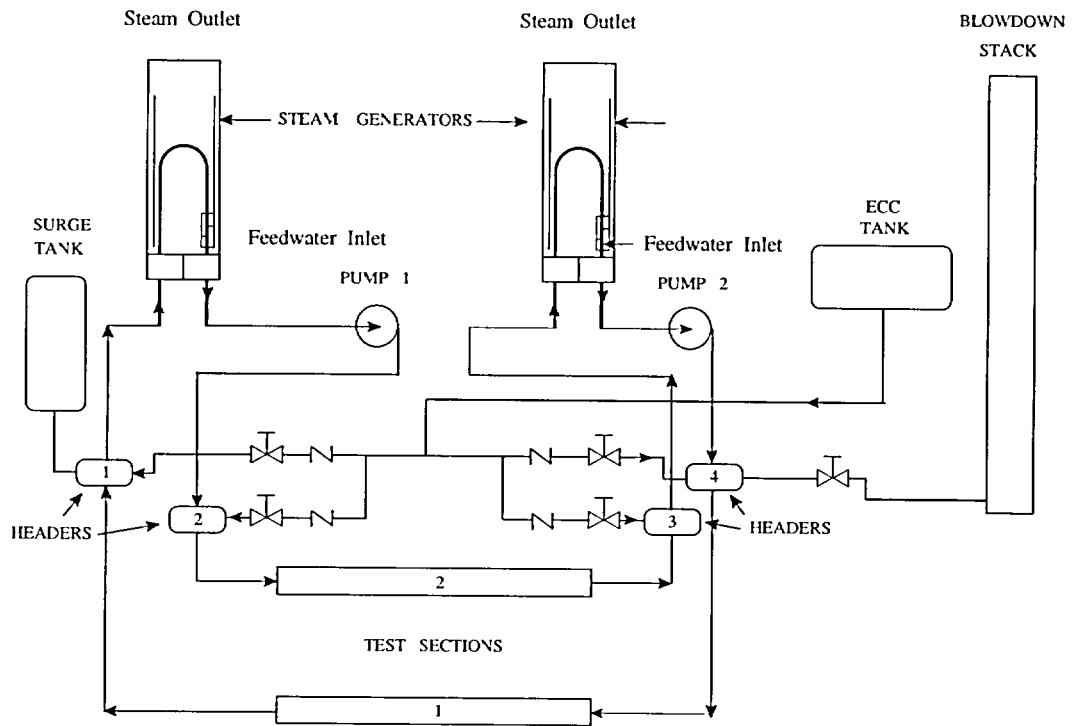


FIGURE 1: Schematic of the RD-12 Test Facility

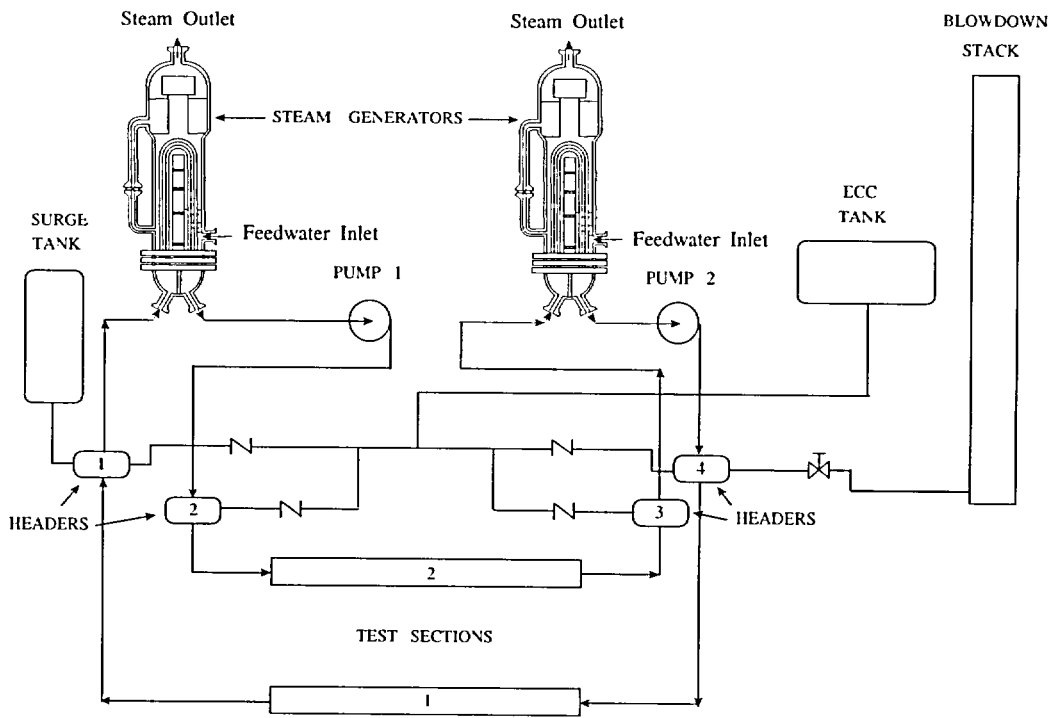


FIGURE 2: Schematic of the RD-14 Test Facility

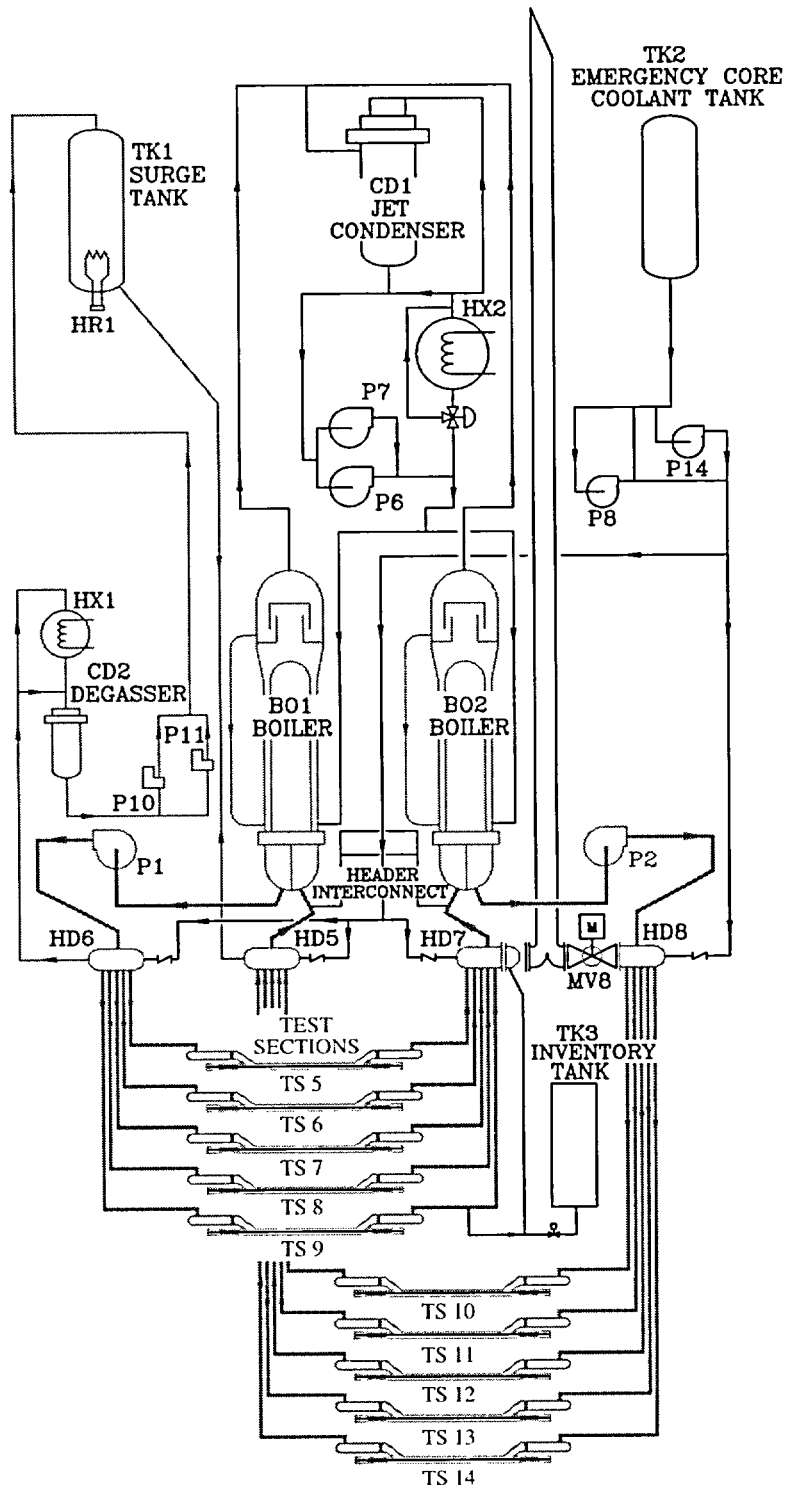


FIGURE 3: Schematic of the RD-14M Test Facility

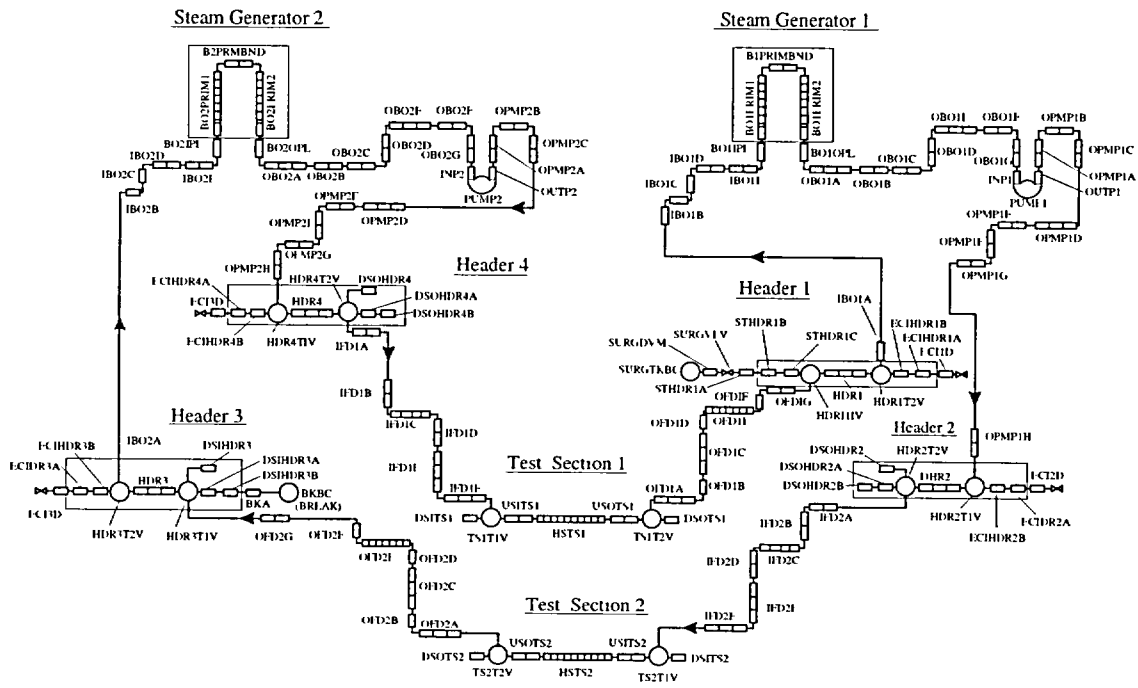


FIGURE 4: Thermalhydraulic Representation of RD-12 Primary Side

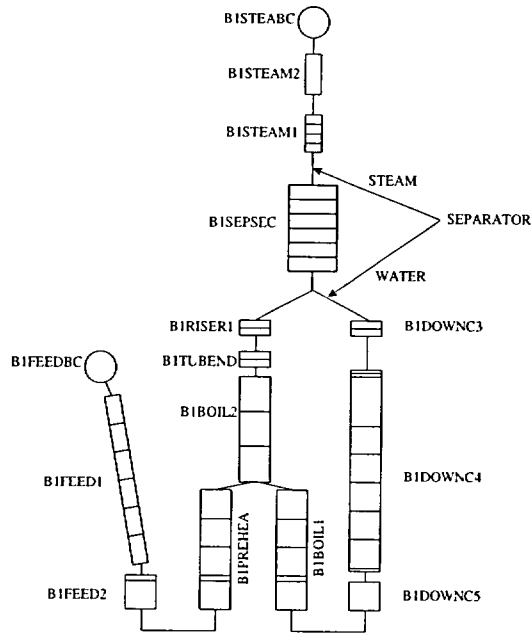


FIGURE 5: Thermalhydraulic Representation of RD-12 Secondary Side

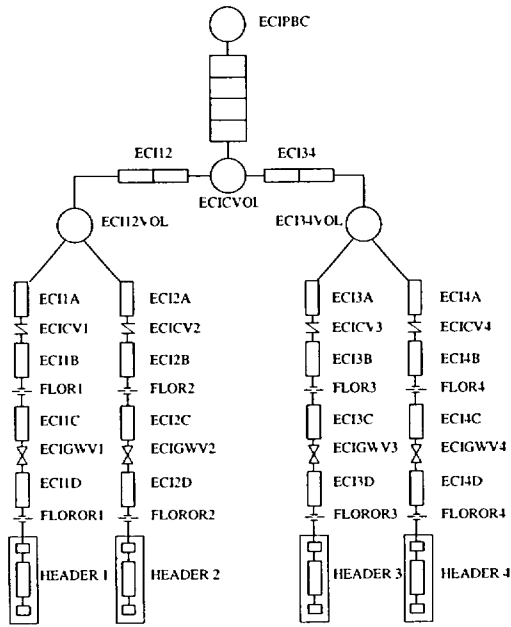


FIGURE 6: Thermalhydraulic Representation of RD-12 ECC System

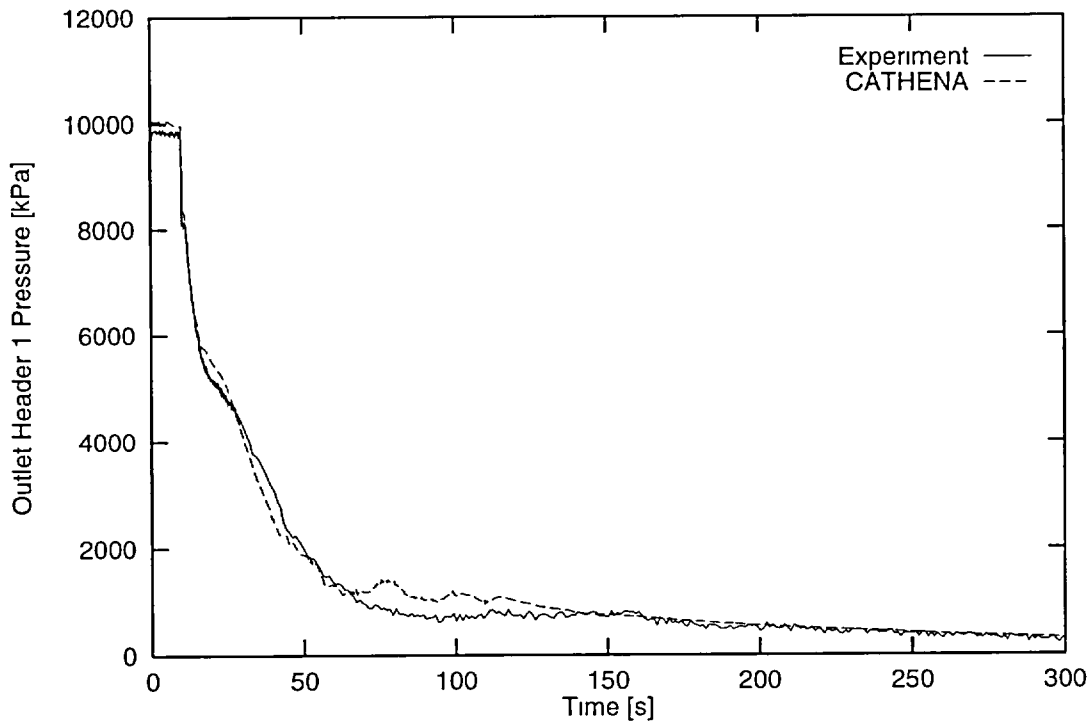


FIGURE 7 RD-12 Outlet Header 1 Pressure for test B8223

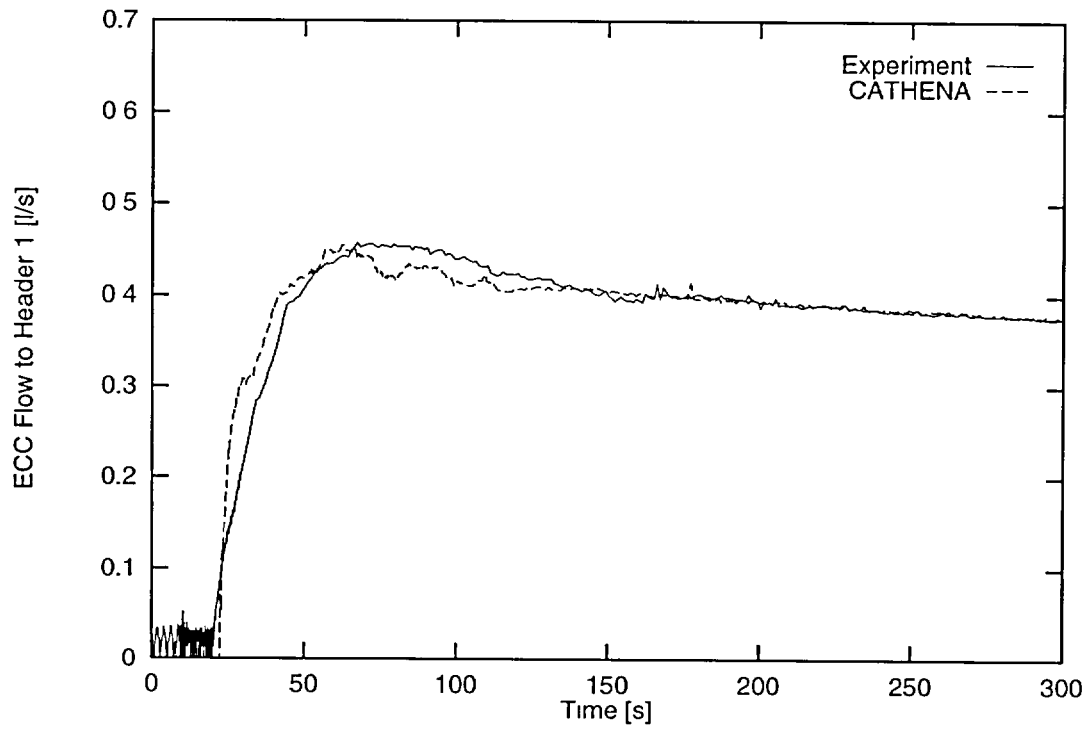


FIGURE 8: RD-12 Outlet Header 1 ECC Flow for test B8223.

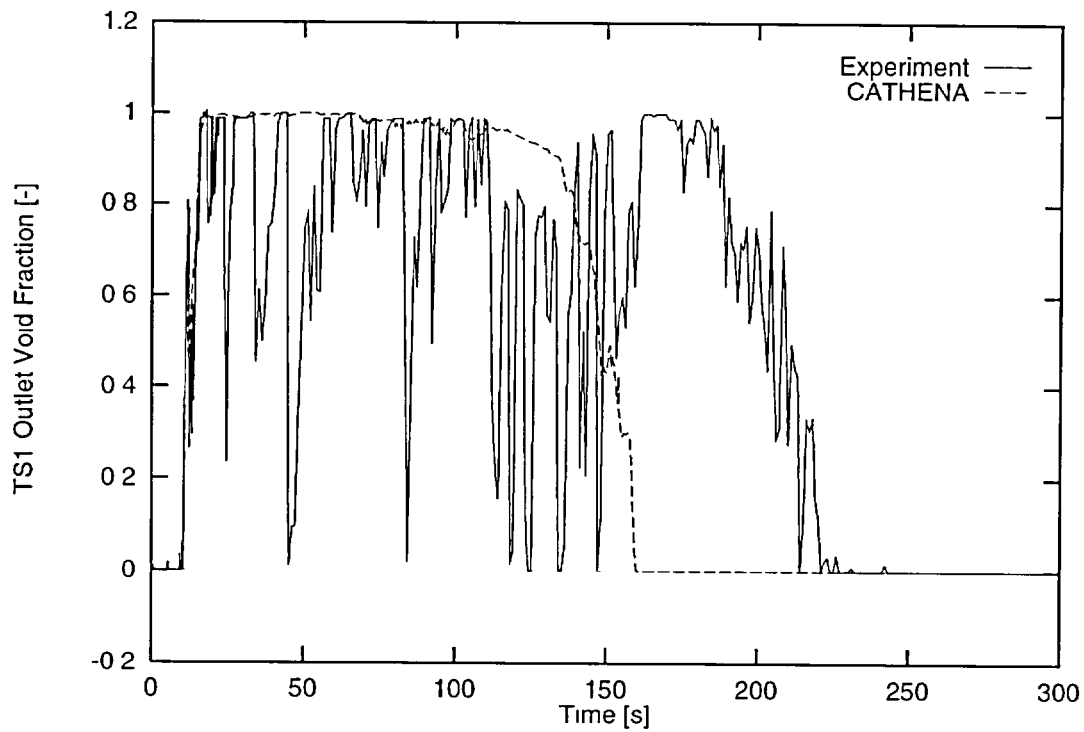


FIGURE 9: RD-12 TS1 Outlet Void Fraction for test B8223.

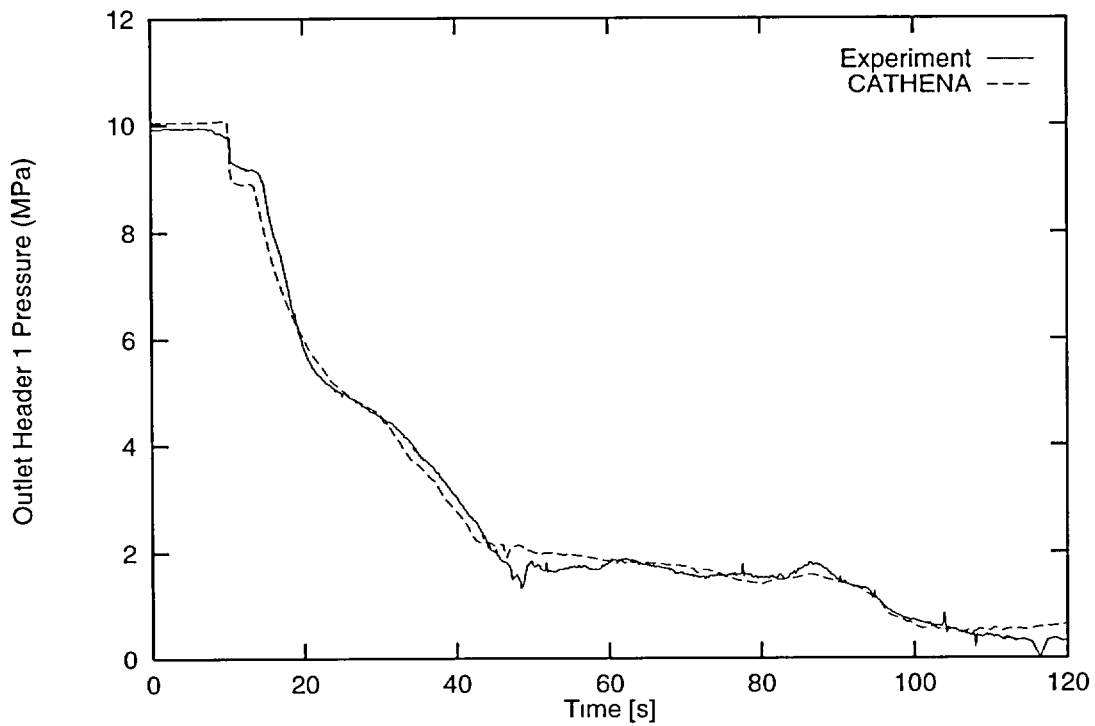


FIGURE 14: RD-14 Outlet Header 1 Pressure for Test B8711.

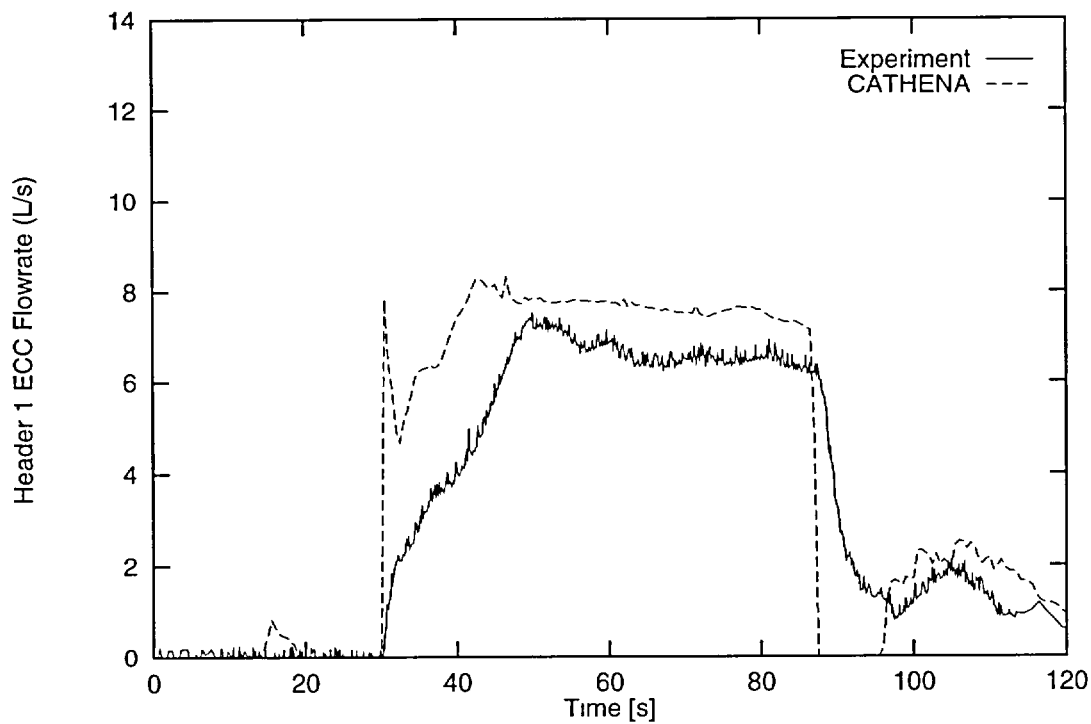


FIGURE 15: RD-14 Outlet Header 1 ECC Flow for Test B8711.

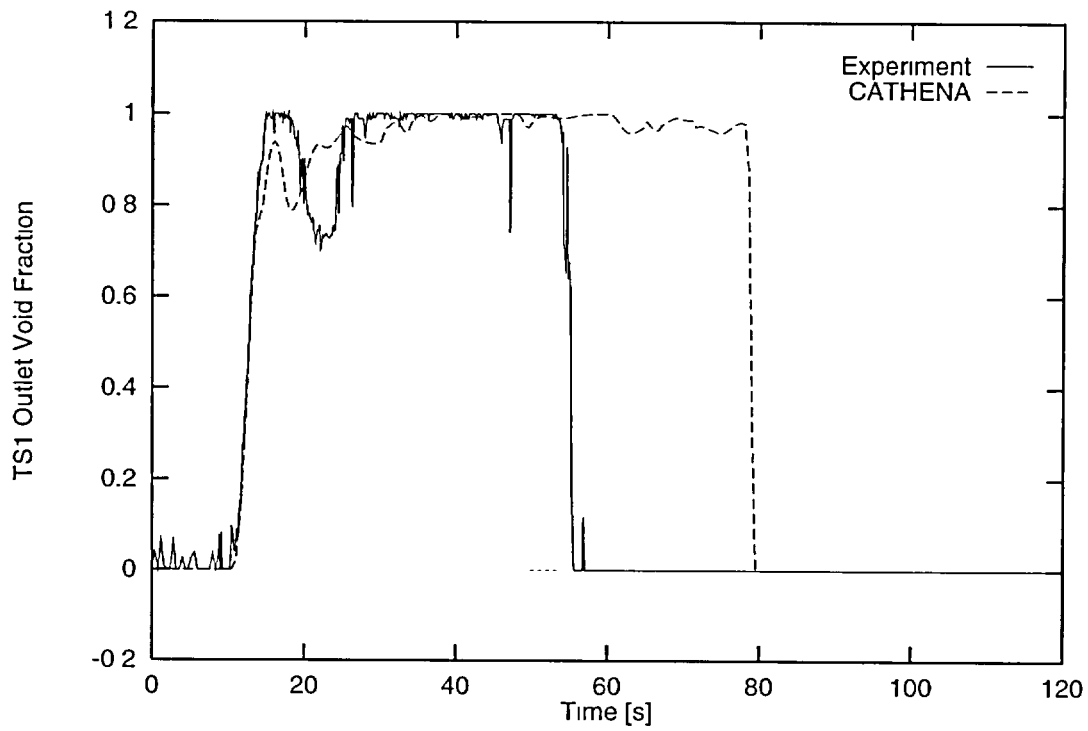


FIGURE 16: RD-14 TS1 Outlet Void Fraction for Test B8711.

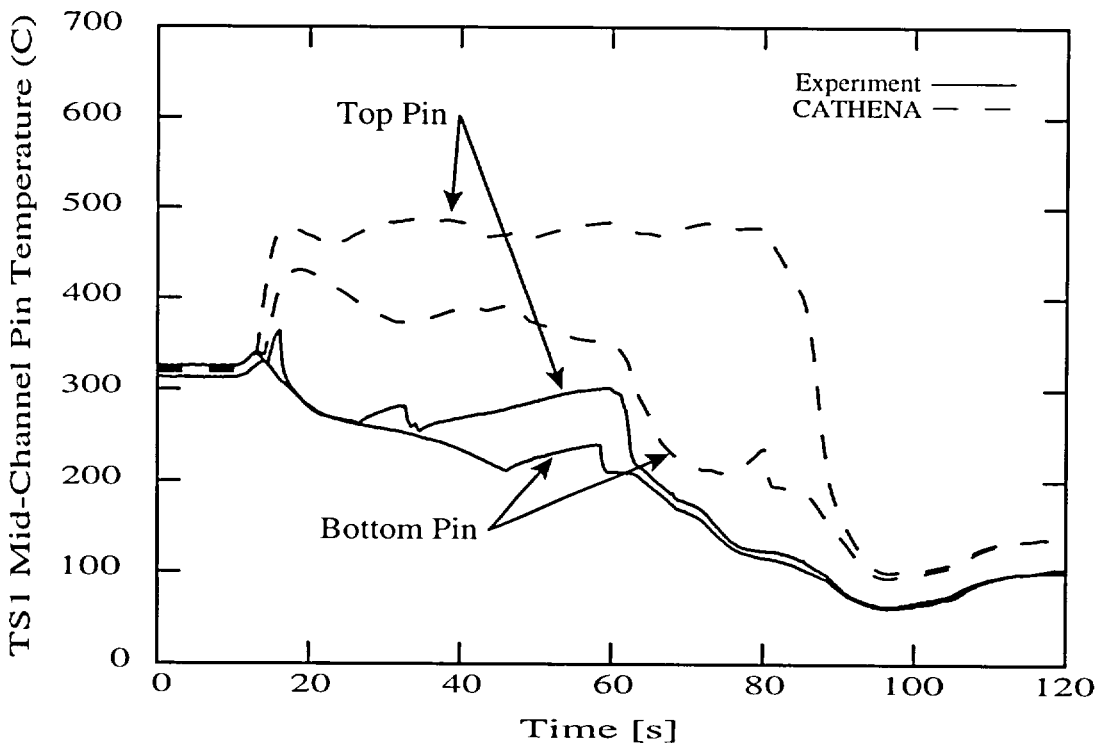


FIGURE 17: RD-14 TS1 Temperature for Test B8711.

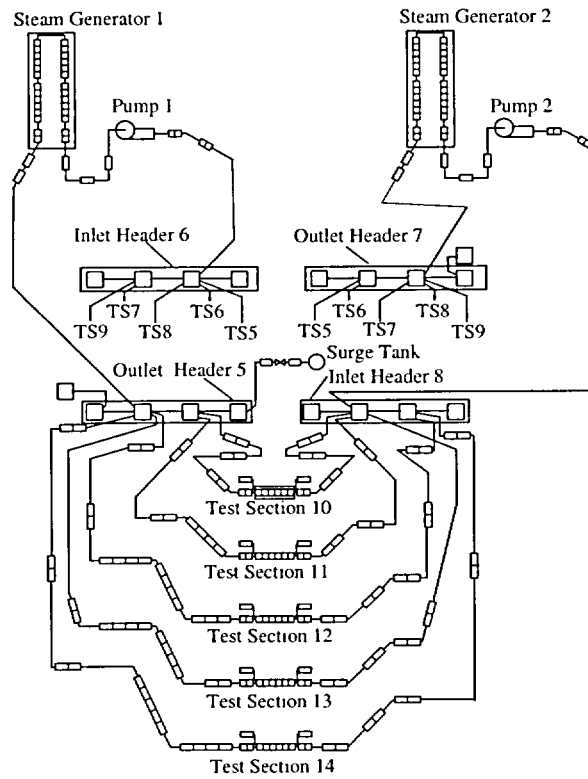


FIGURE 18: Thermalhydraulic Representation of RD-14M Primary Side

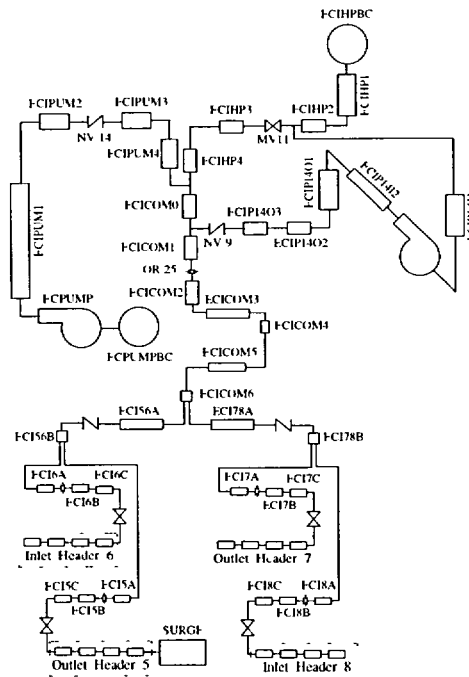


FIGURE 19. Thermalhydraulic Representation of RD-14M ECC System

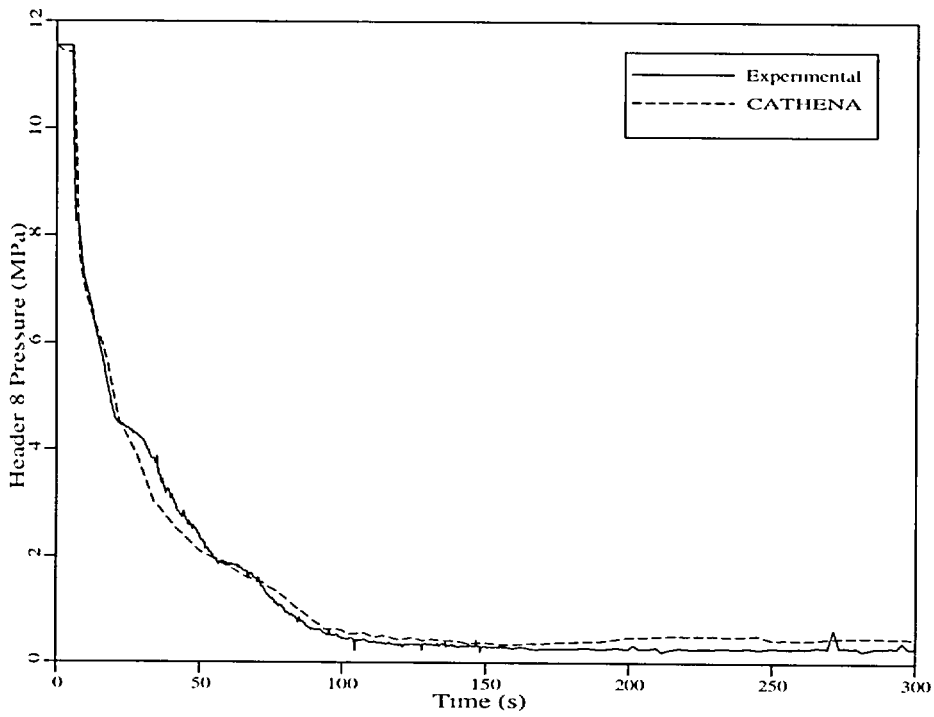


FIGURE 20: RD-14M Inlet Header 8 (Broken Header) Pressure for Test B9013

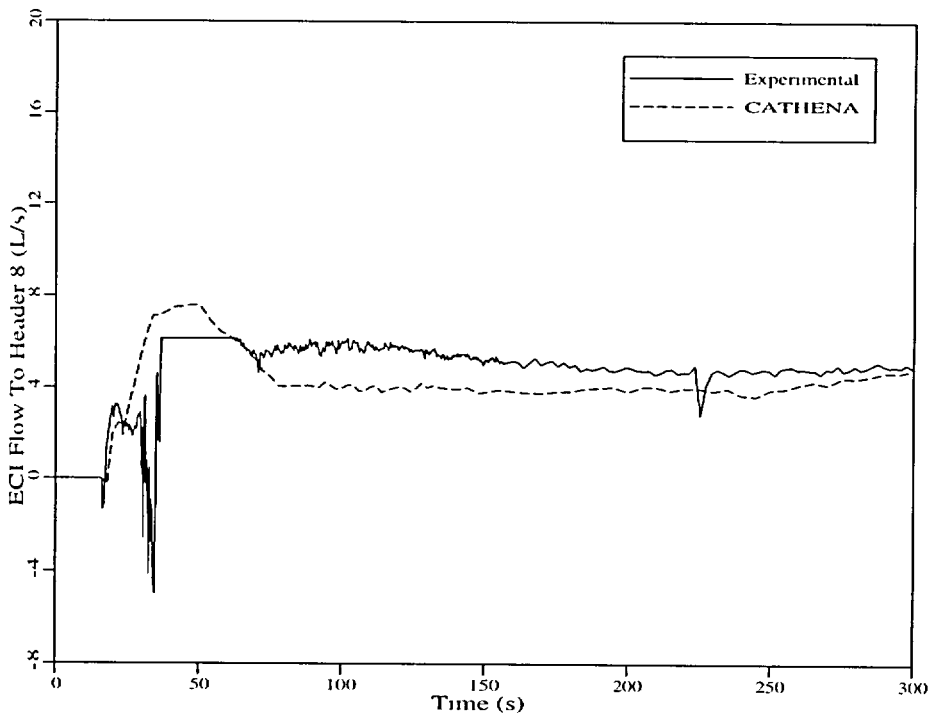


FIGURE 21: RD-14M Inlet Header 8 (Broken Header) ECC Flow for Test B9013

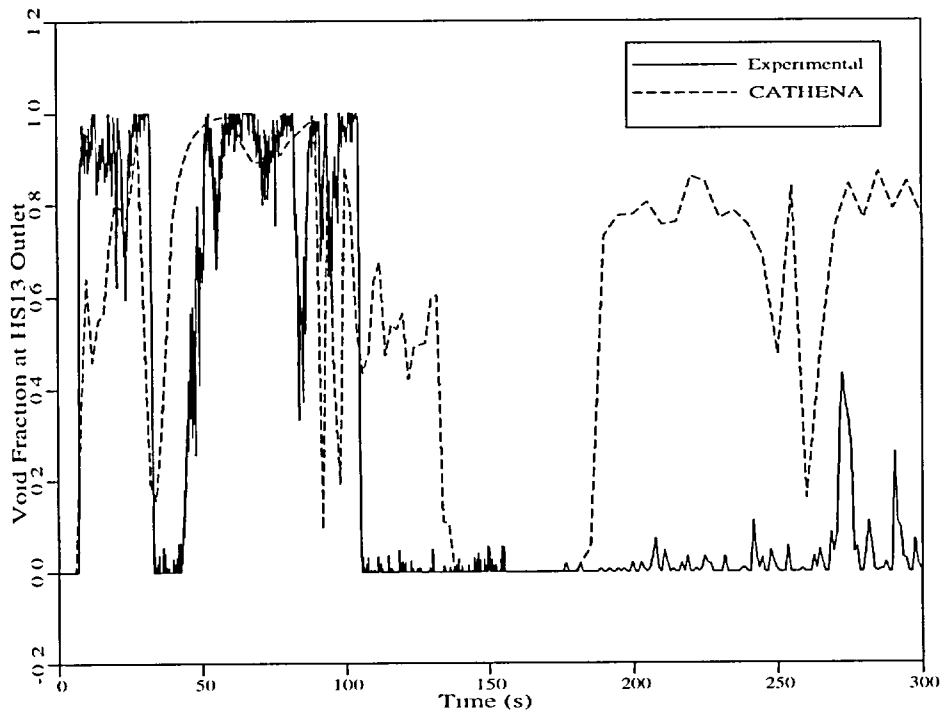


FIGURE 22: RD-14M Test Section 13 Outlet Void Fraction for Test B9013.

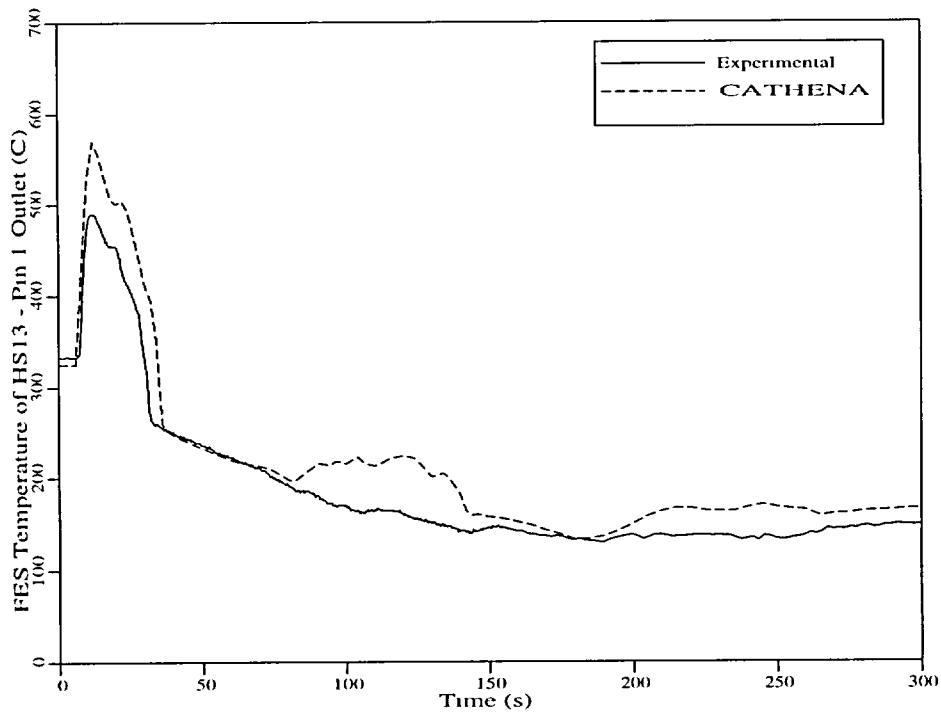


FIGURE 23: RD-14M Test Section 13 Outlet Top Pin Temperature for Test B9013.

HIGH-TEMPERATURE VALIDATION OF CATHENA AGAINST A 28-ELEMENT THERMAL-CHEMICAL EXPERIMENT *

Q.M. Lei and D.B. Sanderson
AECL Research - Whiteshell Laboratories
Pinawa, Manitoba, Canada ROE ILO
(204) 753-2311

ABSTRACT

An out-of-pile 28-element fuel channel experiment (CS28-1) has been performed to improve the understanding of fuel channel behaviour under postulated loss-of-coolant accident conditions and to provide data for validating various high-temperature thermal-chemical codes. Measured variables included test-section temperatures and pressures, steam outlet temperatures, and hydrogen production from the exothermic zirconium/steam reaction. The experiment was successful in obtaining fuel element simulator temperatures as high as 1730°C, with a peak hydrogen production rate of 0.28 mol/s.

This paper demonstrates the capabilities of the computer code CATHENA to predict the thermal-chemical behaviour of a 28-element fuel channel under these experimental conditions. Simulations of the experiment using CATHENA MOD-3.4b/Rev 7 were performed using the oxidation correlations of Urbanic-Heidrick and Leistikow-Prater-Courtright. The work was intended to examine various models in CATHENA, particularly the calculation of the zirconium/steam reaction and high-temperature heat transfer.

CATHENA accurately calculated fuel element simulator temperatures up to 1500°C using these oxidation correlations. Above 1500°C, the calculated test-section temperatures using the Urbanic-Heidrick correlation continued to be in good agreement with experimental data. The calculated peak hydrogen production rate using this correlation was within 2% of the measured value. The code overestimated temperature escalations above 1500°C when the Prater-Courtright oxidation correlation was used. A significant overestimation of pressure-tube temperatures was noted for both the simulations. The discrepancies are examined in this paper and areas for improvement of CATHENA's high-temperature calculation are addressed.

The work reported in this paper was funded by the CANDU** Owners Group (COG).

1. INTRODUCTION

To demonstrate the safety of current and future CANDU-PHW reactors during postulated loss-of-coolant accidents, it is important to have a thorough understanding of fuel channel behaviour at high temperatures under accident conditions. This understanding is achieved by studying the underlying phenomena using mathematical models and single-effect tests. These models are coupled into an integrated code which can then predict the behaviour of the fuel channel. Data for the validation of the codes come from integrated experiments involving the complex interaction of pressure, temperature, material properties, heat transfer and reaction kinetics on fuel channel components subjected to severe temperature transients. One such series of experiments are the CHAN Thermal-Chemical Experiments [1].

* Presented at the CNA/CNS Annual Conference, June 5-8, 1994, Montreal.

** CANDU (CANadian Deuterium Uranium) is a registered trademark of AECL.

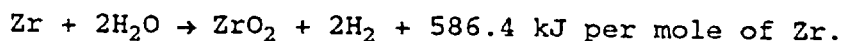
Computer codes, such as CHAN II [2] and CATHENA [3], are designed to predict the thermal and chemical responses of a CANDU fuel channel under postulated accident conditions. CATHENA has been used to model the thermal-chemical behaviour of seven-element high-temperature CHAN experiments as part of post-test analysis [4]. This code has also been used in a blind simulation study where it adequately predicted the behaviour of a seven-element experiment when only the input parameters were known [5]. These post-test comparisons between measured and simulated results help interpret the experimental results and improve our understanding of the physical phenomena involved. As well, these studies provide an increased validation base for use of CATHENA in CANDU fuel-channel safety calculations. This paper reports on a post-test CATHENA simulation of the 28-element CHAN experiment CS28-1.

2. THE CODE CATHENA AND ITS OXIDATION MODEL

CATHENA [3] is a one-dimensional thermalhydraulic computer code developed by AECL at Whiteshell Laboratories primarily to analyse postulated loss-of-coolant accident scenarios for CANDU nuclear reactors. The code uses a nonequilibrium, two-fluid thermalhydraulic model to describe two-phase fluid flow. Conservation equations for mass, momentum, and energy are solved for each phase (liquid and vapour). Interphase mass, momentum, and energy transfers are specified using a set of flow regime dependent constitutive relations. The code uses a staggered-mesh, one-step, semi-implicit, finite-difference solution method.

CATHENA has the ability to model a reactor channel in detail. Radial and circumferential conduction are calculated for individual pins within a bundle, the pressure tube, and the calandria tube. No axial conduction is calculated; however, the thermal response in the axial direction is accounted for in the axial nodalization of the channel. The effects of thermal radiation, pressure-tube deformation, zirconium/steam reaction, steam starvation, solid surface contact, and the presence of noncondensables can all be modelled.

The zirconium/steam reaction is exothermic and can be expressed as



Under severe accident conditions, the oxidation of zirconium alloy fuel cladding and pressure tubes can add a substantial amount of heat to the nuclear decay heat in the fuel channels. If sufficient steam and Zircaloy are available for the reaction, the heat generation will be determined by the temperature. CATHENA provides several correlations for calculating oxidation rates at different temperature ranges. Two sets of oxidation correlations were examined in this study, the Urbanic-Heidrick correlation [6] (UH) and the Leistikow [7] with Prater-Courtright [8] correlation (LE) (see Figure 1).

3. THE EXPERIMENT

Experimental Apparatus

The 28-element test section consisted of three rings of fuel element simulators concentrically located inside a Zr-2.5 Nb pressure tube (Figure 2a). Each fuel element simulator consisted of Zr-4 cladding, 15.2-mm outside diameter and 14.4-mm inner diameter, within which annular alumina pellets electrically insulate the cladding from a 6-mm diameter graphite rod heater. The length of the heated section was 1800 mm.

The fuel element simulator bundle was surrounded by a 2105-mm-long section of autoclaved Zr-2.5 Nb pressure tube mounted inside a 1780-mm-long Zr-2 calandria

tube (Figure 2b). The calandria tube was surrounded by heated, stirred water in an open tank. Five spacer plates, machined out of 0.90-mm-thick Zr-4, were uniformly placed in the heated zone of the test section (Figure 2b). Their purpose was to simulate the effects of CANDU bundle end plates on steam flow patterns through the fuel element simulator bundle and to help minimize sag of the bundle at high temperatures.

A schematic of the test apparatus is shown in Figure 2c. Steam produced in the boiler passed through the steam superheater and into the test section. The steam picked up energy from the hot fuel element simulators as it passed through the test section and some of the steam reacted exothermically with the zirconium, releasing hydrogen. The hot steam-hydrogen mixture exiting the test section was directed through a condenser to condense the steam. The resulting mixture of condensate and hydrogen entered a water trap where the condensate was collected. The remaining hydrogen gas flowed through a mass flowmeter and was vented to atmosphere.

Instrumentation

The fuel element simulators were connected in parallel to a DC power supply. The power connections were set up in three distinct rings: outer, middle, and inner (Figure 2a). This allowed the radial power distribution through the bundle to approximate that found in a typical CANDU 28-element bundle. One of the four inner ring pins was not powered in this test and was used for instrumentation purposes.

Test section temperatures were monitored at 12 axial locations using a total of 80 thermocouples. Thirty-seven C-type thermocouples were installed through holes in the alumina pellets inside the fuel element simulators. These thermocouples were about 1.4-mm away from the inner surface of the Zr-4 cladding. Steam flow to the test section was determined using an orifice plate and the pressure was measured using gauge pressure transmitters. The accuracy of these measurements was estimated as follows:

Electric power	±4.5%
Temperature up to 1800°C	±2%
Steam flow at 10 g/s	±0.5 g/s
H ₂ flow up to 0.44 mol/s	±2%
Pressure up to 500 kPa	±1%

Experimental Procedure

The test was divided into five distinct stages and the controlled input parameter histories are shown in Figure 3. The steam superheater and test section were heated in nitrogen until pressure-tube temperatures exceeded 200°C (stage 1). Steam was then introduced into the test section at 10 g/s and the nitrogen flow stopped at the end of stage 1. This flow rate of steam was maintained until the end of the test. During stage 2, the test section was heated for roughly 4800 s with 10 kW of electric power. Power was ramped to 20 kW at the start of stage 3 and subsequently increased to 40 kW to increase fuel element simulator temperatures to about 900°C. Power was further increased to 135 kW at the start of stage 4 (Figure 3). Power remained at this level until recorded temperatures exceeded 1650°C, after which the power was shut off to study the heat released from the zirconium/steam reaction. The test was terminated by shutting off the steam flow 16 s after the electric power was shut off.

Experimental Results

The experiment achieved fuel element simulator temperatures as high as 1730°C at an axial location of 1725 mm into the heated zone. Figure 4 shows fuel element

simulator temperature histories at various radial locations at 1575 mm into the heated zone. Significant radial temperature gradients indicated that the dominant heat flow path was in the radial direction (not axially). Electric power to the test section was shut off at 852 s, when peak recorded temperatures reached 1680°C. Fuel element simulator temperatures toward the end of the heated zone continued to increase after the electric power was turned off. Temperatures continued to increase for 16 s to a maximum of 1730°C when the zirconium/steam reaction was stopped by shutting off the steam flow to the test section.

Hydrogen production from the zirconium/steam reaction started when maximum measured temperatures reached about 750°C. The hydrogen production rate remained below 0.007 mol/s until temperatures reached 950°C (stage 4), after which the rate steadily increased, reaching 0.23 mol/s by the end of stage 4. The peak hydrogen production rate during the experiment was 0.28 mol/s, which occurred just before the steam flow was shut off.

4. MODELLING METHODOLOGY AND ASSUMPTIONS

The experimental conditions were simulated using CATHENA MOD-3.4b/Rev 7. The modelling methodology and assumptions were:

- 1) The heated portion of the test section was axially discretized into 12 equal-length segments. In each axial segment, the pins and the pressure tube with the calandria tube were sectorized as shown in Figure 5a to enable CATHENA to represent the flow subchannels and predict circumferential temperature variations. Each of the 28 pins was divided into 2 sectors, whereas the pressure and calandria tubes were divided into 10 sectors. All 28 pins had to be modelled individually (no grouping) because one of the inner-ring pins was not electrically heated, thus removing the symmetrical advantage for modelling.
- 2) The total flow area was divided into four subchannels as shown in Figure 5a. Each flow subchannel was treated as a horizontal pipe with a different flow area and hydraulic diameter. Figure 5b shows the thermalhydraulic connections for the steam/hydrogen flow. No mixing was assumed to take place among the four subchannels along the test section except at the ends of the test section and at the locations of the five spacer plates (mixers). At these locations the subchannel flows were assumed to be completely mixed.
- 3) The measured normalized pin power ratios for the inner, middle, and outer rings of the fuel element simulators were 0.78, 0.87, and 1.10, respectively, and were used in the simulations. Electric power for each heated pin was assumed to be distributed uniformly along the 12 axial segments.
- 4) Radiation view factors for the pin surfaces and inner pressure-tube surfaces (Figure 5a) were calculated by CATHENA. Each surface was treated to be isothermal, opaque, diffuse, gray and surrounded by a nonabsorbing and nonscattering medium.
- 5) Deformation of the test section was neglected. Post-test cross sections of the test section have shown minimal bundle slumping and pressure-tube sag during the experiment. Therefore, this assumption should not have a significant impact on predicted results.
- 6) Conduction and radiation in the axial direction were not modelled. Relatively flat axial temperature profiles were seen from the measured

data, indicating negligible axial heat flow except near the ends of the test section. Axial heat losses to the end hubs during the experiment were not accounted for in this analysis.

- 7) Emissivities for the fuel element simulator cladding and the inner and outer surfaces of the autoclaved pressure tube were assumed to be constant at 0.8 [9]. Emissivity for the inner surface of the calandria tube was assumed to be 0.34 [9].
- 8) The CATHENA simulations were started at an experimental time of 400 s (the middle of stage 3). Initial conditions for the simulations were taken from the measured values at 400 s. Test input conditions were linearly interpolated from the measured values (Figure 3). Results from a simulation started at a much earlier time showed a negligible effect on simulation results for the later transient.

5. COMPARISON BETWEEN EXPERIMENTAL AND SIMULATED RESULTS

Two CATHENA simulations were performed using identical input conditions. One simulation used the Urbanic-Heidrick (UH) correlation and the other simulation used the Leistikow-Prater-Courtright (LE) correlation. These two simulations were designed to determine the impact of different oxidation correlations on the predicted behaviour of the 28-element test section.

Fuel Element Simulator Temperatures

Measured and simulated temperatures for the inner ring of fuel element simulators are compared at three axial locations in Figure 6. The calculated temperatures using both the UH and LE oxidation rates agree well with the measured values until temperatures exceed 1500°C. At 1500°C, there is a dramatic increase in the oxidation kinetics within the LE correlation (Figure 1), credited to allotropic changes in the structure of ZrO₂ from tetragonal to cubic. The increase in oxidation kinetics with the UH correlation occurs at 1580°C. This theoretical increase in oxidation kinetics results in a substantial increase in the predicted heating rate of the fuel element simulators. The measured temperatures for the powered simulator (TC37 in Figure 6a) show that this heatup rate increase occurred at about 1550°C in the experiment.

In the simulation using the LE-oxidation rate, local steam starvation was predicted in the inner-ring subchannel near the test-section exit end. This localized steam starvation limited predicted cladding temperature escalations during the latter part of stage 4 and during stage 5 (Figures 6). Temperatures recorded by thermocouples showed no evidence of steam starvation nor was there any steam starvation predicted within the bundle when the UH-oxidation rates were used.

Simulated pin temperatures using both the UH- and LE-oxidation rates at some axial locations (Figure 6) show a continuous increase after electric power to the test section was turned off in stage 5. These localized temperature escalations were observed in the experiment, indicating a self-sustaining zirconium/steam reaction under the test conditions studied.

Similar trends are noted in measured and simulated temperature histories for the middle- and outer-rings of the fuel element simulators (Figures 7 and 8). The simulated temperatures using the UH-oxidation rates followed the experimental data closely, with a maximum overestimation of 100°C in stage 5. The simulated pin temperatures using the LE-oxidation rates increased sharply when they exceeded 1500°C. The temperature escalation stopped once a local steam-starved

condition was predicted or the steam flow was shut off at 866 s. These early temperature escalations resulted in CATHENA overestimating middle-ring and outer-ring pin temperatures by as much as 200°C.

Pressure-Tube Temperature

Measured and simulated pressure-tube temperatures are compared in Figure 9 at three axial locations. The difference between the simulations using the two different oxidation correlations was small, except in stage 5. Both the UH- and LE-based simulations overestimated pressure-tube temperatures. The overestimation started with a significant difference between measured and simulated pressure-tube heatup rates in stage 3. Possible reasons for this overestimation are addressed in the discussion section of this paper.

Calandria-Tube and Steam Temperatures

Simulated calandria-tube temperatures (Figure 10a) agree with measured values. Slight overestimations are seen near the end of stage 4 and thereafter when significant nucleate boiling was predicted to take place on the outer surface of the calandria tube.

Measured and simulated steam (steam-hydrogen mixture) temperatures at Z=1575 mm are compared in Figure 10b and 10c. CATHENA accurately calculated the steam temperatures for the different subchannels, with the central subchannel (TC65) being hottest. The simulated steam temperatures for both the UH- and LE-oxidation rates prior to the end of stage 4 were within the uncertainty of the steam temperature measurement.

Hydrogen Production

The measured and simulated hydrogen production rate and cumulative hydrogen production from the zirconium/steam reaction are compared in Figure 11a and 11b. These hydrogen production values are over the entire test section and reflect the average test-section temperature, total zirconium/steam reaction area, and steam available for the reaction along the test section.

The simulated hydrogen production rates with both LE and UH oxidation correlations agreed reasonably well with each other prior to 750 s. The two simulations were consistently higher than the measured values (Figure 11a). The LE-based hydrogen production rate curve rose sharply when the calculated test-section temperatures exceeded 1500°C. This was because the LE correlation has a step increase in oxidation kinetics at this temperature (Figure 1). A similar increase in hydrogen production rate was noted to occur in the experiment when the measured test-section temperature exceeded 1550°C. As a result, the simulated (LE) hydrogen production rates elevated at 810 s, 25 s earlier than the experimental data. This predicted earlier escalation resulted in a further overestimation of hydrogen production rate towards the end of the simulation when the LE correlation was used.

The measured peak hydrogen production rate was 0.28 mol/s which occurred just prior to shutting off the steam flow to the test section. The simulated peak rate of 0.285 mol/s using the UH correlation was within 2% of the measured value.

The peak hydrogen production rate was overestimated by a factor of two when the LE-oxidation rates were used. The simulated peak rate was limited by the amount of steam available in the test section. For this case, the code predicted that all 10.5 g/s of steam was fully converted to H₂ as it flowed to the test-section exit end.

The cumulative hydrogen production (obtained by integrating the hydrogen production rate with respect to time) is shown in Figure 11b. A total of 18.5 mol of hydrogen was collected during the experiment by the time steam to the test section was shut off at 866 s. The predicted hydrogen production using the UH correlation up to 866 s was 24 mol, 30% more than collected during the experiment. A total of 39 mol of hydrogen was predicted using the LE-oxidation rates, 110% more than that measured.

Energy Balance

The measured and simulated energy components over the entire test section are compared in Figure 12. Heat was generated by electric current flowing through the graphite heater and by the zirconium/steam reaction. Some of this heat was removed by the steam flow and some by surrounding moderator. Energy lost by conduction to the end connections could not be determined for the apparatus, but was estimated to be a low percentage of the total energy input.

The experimental heat generation rate from the zirconium/steam reaction (Figure 12b) was obtained by multiplying the hydrogen production rate by 293.2 kJ/(mol H₂). The simulated values for the reaction heat generation using the UH-oxidation rates were within the measurement uncertainty (Figure 12b). The LE curve was higher than the experimental data after 810 s as expected from the calculated test-section temperatures and hydrogen production rate.

Energy removed by the steam flow was estimated as the product of the measured steam flow rate and the measured steam temperature difference between axial locations Z = 0 and Z = 1575 mm (Figure 12c). The simulated (UH and LE) curves for energy removal rates by the steam flow matched with the experimental results.

Figure 12d compares the simulated heat removal rate by the water surrounding the calandria tube with the heat removal rate estimated using measured temperatures. The heat removal rate in the experiment was estimated by calculating conduction and radiation heat transfer through the CO₂ gas annulus between the pressure and calandria tubes (solid line in Figure 12d). Effects of the flowing CO₂ in the annulus and the flow disturbance by the pressure-tube thermocouple wires, and axial heat losses to the end fittings were not included in these calculations. Although the predicted heat removal rates were higher than the experimental values, the actual heat removal rates during the experiment are expected to be higher than the values shown in Figure 12d.

6. DISCUSSION OF THE RESULTS

CATHENA accurately predicted fuel element simulator temperatures up to 1500°C using both the UH- and LE-oxidation rates. This indicates an adequate calculation by CATHENA in high-temperature heat transfer (e.g., for convection, zirconium/steam reaction, and radiation).

Above 1500°C, the UH-based simulation results continued to follow the experimental data closely. The calculated hydrogen production rates with this correlation were within the uncertainty of the hydrogen flow-rate measurement. Test-section temperatures and hydrogen production rates, however, were overestimated when temperatures exceeded 1500°C and the LE-oxidation correlation was used.

The overestimated temperature escalation with the LE-oxidation rates above 1500°C suggests that deposition of the oxidation reaction heat may not be properly handled. The current CATHENA model assumes that the heat generated from the

zirconium/steam reaction is deposited in the zirconium (Zr) layer immediately adjacent to the interface between ZrO_2 and Zr. This can result in localized heating of the region at high oxidation rates which further escalate the temperature and the reaction rate. A further study is under way to assess the impact of this assumption.

Increases in oxidation kinetics between 1500 and 1600°C are credited to allotropic changes in the structure of ZrO_2 from tetragonal to cubic around these temperatures [6,8]. There exists a large uncertainty in the temperature at which the ZrO_2 phase change initiates. Prater and Courtright [8] reported that the ZrO_2 phase change was observed around 1510°C. Urbanic and Heidrick [6] reported that at about 1580°C a discontinuity was seen on the plot of the temperature-dependent growth constants for the combined ZrO_2/α -Zr layer. This uncertainty affects the CATHENA results significantly (e.g., see Figure 6) because the correlations switch from a low oxidation rate to a much higher rate once this phase-change temperature is reached.

The microstructure change in the ZrO_2 layer is also unlikely to be instantaneous (a step increase) as assumed by the correlation. Any lag in the phase change will result in lower oxidation rates and hence lower predicted temperatures until the change is complete. Therefore, reducing the uncertainties in this phase-change temperature and the time required for the completion of the phase change will improve CATHENA predictions above 1500°C.

Good agreement between measured and simulated steam temperatures and heat removal rates by steam flow was found. This suggests convective heat transfer in the 28-element bundle for superheated steam (with noncondensable hydrogen) was correctly modelled in CATHENA.

The simulated pressure-tube temperatures were significantly higher than measured, regardless of the oxidation rates used. This discrepancy can partly be attributed to neglecting the effect of flowing CO_2 in the fuel channel annulus. The CO_2 flow in the annulus between the pressure and calandria tubes was 0.18 g/s in this experiment and could reduce the thermal boundary layer thicknesses and enhance radial heat removal. As well, the presence of thermocouple wires and standoffs on the outside surface of the pressure tube may cause disturbances in the flow which further increase radial heat transfer. Analysis is needed to clarify this impact.

7. CONCLUSION

From the present validation work, the following conclusions can be drawn

- 1) CATHENA (MOD-3.4b/Rev 7) accurately predicted fuel element simulator temperatures up to 1500°C using both the Urbanic-Heidrick and Leistikow-Prater-Courtright oxidation rates, indicating an adequate prediction of high-temperature heat transfer and oxidation rates.
- 2) Above 1500°C, the simulation results using the Urbanic-Heidrick oxidation correlation continued to follow the experimental data closely. With this correlation, the calculated hydrogen production rates were within the uncertainty of the hydrogen flow-rate measurement.
- 3) CATHENA predicted rapid temperature escalations when the calculated test-section temperatures exceeded 1500°C and the Prater-Courtright oxidation correlation was used. The resultant calculated hydrogen production rates using this oxidation correlation were about twice as high

as the measured values. Potential reasons for the overestimation are being investigated.

- 4) A significant overestimation of pressure-tube temperatures was noted during this study, regardless of the oxidation correlation used. Possible reasons for the overestimation were discussed, and further studies are required to fully understand this discrepancy.

REFERENCES

1. D.B. Sanderson, K.A. Haugen, R.G. Moyer and H.E. Rosinger, "Out-of-Pile Fuel Channel Experiments for Severe Accident Conditions," In Proceedings of the ANS International Topical Meeting on the Safety of Thermal Reactors, Portland, OR, 92-100, 1991.
- V.Q. Tang and D.G. Vandenberghe, "CHAN II: A Computer Program Predicting Fuel Channel Thermal Behaviour in a Typical CANDU-PHW Reactor Core Following a Loss-of-Coolant Accident," Internal Atomic Energy of Canada Limited Report, WNRE-494, 1981.
3. D.J. Richards, B.N. Hanna, N. Hobson and K.H. Ardron, "CATHENA: A Two-Fluid Code for CANDU LOCA Analysis, (renamed from ATHENA)," Presented at the 3rd International Topical Meeting on Reactor Thermalhydraulics, Newport, RI, 1985.
4. J.P. Mallory, M.A. Wright and H. Huynh, "Validation of CATHENA at High-Temperature Conditions Using CHAN Thermal-Chemical Experimental Results," Presented at the 12th Annual CNS Conference, Saskatoon, SK, 1991.
5. D.B. Sanderson, Q.M. Lei, J.P. Mallory and M. Bayoumi, "A Blind Simulation Study of an Out-of-Pile High-Temperature Fuel Channel Experiment," Presented at the 16th Annual Nuclear Simulation Symposium, Saint John, NB, 1991.
6. V.F. Urbanic and T.R. Heidrick, "High-Temperature Oxidation of Zircaloy-2 and Zircaloy-4 in Steam," Journal of Nuclear Materials **75**, 251-261, 1978.
7. S. Leistikow and G. Schanz, "Oxidation Kinetics and Related Phenomena of Zircaloy-4 Fuel Cladding Exposed to High Temperature Steam and Hydrogen-Steam Mixtures Under PWR Accident Conditions," Nuclear Engineering and Design **103**, 65-84, 1987.
8. J.T. Prater and E.L. Courtright, "Zircaloy-4 Oxidation at 1300 to 2400°C," Pacific Northwest Laboratories Report, PNL-6166, NUREG/CR-4889, 1987.
9. P.M. Mathew, M. Krause, M. Dean and M.H. Schankula, "Emission of Zircaloy-4 Sheath at High Temperatures in Argon and Steam Atmospheres," In Proceedings of the 10th Annual CNS Conference, Ottawa, ON, Vol.2, 9-12, 1989.

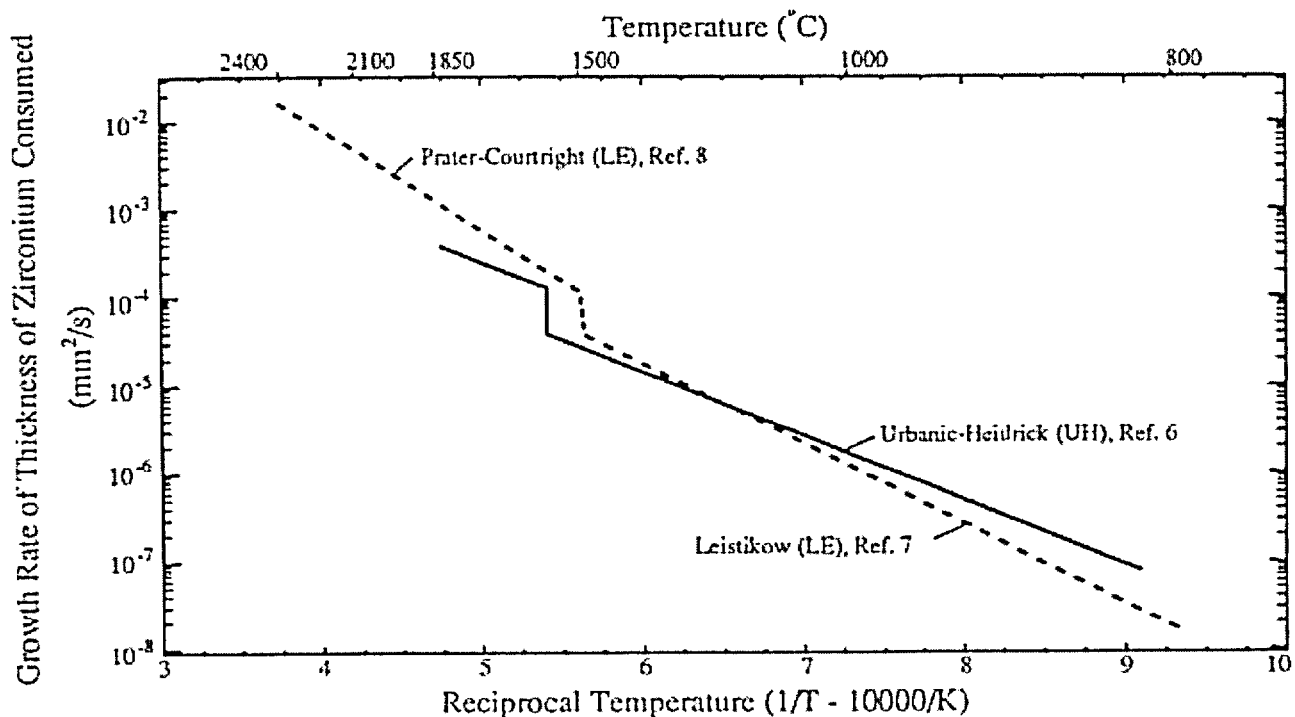


FIGURE 1: Two Oxidation Rate Correlations used in CATHENA Zirconium/Steam Reaction Model

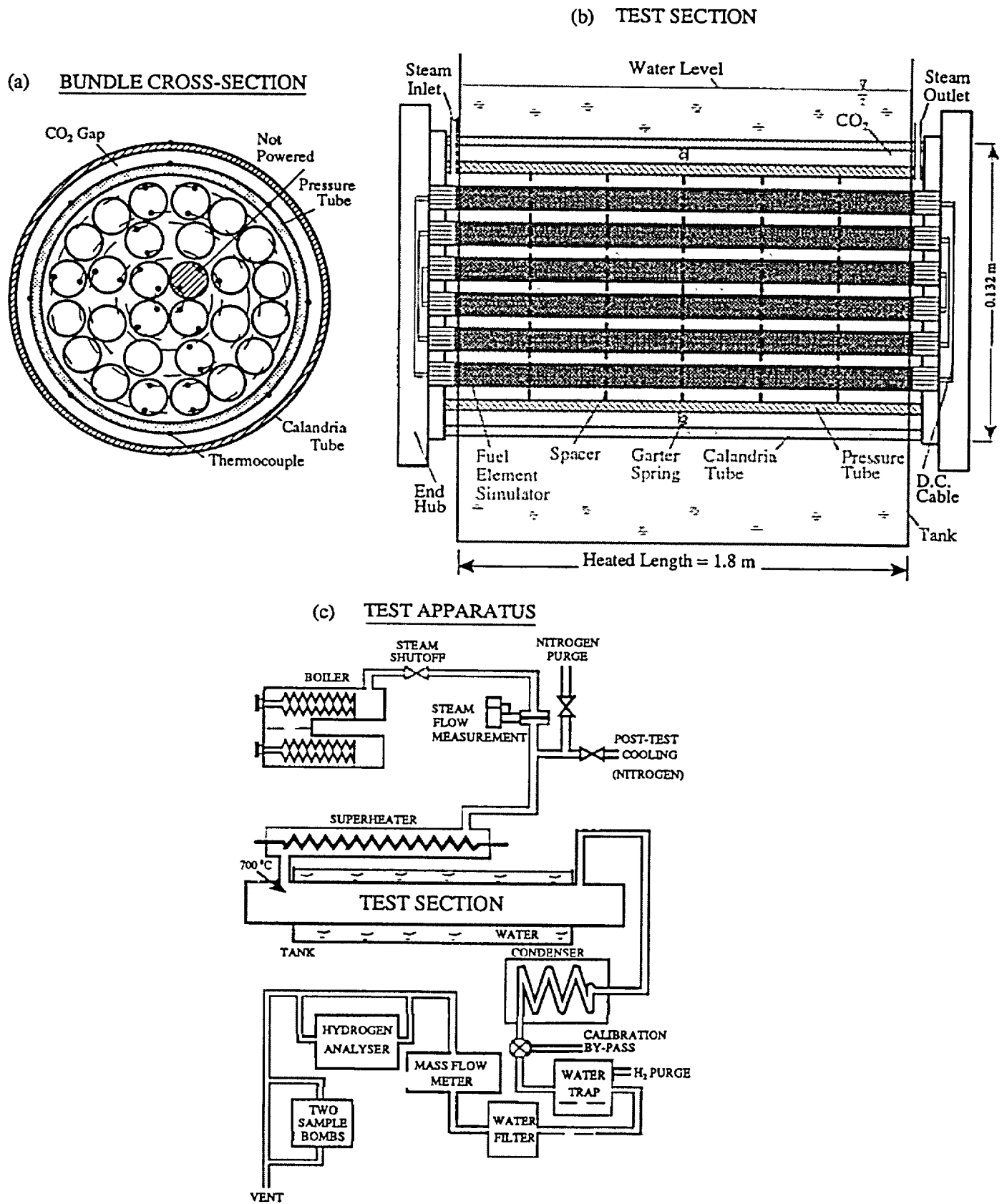


FIGURE 2: Schematics of (a) Bundle Cross-Section, (b) Test Section, and (c) Test Apparatus for Test CS28-1.

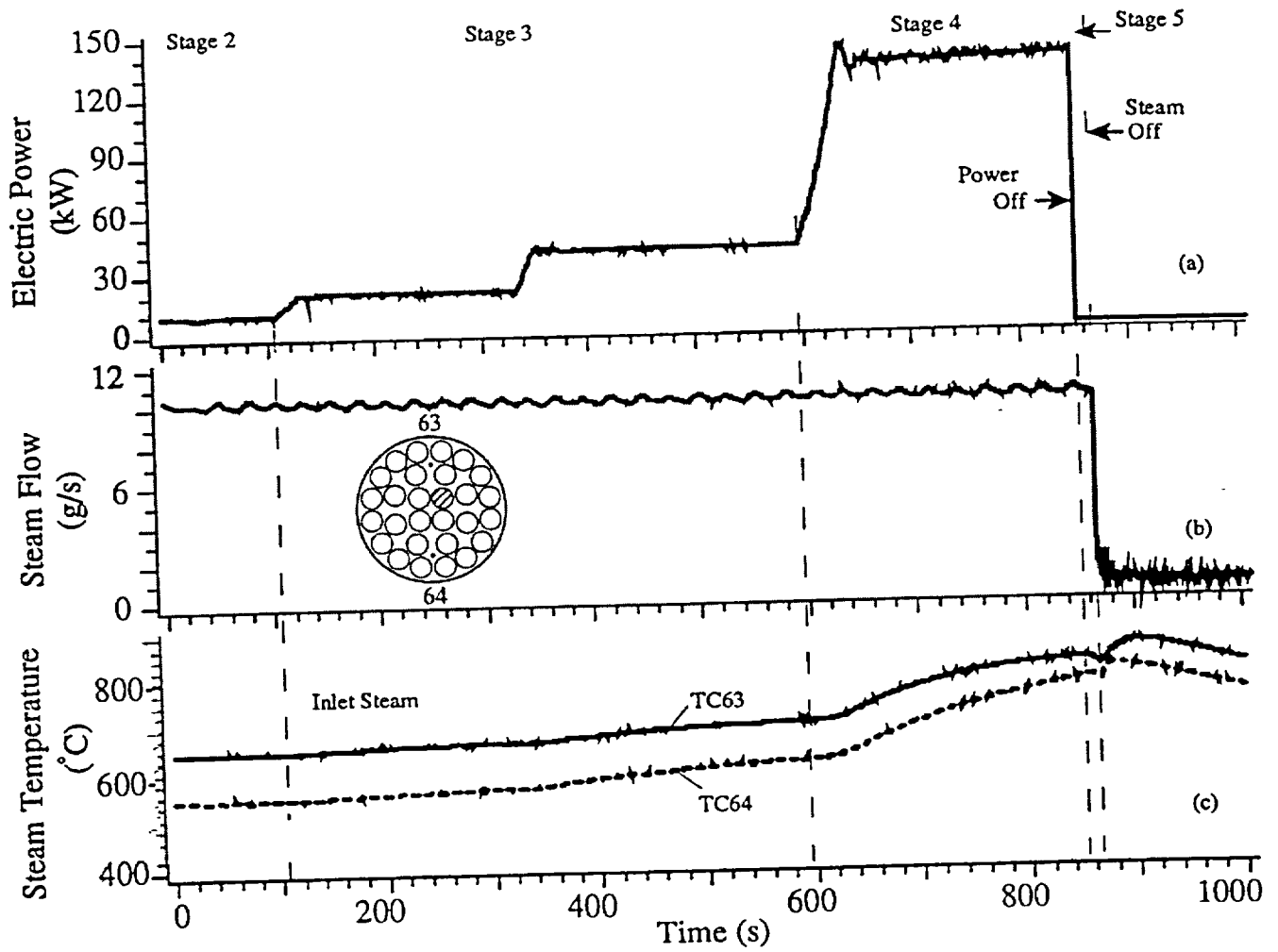


FIGURE 3: Controlled Input Parameters for Test CS28-1: (a) Test Section Electric Power, (b) Steam Flow Rate, and (c) Steam Inlet Temperatures (Test Section Absolute Pressure at 120 kPa)

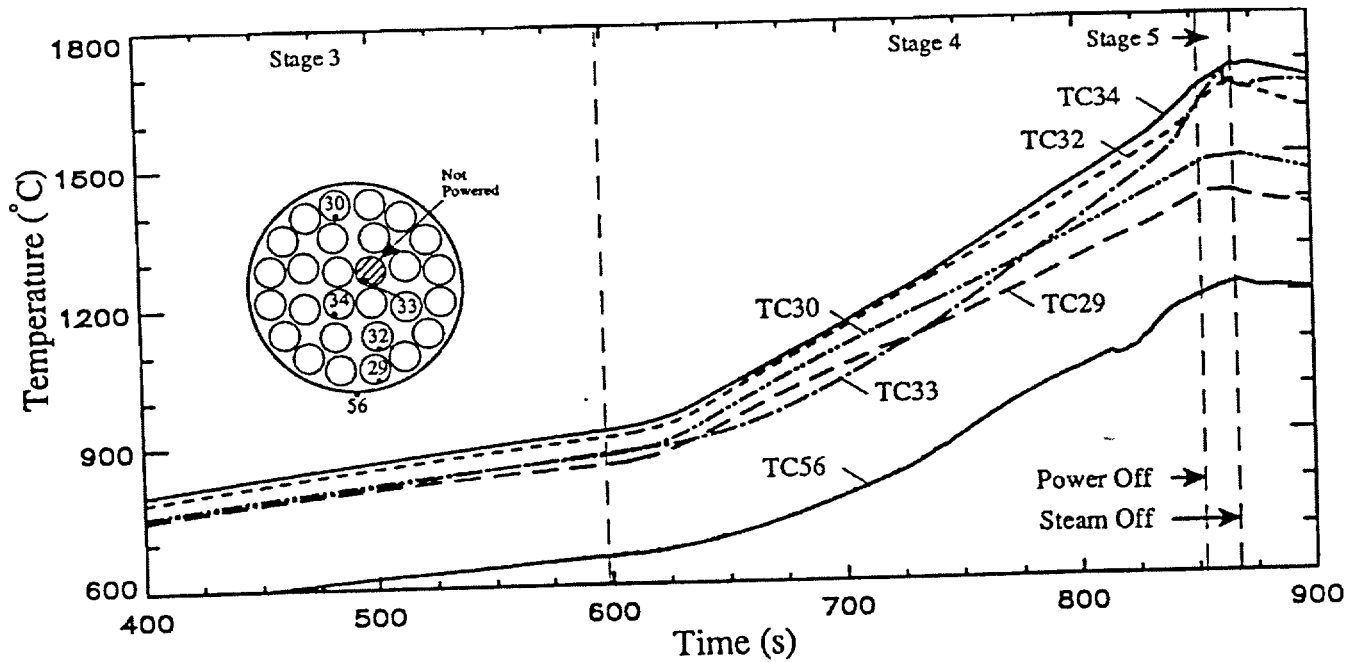
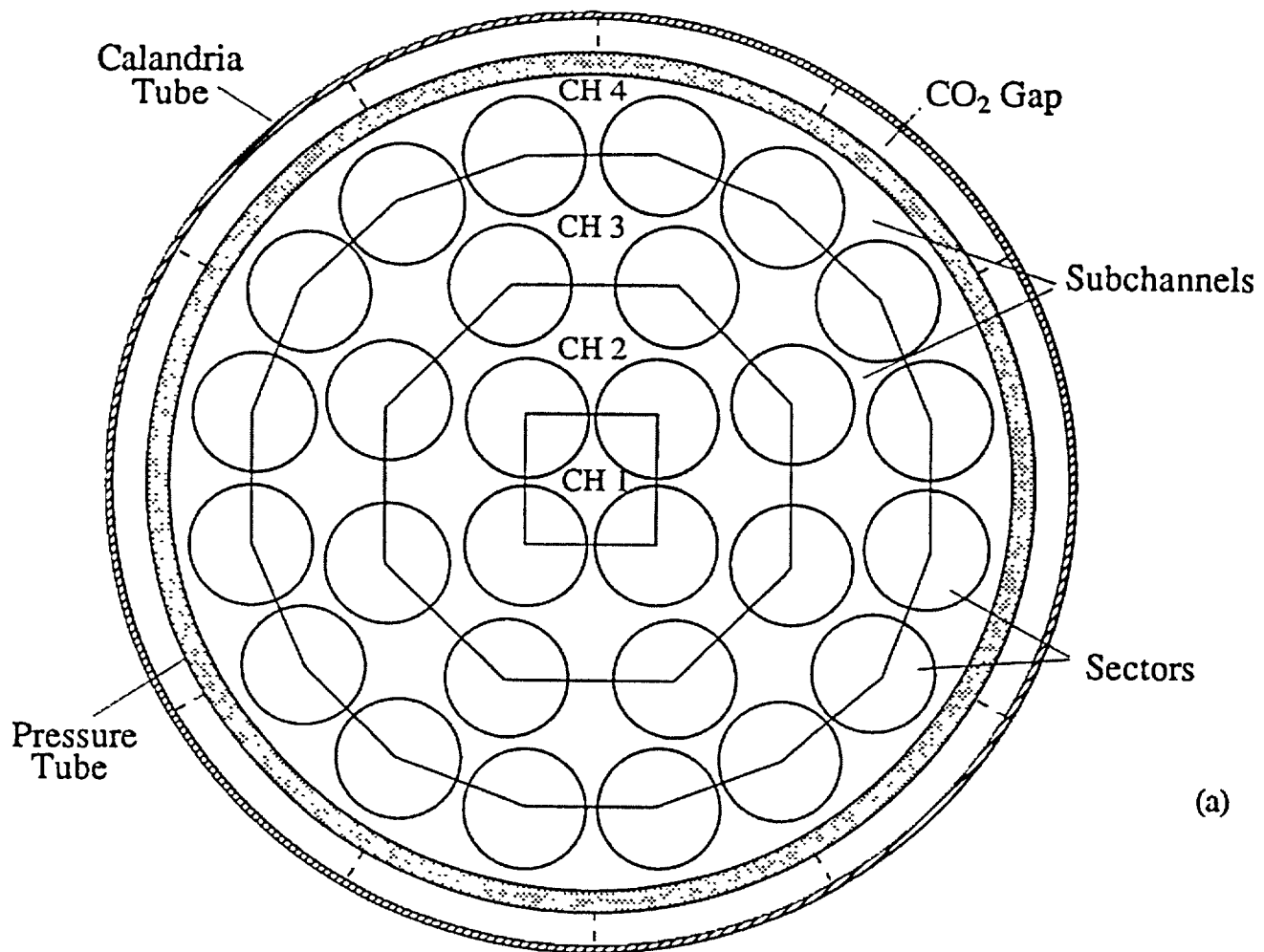
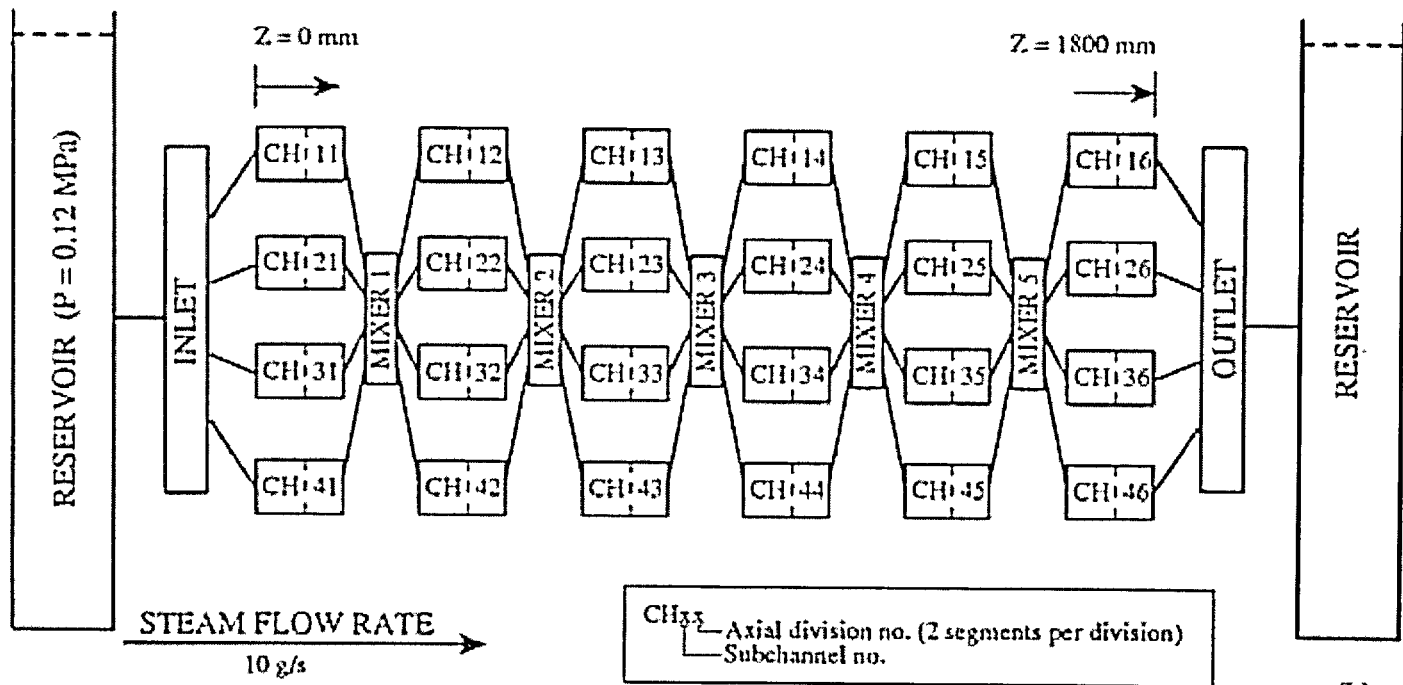


FIGURE 4: Measured Radial Temperature Profile 1575 mm into the Heated Zone from Test CS28-1



(a)



(b)

FIGURE 5: CATHENA 28-Element Model for Simulating Test CS28-1: (a) Divided Sectors and Subchannels and (b) Thermalhydraulic Connections

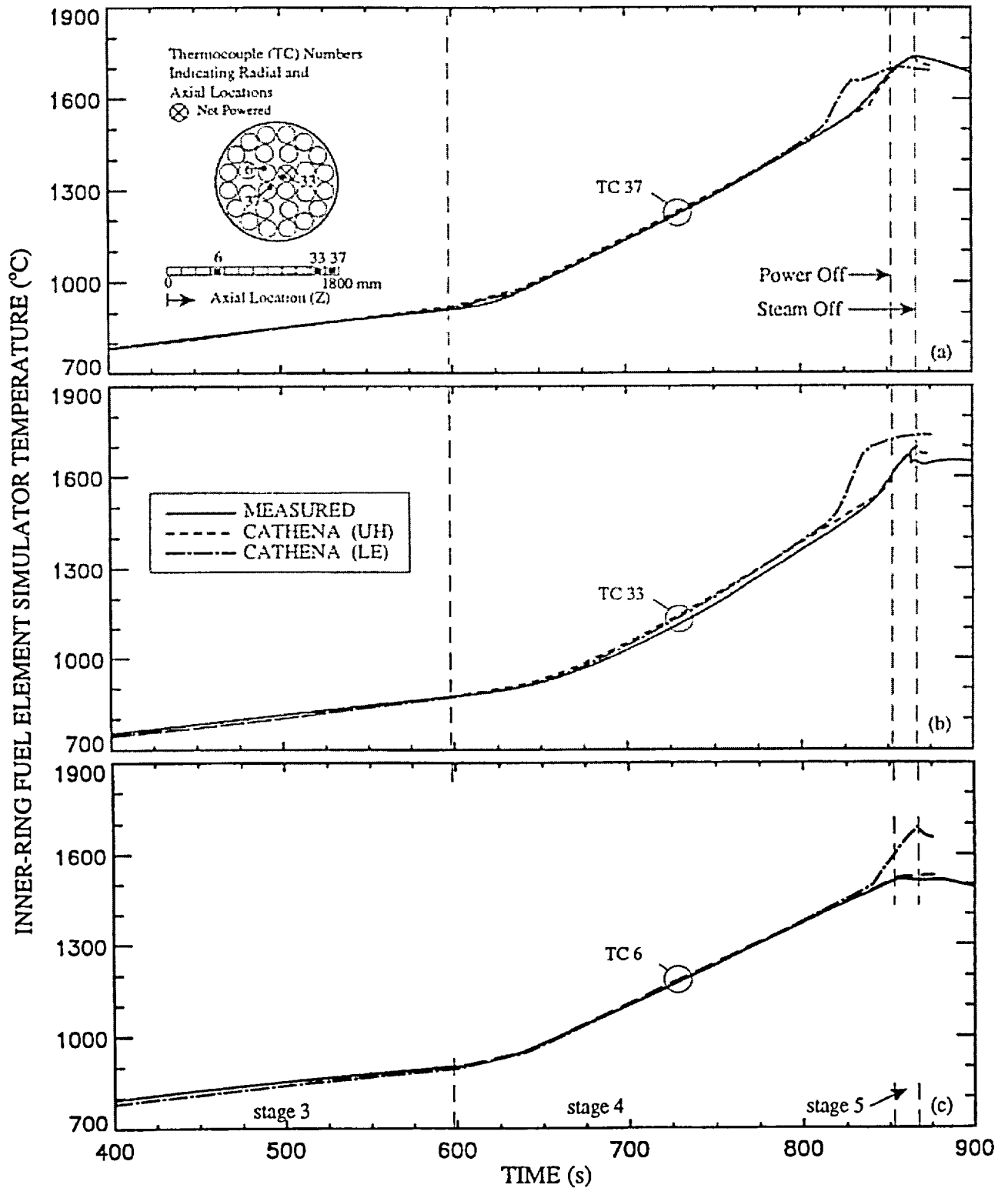


FIGURE 6: Comparison of CATHENA Simulations with Experimental Results of CS28-1 for Inner-Ring Fuel Element Simulator Temperature History at Z = 1725, 1575 and 525 mm

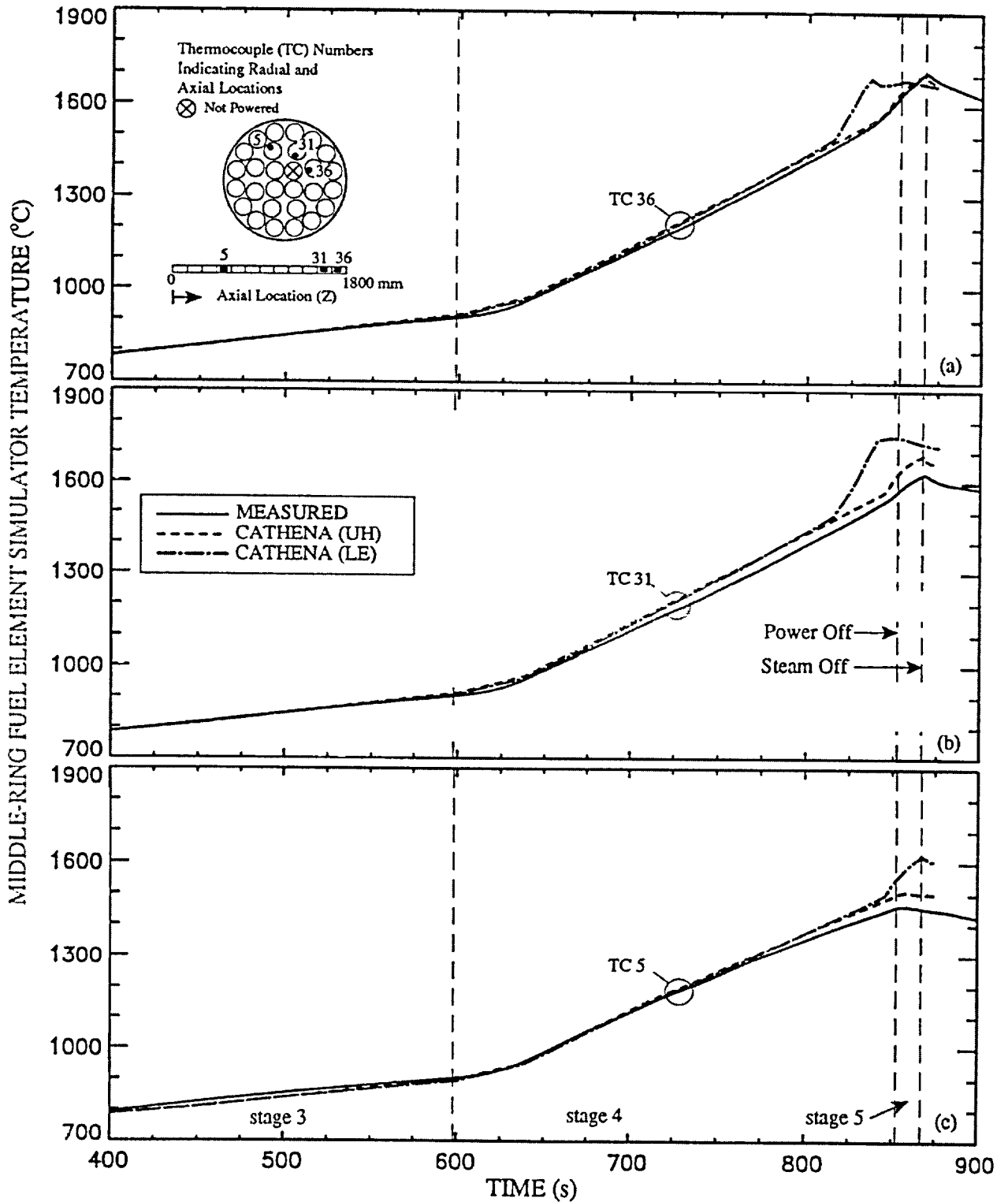


FIGURE 7: Comparison of CATHENA Simulations with Experimental Results of CS28-1 for Middle-Ring Fuel Element Simulator Temperature History at Z = 1725, 1575 and 525 mm

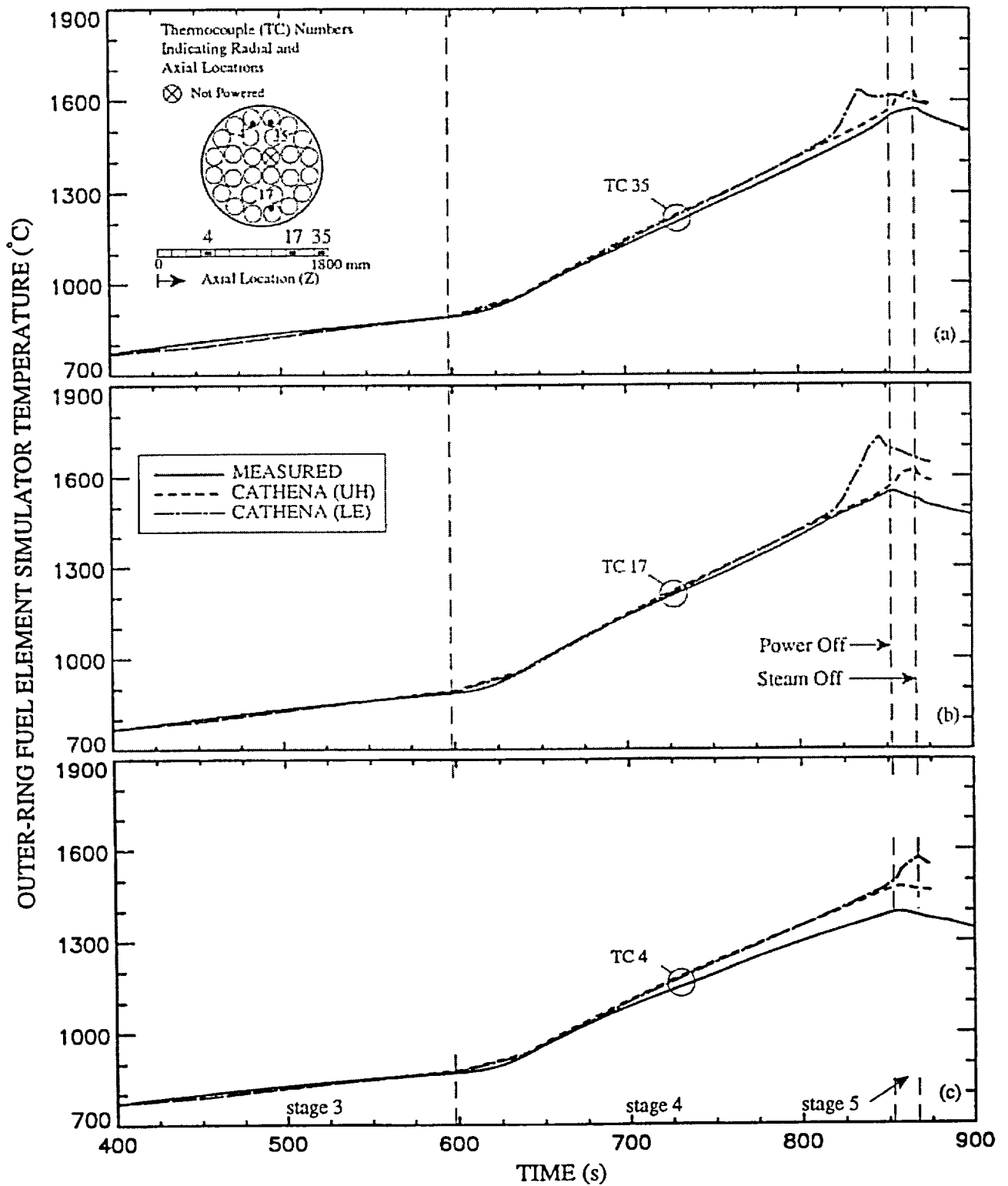


FIGURE 8: Comparison of CATHENA Simulations with Experimental Results of CS28-1 for Outer-Ring Fuel Element Simulator Temperature History at $Z = 1725, 1425$ and 525 mm

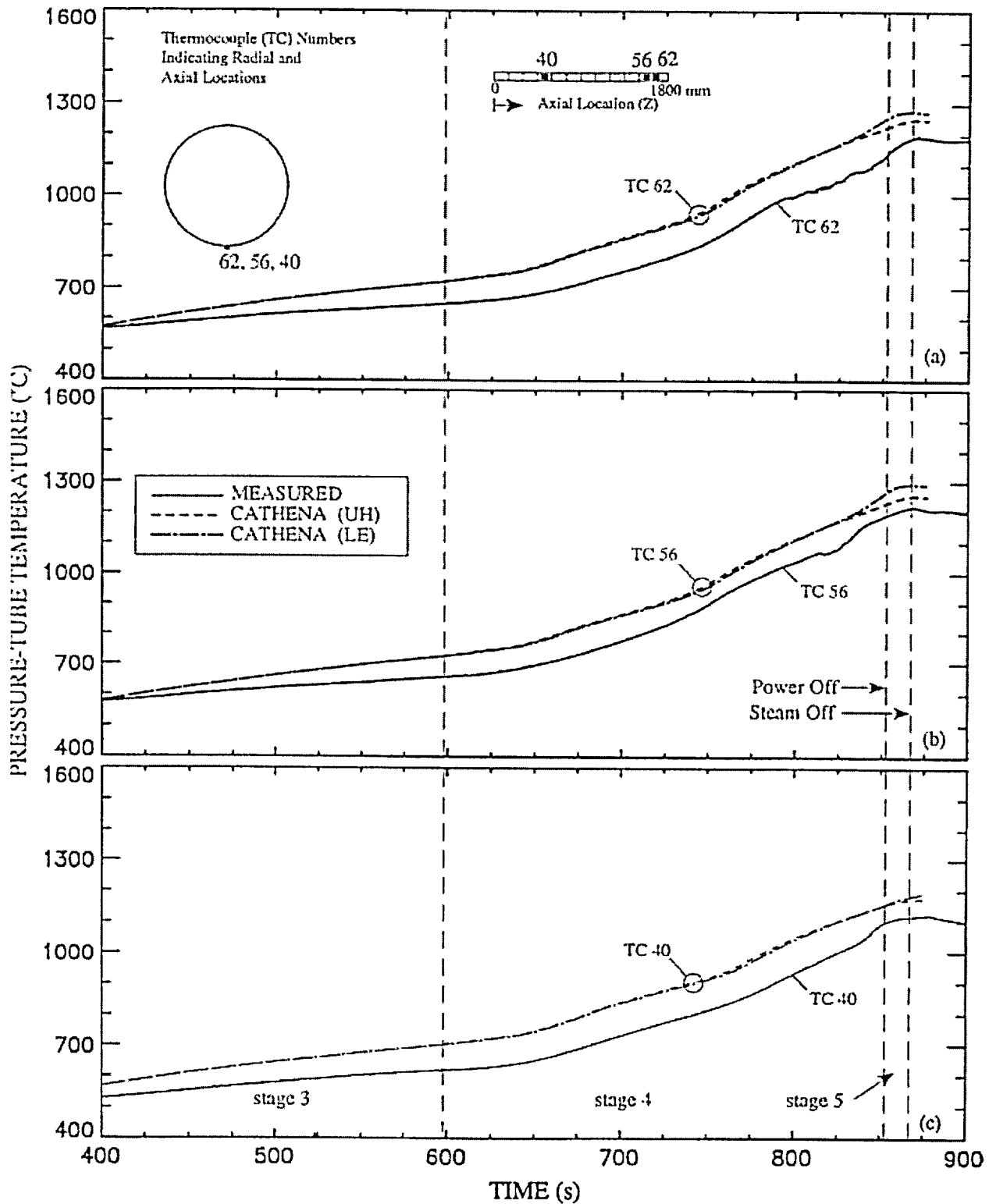


FIGURE 9: Comparison of CATHENA Simulations with Experimental Results of CS28-1 for Pressure-Tube Temperature History at Z = 1650, 1575 and 525 mm

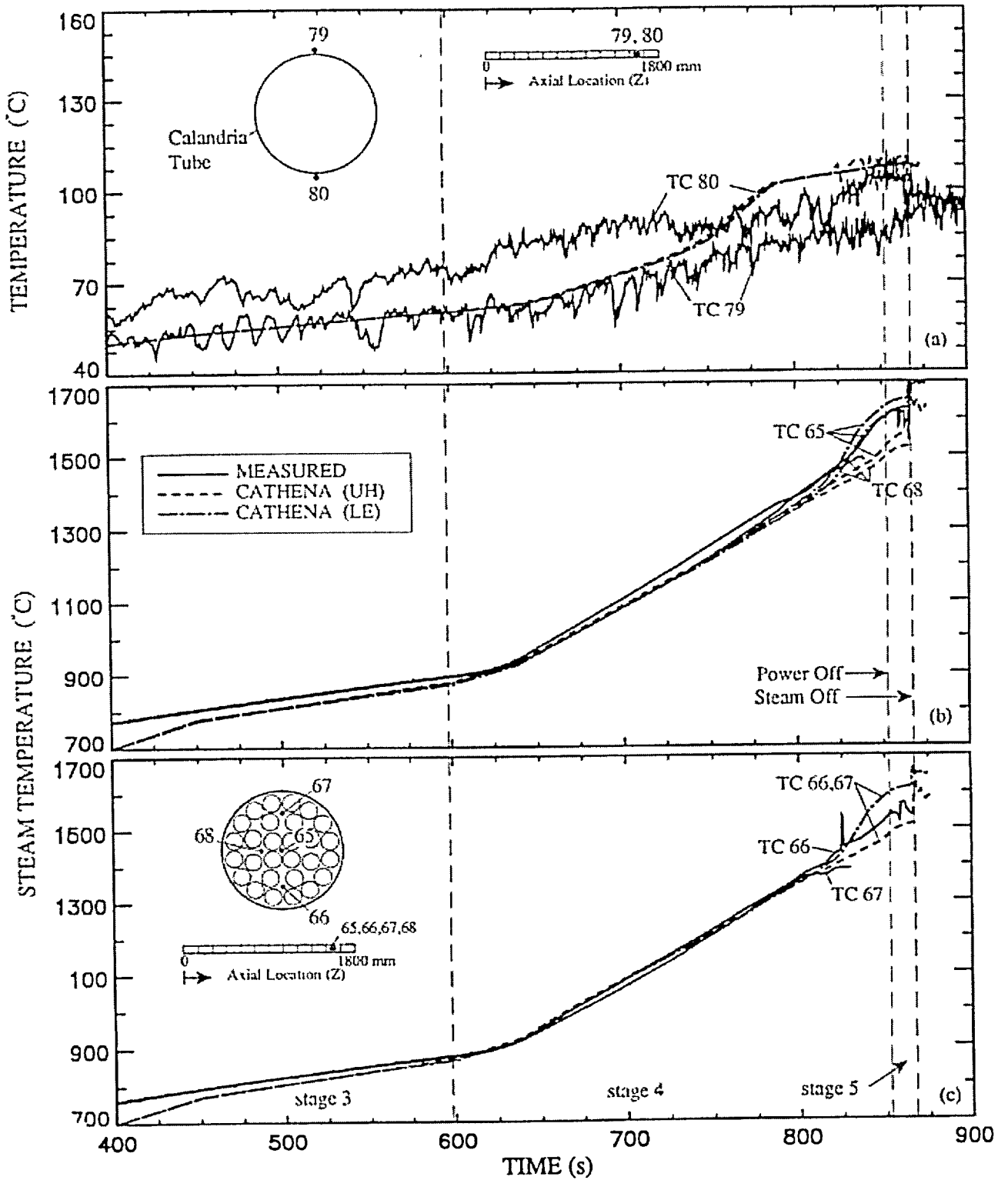


FIGURE 10: Comparison of CATHENA Simulations with Experimental Results of CS28-1 for (a) Calandria-Tube and (b and c) Steam Temperatures at $Z = 1575$ mm

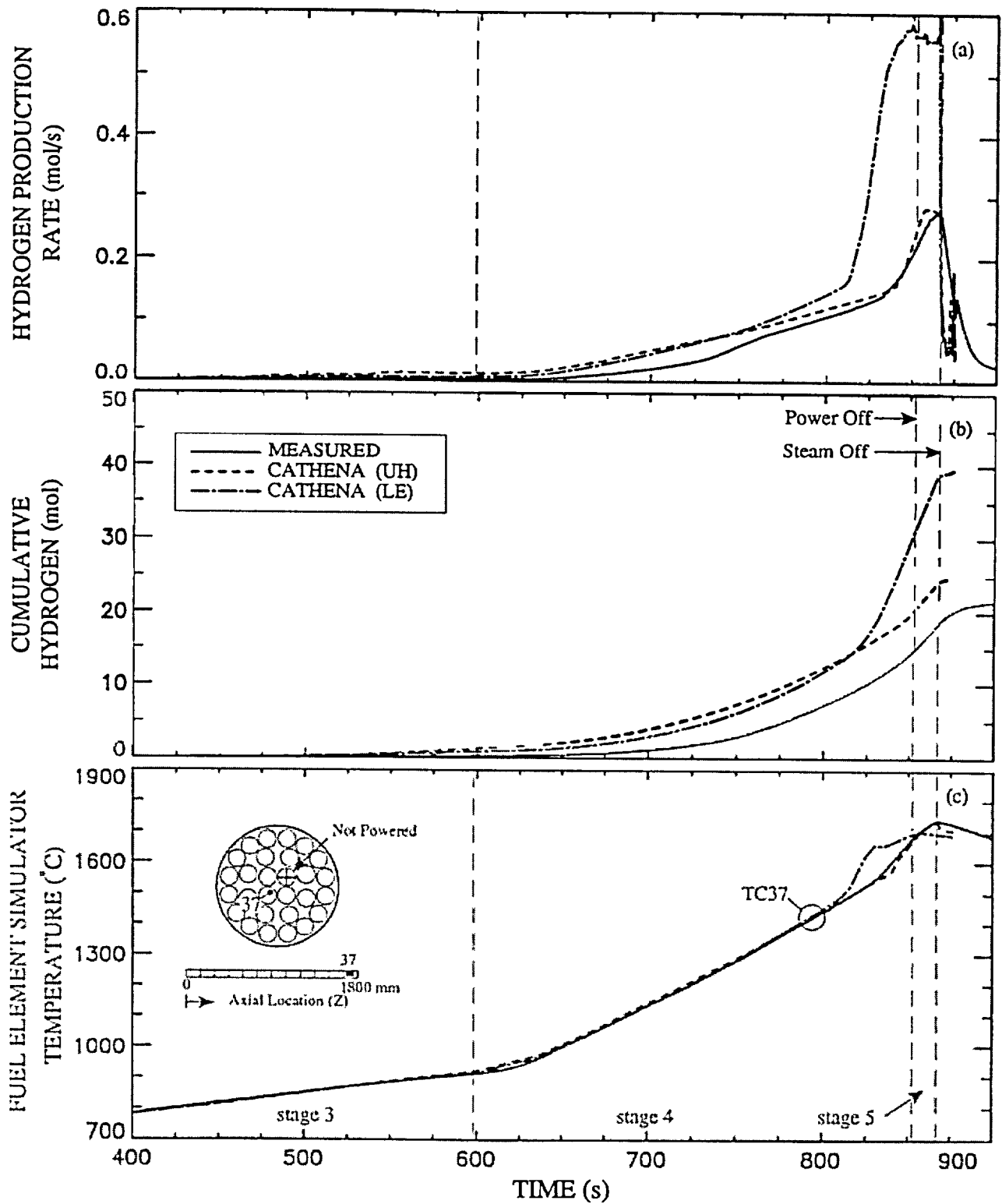


FIGURE 11: Comparison of CATHENA Simulations with Experimental Results of CS28-1 for (a) Hydrogen Production Rate, (b) Cumulative Hydrogen over the Entire Test Section, (c) Temperature Reference

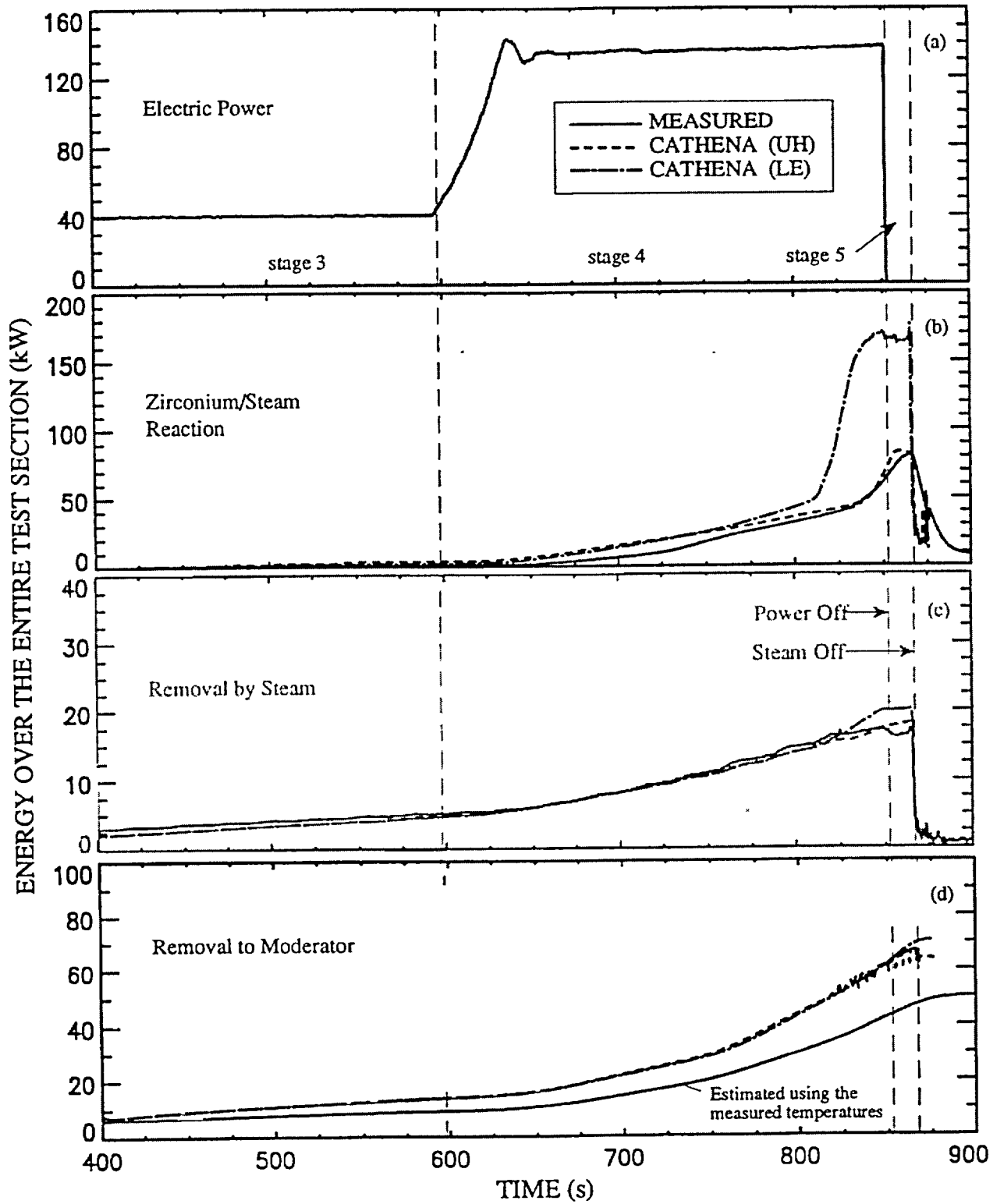


FIGURE 12: Comparison of CATHENA Simulations with Experimental Results of CS28-1 for Energy Components over the Entire Test Section

VALIDATION OF RADIATION HEAT TRANSFER IN CATHENA

Q.M. Lei and T.M. Goodman

Atomic Energy of Canada Limited
Whiteshell Laboratories
Safety Thermalhydraulics Branch
Pinawa, Manitoba
Canada R0E 1L0

ABSTRACT

The coolant inside a fuel channel may boil off during a postulated loss-of-coolant accident (LOCA) in a CANDU® (CANada Deuterium Uranium) reactor. If the loss of emergence core cooling (LOECC) is also postulated, superheated steam becomes the only coolant available to the fuel channel. Under such conditions thermal radiation is the dominant mode of heat transfer to reject the stored and decay heat in the fuel. Most fuel channel codes employ a diffuse-gray, nonparticipating medium radiation model to calculate thermal radiation exchanges among fuel channel surfaces. Validation of the thermal radiation calculation is important to qualify the code for assessing fuel channel behaviour under postulated LOCA conditions.

This paper reports a validation study to assess the ability of CATHENA MOD-3.5b/Rev 0 to model fuel bundle to pressure tube radiation heat transfer. Analytical or "exact" solutions to three numerical thermal radiation-only problems were used to validate radiation heat transfer in CATHENA. Exact pin-to-pin view factors were used to examine the accuracy of the view factor calculation by the CATHENA utility program MATRIX V1.03. Data from three fuel channel experiments were used to evaluate the performance of the CATHENA radiation heat transfer model. The results show that the MATRIX program provides accurate radiation view factors for CANDU bundle geometries. The results also show that CATHENA can accurately model fuel channel temperature behaviour under conditions where thermal radiation is the dominant mode of heat transfer. The work described in this paper was funded by the CANDU Owners Group (COG).

1. INTRODUCTION

Several postulated events in the licensing and safety assessments of CANDU reactors involve the degradation of the normal heat removal mechanisms from the fuel. During a postulated LOCA with LOECC, for instance, superheated steam becomes the only coolant available to the fuel channel. Heat is removed axially by steam flow and radially to the moderator by conduction and thermal

radiation. The dominant mode of heat transfer under such conditions is thermal radiation. In the absence of significant convective heat transfer, radiative heat transfer between the fuel elements and the pressure tube and between the pressure tube and the calandria tube can limit fuel temperature escalation, hydrogen generation and fission product release.

Most fuel channel codes model thermal radiation exchange among fuel channel surfaces. The basic assumptions in such modelling are that each radiant surface has uniform temperature, uniform radiative properties, and uniform radiosity (that accounts for all of the radiant energy leaving the surface). For enclosures, the medium that separates the surfaces, e.g., steam or steam-hydrogen mixture inside a pressure tube, is assumed to be nonparticipating; that is, it neither absorbs nor scatters the surface radiation, and it emits no radiation. Furthermore, these radiation heat transfer models employ a two-dimensional view (configuration or shape) factor matrix. This implies that the cross-sectional geometries specified for thermal radiation are assumed to be axially infinitely long. The reciprocity relation (determining one view factor from knowledge of the other) and the closure relation (all view factors in an enclosure summing to be one) are also used in the view factor matrix calculation.

Such radiation heat transfer models in fuel channel codes can provide adequate thermal radiation calculations for conditions when the model assumptions are valid. If the fuel channel code is to be used to analyse LOCA/LOECC scenarios, validation of the radiation heat transfer model using analytical and/or experimental data must be shown. Such validation will help reduce uncertainties, and thus increase confidence, in the code prediction when the code is used to predict fuel channel behaviour under these postulated accident conditions. This paper reports a validation study of the radiation heat transfer model in CATHENA MOD-3.5b/Rev 0 with a focus on demonstrating its ability to model fuel bundle to pressure tube radiation heat transfer.

2. THERMAL RADIATION MODEL IN CATHENA

CATHENA [1] is a multipurpose thermalhydraulic computer code developed primarily to analyse postulated LOCA scenarios for CANDU nuclear reactors. The code contains a generalized heat transfer package (GENHTP) that enables it to model the behaviour of a fuel channel in considerable detail. The radiation heat transfer model in GENHTP describes an enclosure of solid surfaces that have the following assumptions: the instantaneous temperature of each surface is uniform; the surface properties are uniform; emissivity, absorptivity, and reflectivity on each surface are independent of wavelength and direction; all energy is emitted and reflected diffusely; the incident and hence reflected energy flux is uniform over each individual surface; and the medium that separates the surfaces in the enclosure is assumed to be nonparticipating. Such a system is often referred to an enclosure of diffuse-gray surfaces. The radiation heat transfer for such an enclosure can be written in the matrix form [2]:

$$\bar{q}'' = \sigma \bar{E} [\bar{I} - \bar{F} (\bar{I} - \bar{E})]^{-1} [\bar{I} - \bar{F}] [\bar{T}^4] \quad 1)$$

where \bar{q}'' is the net radiant surface heat flux vector, σ is Stefan-Boltzmann constant (5.67×10^{-8} W/(m²·K⁴)), \bar{E} is the diagonal matrix containing the emissivities, ϵ , \bar{I} is an identity matrix, \bar{F} is the

view factor matrix, and \bar{T}^4 is the vector containing the fourth power of the temperature of the surfaces.

The view factor matrix, \bar{F} , is calculated using the CATHENA utility program MATRIX. The MATRIX program uses the Hottel's crossed-string method [2] to describe an enclosure of surfaces that are assumed to be cylindrical and infinitely long in the axial direction. The program can be used to calculate view factors for an axisymmetric geometry (e.g., a normal intact CANDU fuel bundle) as well as for a non-axisymmetric geometry (e.g., an off-normal slumped fuel bundle [3]). Currently, CATHENA MOD-3.5b/Rev 0 performs the inversion of the radiation matrices in equation 1 only at the beginning of a CATHENA run (including at restart). This means that the view factor matrix, \bar{F} , and the emissivity matrix, \bar{E} , are assumed to be constant during a transient.

CATHENA has been used to simulate various fuel channel experiments [4,5] where radiative heat transfer is significant. In these simulations, the CATHENA radiation heat transfer model has been used together with other CATHENA models to simulate experimental conditions. No effort has been made to assess thermal radiation calculations while isolating other modes of heat transfer. This paper is directed at showing adequate performance of the CATHENA radiation heat transfer model when it is isolated.

There have been no "radiation only" experiments conducted with CANDU fuel channel geometries. The experiments selected in this study involve high temperature radiation heat transfer in a simulated fuel channel. Effort has been thus placed on best estimating other modes of heat transfer (convection and conduction) that were present in each experiment so that the effects of thermal radiation could be isolated. Validation using analytical or "exact" solutions is also reported in this paper to demonstrate the ability of CATHENA to accurately model thermal radiation when it is the only mode of heat transfer. In addition, validation of the MATRIX-calculated view factors using analytical results is included.

3. VALIDATION USING ANALYTICAL SOLUTION

3.1 Two-Surface Enclosure Radiation

This validation case involves radiation heat exchange within an enclosure of two diffuse-gray surfaces, as shown in Figure 1. A long solid radiating pin with a radius of r_1 is surrounded by a long tube having an inside radius of r_2 . The geometry and property data are given in Figure 1. The hot pin has an initial temperature of T_1 and the outside surface of the tube is kept at a constant temperature T_2 . Both the pin and the tube are assumed to have a high thermal conductivity (k) so that temperature gradients across the walls are negligible. Emissivities of the pin outer surface and the tube inner surface are assumed to be constant at ϵ_1 and ϵ_2 , respectively. Heat transfer from the pin (surface 1) to the tube inner surface (surface 2) is assumed to be by thermal radiation only.

The transient pin temperature T_1 and net pin-to-tube radiative heat flux q''_{12} can be determined analytically. Figure 1 shows the CATHENA-calculated results (see the "+" symbol) for T_1 and q''_{12} and the analytical solutions (solid lines). An excellent agreement is seen. This indicates that

CATHENA accurately calculates the pin-to-tube radiation heat transfer for this enclosure of two diffuse-gray surfaces.

3.2 Three-Surface Enclosure Radiation

This problem describes radiation heat transfer within a three-surface enclosure. Figure 2a shows the geometry to be considered and the network representation of the enclosure for thermal radiation exchange. Two long identical radiating pins (to represent fuel elements), each with a radius of r (0.00654 m), contact each other at the bottom of a large long tube (to represent a pressure tube) with an inside radius of R (0.051905 m). Line contact occurs at points a, b, and c, forming a three-surface enclosure. The large tube (surface 3) is assumed to be characterized by zero net radiation transfer. The temperatures of the outside surfaces (surfaces 1 and 2) of the two pins remain constant at $T_1 = 1473$ K and $T_2 = 573$ K, respectively. These three surfaces are assumed to be opaque, diffuse, gray and surrounded by a nonparticipating medium. Emissivities of these three surfaces are assumed to be constant at $\varepsilon_1 = 0.8$, $\varepsilon_2 = 0.4$, and $\varepsilon_3 = 0.8$. Temperature gradients across the walls and the pin-to-pin contact heat transfer are assumed to be negligible. The problem is to determine the temperature of the large tube (T_3) and the net radiation heat exchange of surface 1 per unit axial length (q_1) under steady-state conditions.

The view factor results for these three surfaces can be determined analytically, i.e., $F_{12} = 0.332736$ where F_{12} is the surface 1 to surface 2 view factor. This exact result was used to validate the MATRIX view factor calculation. Figure 2b shows the percent error of the MATRIX-calculated F_{12} , as a function of the number of internal circumferential segments, N , used on arc length ab or ac. Arc length bc was divided into twice as many circumferential segments as arc length ab or ac. For $N = 1$, the MATRIX-calculated F_{12} was 0.214844, which is in error by 35%. When N was increased to 20, the view factor error was reduced to 1%. Further increasing N results in a negligible difference between the MATRIX result and the exact value. This indicates that MATRIX is able to accurately calculate the view factors for a CANDU fuel pin geometry, provided that each surface is divided into a sufficient number of circumferential segments. From this study, the entire circumference of a fuel pin should be divided into at least 80 circumferential segments and the entire circumference of the pressure tube should be divided into at least 800 circumferential segments in order to obtain a bundle to pressure tube view factor matrix that has an error of less than 1%.

The analytical solution to the network representation of the three-surface radiation enclosure (Figure 2a) can be readily obtained: $q_1 = 900.51$ W/m and $T_3 = 1347.15$ K. These exact results were used to validate the CATHENA radiation heat transfer calculation. Figure 2c shows the transient results by CATHENA. Both the predicted q_1 and T_3 results reached steady-state values within 5 s from the start of the simulation. The CATHENA-predicted steady-state result for q_1 was 900.92 W/m, which agrees with the exact value within 0.05%. The CATHENA-predicted steady-state result for T_3 was 1347.0 K, which agrees with the exact value within 0.01%. The comparison indicates that CATHENA is able to accurately calculate radiation heat transfer within the enclosure of the three diffuse-gray surfaces, one of which is reradiating (insulated).

3.3 Blackbody Radiation Exchange

This problem describes radiation heat transfer within a 37-element bundle and pressure-tube enclosure in which blackbody surfaces are assumed. Such a problem is a special case of the diffuse-gray radiation assumption. When emissivities of all surfaces are set to be 1 in the CATHENA radiation heat transfer model, the code is able to simulate the blackbody radiation exchange. Comparing the CATHENA calculation with the analytical solution to this special case can serve as a "full-scale" (multi-surfaces) validation of the CATHENA radiation heat transfer calculation.

A CANDU 37-element bundle geometry (Figure 3) is considered in this problem. Elements on the same ring are assumed to have the same temperature. Therefore, the 37-element bundle and the pressure tube are grouped as a five-surface enclosure, namely, the surfaces of the centre element, the inner-, middle- and outer-ring elements, and the inside surface of the pressure tube. Each of the surfaces is assumed to be isothermal and function as a blackbody (perfect absorber and emitter). Each surface is kept at either a constant temperature (T) or a constant heat flux (q") under steady-state conditions. The problem is to determine the temperature of the surface when it is imposed to a constant heat flux or determine the heat flux on the surface when a constant temperature is imposed.

The analytical or exact view factor from the centre element to one element on the inner ring can be calculated using the Hottel's crossed-string method [2]. The calculated exact view factor from the centre element to all six inner-ring elements (F_{12}) is 0.9136494. MATRIX was used to calculate the 5-by-5 view factor matrix for this problem. Each fuel element was internally divided into N circumferential segments, where N was varied from 10 to 200 to assess its impact on the view factor results. The entire circumference of the pressure tube was internally divided into 10N circumferential segments. For N = 10, the MATRIX-calculated F_{12} was 0.916811, which is 0.346% greater than the exact value. When N was increased to 80, the MATRIX-calculated F_{12} was 0.913801, which agrees with the exact value within 0.017%. Figure 3 shows the percentage variations of the MATRIX-calculated view factors with the input values of N. The calculated view factors for N = 200 were used as a reference for each view factor variation curve. As seen from the plot, the variations reduced to below 0.2% as the number of circumferential segments used on each fuel element (N) was increased to 80. Further increasing N marginally increased accuracy in the view factor results, but increased computing time significantly. The MATRIX-calculated 5-by-5 view factor matrix for N=100 is given in Table 1.

The net radiation heat flux, q_i'' (W/m²), on surface i within an enclosure of M black surfaces can be expressed as [2]:

$$q_i'' = \sum_{j=1}^M F_{ij} \sigma (T_i^4 - T_j^4) \quad (2)$$

where T_i is the temperature of surface i (K), and T_j is the temperature of surface j (K). In this problem, M=5. If a constant temperature is prescribed on each surface (Case 1), the surface heat flux (q_1'' to q_5'') can be calculated directly using equation 2. If a mixed set of temperature and heat flux conditions are imposed within the enclosure (Case 2), the heat flux or the temperature required to be determined can be calculated by solving a set of equations resulting from equation 2.

Comparisons of the CATHENA steady-state results with the analytical results are given in Table 1. An excellent agreement was found. The maximum difference between the CATHENA-calculated results and the analytical results was 0.12%. The comparison indicated an accurate calculation of the fuel bundle to pressure tube radiation heat transfer by CATHENA when all surface emissivities were set to 1. Since this blackbody radiation problem is a special case of the diffuse-gray problems, the comparison results indicate that the radiation heat transfer model had been implemented correctly in CATHENA.

4. VALIDATION USING EXPERIMENTAL DATA

4.1 Fuel Channel Ballooning Test

This experiment was performed at AECL Whiteshell laboratories to study the heat transfer characteristics of a fuel channel where the pressure tube was heated up by a graphite-rod heater and ballooned into contact with a calandria tube submerged in a pool of water. The test apparatus, shown in Figure 4, consisted of a 1750-mm long section of Zr-2.5 Nb pressure tube placed concentrically inside a 1700-mm long Zr-2 calandria tube. The electric heater was a 950-mm long, 38-mm diameter graphite rod concentrically located inside the test section assembly. The pressure tube was pressurized with helium to 1.0 MPa (gauge). The annulus between the pressure tube and the calandria tube was purged with a 0.55 g/s flow of CO₂. Test section temperatures were monitored at four axial locations using K-type thermocouples (TCs). Figure 4 shows the thermocouples at one axial location (Ring 2). The junction end of each pressure tube thermocouple was placed into a small diameter blind hole drilled part way through the pressure-tube inner wall. The accuracy of the pressure tube temperature measurement was estimated to be less than $\pm 4^\circ\text{C}$ for temperatures above 300°C. The junction end of each calandria tube thermocouple was spot-welded directly onto the calandria tube outer surface. The estimated accuracy of the calandria-tube temperature measurement was $\pm 2.4^\circ\text{C}$.

CATHENA MOD-3.5b/Rev 0 was used to model the thermal behaviour of the test section at axial location Ring 2. A unit axial length of the test section was modelled to represent this axial location. Only radial conduction was modelled in this analysis. An average measured calandria-tube temperature (TCs 21 to 26 in Figure 4) was used as a prescribed boundary condition. Therefore, pool boiling on the outside surface of the calandria tube need not be considered in this analysis. The graphite-rod heater was modelled using 10 radial nodes. The experimental power transient was applied directly to the heater. The pressure tube and the calandria tube were modelled each using 5 radial nodes. Thermal radiation between the heater and the pressure tube and between the pressure tube and the calandria tube was modelled. Emissivities of the graphite rod, the pressure-tube inner and outer surfaces, the calandria-tube inner surface were assumed to be constant at 0.9, 0.8, 0.8, and 0.3. A thermalhydraulic branch was used inside the pressure tube to include molecular conductive heat transfer through the stationary helium fluid. Convective heat transfer in the CO₂ gas annulus between the pressure tube and the calandria tube was also modelled using a thermalhydraulic branch. Deformation of the pressure tube was not modelled.

Buoyancy-induced free convection currents developed in the pressure tube in this experiment due to the significant temperature difference between the heater and the pressure tube. Figure 5a shows

that the measured (solid lines) temperatures at the top of the pressure tube are significantly greater than the temperature at the bottom, which is a result of the influence of free convection. Such free convection heat transfer can be estimated using the correlation of Raithby and Hollands [6] through a CATHENA system control model. Thus, the total heat flow due to free convection could be calculated, but the top-to-bottom temperature difference could not be modelled because the heat flow distribution in the circumferential direction was not known.

The goal of this simulation was to confirm that CATHENA was able to correctly calculate the circumferentially averaged (uniform) temperature of the pressure tube under the experimental conditions where the dominant mode of heat transfer from the heater to the pressure tube was thermal radiation. Two CATHENA runs were performed. The estimated mean free convection heat flux was included in one run and not included in the other run. Figure 5a shows that the pressure tube temperatures calculated from both the runs fall between the measured pressure-tube top temperature and the measured temperature at the bottom. This indicates a correct uniform temperature calculation by CATHENA. Figure 5b shows the CATHENA-calculated radiative and conductive/convective heat fluxes into the pressure tube. The radiative heat flux at temperatures above 400°C was at least 10 times higher than the conductive/convective heat flux, indicating the dominant radiation heat transfer from the heater to the pressure tube in this experiment. Therefore, the agreement between the measured and calculated pressure tube temperatures indicates an adequate thermal radiation calculation by CATHENA under these experimental conditions.

4.2 Bearing-Pad/Pressure-Tube Rupture Test

Experimental data from the Bearing-Pad/Pressure-Tube Rupture Test 6 [7] were used to assess the CATHENA calculation of bundle to pressure-tube radiation heat transfer. This experiment was performed to measure the influence of hot bearing pads on the temperature transients of ballooning pressure tubes under postulated LOCA/LOECC conditions. The test apparatus, shown in Figure 6a, consisted of a 1.2-m long section of Zr-2.5 Nb pressure tube mounted inside a 1.1-m long Zr-2 calandria tube. The annulus between the pressure tube and the calandria tube was purged with CO₂ prior to the start of the test and remained at atmospheric pressure throughout the test. The calandria tube was surrounded by heated, non-flowing water in an open tank. The pressure tube was pressurized to 6 MPa with a 75%-argon and 25%-oxygen gas mixture. The pressure tube contained a fuel element simulator (FES) bundle where 16 FESs were arranged to represent the outer ring of fuel elements in a typical 28-element CANDU fuel channel. Central tungsten weight cans were placed inside the ring of FESs so that the mass per unit length of the FES bundle was similar to 28-element CANDU bundles.

The experimental data from a cross section of the FES bundle at an axial location without bearing pad rings were used in this analysis. The maximum electric power to each FES per unit axial length was 7.7 kW/m (Figure 6b). Thermocouple 12 indicated the cladding temperature of the bottom FES increased sharply as the electric power was increased (Figure 6c). The pressure tube was heated up by the hot FESs mainly via thermal radiation. The pressure-tube temperatures continued to increase until the test was terminated at 192 s. The estimated accuracy of the temperature measurement was within ±10°C above 400°C.

A 1/16 sector of the FES bundle (Figure 7) was modelled using CATHENA to simulate the radial and circumferential temperature behaviour of the bundle at the bottom. Heat transfer in the axial direction was neglected. The measured pressure tube temperatures (by TCs 43, 44, and 45) were imposed to the outside surface of the pressure tube. Hence, the calandria tube was not modelled and uncertainties in modelling pressure tube to calandria tube heat transfer were absent in this analysis. Thermal radiation within the FES bundle was modelled with the view factors calculated by MATRIX. The emissivity of the tungsten weight can surface was best estimated to be constant at 0.3. Varying this emissivity from 0.3 to 0.5 was found to result in a small temperature variation (less than 10 °C) in the calculated FES temperature (TC 12) for the temperature below 1100 °C. The emissivity of the inner surface of the autoclaved pressure tube was assumed to be constant at 0.8. The emissivity of the unoxidized Zr-4 FES cladding was assumed to be 0.3 [8]. In this experiment, the cladding emissivity possibly varied from 0.3 to 0.5 in the Ar/O₂ mixture environment when the cladding temperature elevated from 30 °C to 1100 °C.

The stagnant Ar/O₂ mixture was modelled to account for gas conduction within the FES bundle. The effect of buoyancy-induced free convection on the temperature behaviour of the FES bundle at the bottom region would be reflected in the measured pressure tube temperatures that were used as a prescribed boundary condition in the CATHENA input model. Therefore, the free convection effect was not included in this analysis. Deformation of the pressure tube was not modelled since only the local temperature behaviour was of interest in this analysis. The feedback effect due to pressure tube ballooning in the experiment on the temperature calculation was neglected.

Three CATHENA runs, each with a different FES cladding emissivity, were performed to cover the emissivity uncertainty in this analysis. Figure 7a shows the CATHENA-calculated cladding temperatures at the TC 12 position all agreed excellently with the measured temperature up to 850 °C. Above this temperature, the calculated temperatures using the emissivity values of 0.4 and 0.5 agreed with the measured temperature better than that with 0.3. This indicated that the FES cladding could be slightly oxidized during the high temperature transient in the experiment. The CATHENA-calculated radiative heat flux from the FES was significantly higher than the convective heat flux after 100 s (Figure 7b). The ratio of the radiative heat flux to the convective heat flux increased from 2.0 at 100 s to 8.5 at 192 s. This implied the dominant mode of heat transfer within the FES bundle was thermal radiation during this period of time. The accurate temperature calculation by CATHENA indicated that the code accurately simulated the FES bundle to pressure tube radiation heat transfer under these experimental conditions.

4.3 28-Element CHAN Thermal-Chemical Test CS28-3

Experimental results from the 28-element CHAN thermal-chemical experiment CS28-3 [9] were used to further assess the CATHENA radiation heat transfer calculation. Only the low-temperature transient data (i.e., bundle temperatures below 750 °C) from this test were used in this analysis. During this low-temperature transient, the heat generated from the zirconium-steam reaction in the test section was negligible. Thus, the only heat source in the test section was the electric power. This helped isolate thermal radiation effects that are to be examined. In addition, the measured temperatures on the outside surface of the pressure tube were used as boundary conditions. Uncertainties in modelling the thermal responses of the components outside the pressure tube were therefore absent in this analysis. The goal of this analysis was to compare the simulated FES

temperatures with the measured temperatures to examine the performance of the CATHENA radiation heat transfer model for a 28-element bundle geometry under flowing steam conditions.

This third 28-element CHAN experiment was reported in detail elsewhere [9]. Briefly, the test apparatus shown in Figure 8a allowed superheated steam from a boiler and a superheater to enter a horizontal test section. The test section consisted of a 28-element FES bundle (Figure 8b) surrounded by a 2330-mm long section of autoclaved Zr-2.5 Nb pressure tube mounted inside a 2030-mm long Zr-2 calandria tube. The calandria tube was surrounded by an insulated cooling water jacket that was used to determine the amount of heat removed from the test section through the calandria tube wall.

Each FES consisted of a 6-mm diameter graphite rod heater (1800 mm in length) inside annular alumina pellets (14.28-mm outer diameter, 6.14-mm inner diameter and 16 mm in length) in a Zr-4 fuel-cladding tube. Test section temperatures were monitored using thermocouples at various radial and axial locations (Figure 8c). Temperatures near the inside surface of the FES cladding were measured using the C-type thermocouples. The maximum error in the FES temperature was estimated to be $\pm 12^\circ\text{C}$ for the temperature ranging from 500 to 750°C. Standard R-type or K-type thermocouples monitored pressure-tube and steam temperatures. The maximum thermocouple error in these temperatures was estimated to be $\pm 9^\circ\text{C}$ for temperatures below 800°C.

Superheated steam at about 700°C and 9 ± 0.2 g/s was supplied to the test section inlet throughout the test. Electric power to the test section was controlled in three stages: stage 1 with 10 kW power, stage 2 with 130 kW power, and stage 3 with zero power to the FES bundle. In this analysis, data from stage 1 were used. Figure 9 shows the electric power to each ring of FESs during stage 1 and the steam temperatures recorded by three thermocouples near the inlet of the test section.

Using lateral symmetry, only half the FES bundle with the pressure tube was modelled (Figure 10a). Each FES was divided into an inner sector and an outer sector. Half of the pressure tube was circumferentially divided into 5 sectors. A total of 33 circumferential sectors were generated for the FES bundle and the pressure tube. Conduction in the radial and circumferential directions was modelled and the thermal responses in the axial direction was accounted for by the steam flow only. Each FES was modelled in detail using 17 radial nodes and the pressure tube wall was modelled using 10 radial nodes. The test section was axially divided into 16 segments with 14 segments for the 1800-mm heated zone. The total flow area of the FES bundle was divided into four flow areas. Steam flow distribution in the bundle was determined by CATHENA based on geometric and thermalhydraulic conditions. Flow mixing was allowed at the inlet and outlet of the test section and at the five spacer plate locations.

Electric power (Figure 9a) was applied directly to each FES ring. The experimental data at time = 0 s were used as initial conditions. The temperatures measured on the outside surface of the pressure tube (Figure 10b,c) were used as prescribed boundary conditions in this CATHENA input model. This was done to isolate the effects of thermal radiation within the FES bundle by removing uncertainties in modelling the thermal responses of the components outside the pressure tube. The measured steam flow rate was applied to the inlet of the test section. The inlet steam temperature that was used in the CATHENA input model was obtained by arithmetically averaging the steam temperatures, as shown in Figure 9b, measured at three different positions near the test section inlet.

This averaged inlet steam temperature was assumed to best represent the thermal response of the components (the piping and the end fittings) at the test section inlet in the experiment.

The emissivity of the inner surface of the autoclaved pressure tube was assumed to be constant at 0.8. For a fresh (unoxidized) Zr-4 cladding, its emissivity value was assumed to be 0.3 [8]. Under the experimental conditions examined, the FES cladding emissivity could vary from 0.3 to 0.5. The bundle to pressure tube radiation heat transfer was modelled using constant emissivity values for the pressure tube inner surface and the FES cladding. The zirconium-steam reaction was not modelled during this low-temperature transient.

Two CATHENA runs were performed, one using the cladding emissivity of 0.3 and the other using 0.5, to bound the CATHENA results due to the uncertainty in the cladding emissivity. The CATHENA results with the cladding emissivity of 0.3 were studied first to determine if thermal radiation was the significant mode of heat transfer in the FES bundle under these low-power and low-flow steam conditions. Figure 11a shows the measured total electric power to the FES bundle and the measured heat addition or removal rate by steam flow along the entire test section. The negative heat removal rate prior to 300 s means that the steam added energy to the test section and the positive heat removal rate after 300 s means that the steam removed energy from the test section. The heat removal rate reached 1.0 kW, about 10% of the total electric power input, towards the end of stage 1. Comparisons are also shown in Figure 11 between the radiative and convective heat fluxes that were estimated by CATHENA at the outer-ring FES sector facing the pressure tube. The ratio of the local radiative heat flux to the local convective heat flux ranged from 2 to 4. This indicated that the radiation heat transfer from the outer-ring FES to the pressure tube was dominant in this experiment.

Comparisons of the simulated FES temperatures with the measured temperatures are made in Figures 12 to 14 at three axial locations. These temperatures were inside FESs, 1 mm away from the inner surface of the FES cladding. The simulated temperatures with the cladding emissivities of both 0.3 and 0.5 are compared with the measured temperatures. All simulated FES temperatures agreed with measured results within the experimental uncertainties. Overall, the temperatures simulated using the cladding emissivity of 0.5 agreed better with measured than those simulated with the cladding emissivity of 0.3. This expected outcome indicated that the FES bundle might be slightly oxidized during the warming-up and low-power stages of the experiment.

The experimental uncertainties that could affect the CATHENA simulation results were uncertainties in the measurements of inlet steam temperatures, inlet steam flow rate, pressure-tube and FES temperatures. The temperature obtained by averaging three inlet steam temperatures was considered to be an appropriate input to CATHENA because heat losses and steam flow patterns near the inlet in this experiment were difficult to model. Uncertainties in using the inlet steam temperature were estimated to have a small influence on the CATHENA results except for the results near the test section inlet. The experimental uncertainty in steam flow rate was $\pm 2\%$ of the flow reading. This uncertainty would have a minor impact on the CATHENA calculation of convective heat transfer coefficients and thus have a small effect on the FES temperature calculation. The experimental uncertainty of $\pm 9^\circ\text{C}$ in pressure tube temperatures was estimated to result in a variation of less than $\pm 9^\circ\text{C}$ in the calculated temperatures of outer-ring FESs. Such a variation in the calculated temperatures of inner- and middle-ring FESs could be even smaller.

Based on the above considerations, the CATHENA-calculated FES temperatures were all in agreement with the measured temperatures except for those near the test section inlet. This agreement implied that thermal radiation between the 28-element bundle and the pressure tube was adequately modelled using the CATHENA radiation heat transfer model.

5. CONCLUSIONS

The thermal radiation model in CATHENA MOD-3.5b/Rev 0 was assessed using analytical solutions to three different thermal radiation problems and data from three different fuel channel experiments in which thermal radiation was the dominant mode of heat transfer. As well, the CATHENA utility program MATRIX V1.03, that is used to calculate the view factor matrix used in the thermal radiation model, was assessed using analytical solutions to two different problems. The results show that the utility program MATRIX can provide accurately-calculated view factor matrices for CANDU fuel channels. The results also show that the CATHENA thermal radiation model is able to accurately simulate radiation heat transfer in a CANDU fuel channel.

REFERENCES

1. D.J. Richards, B.N. Hanna, N. Hobson and K.H. Ardron, "CATHENA: A Two-Fluid Code for CANDU LOCA Analysis, (renamed from ATHENA)," Presented at the 3rd International Topical Meeting on Reactor Thermalhydraulics, Newport, RI, 1985.
2. R. Siegel and J.R. Howell, "Thermal Radiation Heat Transfer," Third Edition, Hemisphere Publishing Co., Washington, 1992.
3. Q.M. Lei, D.B. Sanderson and R. Dutton, "Modelling Disassembled Fuel Bundles using CATHENA MOD-3.5a under LOCA/LOECC Conditions," Presented at the CNA/CNS Annual Conference, Saskatoon, SK, June 4-7, 1995.
4. Q.M. Lei, D.B. Sanderson and H.E. Rosinger, "High-Temperature Validation of CATHENA against a 28-Element Thermal-Chemical Experiment," Presented at the 15th Annual CNS Conference, Montreal, PQ, 1994.
5. T. Nitheanandan, Q.M. Lei and R.G. Moyer, "The Analysis of Bearing-Pad to Pressure-Tube Contact Heat Transfer Experiments," Proceedings of the 17th Annual CNS Conference, Fredericton, NB, June 1996.
6. F.P. Incropera and D.P. DeWitt, "Fundamentals of Heat and Mass Transfer," 3rd Edition, John Wiley & Sons, New York, 1990.
7. R.G. Moyer, D.B. Sanderson, R.W. Tiede and H.E. Rosinger, "Bearing-Pad/Pressure-Tube Rupture Experiments," Presented at the 13th Annual CNS Conference, Saint John, NB, June 1992.

8. P.M. Mathew, M. Krause, M. Dean and M.H. Schankula, "Emittance of Zircaloy-4 Sheath at High Temperatures in Argon and Steam Atmospheres," Proceedings of the 10th Annual CNS Conference, Ottawa, ON, Vol.2, 1989.
9. P.J. Mills, D.B. Sanderson, K.A. Haugen and G.G. Haacke, "Twenty-Eight-Element Fuel-Channel Thermal-Chemical Experiments," Proceedings of the 17th Annual CNS Conference, Fredericton, NB, June, 1996.

TABLE 1

CATHENA CALCULATION VERSUS ANALYTICAL SOLUTION FOR BLACKBODY RADIATION EXCHANGE

(see Figure 3 for the five-surface enclosure)

MATRIX-CALCULATED VIEW FACTORS (N=100)

i	F_{ij}				
	j=1	j=2	j=3	j=4	j=5
1	0.000000	0.912994	0.071499	0.006807	0.008700
2	0.152137	0.333350	0.487999	0.024861	0.001653
3	0.005958	0.244046	0.318836	0.408186	0.022973
4	0.000378	0.008286	0.272044	0.314009	0.405283
5	0.001096	0.001250	0.034718	0.919005	0.043932

Exact $F_{12} = 0.9136494$

CASE 1: $T_1 = 1200$ K $T_2 = 1300$ K
 $T_3 = 1400$ K $T_4 = 1500$ K
 $T_5 = 900$ K

RADIATION HEAT FLUX		ANALYTICAL	CATHENA	ERROR (%)
q_1^*	(kW/m ²)	-48.1293	-48.1319	-0.0054
q_2^*	(kW/m ²)	-23.4223	-23.4272	-0.0209
q_3^*	(kW/m ²)	-9.8733	-9.8660	0.0739
q_4^*	(kW/m ²)	121.1900	121.2144	-0.0201
q_5^*	(kW/m ²)	-236.1216	-236.2203	-0.0418

CASE 2: $q_1^* = -10$ kW/m²
 $T_2 = 1300$ K
 $T_3 = 1400$ K
 $T_4 = 1500$ K
 $q_5^* = -250$ kW/m²

RADIATION RESULTS		ANALYTICAL	CATHENA	ERROR (%)
T_1	(K)	1287 0346	1287.05	-0.0012
q_2^*	(kW/m ²)	-29.1801	-29.1887	-0.0295
q_3^*	(kW/m ²)	-9.7673	-9.7624	0.0502
q_4^*	(kW/m ²)	127 0411	127.0223	0.0148
T_5	(K)	795 6939	796.65	-0.1202

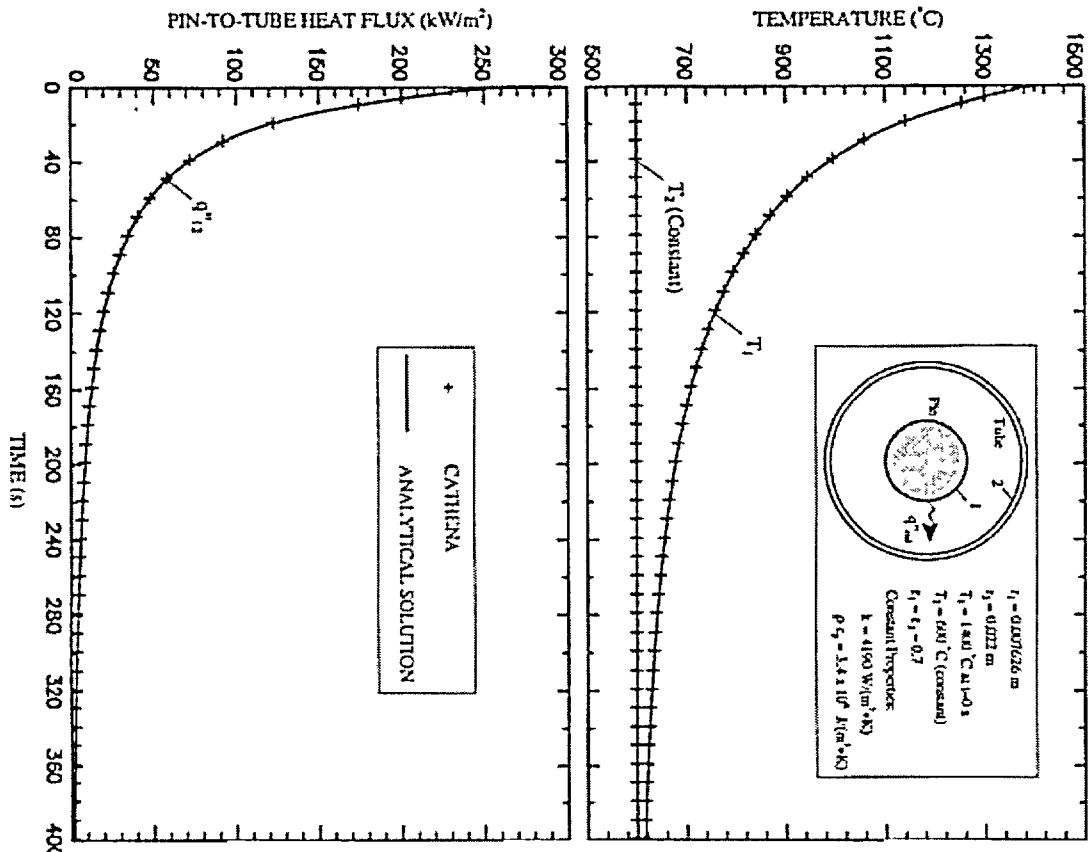


FIGURE 1: Comparison of CATHENA Results with Analytical Solution of Two-Surface Enclosure Radiation

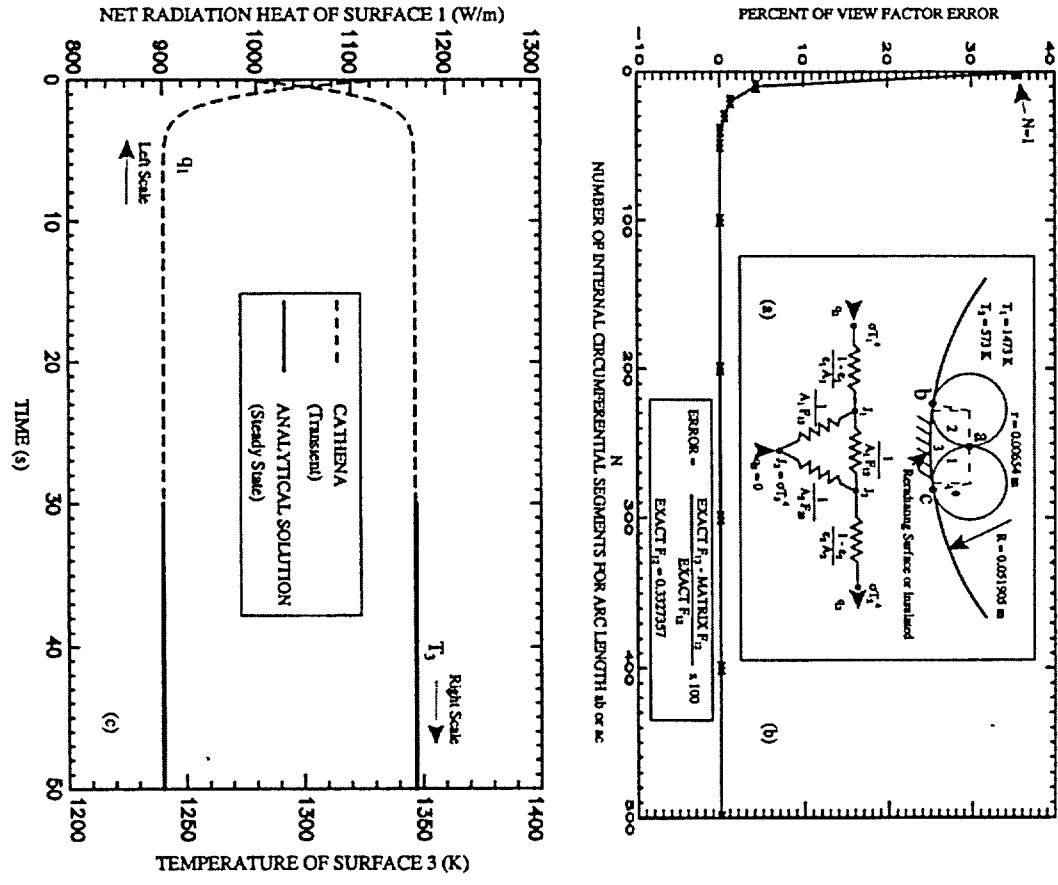


FIGURE 2: Three-Surface Enclosure with One Surface Reradiating and Network Representation (a), Error of the Matrix-Calculated View Factor F_{12} as a Function of the Number of Internal Circumferential Segments (b), and Comparison of CATHENA Results with Analytical Solution (c)

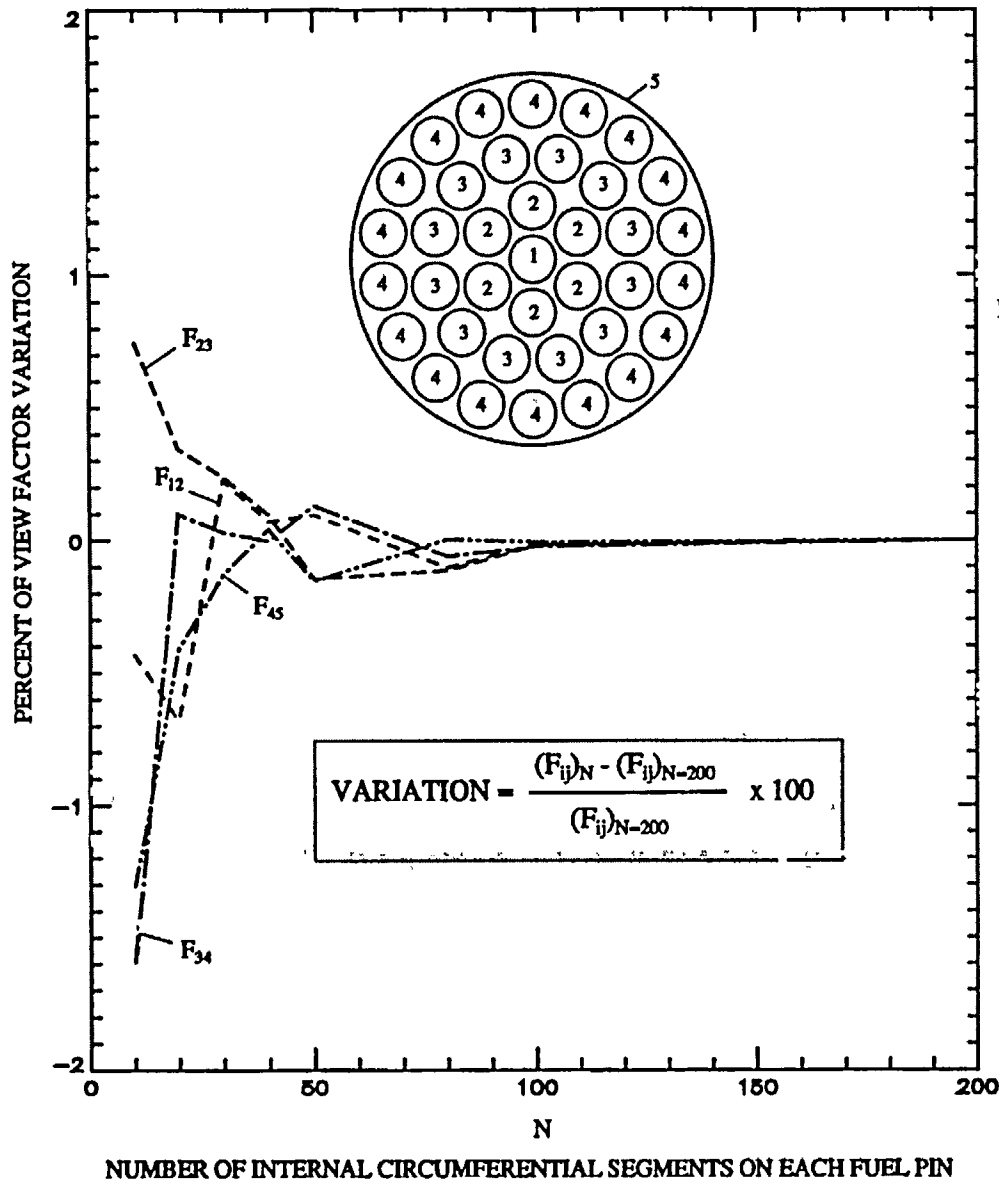
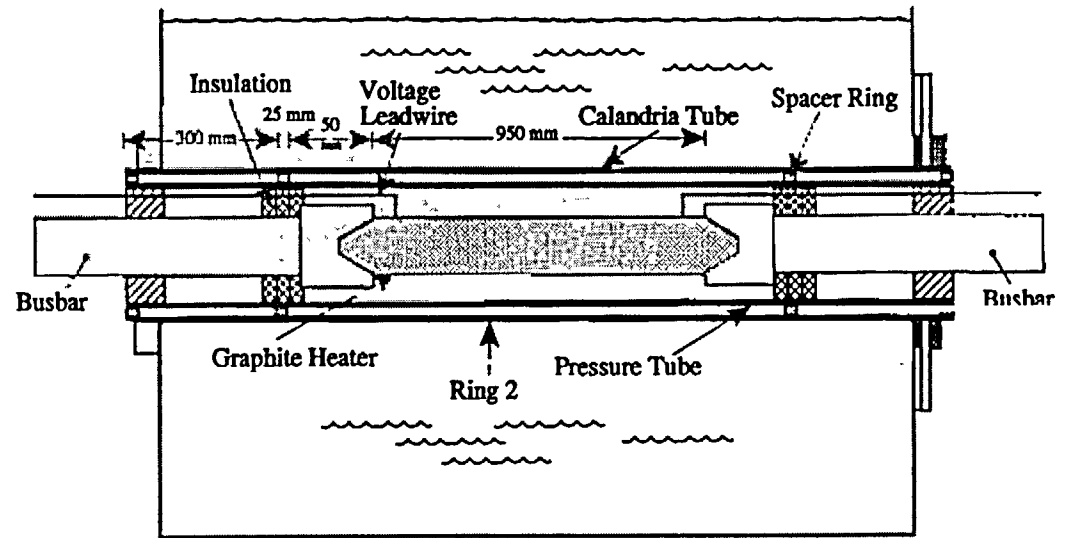


FIGURE 3: Variations of the MATRIX-Calculated View Factors with the Number of Internal Circumferential Segments, N, Used on Each Fuel Pin (the Number of the Segments on the Pressure Tube = 10 N)



THERMOCOUPLES AT THE AXIAL LOCATION OF RING 2

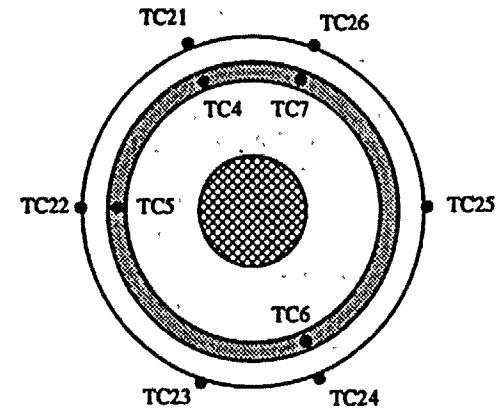


FIGURE 4: Test Apparatus Used in Roll-Extruded Calandria Tube Test 1, Also Showing the Thermocouple Locations at Ring 2

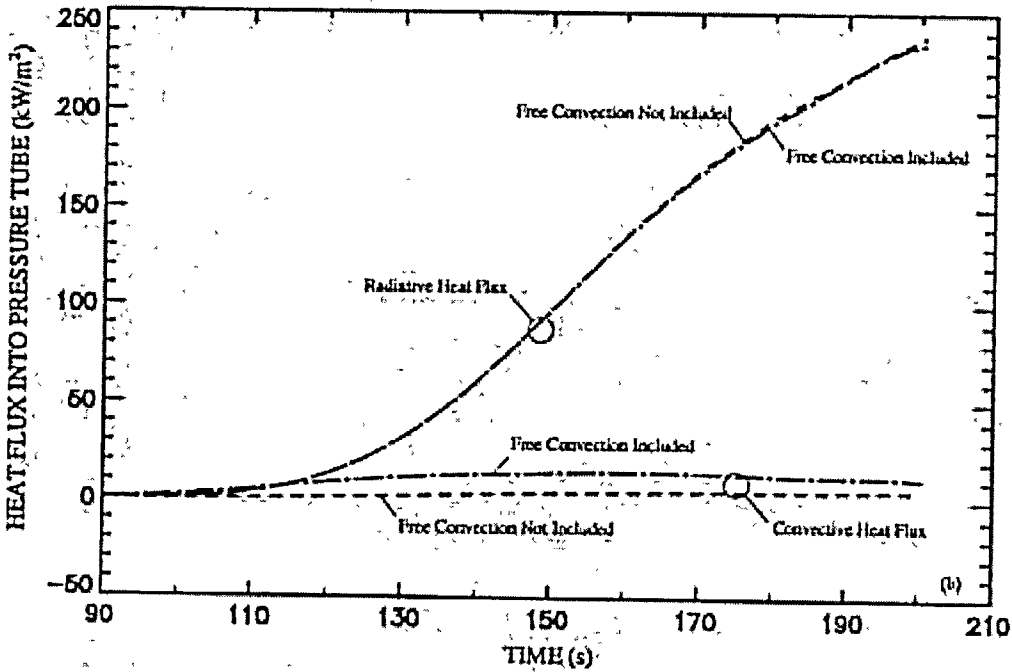
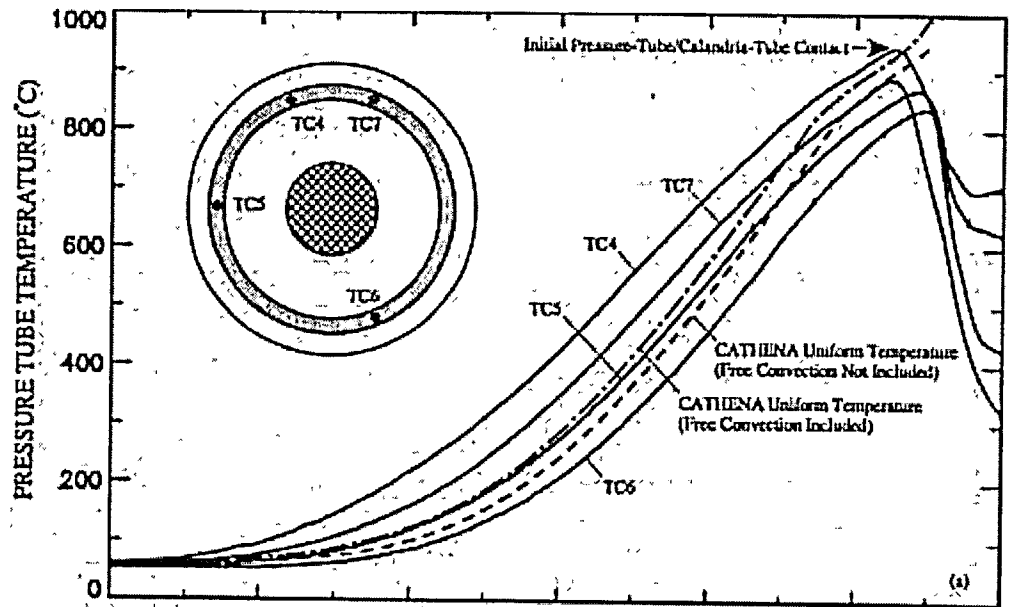


FIGURE 5: Comparison of CATHENA-Calculated Uniform Pressure Tube Temperature with the Measured Temperatures (a) from Roll-Extruded Calandria Tube Test 1, Also Showing the CATHENA-Calculated Heat Flux Components (b) to Indicate Dominant Thermal Radiation from the Heater to the Pressure Tube

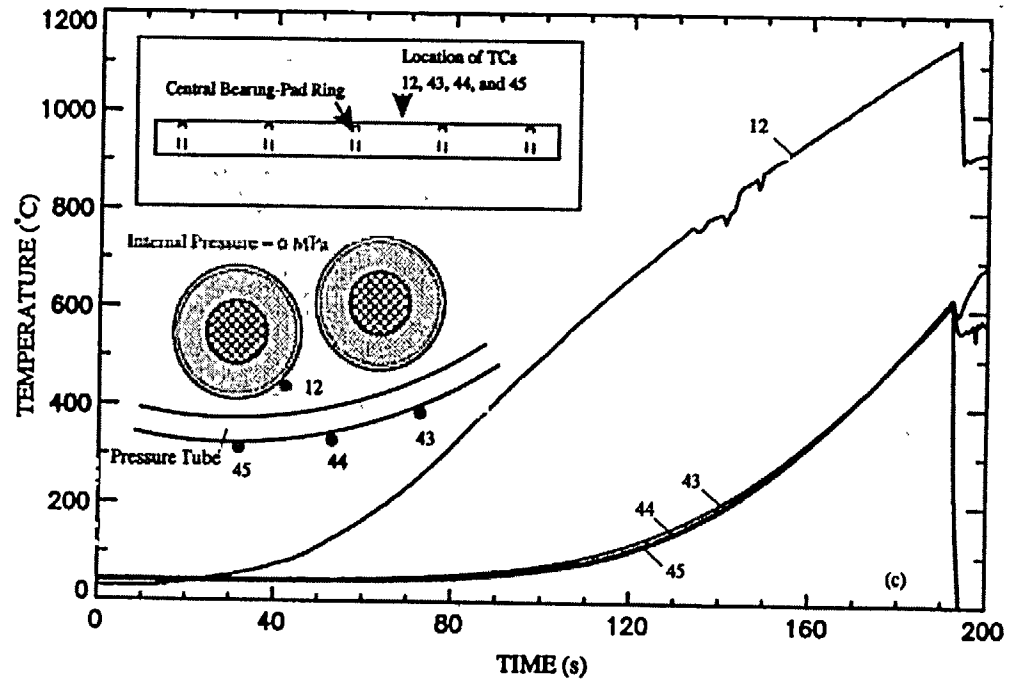
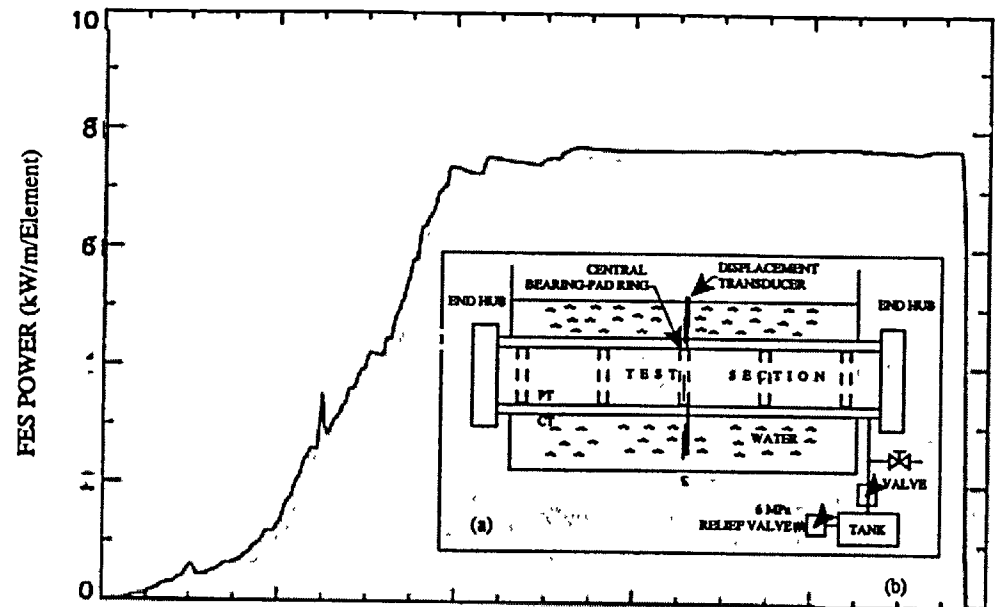


FIGURE 6: Bearing-Pad/Pressure-Tube Rupture Test 6: Test Apparatus (a), Test Section Power (b) and Measured Temperatures (c) at the Bottom of the Test Section Between Bearing-Pad Rings

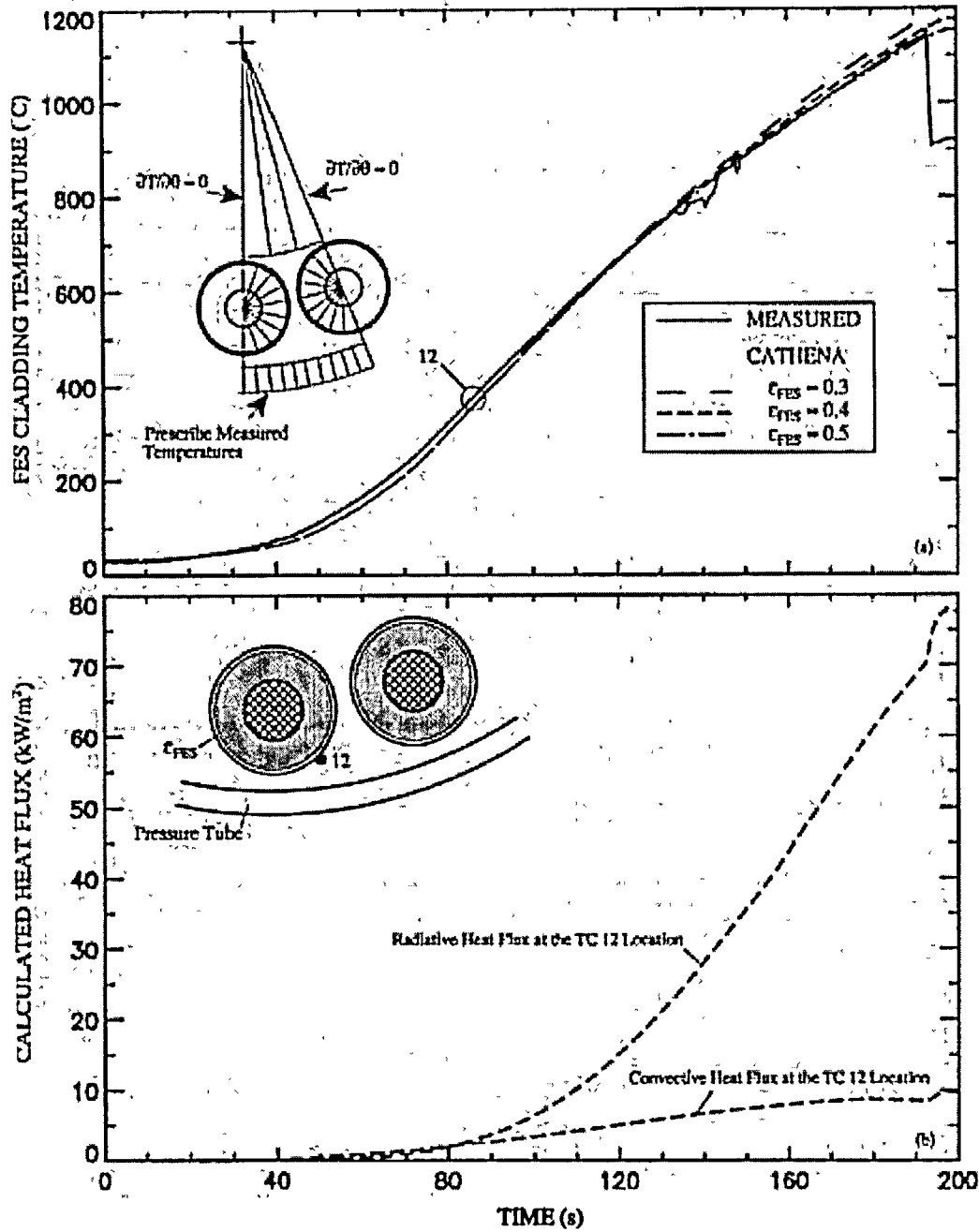


FIGURE 7: Comparison of CATHENA-Calculated FES Cladding Temperatures with Measured (a) and the CATHENA-Calculated Heat Flux Components at the TC 12 Location (b) for Bearing-Pad Test 6

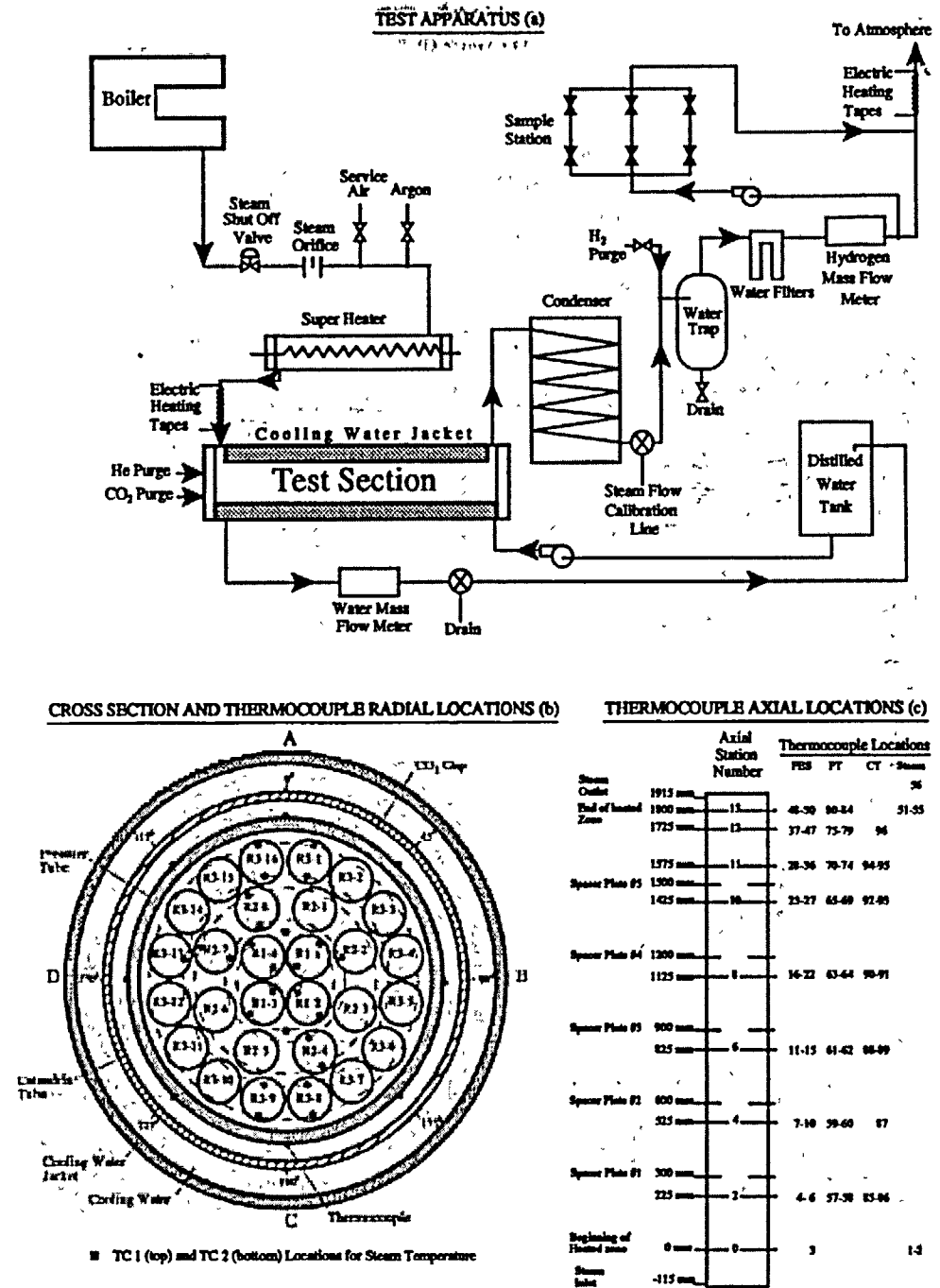


FIGURE 8: Test Apparatus (a), Cross Section and Thermocouple Radial Locations (b), and Thermocouple Axial Locations (c) for CHAN Test CS28-3

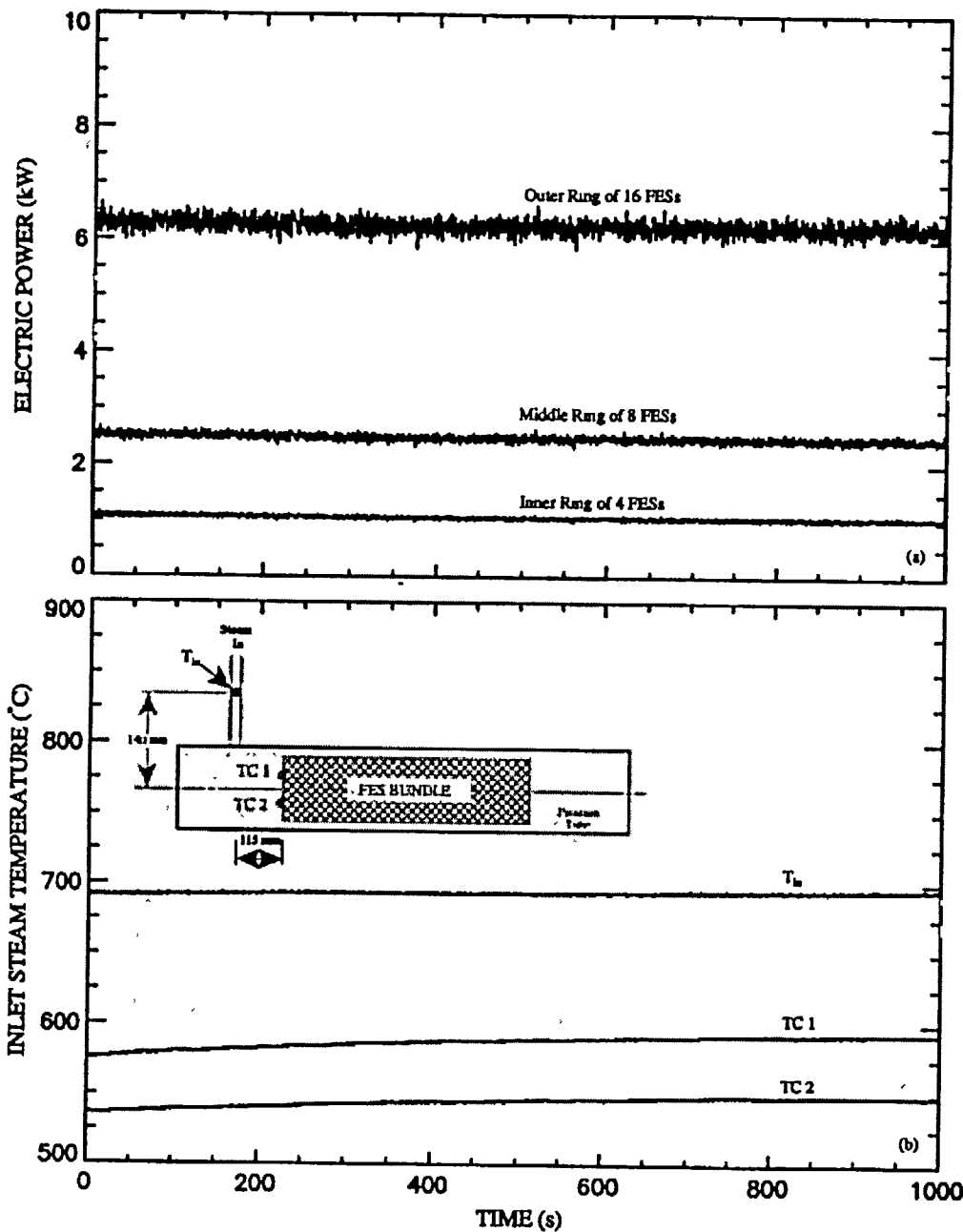


FIGURE 9: Electric Power to Each FES Ring (a) and Steam Temperatures Measured near the Inlet of the Test Section (b) during CHAN Test CS28-3

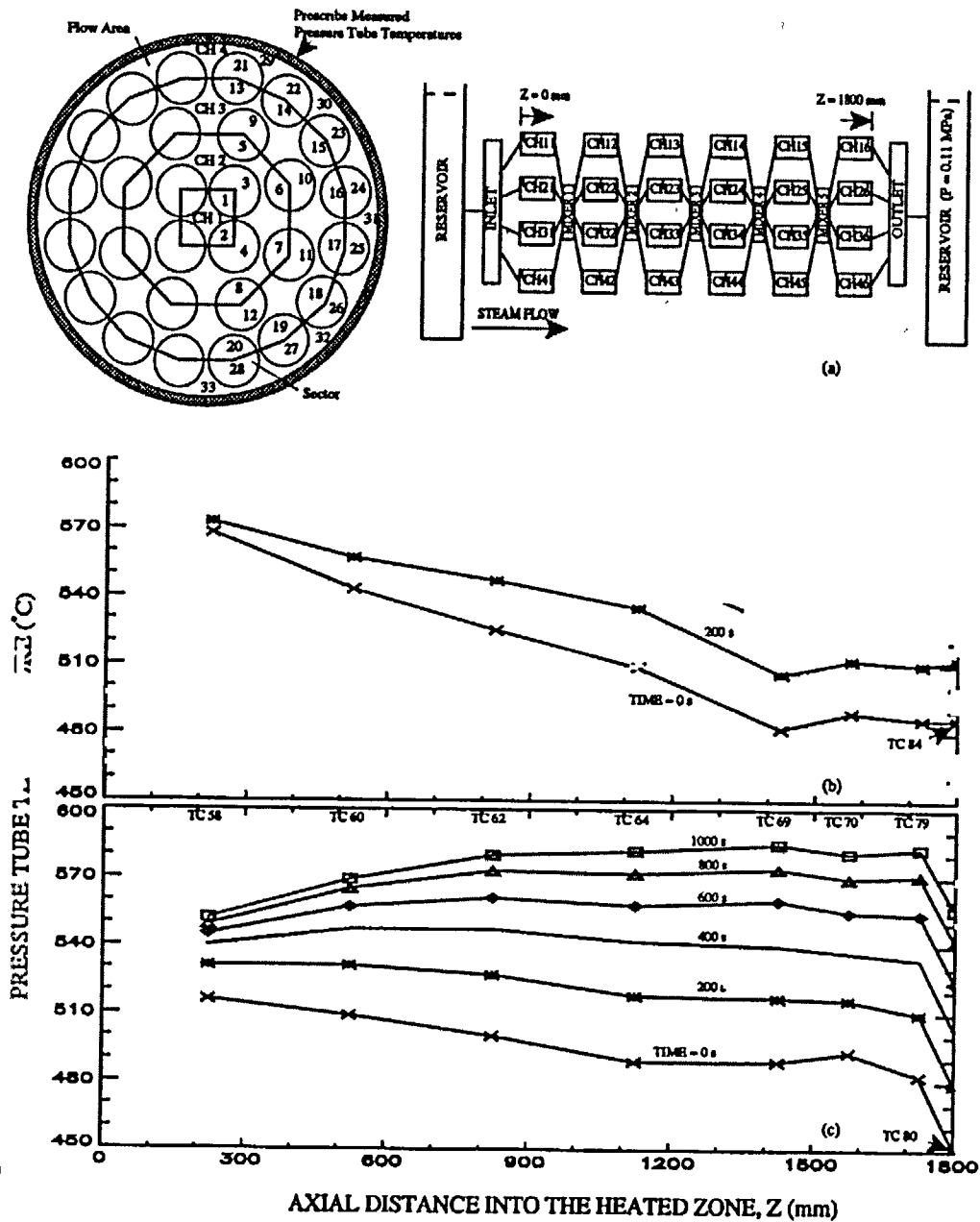


FIGURE 10: CATHENA 28-Element Model (a), Temperatures (Used as Prescribed Boundary Conditions) Measured on the Pressure-Tube Outer Surface at Top (b) and Bottom (c) in CHAN Test CS28-3

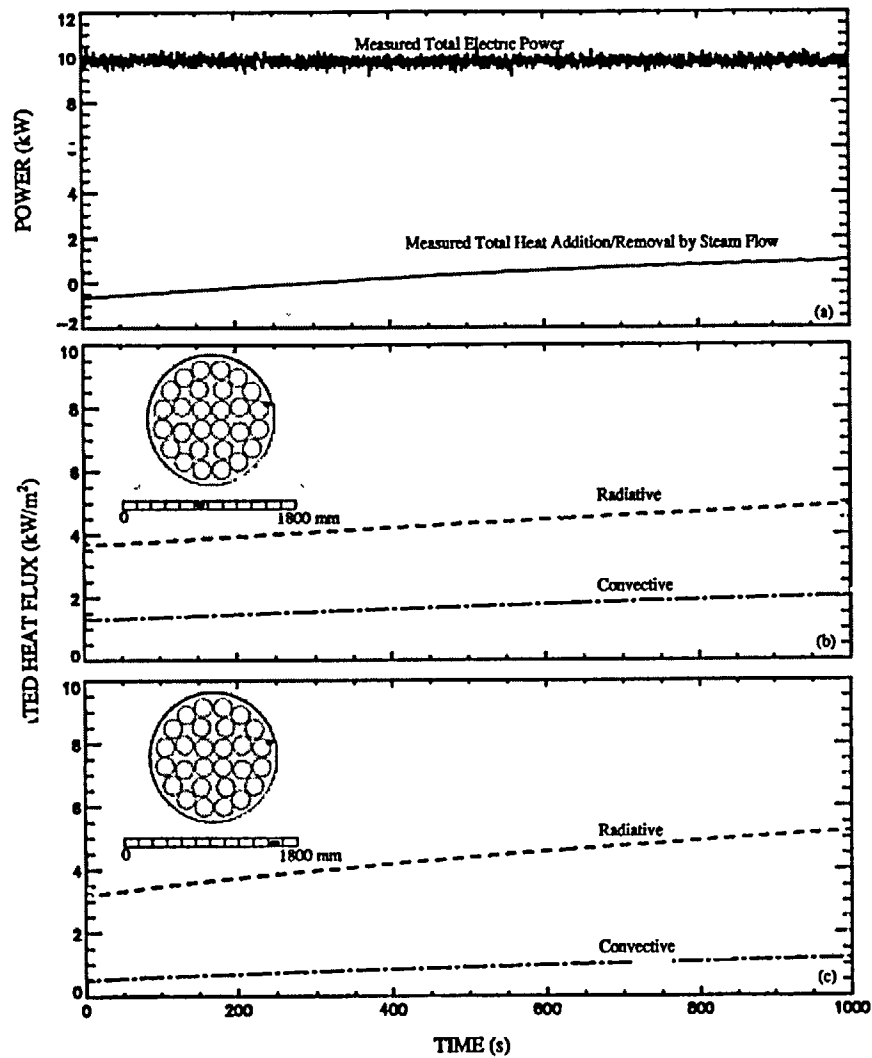


FIGURE 11: Measured Total Electric Power and Total Heat Addition/Removal by Steam (a) and Comparisons of the Simulated Radiative Heat Flux with the Simulated Convective Heat Flux at Two Locations (b and c) for CHAN Test CS28-3

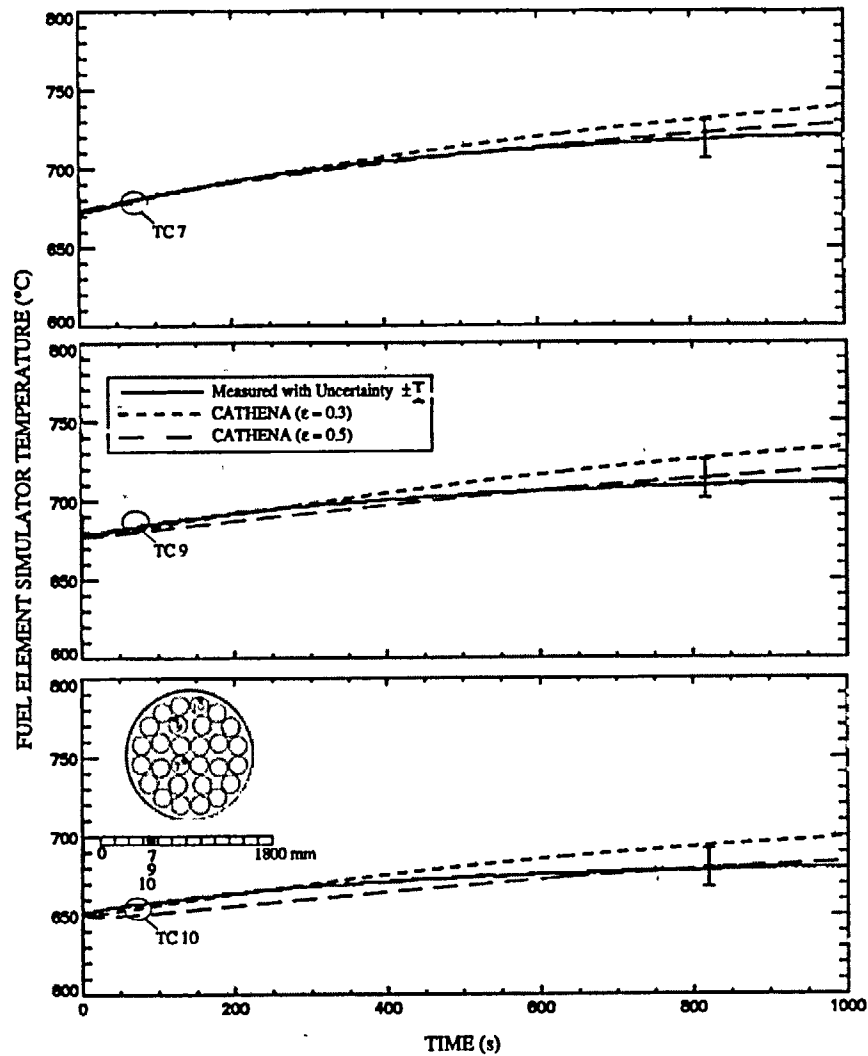


FIGURE 12: Comparison of CATHENA-Simulated Fuel Element Simulator Temperatures with the Measured Temperatures at the Axial Location 525 mm into the Heated Zone for CHAN Test CS28-3

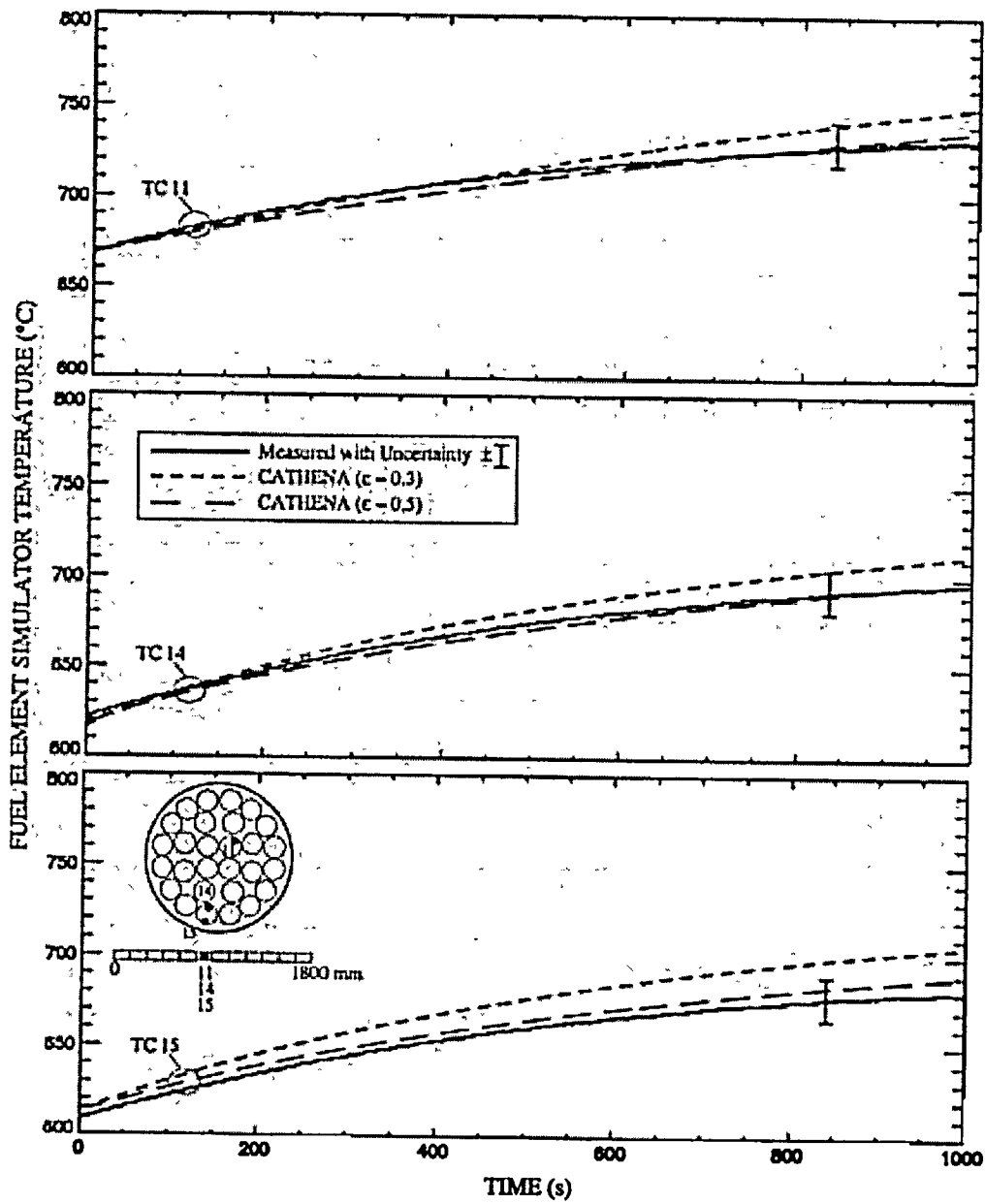


FIGURE 13: Comparison of CATHENA-Simulated Fuel Element Simulator Temperatures with the Measured Temperatures at the Axial Location 825 mm into the Heated Zone for CHAN Test CS28-3

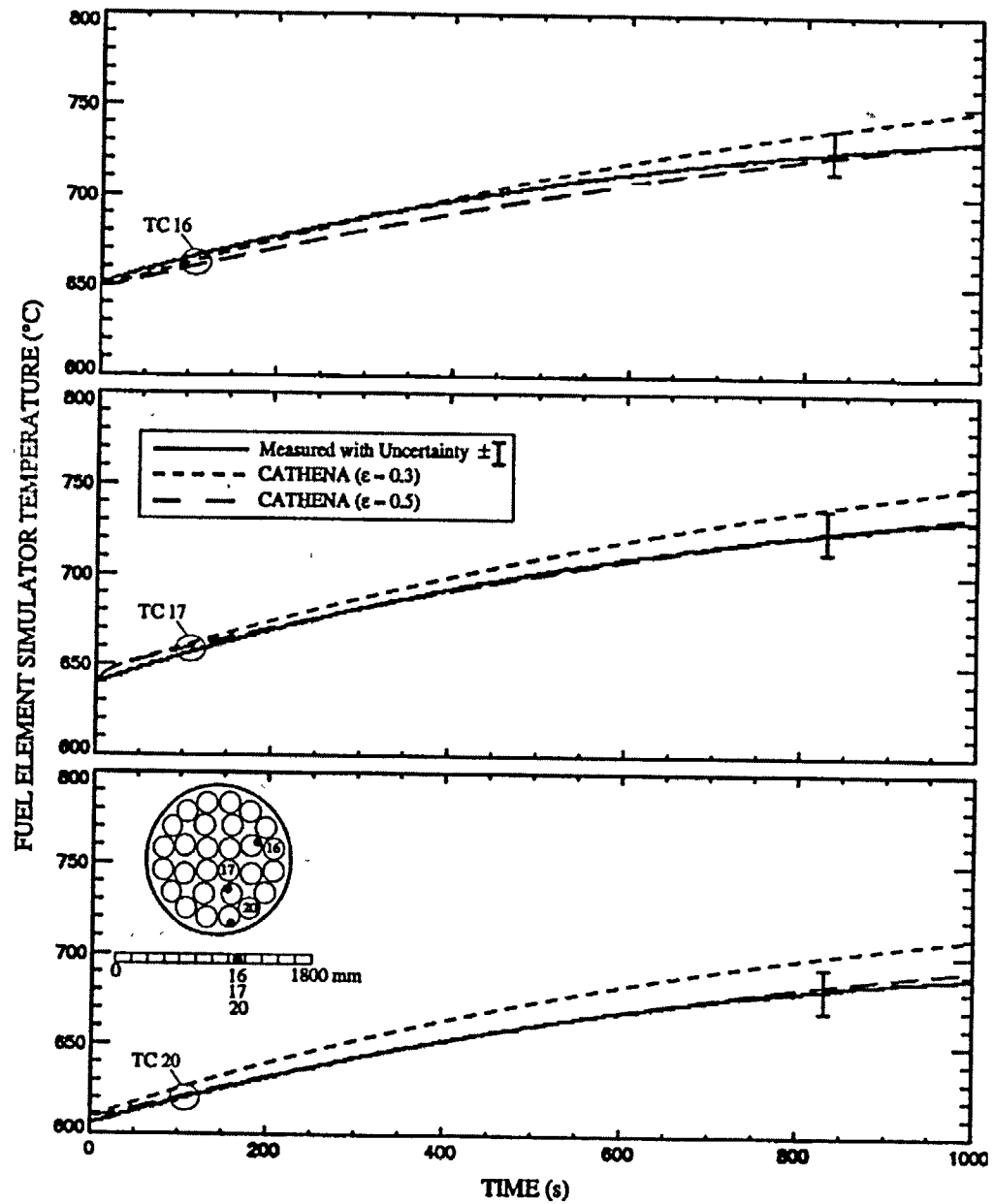


FIGURE 14: Comparison of CATHENA-Simulated Fuel Element Simulator Temperatures with the Measured Temperatures at the Axial Location 1125 mm into the Heated Zone for CHAN Test CS28-3

MODELLING THERMALHYDRAULIC/THERMAL-MECHANICAL BEHAVIOUR OF
A FUEL CHANNEL WITH STRATIFIED TWO-PHASE FLOW USING CATHENA

Q.M. Lei, T.M. Goodman and D.B. Sanderson

Atomic Energy of Canada Limited
Whiteshell Laboratories
Safety Thermalhydraulics Branch
Pinawa, Manitoba
Canada ROE 1L0

ABSTRACT

Under some postulated accident scenarios in a CANDU® (CANada Deuterium Uranium) reactor, some fuel channels may experience periods of stratified flow in which the top portion of the pressure tube and fuel elements are exposed to superheated steam while the bottom portion is cooled with water. As a result, the circumferential temperature gradient that develops on the pressure tube could result in nonuniform deformation and potential failure of the pressure tube. The ability to model the transient thermalhydraulic and thermal-mechanical behaviour of the fuel channel during such a scenario is an important part of the licensing analysis for CANDU reactors during a postulated loss-of-coolant accident (LOCA).

Four pressure tube circumferential temperature distribution experiments were simulated using the thermalhydraulic code CATHENA MOD-3.5a/Rev 0 to demonstrate its ability to model the combined thermalhydraulic and thermal-mechanical behaviour of a fuel channel subjected to stratified two-phase flow. The experiments simulated involved boil-off of the coolant in a horizontal channel with or without make-up water or steam. These experiments had channel absolute pressures ranging from 1.1 to 5.6 MPa and pressure-tube heating rates up to 5.4° C/s. CATHENA accurately simulated boil-off rates, test-section temperatures, and nonuniform pressure-tube deformation during coolant boil-off without make-up water or steam. When make-up water or steam was provided, the simulated fuel channel behaviour agreed with experimental results, provided the cross-sectional steam temperature gradients in the horizontal channel and the flows near the test section inlet were correctly modelled. The work described in this paper was funded by the CANDU Owners Group (COG).

1. INTRODUCTION

Horizontal fuel channels separate the fuel and coolant from the heavy-water neutron moderator in CANDU reactors. During a postulated LOCA, coolant flow in some fuel channels may become stagnated and stratified. The coolant inside the pressure tubes may boil off, causing upper portions

CANDU® is a registered trademark of Atomic Energy of Canada Limited (AECL)

of the fuel bundle and the pressure tube to become exposed to superheated steam as the coolant level drops. In this case, a large temperature gradient will develop around the circumference of the pressure tube. Creep deformation may occur in the hot zone of the pressure tube if it remains pressurized. This deformation may cause the pressure tube to balloon into contact with its surrounding calandria tube and increase heat transfer to the moderator. Alternatively, the pressure tube may rupture due to excessive strain caused by localized temperature gradients. Therefore, the ability to assess the combined thermalhydraulic and thermal-mechanical behaviour of a pressure tube under stratified two-phase flow conditions is an important aspect of assessing fuel channel behaviour under postulated LOCA conditions.

Both experimental and analytical studies have been conducted to understand and predict the circumferential temperature distribution and resulting pressure-tube deformation. Shewfelt et al. [1] developed creep correlations for Zr-2.5 Nb pressure tubes based on data from uniaxial constant temperature creep experiments. These creep correlations were incorporated into a one-dimensional pressure tube deformation model. The model was shown to be capable of predicting nonuniform pressure-tube deformation provided the circumferential temperature gradients on the pressure tube are known [2]. A series of full scale boil-off experiments [3] were performed to investigate the circumferential temperature distribution and resulting deformation that could develop on a pressure tube containing stratified two-phase coolant. The experiments produced an understanding of pressure tube circumferential temperature gradients under a variety of conditions. The experiments, in turn, provided a data base of experimental results for use in the validation of thermalhydraulic and fuel channel codes, such as CATHENA, used in the safety and licensing analysis of fuel channel behaviour. This paper reports the CATHENA modelling methodologies and validation results.

2. DESCRIPTION OF THE CATHENA CODE

CATHENA [4] is a multipurpose thermalhydraulic computer code developed primarily to analyse postulated LOCA scenarios for CANDU nuclear reactors. The code uses a nonequilibrium, two-fluid thermalhydraulic model to describe two-phase fluid flow. Conservation equations for mass, momentum, and energy are solved for each phase (liquid and vapour). Interphase mass, momentum, and energy transfers are specified using a set of flow regime dependent constitutive relations. The code uses a staggered-mesh, one-step, semi-implicit, finite-difference solution method.

CATHENA contains a generalized heat transfer package that enables it to model the behaviour of a fuel channel in considerable detail. It allows multiple wall surfaces to be attached to each thermalhydraulic node. Thermal conduction in the radial and circumferential directions can be calculated for individual elements within a bundle, the pressure tube, and the calandria tube. Although axial conduction is not explicitly calculated, thermal variation in the axial direction is accounted for by the axial nodalization of the channel. The effects of thermal radiation, pressure-tube deformation, zirconium-steam reaction, steam starvation, solid surface contact, and the presence of noncondensables can all be modelled by the code.

A number of models are available in CATHENA to describe various phenomena encountered in postulated LOCA scenarios. Principal CATHENA models assessed during this study include the

fuel channel deformation model, the steam-bubble model, the separator model, and the thermal radiation model. The fuel channel deformation model in CATHENA keeps track of individual subsector circumferential lengths and wall thicknesses based on the temperature and stress calculated for each circumferential subsector. The model assumes the pressure tube remains circular as it deforms. This approach allows CATHENA to predict local pressure-tube strain and full circumferential contact between the pressure tube and the calandria tube. The steam-bubble model in CATHENA simulates the cross-sectional phase (steam and liquid) temperature gradients that may occur in a horizontal fuel channel subjected to stratified two-phase flow. The separator model in CATHENA models phase separation under stratified flow conditions. The CATHENA radiation heat transfer model calculates thermal radiation interchanges within an enclosure of solid diffuse-gray surfaces. The model uses constant surface emissivities and the view factors calculated by assuming the fuel channel cross-sectional geometries for thermal radiation are axially infinitely long.

Considerable effort has been devoted to evaluate, validate, and document the ability of CATHENA to predict fuel channel behaviour under LOCA conditions [5-8]. These documented studies represent an important step in the development of CATHENA for use as a best-estimate fuel channel code for reactor licensing calculations.

3. THE EXPERIMENTS

The Pressure Tube Circumferential Temperature Distribution experimental program [3] was divided into five test series. A total of 17 tests were performed to examine the influence of electric power, channel pressure, make-up water level, and steam-cooling rate on the pressure-tube circumferential temperature gradients and resulting pressure-tube deformation. Four experiments simulated in this study are: boil-off test S-1-2, steam-cooling test S-3-3, variable make-up water test S-4-3, and supplementary boil-off test S-5-2. The CATHENA simulations of the other tests in the program were reported elsewhere [2,6]. The experimental conditions of these four tests are summarized in Table 1.

Figure 1a is a schematic of the experimental apparatus used for test S-1-2. Other tests in the program required various modifications of this equipment. For all tests, the test sections consisted of a section of autoclaved Zr-2.5 Nb pressure tube (PT) mounted inside a Zr-2 calandria tube (CT). The annulus between the pressure tube and the calandria tube was purged with CO₂ and remained at atmospheric pressure throughout the experiments. The calandria tube was surrounded by heated, nonflowing water in an open tank. One end of the pressure tube was either closed to simulate stagnant flow or attached to inlet lines to allow make-up water and/or steam to enter. The other end of the pressure tube was opened to a vertical pipe which had an inner diameter of 24.3 mm.

In tests S-1-2, S-3-3, and S-4-3, fuel element simulators (FESs) were arranged to represent a CANDU 37-element fuel bundle (Figure 1b). Each FES consisted of a Zr-4 fuel sheath (outer diameter 13.1 mm and inner diameter 12.1 mm) surrounding a Zircaloy heater element (outer diameter 9.5 mm and inner diameter 9.0 mm). The heated length was 2300 mm. In test S-5-2, the pressure tube contained a 28-element bundle and was mounted eccentrically in the calandria tube, leaving a 5-mm gap at the bottom and a 12.2-mm gap at the top (Figure 1c). This arrangement was used to simulate a condition where the pressure tube has sagged and the garter spring has contacted

the calandria tube. Each FES consisted of Zr-4 cladding (15.2-mm outer diameter, 14.4-mm inner diameter) within which annular alumina pellets electrically insulated the cladding from a 6-mm diameter graphite heater. The heated length was 1800 mm.

The FESs were connected to a DC power supply. The central FES of the 37-element bundle was not electrically heated. The 36 heated FESs were grouped into three (inner, middle and outer) rings and electric power was supplied to these rings approximately in proportion to the radial power profile in a CANDU fuel bundle. Test section temperatures were monitored at three or five axial locations using thermocouples within the heater elements, on the FES cladding, pressure and calandria tubes, and in steam and water throughout the tests. The sensing wires were spot-welded directly on the surface. Steam flow was determined using orifice plates and the pressure was measured using pressure transmitters. The estimated accuracy of these measurements was: $\pm 5\%$ for electric power, $\pm 3.5^\circ\text{C}$ for pressure-tube temperature below 300°C , $\pm 1\%$ for pressure-tube temperatures between 300°C and 1000°C , $\pm 2\%$ for steam flow, $\pm 5\%$ for make-up water flow, and $\pm 0.3\%$ for pressure.

At the beginning of each test, the pressure tube was filled with water at room temperature and pressurized to the desired test section pressure. The temperature of the water in the pressure tube was gradually raised to the saturation temperature. After the water in the pressure tube had reached the saturation temperature, valves were opened (if appropriate) to allow the make-up water and/or steam to enter and steam to exit the test section. A pre-determined power setting was then applied to the entire FES bundle. The tests were terminated when a FES failed, the pressure tube ruptured or steady-state operation of the test was apparent.

4. MODELLING METHODOLOGY AND ASSUMPTIONS

The test section was axially divided into 12 segments (Figure 2a). A separator model was applied at the junction between the pressure tube and the vertical venting pipe to model the preferential venting of steam in the experiments. Based on the known geometry (pressure tube and venting pipe diameters), the minimum and maximum void fractions required as input for the CATHENA separator model were 0 and 0.005, respectively. The separator efficiency was assumed to be 100%. Due to symmetry, half of the bundle cross section was modelled within each axial segment. Each FES modelled was divided into four equal sectors, and each half circumference of the pressure tube and the calandria tube was divided into 19 sectors (Figure 1). This mesh, determined via a sensitivity study, produced sufficiently converged solutions for the experimental conditions simulated.

Conduction heat transfer in the radial and circumferential directions was calculated for the FESs, the pressure and calandria tubes. Conduction and radiation in the axial direction were neglected. Thermal radiation heat transfer among all divided surfaces inside the pressure tube and from the pressure tube to the calandria tube was calculated at each axial segment. The view factors were calculated using a CATHENA utility program. Emissivities of the inner and outer surfaces of the autoclaved pressure tube were assumed to be constant at 0.8. Emissivity of the calandria-tube inner surface was assumed to be constant at 0.3 [9]. Emissivity of the FES cladding was assumed to be constant at 0.6. In the experiments, the FES cladding emissivity varied as the coolant inside the pressure tube boiled off and the Zircaloy cladding became oxidized in a steam environment [9].

Transient emissivity values are not currently accommodated in CATHENA. Uncertainties in using this constant emissivity value were assessed and deemed to have a small impact on the overall simulation results.

Effects of pressure-tube ballooning on thermalhydraulic and heat-transfer calculations (e.g., increasing flow and heat-transfer areas, changing radiation view factors, and decreasing conduction path between the pressure and calandria tubes) were neglected. The exothermic zirconium/steam reaction was modelled using the Urbanic-Heidrick reaction rate correlation; the calculated maximum reaction heat for these experiments was found to be below 5% of the total electric power.

5. SIMULATION RESULTS

5.1 Boil-Off Test S-1-2

This boil-off test [2] was conducted at a constant absolute channel pressure of 1.1 MPa with one end of the test section closed to simulate stagnant flow. At 300 s, the water inside the pressure tube approached saturation temperature and the apparatus was considered to have reached the "initial condition" of the test. Some top FESs were exposed to steam as total channel power reached 80 kW (Figure 2b). As the water level dropped, the top portion of the pressure tube heated up, deformed, and contacted the surrounding calandria tube. This local contact occurred initially at 538 s near the closed end when the maximum pressure-tube temperature recorded was 840°C. Contact near the steam exit end did not occur until 10 s later. At 586 s, some heaters failed causing the test to be terminated.

As the stagnant water in the test section boiled off, superheated steam remained at the top of the bundle due to buoyancy while the steam temperature near the steam-liquid interface was close to saturation temperature. The steam temperature gradient was expected to increase as heating continued and the water level in the pressure tube decreased. The CATHENA steam-bubble model was used in this simulation to approximate the vertical steam temperature gradient which developed within the channel during the experiment. When this vertical steam temperature gradient was not taken into account under these experimental conditions, CATHENA underestimated pressure-tube temperatures and resultant deformation during high-temperature transients (Figure 2c) [10].

Measured and simulated FES temperature, void fraction, and pressure-tube temperature histories at axial location 1 (286 mm from the steam exit end) are compared in Figure 3. Most FES thermocouples failed before temperatures reached 1300°C. Temperature traces after thermocouple failure were removed from this plot. The simulated FES temperatures at thermocouples 12, 13 and 14 follow the experimental data closely. CATHENA calculated a slightly earlier start of channel void than in the experiment (Figure 3b). This was caused by an overestimation of water transported to the test-section exit. As the water level inside the channel dropped, differences were seen between measured and simulated surface dryout times indicated by thermocouples 15 and 16. The maximum void fraction was 0.84 at the end of the simulation. As a result, CATHENA did not simulate dryout of the bottom FES (thermocouple 17) although dryout occurred in the experiment as indicated by the FES and pressure-tube temperature traces.

CATHENA did a good job calculating coolant boil-off (Figure 3b). The calculated void fractions after 370 s were lower than the experimental values, indicating a higher simulated water level. Water inside the pressure tube could have been entrained with steam and moved up the vertical venting pipe as steam was moving towards the exit end. This could occur especially when the water level and the steam velocity near the exit end were high (>3 m/s). Entrainment of liquid from water levels below the entrance of a downstream pipe had been experimentally observed for high gas velocities [11]. Liquid entrainment was not taken into account in this simulation. As seen in Figure 3c, the simulated higher water level in the pressure tube resulted in an underestimation of temperatures near the bottom of the pressure tube (e.g., thermocouple 8).

Measured and simulated pressure-tube temperature transients at axial location 3 (286 mm from the closed end) are shown in Figure 4. The simulated transient temperatures at the top half of the pressure tube matched well with the measured temperatures. The simulated maximum temperatures at the top of the pressure tube agreed with the measured temperatures within 2°C . The simulated temperatures near the top of the pressure tube increased above the saturation temperature earlier than in the experiment. This was caused by the simulated earlier start of channel voiding as noted above. The pressure-tube temperatures at thermocouples 1, 2, 10 and 3 were overestimated as high as 60°C between 380 s and 450 s. The higher simulated temperatures were attributed to the use of the steam-bubble model which overestimated the steam temperature gradient within the channel during the early boil-off transient (Figure 2c). In this period of time, the vertical steam temperature gradient at an axial location could not be fully established because there was only a small steam flow area or significant flow mixing available. Forcing a cross-sectional steam temperature gradient by the steam-bubble model regardless of flow conditions (e.g., flow mixing) during this early transient resulted in the pressure-tube temperature overestimation. This was confirmed by a re-simulation of this experiment (Figure 5a) using a newer version of CATHENA in which application of the steam-bubble model was automatically controlled by calculated flow parameters characterizing viscous and buoyant forces (which will be further described in this paper).

As the channel continued to void, an increasing portion of the pressure-tube inner surface was exposed to superheated steam and a significant temperature gradient developed on the circumference of the pressure tube (Figure 5b). During this high-temperature transient, the steam-bubble model represented the cross-sectional steam temperature profile that developed along the test section. As a result, the simulated pressure-tube temperatures at the top half of the pressure tube agreed well with the measured temperatures (Figures 3c and 4).

As indicated by the pressure-tube temperature traces (Figures 3c and 4), the pressure tube deformed in an egg-shaped pattern during the ballooning transient. Most of the deformation occurred near the top due to the circumferential temperature gradient on the pressure tube. At axial location 3, the pressure-tube top first contacted the calandria tube at 538 s (Figure 4). The contact then spread in the circumferential direction. The heaters failed at 586 s before the entire pressure tube circumference contacted the calandria tube. CATHENA simulated full circumferential contact at 537 s at this axial location. At axial location 1, the simulated full contact time was 8 s later than the time of first contact occurred in the experiment (Figure 3c). The code assumes that the pressure tube remains circular during deformation. Although this conservative approximation of pressure-tube deformation limited CATHENA's ability to model the local contact phenomenon observed in the experiment, the code correctly calculated the pressure-tube circumferential

temperature gradient (Figure 5b) and adequately approximated nonuniform deformation under these experimental conditions.

Figure 5c shows the measured and simulated pressure-tube wall thicknesses at axial location 3. The simulated wall thicknesses were taken at the end of the simulation (or after contact). The measured wall thicknesses were the values taken after the experiment was conducted and reflect the entire temperature transient experienced by the pressure tube. Both the experiment and the simulation show a maximum pressure-tube wall reduction near the top. CATHENA overestimated the maximum wall reduction because of the overestimated pressure-tube temperatures (Figure 4). Only the top quarter of the pressure tube experienced significant strain in the simulation. In the experiment, pressure-tube strain was recorded to have taken place over roughly two-thirds of the circumference. This discrepancy in deformation patterns is attributed to the circular cross-section assumption during ballooning in CATHENA.

5.2 Steam-Cooling Test S-3-3

This test had an inlet pipe to provide slightly superheated steam (27 g/s at 300°C) to one end of the pressure tube (Figure 6). The other end of the pressure tube was open to a vertical pipe as in the other tests. The pressure tube was pressurized to 3.8 MPa (absolute). Once the water was heated to near the saturation temperature, steam was supplied to the test section. The inlet steam temperature before 85 s was slightly below the saturation temperature (Figure 6c), indicating that condensation occurred as the steam flowed along the inlet piping. The experiment ended at 436 s as a result of severe heater damage.

Measured temperatures from the top FES and the central FES at two axial locations are shown in Figure 7, with a schematic of steam flow stratification. The FES temperatures varied significantly in the axial direction, being much cooler near the steam inlet. The top portion of the FES bundle shows the effects of steam flow and steam temperature variation:

At the steam inlet, steam entered the test section from the top of the pressure tube at 90 degrees to the test section axis. Turbulent mixing took place near the inlet, resulting in uniform steam temperatures. Cooling of the test section walls was enhanced at axial location 3 where the steam flow was developing.

Flow mixing reduced as the steam flowed further away from the inlet. Steam cooling at axial location 2 was not as enhanced as near the inlet. There was a negligible vertical steam temperature gradient at this axial location.

As the flow became fully developed and stratified (e.g., at axial location 1), significant steam temperature gradients developed between the top FES and the steam-liquid interface.

The above observations indicate that, in the simulation of the experiment, the effects of thermal stratification should not be included near the steam inlet where flow mixing was significant. However, the effects should be included near the steam exit end where significant vertical steam temperature gradients developed in this experiment. The steam-bubble model in CATHENA MOD-3.5a/Rev 0 was a user-activated option and was not linked with any flow parameters. In order to enhance the code's ability to model fuel channel behaviour under postulated LOCA

conditions, it became apparent that inclusion of the effects of thermal stratification would have to be automatically controlled by CATHENA. This effort is briefly described as follows.

The vertical steam temperature gradient is the result of flow stratification and temperature-induced buoyancy forces. The latter can be correlated using a modified Grashof (Gr_L^*) number, which is a ratio of buoyancy to viscous forces and can be defined as:

$$Gr_L^* = g \beta \rho^2 (T_{top-pin} - T_{sat}) (L^*)^3 / \mu^2$$

where g is the gravitational acceleration (m/s^2), β is the thermal expansion coefficient of steam ($1/K$), ρ is the density of steam (kg/m^3), μ is the dynamic viscosity of steam ($N \cdot s/m^2$), $T_{top-pin}$ is the cladding temperature of the top pin ($^{\circ}C$), T_{sat} is the saturation temperature ($^{\circ}C$), and L^* is the modified characteristic length (m) that can be calculated based on the height (L) between the top inner surface of the pressure tube and the steam-liquid interface and the effect of flow entry length. For stratified two-phase flow in a horizontal channel, the significance of free convection may be decided by comparing Gr_L^* with the Reynolds number ($Re_L = \rho VL/\mu$, where V is the local steam velocity) which signifies forced convection. A conventional comparison between free convection and forced convection employs the parameter of $Gr_L^*/(Re_L)^2$.

The values for $Gr_L^*/(Re_L)^2$ were calculated using the experimental data of Figures 2c and 7. It was found that significant vertical steam temperature gradients occurred when $Gr_L^*/(Re_L)^2$ exceeded 1.0 and that insignificant vertical steam temperature gradients occurred when $Gr_L^*/(Re_L)^2$ was below 0.3. When $Gr_L^*/(Re_L)^2$ was between 0.3 and 1.0, a smooth treatment could be applied.

For comparison, test S-3-3 was simulated twice, once using CATHENA MOD-3.5a/Rev 0 where the steam-bubble model was manually activated along the entire test section during the entire simulation transient and once using CATHENA MOD-3.5b/Rev 0 where the above criterion was used to automatically activate the steam-bubble model. Figure 8a shows the comparisons of the simulated FES temperatures and void fractions at axial location 1 (1755 mm from the steam inlet) with the measured values. The results from both the simulations agreed with the experimental data. The differences in FES temperature at this vertical location and void fraction between the two simulations were small. There were, however, significant differences of the simulated pressure-tube temperatures between the two simulations (Figure 8b). Failure of the pressure tube was simulated at 333 s in the simulation using the manually activated steam-bubble model due to the simulated high pressure-tube temperatures and excess strains. Failure of the pressure tube was not simulated using the modified steam-bubble model, which agreed with the experiment (the pressure tube did not fail due to excess strains). Figure 8b shows an improved agreement between the simulated pressure-tube temperatures using the automatically controlled steam-bubble model and the measured temperatures. This improvement is further shown in Figure 8c where comparisons are made between the simulated and measured circumferential temperature gradients on the pressure tube.

5.3 Variable Make-Up Water Test S-4-3

This test had an inlet pipe to inject saturated water at one end of the test section (Figure 9). A stepwise decline in make-up water flow rate ranging from 36 to 0 g/s was applied in this test to determine the effect of decreases in make-up water flow rate. The pressure tube was pressurized to 3.9 MPa (absolute). As the pressure tube heated up, it ballooned into contact with the calandria tube

long most of its axial length. Some heaters began to fail at 805 s in the experiment, causing the pressure tube to rupture at 845 s due to intense localized heating as a result of the electrical arcing. This failure mode is not representative of any plausible scenario in a CANDU reactor.

The simulation of this test started at 376 s, using measured data as initial conditions. Figure 10 shows measured and simulated FES temperatures and channel void fractions at axial location 1 (1755 mm from the water inlet) and pressure-tube temperatures at axial location 3 (350 mm from the water inlet). CATHENA accurately simulated the channel void fraction up to 570 s at axial location 1. After that, the water level in the test section continued to drop (indicated by thermocouple 15). The simulated water level declined more slowly with no dryout of the FES containing thermocouple 15, prior to heater failure. As seen from Figure 9b, the make-up water flow rate decreased below 18 ± 0.9 g/s after 550 s. At low make-up water flow rates, the accuracy in the prediction of water level in the test section could become sensitive to the experimental uncertainties in make-up water flow rate.

The simulated pressure-tube temperatures at axial location 3 compare favourably with the measured data (Figure 10c). Thermocouples 1 and 2 indicated local contact between the pressure tube and the calandria tube in the experiment. CATHENA simulated full circumferential contact at 723 s, 41 s later than the local contact in the experiment. There was a significant discrepancy between the measured and simulated pressure-tube temperatures after 723 s due to the difference of local contact versus full circumferential contact. Prior to contact, CATHENA accurately simulated the circumferential temperature gradients on the pressure tube (Figure 11a). The pressure-tube wall thickness variations were also adequately simulated, as shown in Figure 11b. An overestimation of the maximum wall thickness reduction at the top was due to the overestimated contact time by the pressure-tube deformation model in CATHENA. This overestimation results from the concentric and circular assumptions in the model.

5.4 Supplementary Boil-Off Test S-5-2

This test was performed to further investigate key results from this experimental program, using more robust CHAN-type FESs [5] to eliminate the heater failures that occurred in the previous test series. A 28-element bundle (Figure 1c) was assembled rather than the 37-element bundle used in earlier test series. In addition, an offset pressure tube was used in this test to simulate a sagged pressure tube. Similar to test S-1-2, one end of the test section was closed to simulate stagnant flow. Before the test was started, the test section and exit piping were filled with water and pressurized to 5.6 MPa. The water temperature was gradually raised to the saturation temperature by applying 5 kW of electric power to the FES bundle. The test was started by increasing the test section power to 200 kW at 80 s (Figure 12a).

Measured temperatures and inferred water level at two axial locations at 0 s are shown in the inset of Figure 12a. There was about 30% channel void at the beginning of the test. This initial condition was the result of a power ramp prior to the referenced zero time. This early power ramp was the result of an aborted attempt to start the test. In this test, the pressure tube developed a maximum top-to-bottom circumferential temperature gradient of 435°C as the water in the pressure tube boiled off. The circumferential temperature gradient and internal pressure of 5.6 MPa resulted in pressure tube failure due to excessive localized strain.

The effects of having an offset pressure tube (to simulate a sagged pressure tube) on the heat transfer calculation were included in the simulation. This was done by calculating radiation view factors based on the non-concentric configuration between the pressure and calandria tubes. As well, conduction through the annulus gas gap, which increases from the bottom to the top, was accounted for. The accuracy of modelling the CHAN-type FESs used in this test had been demonstrated elsewhere [5]. The manually activated steam-bubble model was used in this simulation. The measured temperatures and inferred water level at 0 s were used as the initial conditions in the simulation.

In this test, the pressure tube ruptured at 226 s at axial locations 2 and 3. Pressure-tube rupture due to local necking was simulated at 220 s between axial locations 4 and 5. The simulated FES temperatures and channel void fraction at axial location 1 closely matched with the experimental data (Figure 12). The water in the channel was assumed to be initially below the position of thermocouple 10. All simulated FES temperatures were within 60 °C of measured values. The comparison shows accurate calculations of water boil-off rate and high temperature heat transfer by CATHENA.

Measured and simulated pressure-tube temperature histories at axial locations 1 and 3 are compared in Figure 13. All simulated temperatures were within 50 °C of the experimental data. The simulated maximum pressure-tube temperature (at the top) at each axial location was within 10 °C of the measured value. As seen from Figure 14, better overall agreement was noted at axial location 3, with a slight underestimation at axial location 1 and a slight overestimation at axial location 5. The simulated maximum top-to-bottom gradient prior to rupture (at 220 s) was 475 °C, which compares well with the measured maximum value of 435 °C that occurred just before rupture (at 226 s) in the experiment.

Ballooning contact at axial location 1 was indicated by the uppermost thermocouples. At thermocouple 1 (Figure 13), the temperature began to decrease due to local contact, from a maximum of 728 °C, 6 s before pressure tube rupture. This local contact behaviour was not simulated by CATHENA due to the circular geometry assumption. Simulated pressure-tube wall thicknesses at three axial locations at the end of the simulation are compared in Figure 15 with the post-test measured values. CATHENA accurately calculated the circumferential variation of pressure-tube wall thickness. The simulated maximum wall reduction (at the top) was within ±6% of the measured value.

6. CONCLUSIONS

Comparisons of the simulation results with data from four pressure tube circumferential temperature distribution experiments indicate that CATHENA is able to predict the combined thermalhydraulic and thermal-mechanical behaviour of a fuel channel subjected to stratified two-phase flow.

For test S-1-2 where the stagnated coolant boiled off at 1.1 MPa, CATHENA accurately simulated the boil-off rates, the maximum temperatures and the circumferential temperature gradients on the pressure tube. The simulated times for full circumferential pressure-tube/calandria-tube contact were within 8 s of the experimentally inferred times for local contact near the top of the pressure tube. Discrepancies between the measured and simulated pressure-tube deformation patterns for

this test were due to the circular geometry assumption in the CATHENA pressure-tube deformation model.

The experimental results from steam-cooling test S-3-3 and boil-off test S-1-2 suggest that there is a need for automating the use of the steam-bubble model in CATHENA to enhance the code's ability to model the cross-sectional steam (or liquid) temperature gradients due to temperature-induced free convection and flow stratification in a horizontal channel. To this end, a physical parameter was proposed and a control criterion was derived based on the experimental data. The steam-bubble model in CATHENA MOD-3.5b/Rev 0 was modified accordingly. When this automated feature was used to re-simulate tests S-3-3 and S-1-2, an improved agreement between the experimental results and the simulation results was achieved.

For test S-4-3 where the make-up water flow rate declined from 36 g/s to 0 g/s, CATHENA adequately modelled the boil-off transient and the circumferential temperature gradient and deformation of the pressure tube. There was a discrepancy between the measured and simulated FES temperatures due to uncertainties in the estimation of fluid conditions near the test section inlet where the water was injected at a 90-degree angle to the channel axis at a declining rate in the experiment.

CATHENA accurately simulated boil-off rates, test-section temperatures, and nonuniform pressure-tube deformation under the conditions of test S-5-2 where the stagnated coolant boiled off at 5.6 MPa and the pressure tube was offset within the calandria tube to represent a sagged pressure tube. The code correctly simulated the pressure-tube rupture that occurred in this experiment due to the internal pressure and the large top-to-bottom circumferential temperature gradient (as high as 435°C) that developed on the pressure tube. The simulated pressure-tube wall thicknesses at the end of the simulation were within $\pm 6\%$ of post-test measured values. The circular deformation model appeared to provide a better approximation of nonuniform pressure-tube straining when the pressure tube was offset towards the bottom of the calandria tube in this experiment. The circular model generally tends to overestimate strain at the top of a concentric pressure tube on which a large top-to-bottom circumferential temperature gradient exists. For an offset pressure tube, this overestimation is reduced because in the experiment the large annular gap distance is available for the top of the pressure tube to bear more strain before it ruptures or comes into contact with the calandria tube.

REFERENCES

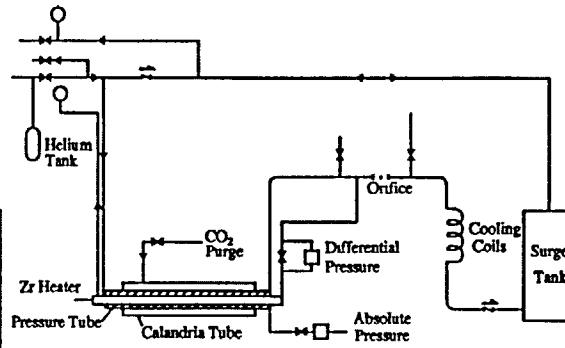
1. R.S.W. Shewfelt, L.W. Lyall and D.P. Godin, "A High-Temperature Creep Model for Zr-2.5 wt% Nb Pressure Tubes," *Journal of Nuclear Materials*, Vol. 125, pp.228-235, 1984.
2. H.E. Rosinger, C.B. So and P.S. Yuen, "The Determination and Verification of Circumferential Temperature Distributions in CANDU-PHW Reactor Fuel Channel Assemblies Under Coolant Flow Stagnation," *Proceedings of International Conference on Thermal Reactor Safety*, Avignon, France, 1988.

3. C.B. So, G.E. Gillespie, R.G. Moyer and D.G. Litke, "The Experimental Determination of Circumferential Temperature Distributions Developed in Pressure Tubes During Slow Coolant Boildown," Proceedings of the 8th Annual CNS Conference, Saint John, NB, 1987.
4. D.J. Richards, B.N. Hanna, N. Hobson and K.H. Ardron, "CATHENA: A Two-Fluid Code for CANDU LOCA Analysis, (renamed from ATHENA)," Presented at the 3rd International Topical Meeting on Reactor Thermalhydraulics, Newport, RI, 1985.
5. Q.M. Lei, D.B. Sanderson and H.E. Rosinger, "High-Temperature Validation of CATHENA against a 28-Element Thermal-Chemical Experiment," Presented at the 15th Annual CNS Conference, Montréal, PQ, 1994.
6. Q.M. Lei, D.B. Sanderson, M.L. Swanson, G.A. Walters and H.E. Rosinger, "Experimental and Theoretical Investigation of Pressure Tube Circumferential Temperature Gradients during Coolant Boil-Off," Proceedings of the 13th Annual CNS Conference, Saint John, NB, 1992.
7. T. Nitheanandan, Q.M. Lei and R.G. Moyer, "The Analysis of Bearing-Pad to Pressure-Tube Contact Heat Transfer Experiments," Proceedings of the 17th Annual CNS Conference, Fredericton, NB, June 1996.
8. Q.M. Lei, D.B. Sanderson and R. Dutton, "Modelling Disassembled Fuel Bundles Using CATHENA MOD-3.5a Under LOCAL/LOECC Conditions," Proceedings of the CNA/CNS Annual Conference, Saskatoon, SK, June 4-7, 1995.
9. P.M. Mathew, M. Krause, M. Dean and M.H. Schankula, "Emittance of Zircaloy-4 Sheath at High Temperatures in Argon and Steam Atmospheres," Proceedings of the 10th Annual CNS Conference, Ottawa, ON, Vol.2, 1989.
10. C.B. So, "Modelling the Steam Temperature Distribution in CATHENA and its Application to Pressure Tube Circumferential Temperature Distribution Analysis," Presented at 13th CNS Reactor Simulation Symposium, Chalk River, ON, 1987.
11. J.E. Kowalski and V.S. Krishnan, "Two-Phase Distribution in a Large Manifold," Presented at AIChE Annual Meeting, New York, 1987.

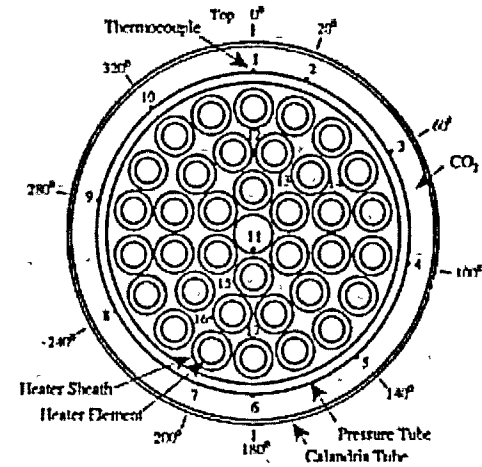
TABLE
SUMMARY OF TEST CONDITIONS AND RESULTS

	S-1-2	S-3-3	S-4-3	S-5-2
Bundle Heating Length (m)	2.3	2.3	2.3	1.8
Number of Bundle Elements	37	37	37	28
Pressure Tube Offset (mm)	0	0	0	3.6
Absolute Channel Pressure (MPa)	1.1	3.8	3.9	5.6
Channel Liquid Level	boil-down	boil-down	decreasing	boil-down
Inlet Flow (g/s)	—	27 (steam)	36 to 0 (water)	—
Pressure Tube (PT) Failure?	no	no	no	yes
Maximum PT Heating Rate (°C/s)	5.3	3.2	2.6	5.4
Maximum PT Temperature (°C)	855	723	693	745

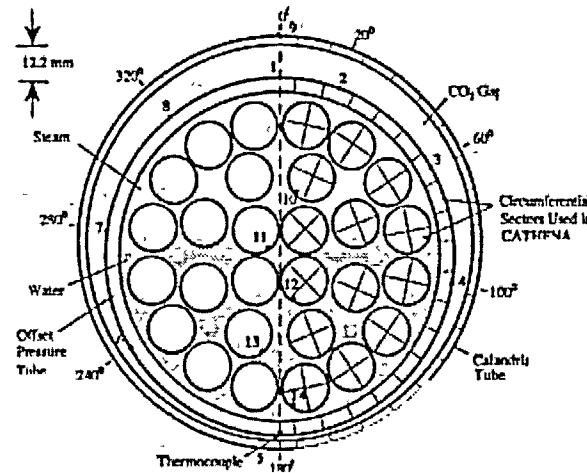
TEST APPARATUS (a)



37-ELEMENT BUNDLE CROSS SECTION (b)



28-ELEMENT BUNDLE CROSS SECTION (c)



SECTORING OF 37-ELEMENT BUNDLE (d)

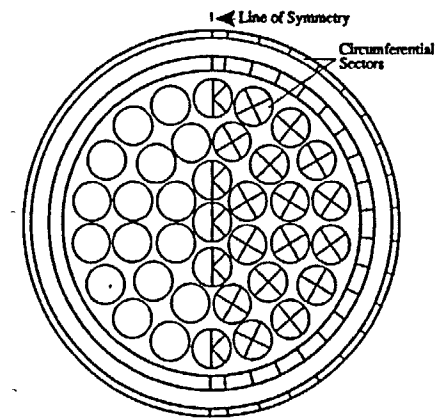


FIGURE Test Apparatus (a) and Test Cross Sections (b and c) of the Pressure Tube Circumferential Temperature Distribution Experiments, Also Showing the CATHENA Sectoring of the Bundle Cross Sections (c and d)

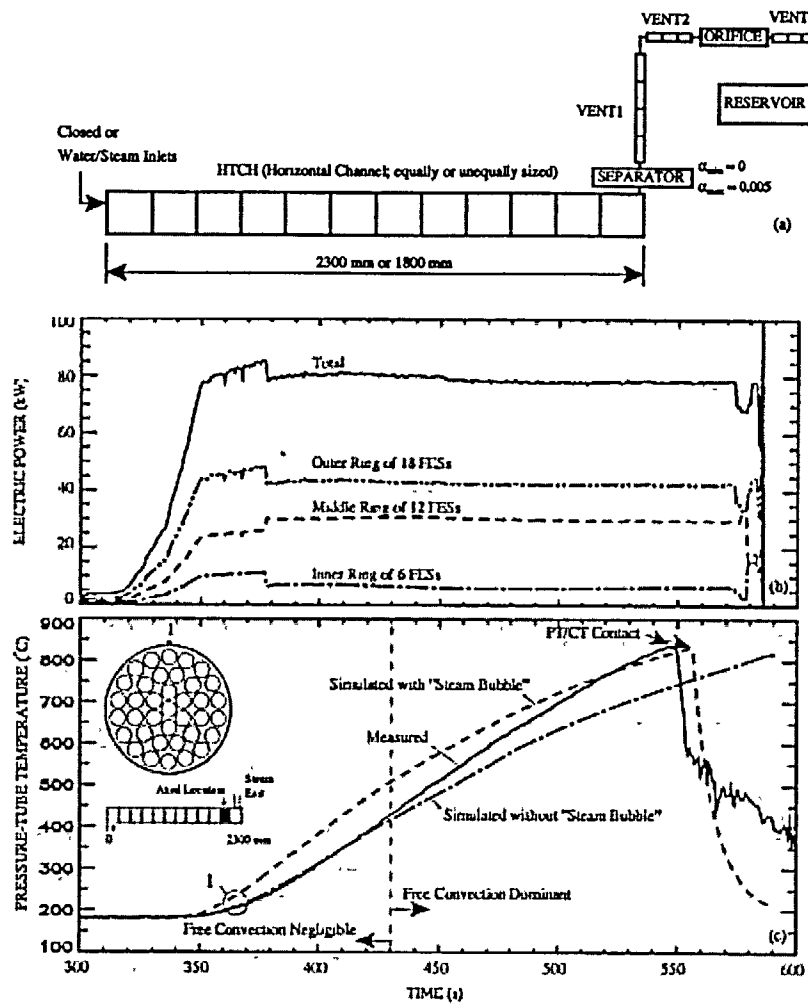


FIGURE 2: CATHENA Thermalhydraulic Representation of the Test Apparatus (a), Electric Power History Used in Test S-1-2 (b), and Effect of the Steam-Bubble Model on the Simulation of Test S-1-2 (c)

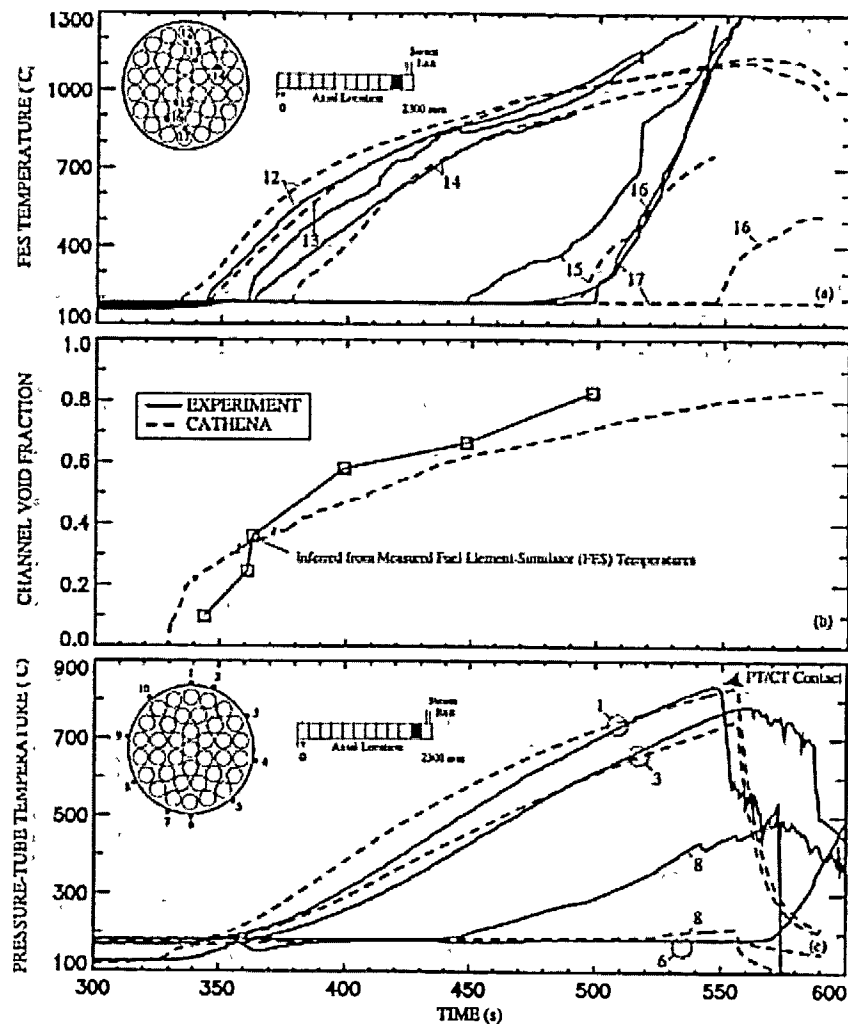


FIGURE 3. Comparison of Simulated FES Temperatures (a), Void Fraction (b), and Pressure-Tube Temperatures (c) at Axial Location 1 (286 mm from the Steam Exit End) with Experimental Results of Test S-1-2

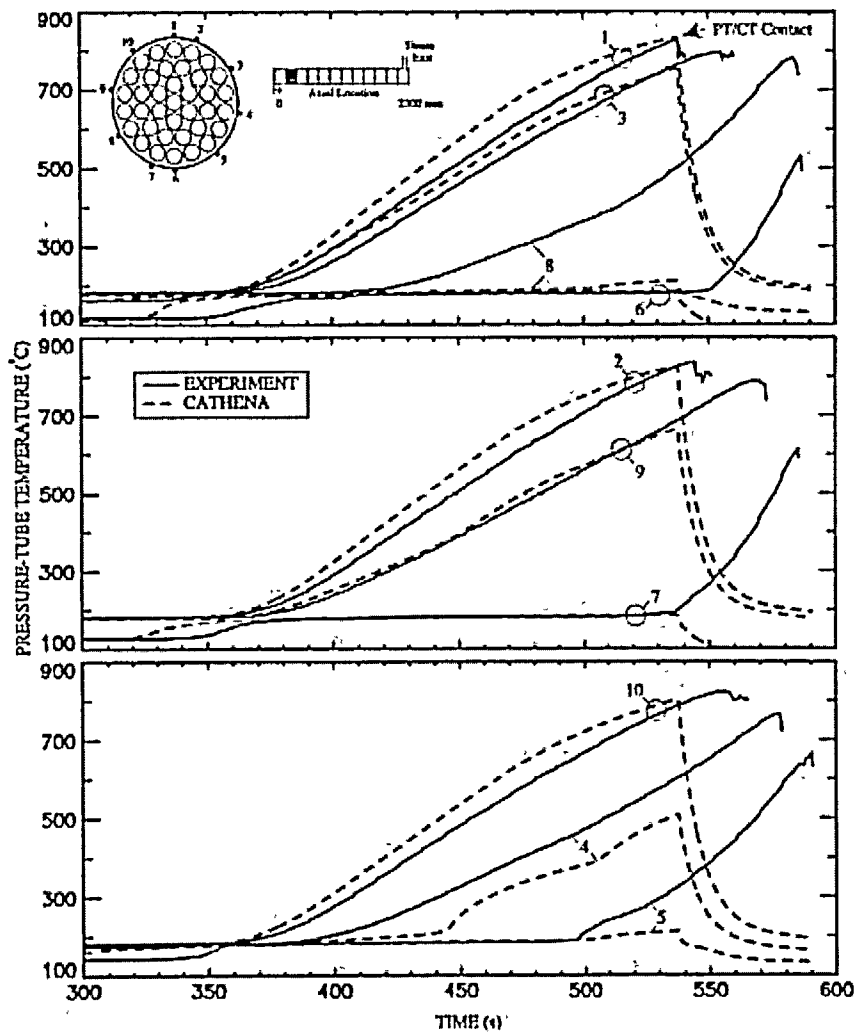


FIGURE 4: Comparison of Simulated Pressure-Tube Temperatures at Axial Location 3 (286 mm from the Closed End) with Experimental Results of Test S-1-2

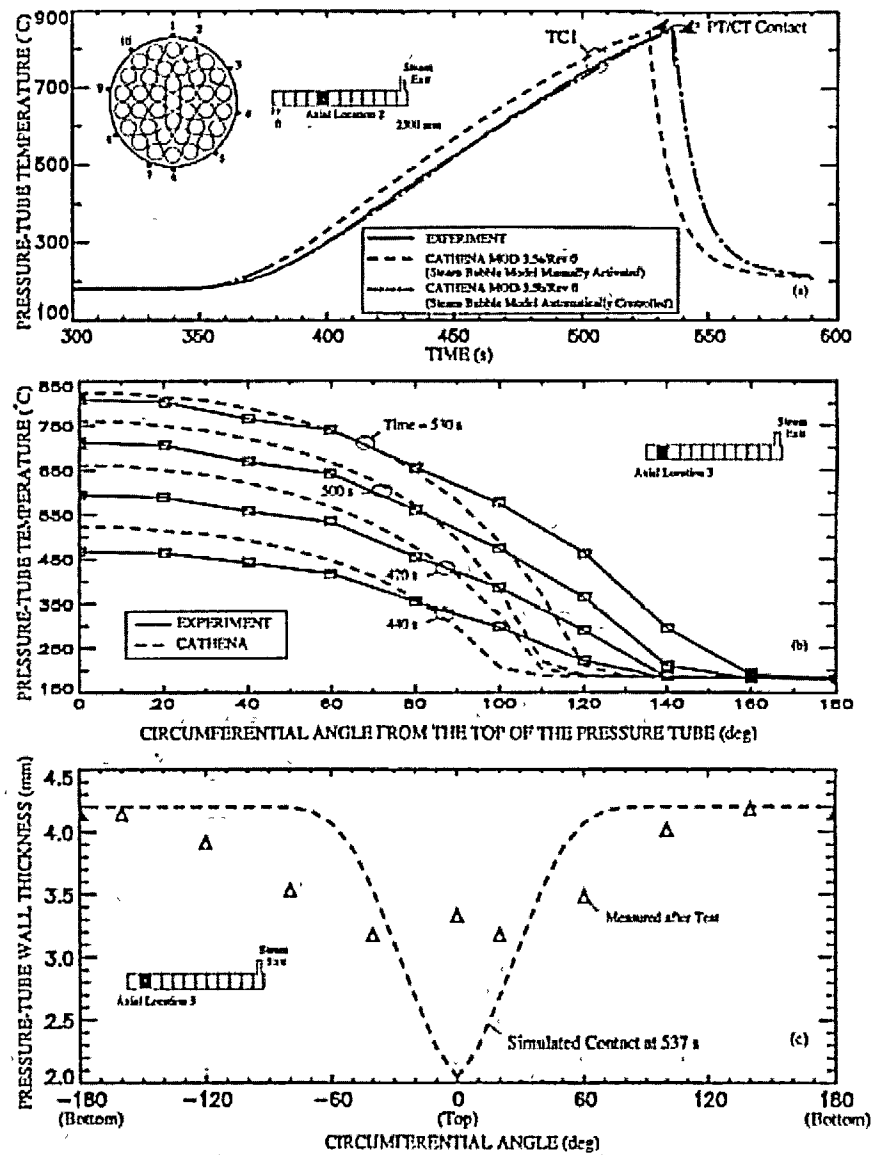


FIGURE 5: Comparison of Simulated Pressure-Tube Temperatures (a), Circumferential Temperatures (b) and Wall Thicknesses (c) with Experimental Results of Test S-1-2

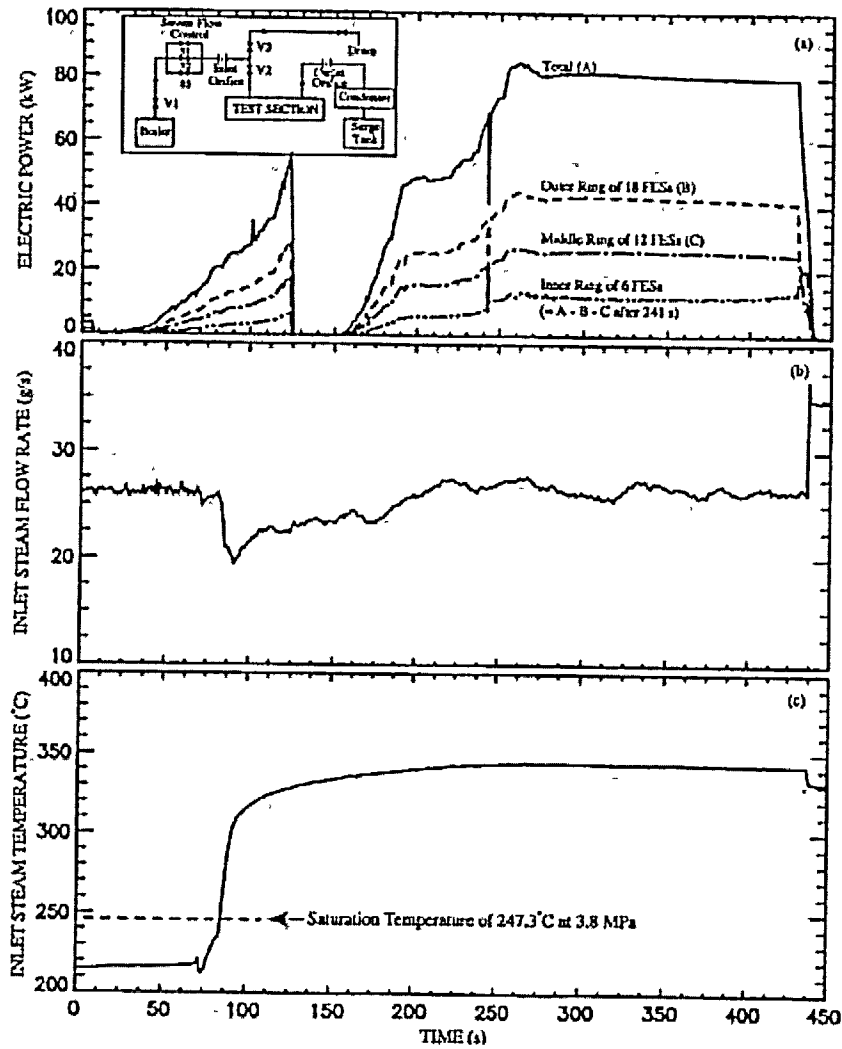
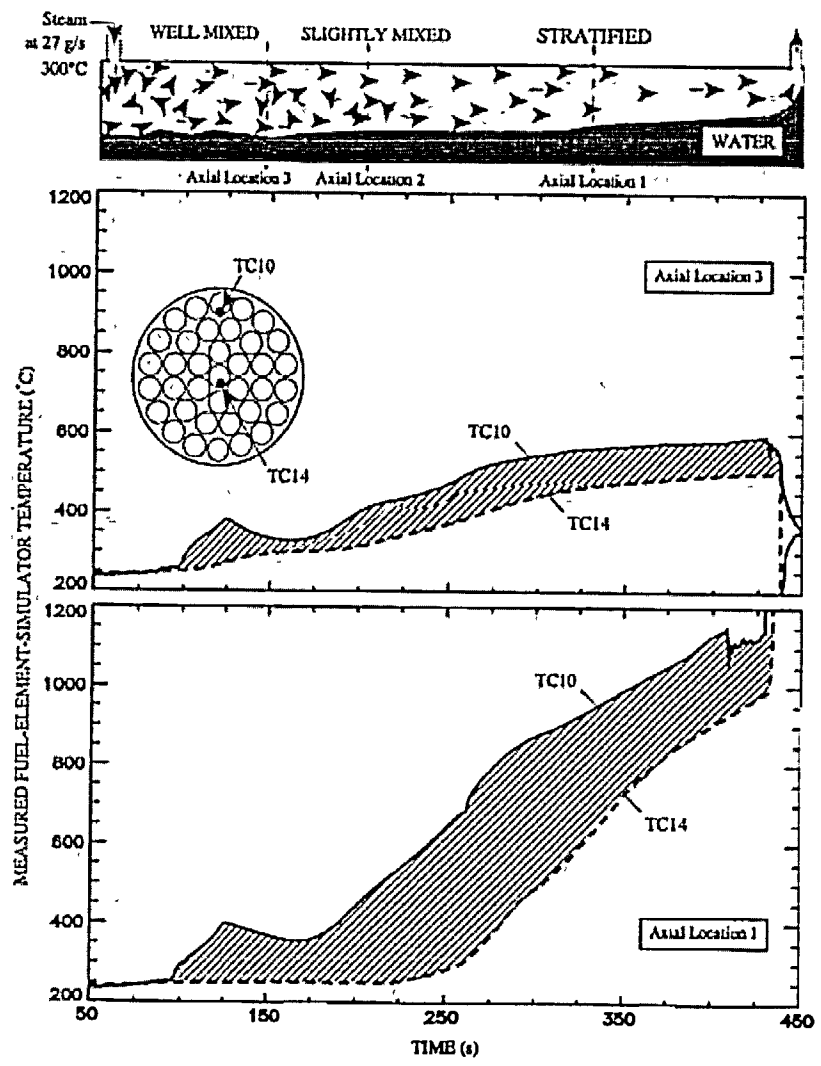


FIGURE 6: Experimental Input Variables. Electric Power (a), Inlet Steam Mass Flow Rate (b), and Inlet Steam Temperature (c) of Steam-Cooling Test S-3-3



Temperature Differences at the Two Axial Locations as a Result of Steam Cooling Effects

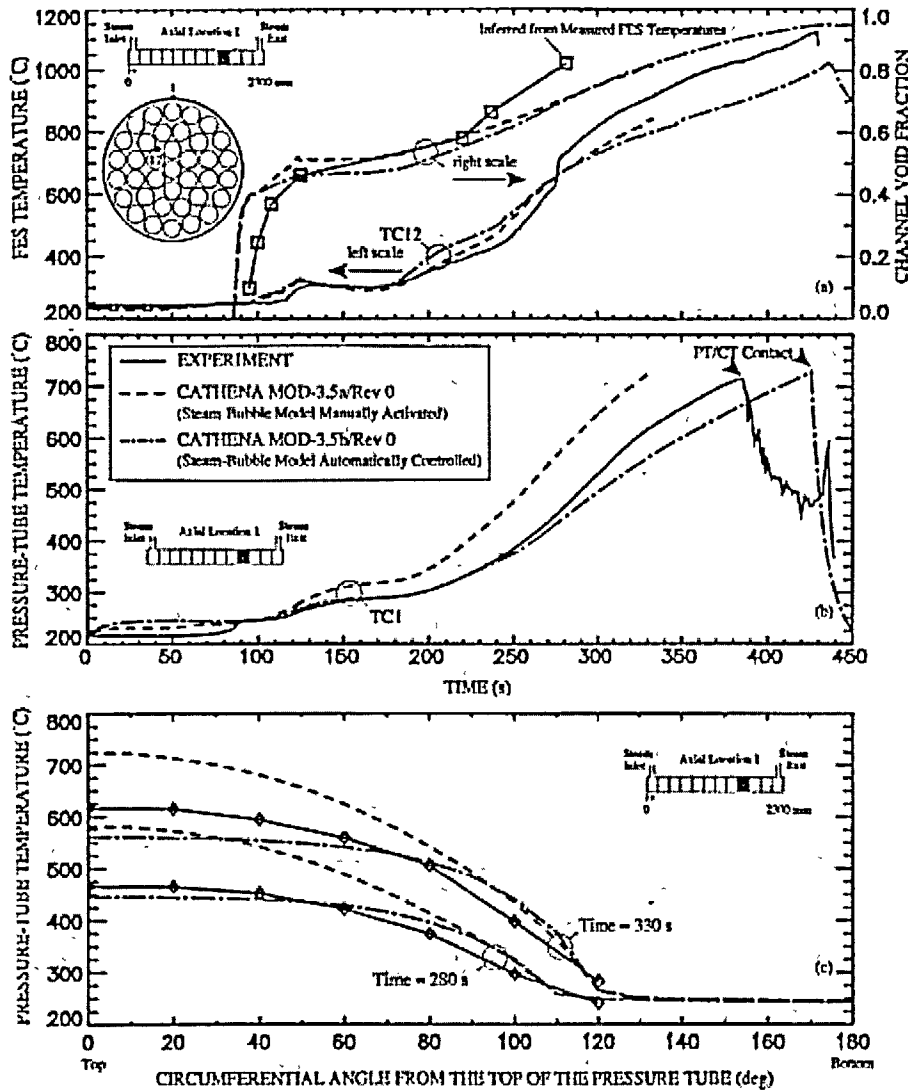


FIGURE 8: Comparison of Simulated FES Temperatures and Void Fractions (a), Pressure-Tube Temperatures (b) and Circumferential Pressure-Tube Temperature Distributions (c) with Experimental Results of Test S-3-3

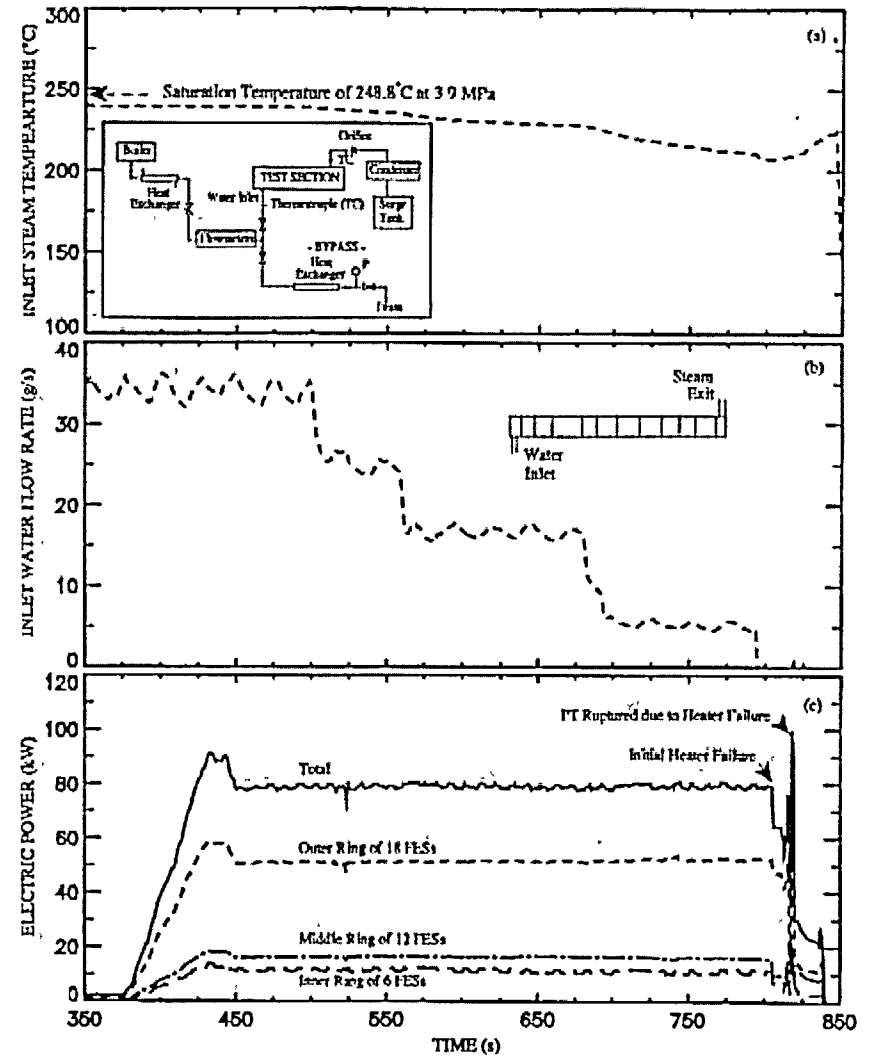


FIGURE 9: Experimental Input Variables: Inlet Water Temperature (a) and Flow Rate (b), and Electric Power History (c) for Test S-4-3

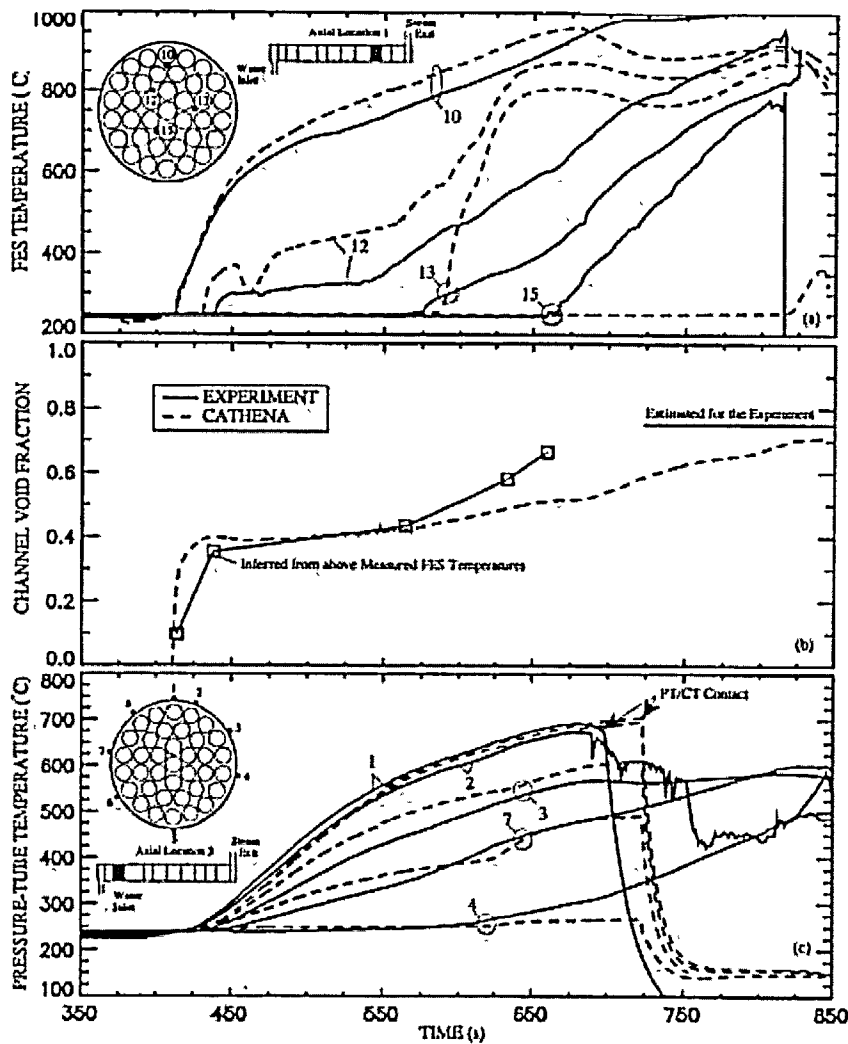


FIGURE 10: Comparison of Simulated FES Temperatures (a), Void Fraction (b), and Pressure-Tube Temperatures (c) with Experimental Results of Test S-4-3

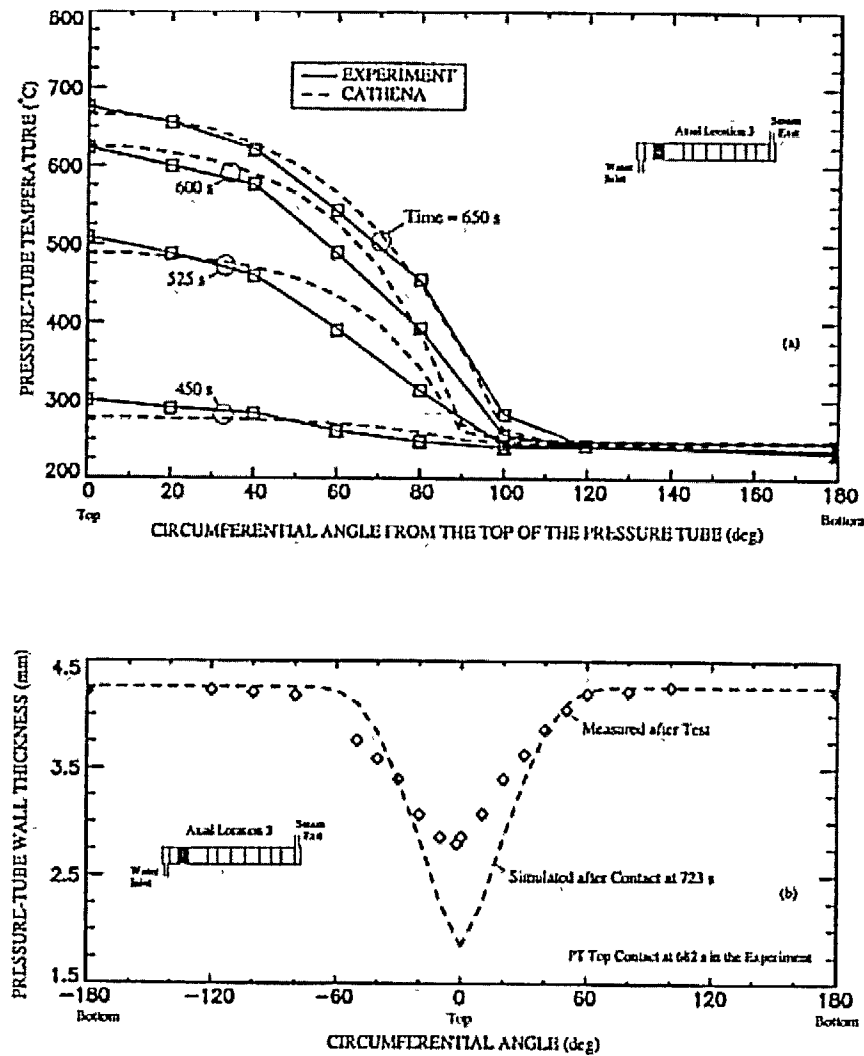


FIGURE 11: Comparison of Simulated Circumferential Temperature (a) and Wall Thickness (b) Variations on the Pressure Tube at Axial Location 3 with Experimental Results of Test S-4-3

**PRE- AND POST-TEST CATHENA SIMULATIONS FOR
RD-14M CRITICAL BREAK EXPERIMENTS**

by

E.J.M. Yetman and T.V. Sanderson

**AECL
Whiteshell Laboratories
Pinawa, Manitoba R0E 1L0**

PRE- AND POST-TEST CATHENA SIMULATIONS FOR RD-14M CRITICAL BREAK EXPERIMENTS

E.J.M. Yetman and T.V. Sanderson

ABSTRACT

Historically, peak fuel element simulator (FES) sheath temperatures in RD-14M Loss of Coolant Accident (LOCA) experiments have not exceeded 550°C. However, in licensing analysis scenarios, peak sheath temperatures during the early blowdown phase of a LOCA have been predicted to reach or exceed 1000°C. Experimental data at these conditions can aid in the validation of codes used for licensing analysis purposes.

A series of critical break LOCA experiments was performed in RD-14M to provide experimental FES sheath temperatures up to 1000°C. This paper summarises the CATHENA simulations used to help design the test series. Post test simulations of selected tests are also discussed.

For this test series, RD-14M was modified to use a single channel per pass; all other channels were isolated at the headers. No emergency core cooling was used. Experiments were conducted either with the power supplies ramped to decay levels 2 s after initiating the break or with the power supplies left at initial conditions until the test was terminated by a process protection trip. The FES trip temperature was increased to 1000°C for the final test.

A CATHENA scoping analysis predicted an inlet header break between 15 mm and 20 mm at a loop flow of 3.7 L/s would produce a critical break with this geometry. Experimental results confirmed these predictions. For experiments conducted with an 18 mm inlet header break with no power ramp down, a peak sheath temperature of 968°C was reached. CATHENA accurately predicted the flow split point in the channel. The code overestimated the top, centre FES temperature by 141°C. This is considered to be a conservative estimation of the peak sheath temperatures.

**AECL
Whiteshell Laboratories
Pinawa, Manitoba R0E 1L0**

INTRODUCTION

Atomic Energy of Canada Limited (AECL), through the CANDU Owner's Group (COG), conducts ongoing research into the safety of CANDU[®] reactors under both normal and off-normal operating conditions. RD-14M is the most recent in a series of integrated thermalhydraulic test facilities designed and operated for this purpose. Experimental data from the RD-14M facility is used to improve the understanding of the thermalhydraulic processes that occur in CANDU geometries and to validate and improve existing computer models to better simulate reactor behaviour.

During a postulated Loss-of-Coolant Accident (LOCA) scenario in a CANDU, the Primary Heat Transport System (PHTS) rapidly depressurises causing voiding of the coolant in the core. At the same time, core coolant will be discharged through the break at a rate dependent on the break size. This loss of coolant from the break discharge and voiding in the core will reduce the heat transfer to the coolant and the temperature of the fuel will increase. During this voiding process the reactor power may also increase resulting in a further increase in fuel temperatures. It is during this early blowdown phase that peak fuel temperatures are expected to be reached.

The effect of break size on peak sheath temperatures and header-to-header pressure drop in RD-14M LOCA experiments is illustrated in Figures 1 and 2, respectively. In a small break LOCA experiment, the break-induced pressure drop is significantly smaller than the head delivered by the primary pump so that the driving force for primary coolant flow through the heated section is maintained during the blowdown. In a large break LOCA experiment, the break-induced pressure drop is significantly larger than the head delivered by the primary pump. The driving force in a large LOCA becomes the break discharge and coolant flow reverses through the broken pass and is maintained in the reverse direction during the blowdown. In a critical break LOCA experiment, the head delivered by the primary pump upstream of the break, is effectively offset by the pressure drop caused by opening the break. Under these conditions, the inlet and outlet header pressures of the broken pass become nearly equal with flow exiting out of both ends of the heated channel. This condition is referred to as a flow split point in the channel.

Previously, RD-14M critical break experiments have reached peak FES sheath temperatures of 539°C during the early blowdown phase. The critical break experiments discussed here were designed to reach FES sheath temperatures near 1000°C to confirm code predictions used in licensing analysis. A critical break in RD-14M is defined as a break that results in a flow split point developing and lasting for several seconds (2 or 3) in the heated part of the test section during the first five or ten seconds of the transient. The two-fluid thermalhydraulic computer code CATHENA, was used in the pre-test design and the post-test simulation of several of the experiments.

Since these tests were designed to reach temperatures outside the normal operating conditions of RD-14M, the facility was modified to only a single channel per pass (TS8 and TS13). This restricted the possibility of damage to only one test section in the broken pass. Emergency core cooling (ECC) was not used in these experiments since the focus of these tests was the early

blowdown period, prior to ECC entering the loop. Unlike a reactor scenario, a power pulse was not simulated due to the limitations of the RD-14M power supplies.

FACILITY DESCRIPTION

RD-14M is an 11 MW, full-elevation-scaled thermalhydraulic test facility possessing most of the key components of a CANDU PHTS. Figure 3 shows a simplified schematic of the RD-14M facility. The facility is arranged in the standard CANDU two-pass, figure-of-eight configuration. The reactor core is simulated by ten, 6 m-long horizontal channels. Each channel has simulated endfittings and seven electrically-heated FES designed to have many of the characteristics of the CANDU fuel bundle. Heated sections are connected to headers via full-length feeders. Above header piping is also CANDU-typical including two full-height, U-tube steam generators or boilers (B01 and B02) and two bottom-suction centrifugal pumps (P1 and P2). Steam generated in the secondary, or shell, side of the steam generators is condensed in a jet condenser (CD1) and returned as feedwater to the boilers. The primary-side pressure is controlled by a pressuriser/surge tank (TK1) using a 100-kW electric heater (HR1). The facility operates at typical CANDU primary system pressures (nominal 10 MPa) and temperatures (up to 310°C) and is designed to produce the same fluid mass flux, transit time, pressure and enthalpy distributions in the primary system as those in a typical CANDU reactor under both forced and natural circulation conditions. A more complete description of the RD-14M facility and its associated instrumentation can be found in Reference [1].

Modifications For This Test Series

Several modifications were made to the RD-14M facility for this test series. These tests were conducted with a single test section connected in each pass. All other test sections were isolated by the installation of blanks at both the inlet and outlet headers. The broken pass, (header 8 to header 5) had only test section 13 (TS13) connected to the headers. Test section 8 (TS8) was the only test section connected in the unbroken pass (header 6 to header 7). Power was individually supplied to each test section. Test sections 8 and 13 were selected for these tests for several reasons. These are "sister" channels which means they are located in different passes but at the same elevation and have the same geometry. Test sections 8 and 13 were also the most accessible for installing supplementary instrumentation for these experiments. These test sections are slightly higher power (nominal 0.946 MW) than some of the other channels (nominal 0.75 MW). The break valve, a 50.8-mm (nominal), remote-control ball valve (MV8), was installed at inlet header 8. The break size was established by placing an appropriately sized orifice immediately upstream of the break valve.

Instrumentation

The RD-14M loop is extensively instrumented. A total of 266 instruments were scanned and recorded using a dedicated data acquisition system for these experiments. Coolant pressures, temperatures, volumetric flow and void fraction measurements were measured both above and below the headers. Fuel element sheath temperatures were measured around the circumference

of the test bundle and along the length of the test section using K-type thermocouples calibrated 0-1050°C (±2°C). In the broken pass (TS13), nine K-type thermocouples were installed on the outside surface of the pressure tube using Thermon (Grade T-63), a high-temperature heat transfer cement. Eight more thermocouples were installed on TS13 inlet and outlet feeders to measure the top and bottom surface temperature near the inlet and outlet endfittings and near the inlet and outlet headers. In a few locations, Resistance Temperature Detectors (RTDs) were also used to measure temperature. Gamma densitometers and conductivity probes provided indications of void in above- and below-header flows. Loop and channel flow rates were measured with turbine flow meters (TFMs).

PROCEDURE

The experiments discussed in this paper consisted of:

- B9603: a “bench-marking” experiment conducted using a typical RD-14M LOCA scenario procedure with the power supplies ramped down to decay power levels 2 seconds after opening the break valve and with the FES sheath trip temperatures set at 700°C, and
- B9605: an experiment conducted with the power supplies left at their initial settings and with the FES sheath trip temperatures set at 1000°C.

Table 1 summarises the initial steady-state conditions used for these tests. Once steady-state conditions were achieved, the data acquisition system and the events sequence timer were simultaneously started. The events sequence timer isolated the surge tank, then four seconds later the break valve opened. Two seconds after opening the break, the power supplies were ramped down to decay levels (for the initial “bench-marking” experiment only). For the high temperature tests, the power supplies were left at their original settings for the duration of the test. All tests were terminated when a process protection trip occurred. The FES trip temperature was set to 1000°C for the high temperature tests in order to limit the potential for damage to the heated sections. (The fuel element simulators are designed to operate at heat fluxes of 0.75 MW/m² and sheath temperatures up to 1000°C.) Deformation of the heated sections was also a concern since it would be difficult to reproduce or characterise experimental results if the heated section deformed during a test. Table 2 summarises the experimental procedure used for these tests.

TABLE 1

NOMINAL INITIAL EXPERIMENTAL CONDITIONS FOR RD-14M LOCA TESTS

Primary System	Outlet header pressure	-	10 MPa(g)
	Input power	-	750 kW/pass
	Flow*	-	3.7 L/s
Secondary System	Steam drum pressure	-	4.5 MPa(g)
	Feedwater temperature	-	187°C

* Flow rates were determined based on the results of the CATHENA scoping analysis.

TABLE 2

EXPERIMENTAL PROCEDURE FOR RD-14M CRITICAL BREAK EXPERIMENTS

1. Evacuate, fill and de-gas the primary-side.
2. Pressurise primary-side to 2 MPa(g) and zero all instruments.
3. Raise power, pump speed and boiler levels to desired initial conditions.
4. Scan all instruments as a final check.
5. Start data acquisition system to collect at a rate of 0.1 second/scan
6. $t = 6 \text{ s}^*$, isolate the surge tank.
7. $t = 10 \text{ s}^*$, break valve opens.
8. $t = 12 \text{ s}^*$, ramp down power supplies if required

* For each experiment, steady-state data was collected for 60 s prior to initiating the break. These times have been referenced to a time 10 s prior to opening the break.

CATHENA

Code Description

CATHENA (Canadian Algorithm for THERmalhydraulic Network Analysis) is a one-dimensional thermalhydraulic code developed by AECL Whiteshell Laboratories (WL), primarily for the analysis of postulated accident conditions in CANDU reactors. The code uses a non-equilibrium, two-fluid thermalhydraulic model to describe the fluid flow. The thermalhydraulic model consists of six partial differential equations for mass, momentum and energy conservation - three for each phase. These conservation equations are coupled by a flow regime dependent set of constitutive equations defining the transport of mass, momentum and energy between the phases and between each phase and the pipe walls. In addition, the gas phase mass consists of the vapour and zero to four noncondensable gas components (non-condensable gases were not required for these calculations). The numerical solution method used is a staggered-mesh, semi-implicit, finite-difference method that is not transit-time limited.

The wall heat transfer model within CATHENA is referred to as the GENeralized Heat Transfer Package (GENHTP). GENHTP consists of three major modelling components: wall-to-fluid heat transfer, wall-to-wall heat transfer and conduction within solid models. Any number of GENHTP models can be coupled to one or more thermalhydraulic nodes. A set of flow-regime-dependent constitutive relations for heat transfer specify the energy transfer between the fluid and the pipe wall and/or fuel element surfaces. Heat transfer by conduction within the piping and fuel can be modelled in the radial as well as the circumferential directions. Radiative heat transfer and the zirconium-steam reaction can also be included (but were not required for these calculations). Built into this package is the ability to calculate heat transfer from individual groups of pins in a fuel bundle subject to stratified flow. Under these conditions the top pins are exposed to steam while the bottom pins are exposed to liquid.

Component models, which describe the behaviour of pumps, valves, steam separators, surge tanks and discharge through breaks, are available to complete the idealisation of a reactor or thermalhydraulic facility. A more complete description of the CATHENA code is available in Reference [2].

RD-14M Idealisation

CATHENA treats a pipe network as a series of connected pipe and volume components. Each pipe component has a uniform geometry along its length. The user can further divide each pipe component into a number of nodes. Since CATHENA is a two-fluid code, horizontal and vertical sections are generally modelled separately unless the sections are very short. Sections of piping that are inclined but vary in degree of inclination, were lumped together to simplify the idealisation.

The primary circuit nodalization is shown in Figure 4. The portion of the primary circuit below the headers consists of two identical passes of five heated channel per pass (for simplification, only one pass is shown). The idealisation was modified for these particular tests to reflect the single-channel per pass configuration (HS8 and HS13). The seven FES in each channel were modelled as three pin groups at a lower, a middle and an upper elevation within the channel. This allows heat transfer from the FES to the liquid and vapour during stratified flow conditions to be accurately represented. Heat losses to the environment from all piping, including the feeders, were modelled using imposed heat transfer coefficients and an ambient temperature of 20°C.

The RD-14M headers are divided into four sections to capture the effect of the volumes in the ends of the headers and any effects resulting from the axial distribution of feeder connections. The piping leading from the headers to the relief valves (over pressure protection) represents a significant volume and was included in the idealisation.

The RD-14M steam-generator secondary-side idealisation is shown in Figure 5. Components outside of the steam generator, such as the feedwater system and the jet condenser were not included in the idealisation. The effects of these systems on the steam-generator secondary-side conditions were included using time-dependent boundary conditions. The secondary-side control systems and heat losses from the steam generators were not included.

The primary-circuit loss coefficients were determined from RD-14M commissioning test data. Pressure-drop data from several steady-state single-phase liquid flow tests at various flow rates and temperatures were examined. For simple area changes between pipe components, the pressure drop calculated internally by CATHENA was in agreement with that observed in tests. For more complicated junctions (steam generator plenums and end-fitting simulators) however, the pressure drops measured were applied through junction resistances to achieve more accurate values. Pressure drop measurements were available only for the primary circuit. Standard handbook minor loss values were used for other circuits. A more complete description of the RD-14M idealisation is available in Reference [3].

RESULTS

Pre-test Simulations

For these simulations, the RD-14M idealisation was modified to reflect the single-channel per pass geometry of the experimental facility. The new input deck was used in a scoping analysis aimed at determining the pump speed (expressed as a percentage of full speed) required to obtain steady-state fluid temperatures of (approximately) 300°C in the outlet headers. These conditions would simulate normal operating conditions in RD-14M. Results of this analysis indicated a pump speed of 55% would produce those header temperatures.

The 55% pump speed was then used in subsequent simulations to determine the break orifice size required to produce a critical break in HS13. Simulations were run using 12, 13, 15, 16, 18 and 20 mm break sizes. Results indicated that a critical break behaviour could be obtained with any of the break sizes tested in combination with the 55% pump speed. Since an 18 mm orifice was available, experiment B9603 was conducted with an 18 mm break and a flow split was observed (see Figure 6).

Following the experiment, results were compared with the pre-test simulations from CATHENA (see Figures 7 to 12). The predictions of CATHENA compared reasonably well with the experimental results, with a few exceptions.

There were two discrepancies between the pressure drop predicted across the heated section of the broken pass and that measured experimentally, shown in Figure 7. Immediately following the break there was a severe dip in the header-to-header and channel differential pressures predicted by CATHENA. This severe dip was not observed experimentally. It is suspected the pressure dip occurred but was damped out by the first order response of the instrument. Somewhat later (Figure 7, 15-20 s), the experimentally measured header and channel pressure drops became substantially more negative than the code predicted. The latter problem seems to occur when steam from the test section is coming back through the header and out the break. The failure to accurately estimate this pressure drop may also explain why CATHENA was slow to predict the FES temperature quench (see Figure 12).

While the inlet and outlet flow rates predicted in the broken pass agreed with experimental values during the initial blowdown, deviations were noted several seconds after the break opened. It should be noted that the experimental flows are measured using bi-directional turbine flow meters calibrated to ± 6 L/s in single-phase liquid conditions. Since voiding occurs in the channel within the first few seconds of opening the break, the TFMs should be used to only indicate flow direction after the first couple of seconds.

Post-Test Simulations

A comparison of initial experimental conditions with the CATHENA steady-state model, revealed a few significant differences. The pump flows obtained in CATHENA, with the pump model set at 55% of full speed, were higher than the experimental values. In the experiment, the RD-14M pumps are manually adjusted so that exact settings are not possible. To resolve the difference, the actual percentage of the pump speed was calculated based on the full speed and the measured speed during the experiment. Experimental results showed this value to be 52.3% and the simulations were re-run with this value.

The power curve used in the pre-test simulations (taken from a previous experiment) was also slightly different than that for of the actual experiments. Following experiment B9603 the power curve used in CATHENA simulations was replaced with the measured power rundown. The results of this new simulation were compared with the experimental data as before and showed an improvement over results from the pre-test simulation.

A post-test simulation of B9605 (an 18 mm break with the power left on) was run to further evaluate the model. The CATHENA simulation was run with the power left constant until a trip at 35.3 s after the break opened (the time of the temperature-dependent trip in the experiment). The comparison of the predicted and experimental results, shows the code predicted most parameters quite well, with the exception of the top centre FES temperature (see Figure 13). In the experiment, the top centre FES temperature increased when the flow split point developed and quenched when flow likely reversed through the channel (Figure 13, 10-20 s). While CATHENA captured the initial temperature excursion, it did not capture this quench. This results in a conservative prediction by CATHENA.

Sensitivity Analysis

In an effort to more fully understand the thermohydraulic behavior during the RD-14M critical break experiments, a sensitivity analysis of several options available in CATHENA was performed. While the default code results provide a conservative estimate of FES temperatures, further investigation of differences between CATHENA and the experiments was desired.

The first of these trends was the dip in the ΔP curves. The influence of the condensation rate in inlet header 8 and the discharge flow through the break were investigated. These two aspects were examined independently by adjusting header modelling (condensation) and the discharge model. However, the calculated ΔP curves were insensitive to both the parameters.

A sensitivity analysis of the FES temperature profiles for experiments conducted with no power ramp was also conducted (Figure 13). It was believed that the code was not capturing the quench following the initial temperature excursion because the heat transfer was not large enough to allow the FES to cool below the rewet temperature. To examine the effect of post-CHF heat transfer the sensitivity of the FES temperature to the post-CHF heat transfer correlation was assessed. The code default post-CHF correlation, Groeneveld-Delorme [4], and an alternative, Bromley, was used in the study. The results showed that the Bromley correlation [5] were able to

capture the initial temperature excursion and quench and was able to delay the FES heat-up as seen in the experiment (see Figure 14). The code, however, did underestimate the magnitude of the excursion and delayed the FES heat-up following the quench longer than seen in the experiment. It was observed that the Bromley correlation appeared to capture the trend (though not the magnitude) during the first 19 s, and the Groeneveld-Delorme appeared to capture the heat-up rate in the latter part of the simulation. To examine this further, a simulation was run using the two correlations in the respective regions. It was found that this combination most accurately reflected the trends of the experiment (see Figure 14).

CONCLUSIONS

CATHENA was successfully used to help determine the experimental conditions (pump speed and break size) required to produce a critical break in a single-channel RD-14M. Post test simulation results agreed well with experimental data. Although not all behaviour was captured exactly, CATHENA provided a conservative estimate of peak sheath temperatures and accurately predicted the flow split point in the channel.

ACKNOWLEDGEMENTS

The experiments presented in this paper are funded by the CANDU Owners Group (COG).

REFERENCES

1. Melnyk, P.J. Ingham and T.V. Murray, Critical-Break Experiments in the RD-14M Thermalhydraulics Test Facility, 16th Annual CNS Nuclear Simulation Symposium, 1991 August 25-27, Saint John, New Brunswick.
2. Richards, B.N. Hanna and N. Hobson, The ATHENA Code: A Two-Fluid, Non-Equilibrium Code for One-Dimensional Transient Analysis of CANDU Reactors, presented at the 3rd International Conference on Reactor Thermalhydraulics, 1985 Oct. 15-18, Newport, RD.
3. Mallory, P.J. Ingham and T.E. MacDonald, CATHENA Idealisation - Documentation of the RD-14M Facility, COG-89-123, February 1990 (protected document).
4. Groeneveld, An Investigation of Heat Transfer in the Liquid Deficient Regime, Atomic Energy of Canada Limited Report, AECL-3281, 1969.

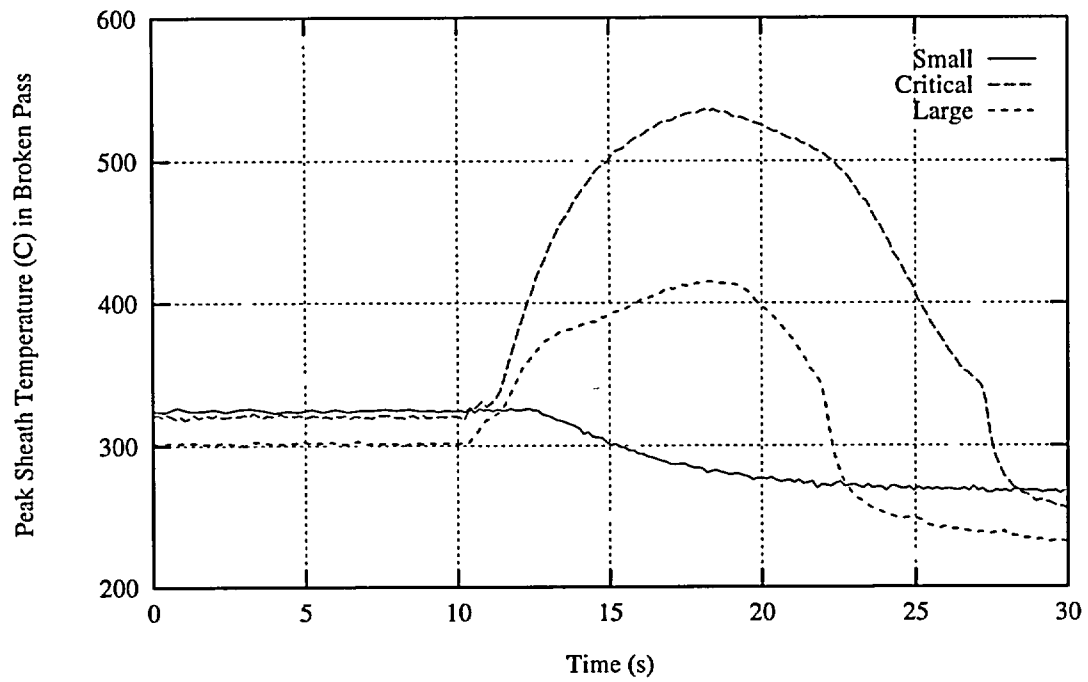


FIGURE 1: RD-14M Temperature Transients for Small, Large and Critical Breaks

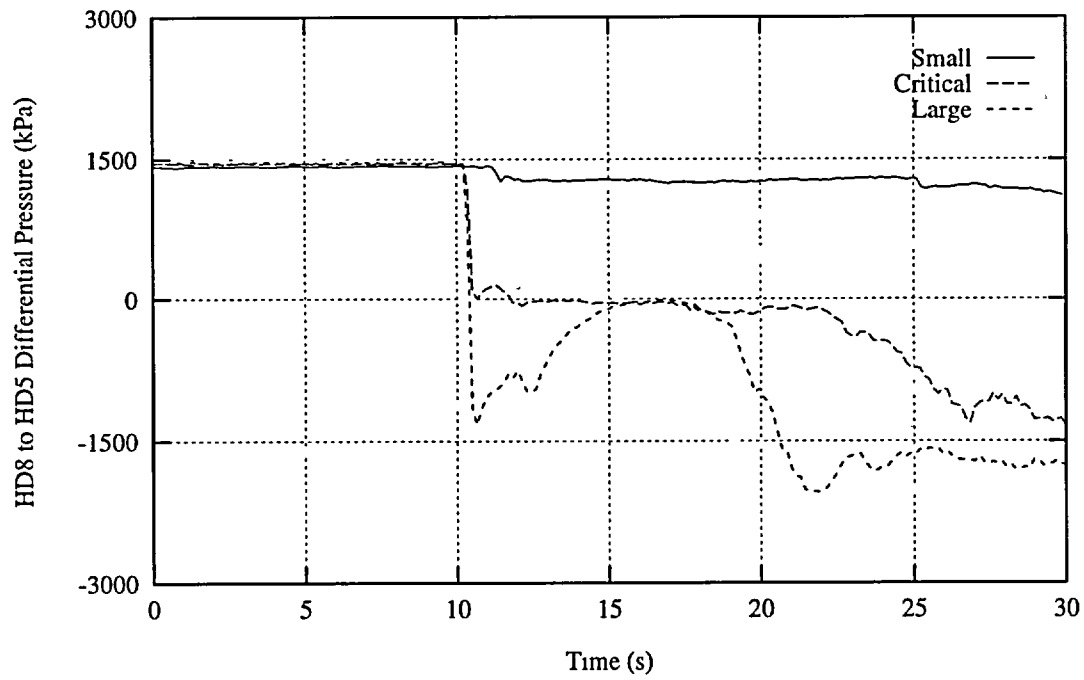


FIGURE 2: RD-14M Pressure Transients for Small, Large and Critical Breaks

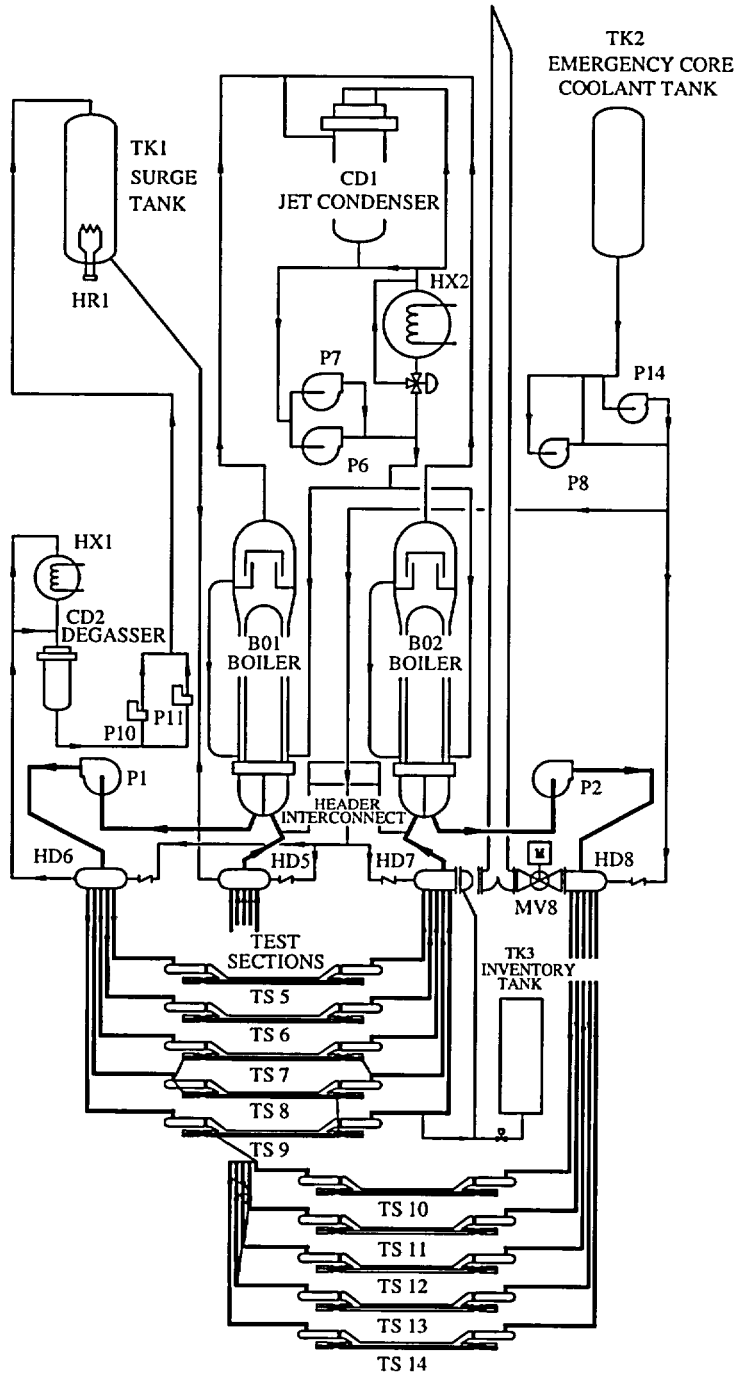


FIGURE 3: Schematic of RD-14M Facility

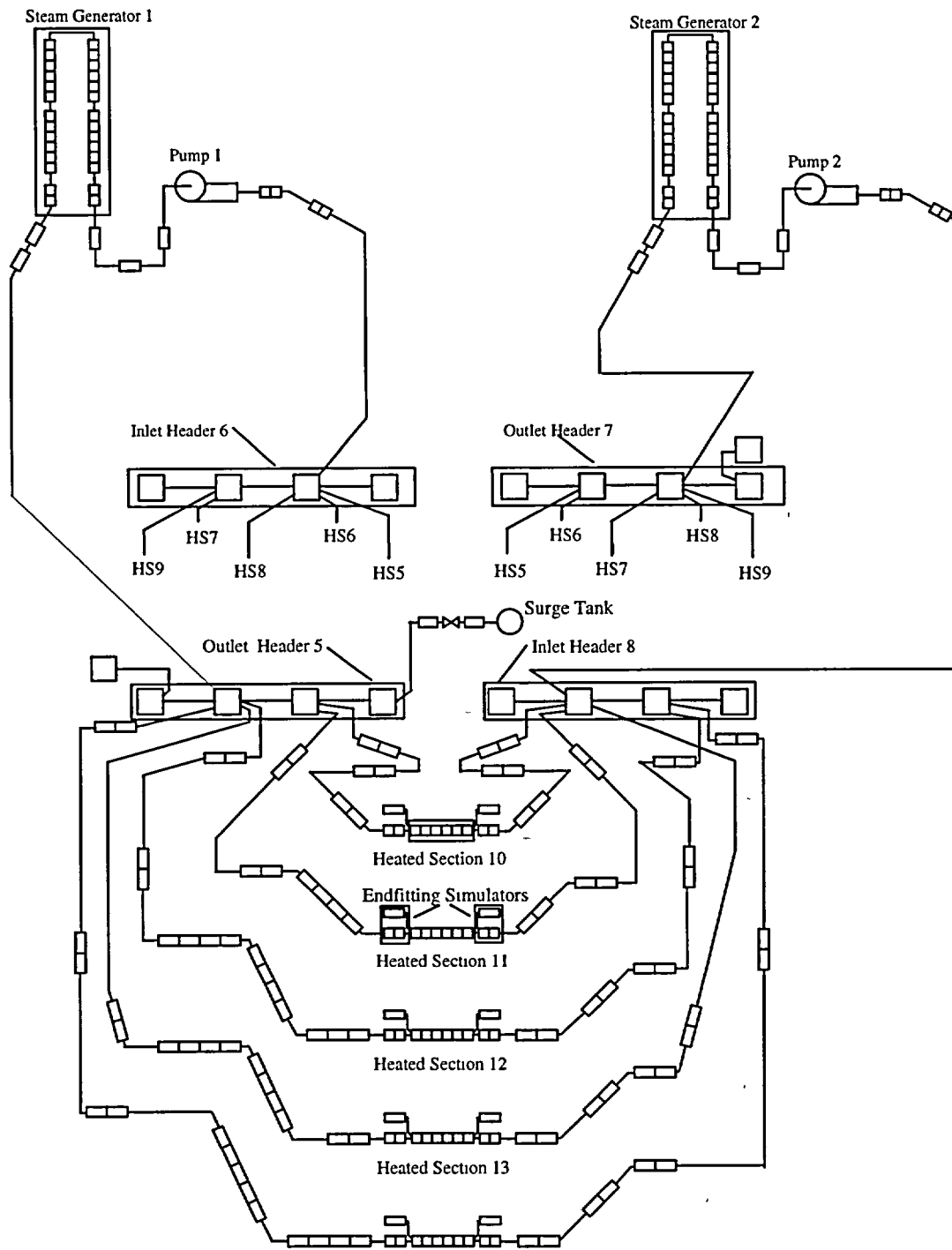


FIGURE 4: CATHENA Idealisation of RD-14M Primary Side

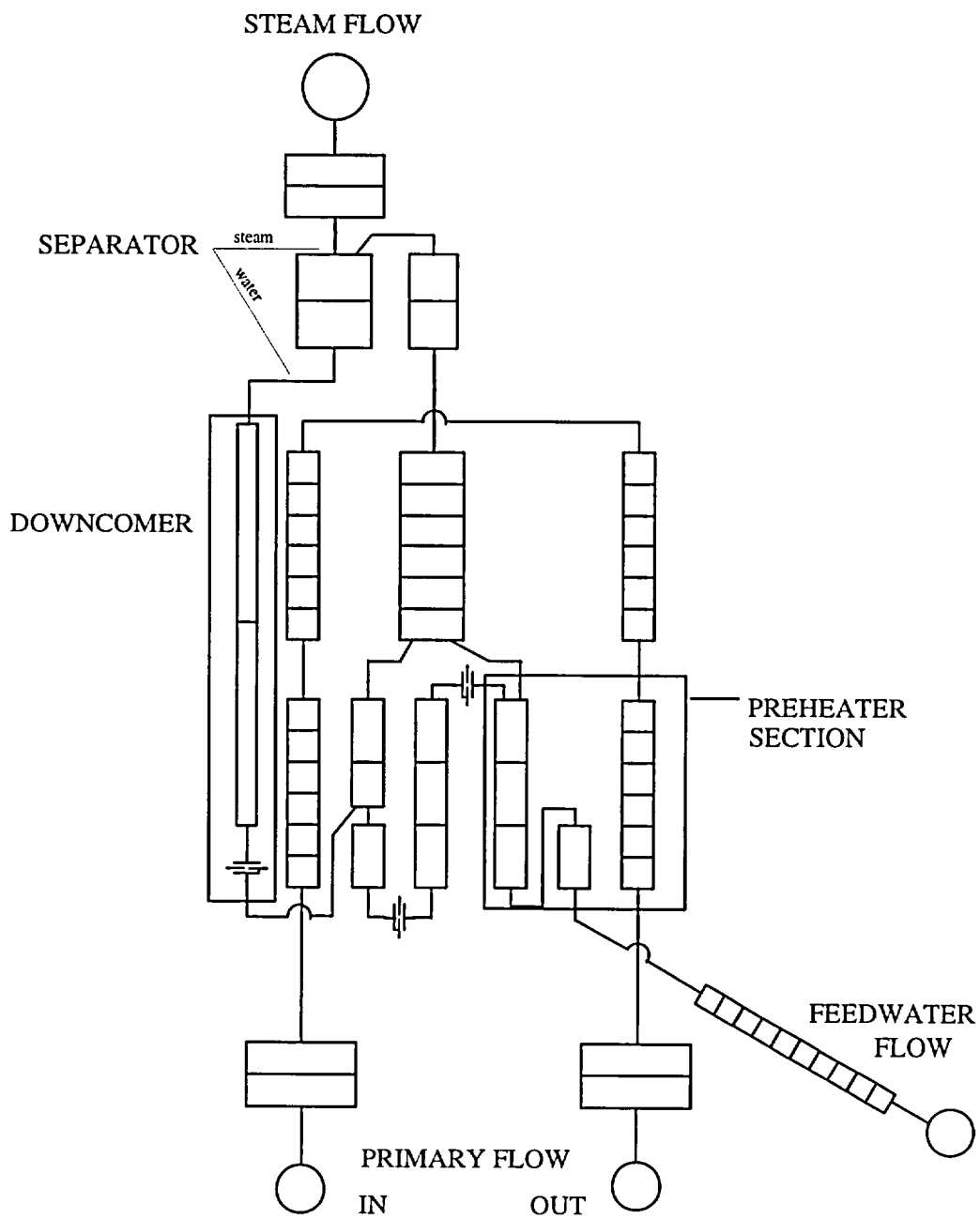


FIGURE 5: CATHENA Idealisation of RD-14M Secondary Side

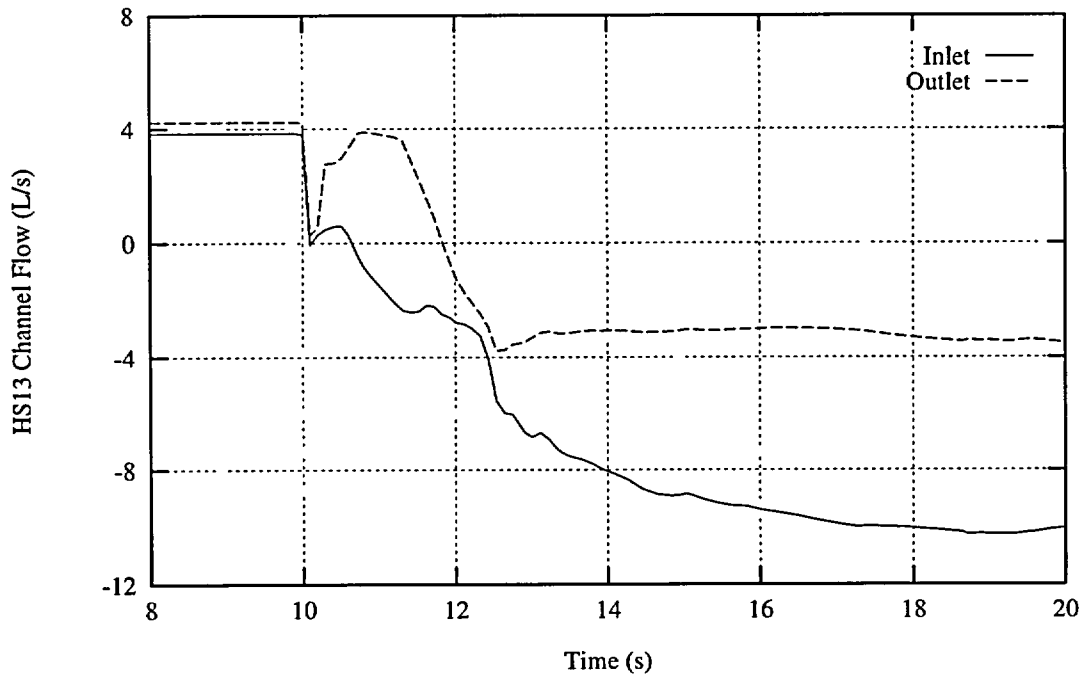


FIGURE 6: Break Size Scoping - 18 mm Break with 55% Pump Speed

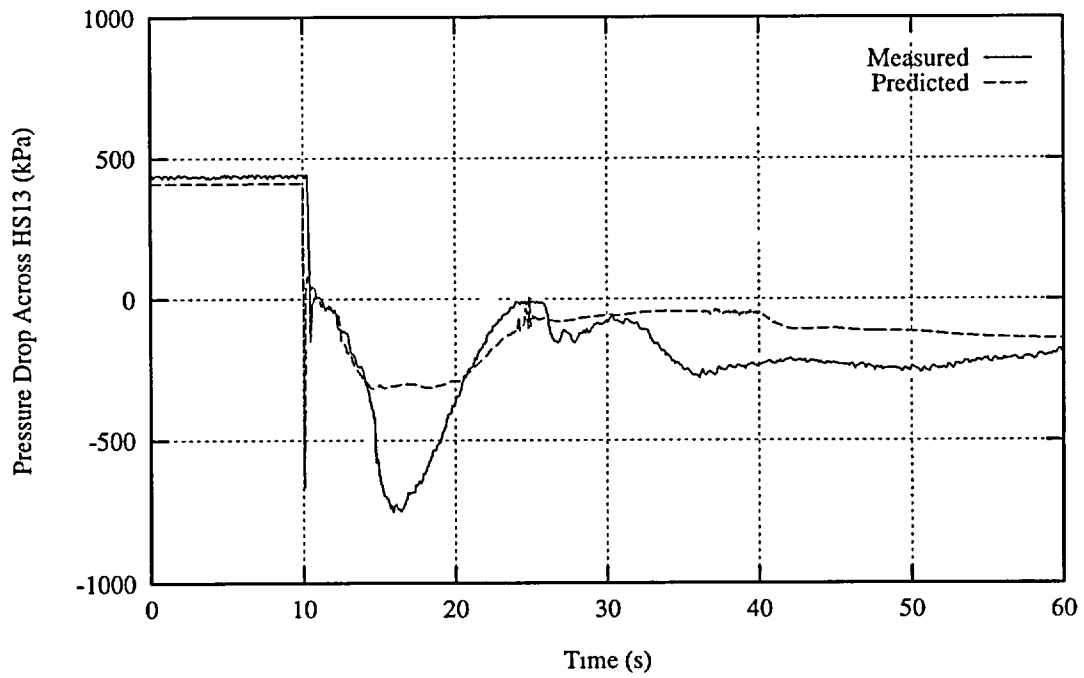


FIGURE 7: B9603 Pre-Test Simulation

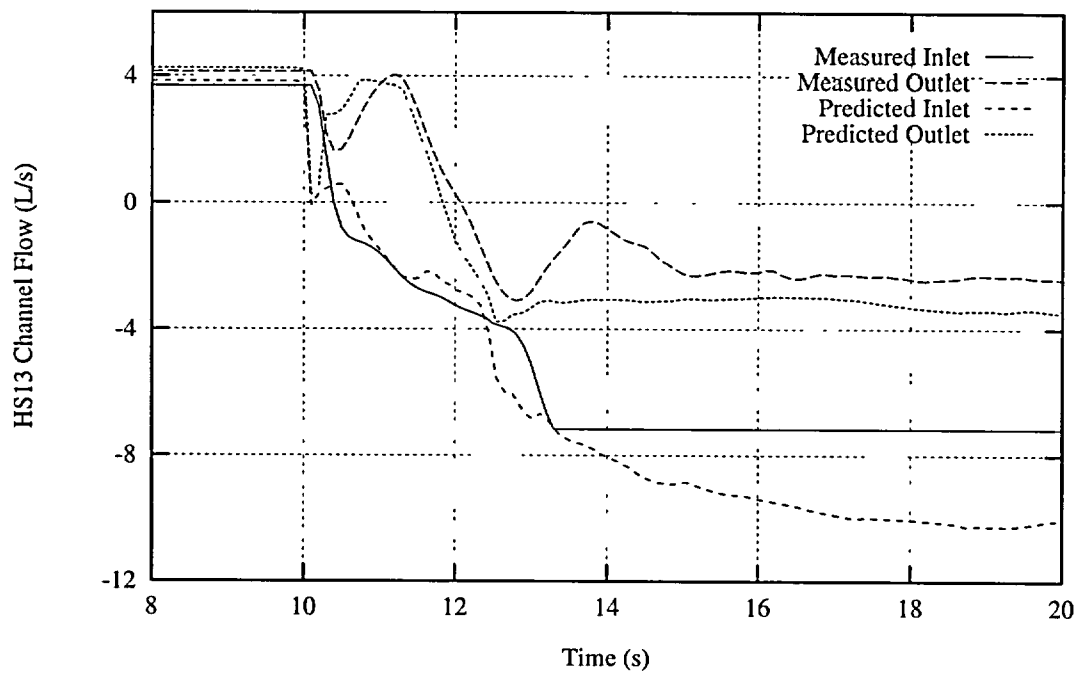


FIGURE 8: B9603 Pre-Test Simulation

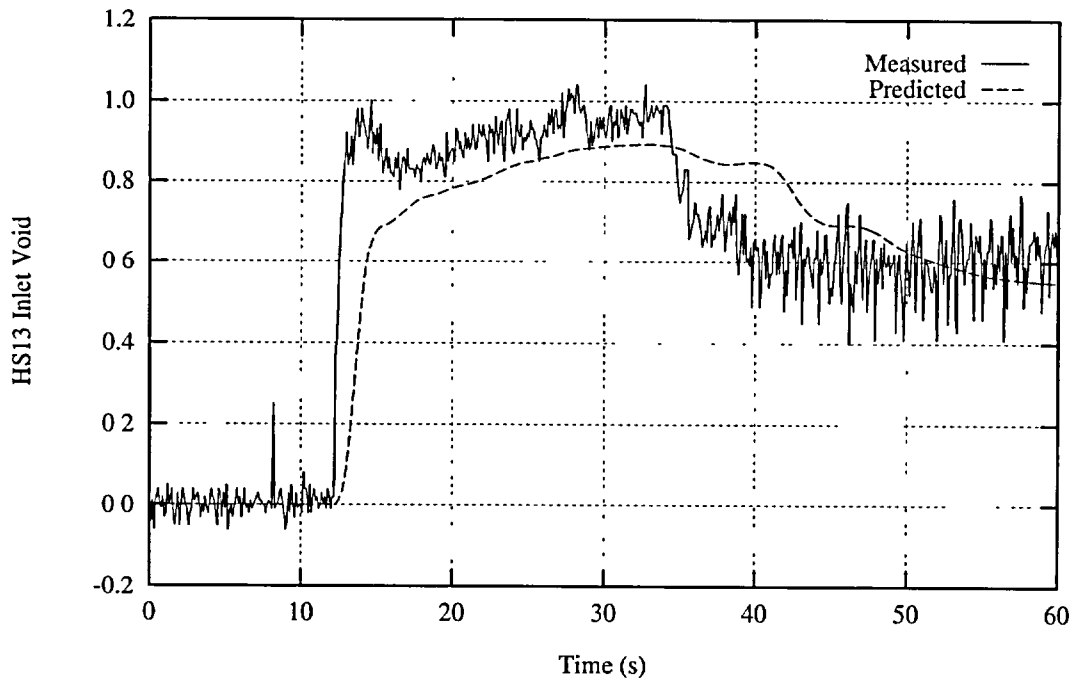


FIGURE 9: B9603 Pre-Test Simulation

FIGURE 11: B9603 Pre-Test Simulation

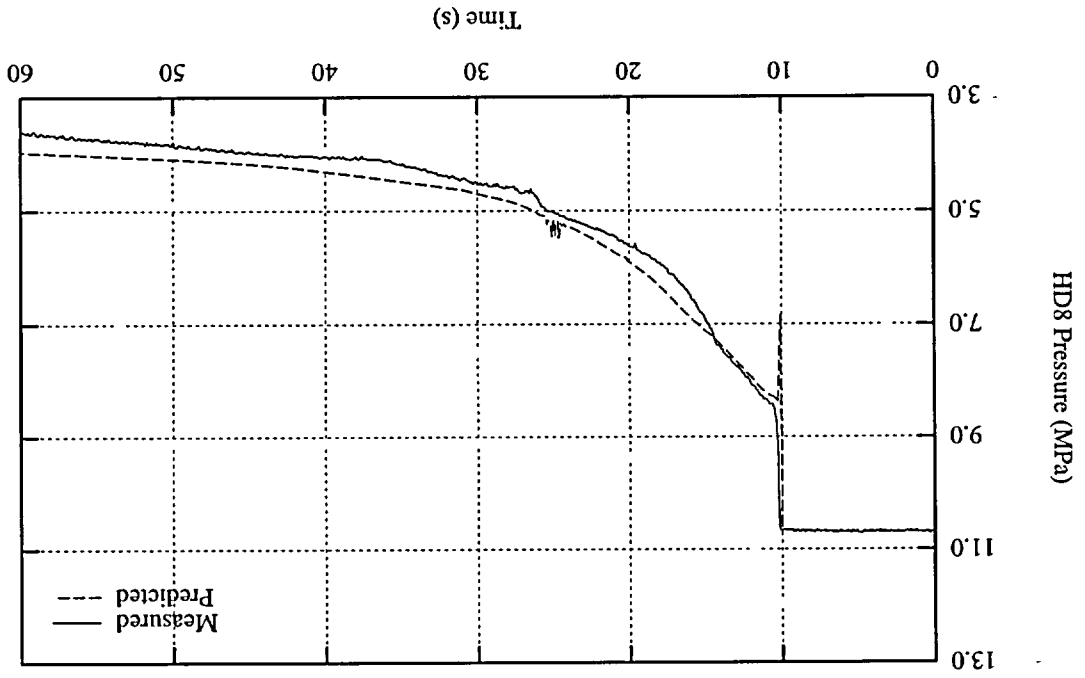
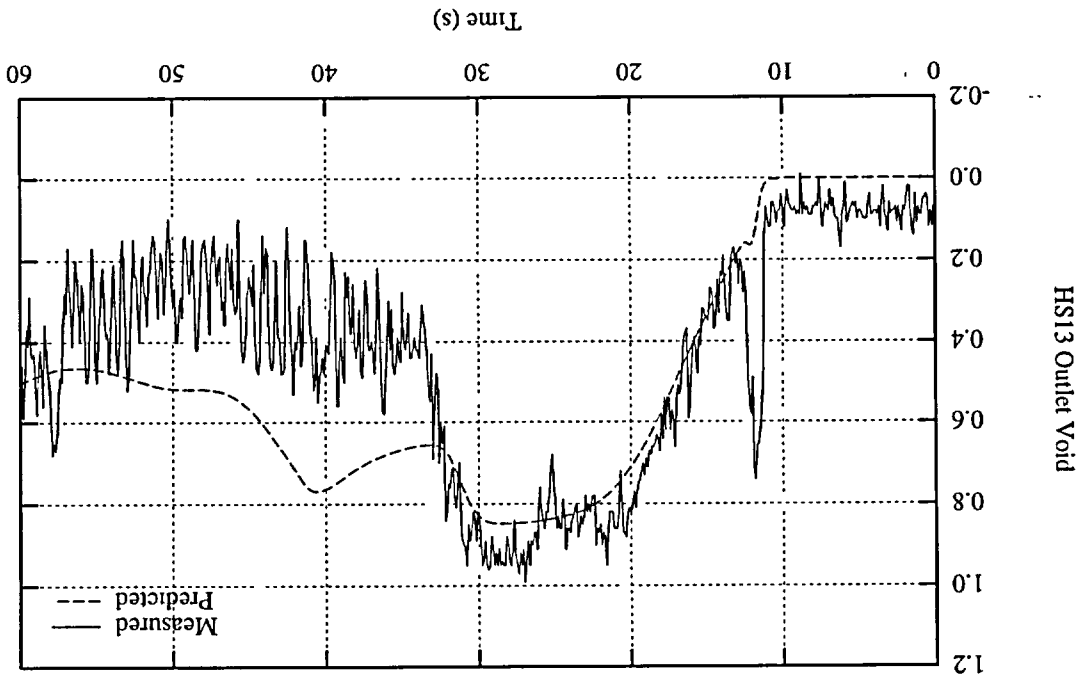


FIGURE 10: B9603 Pre-Test Simulation



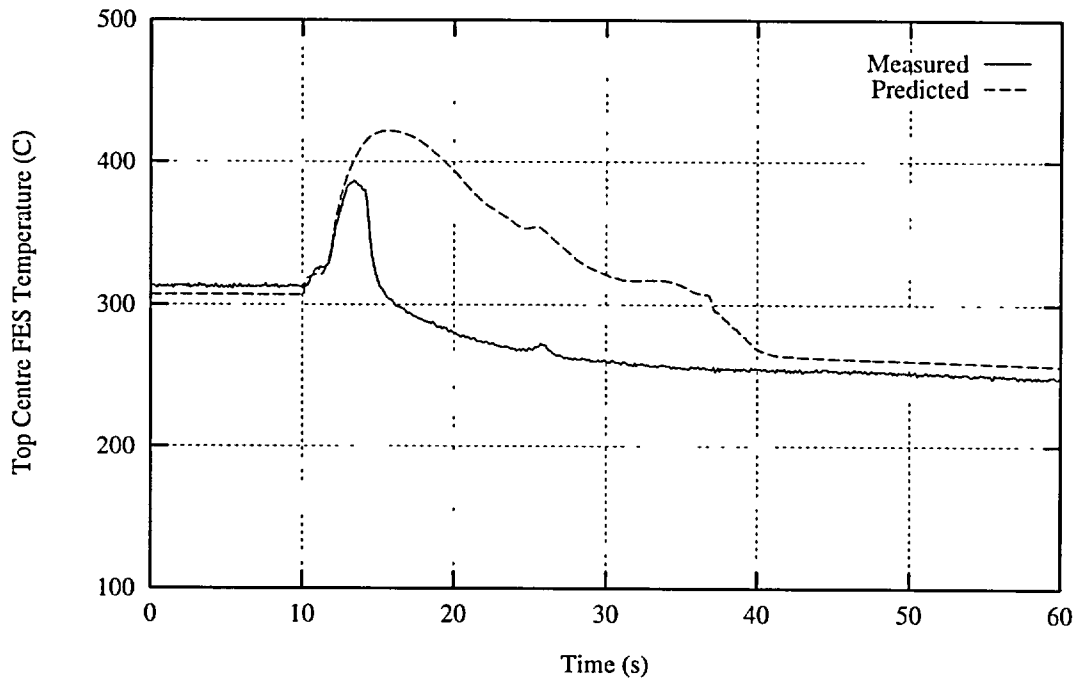


FIGURE 12: B9603 Pre-Test Simulation

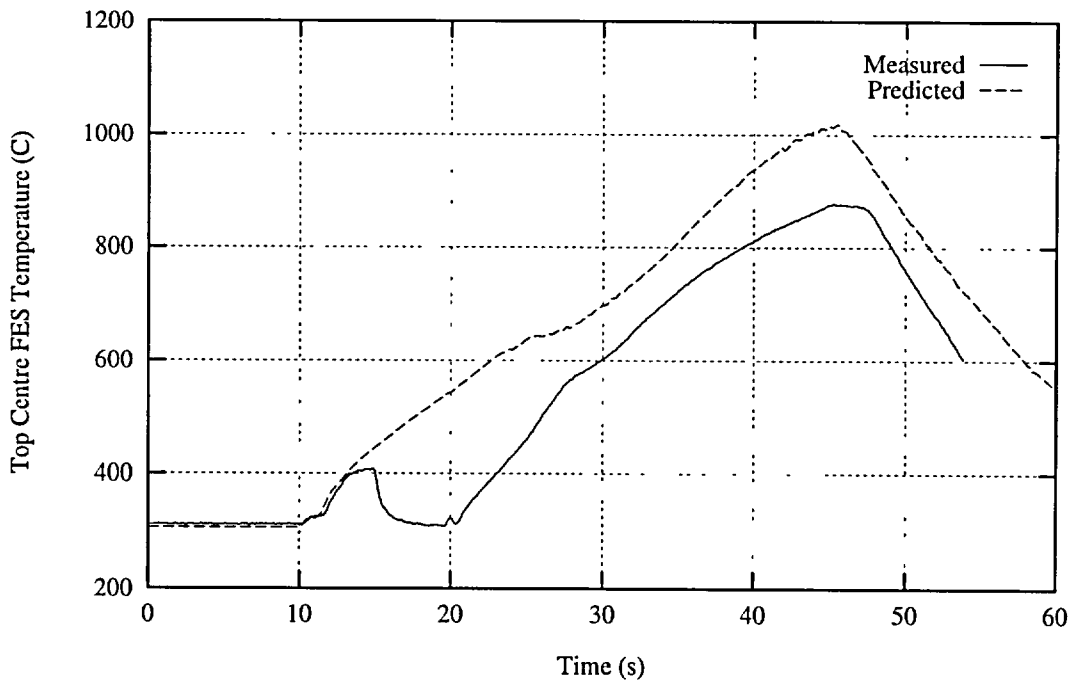


FIGURE 13: B9605 Post Test Simulation with Default Film Boiling Correlation

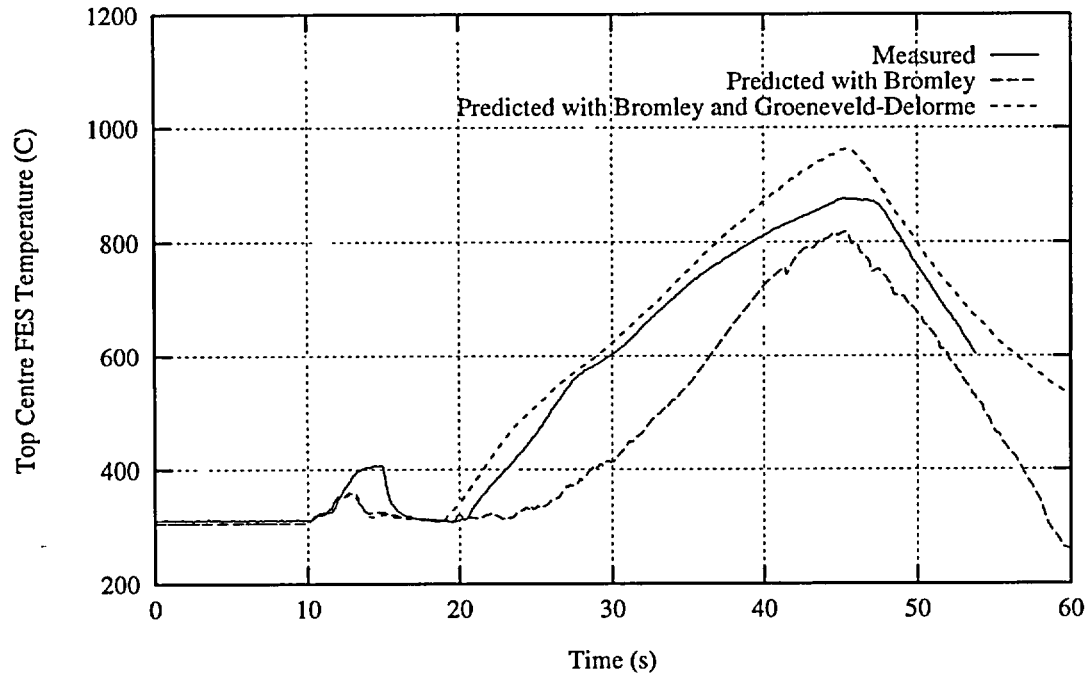


FIGURE 14: B9605 Post-Test Simulation with Bromley Correlation and with Combined Bromley and Default Correlations

POST-TEST ANALYSIS OF THE BTF-107 SEVERE-FUEL-DAMAGE EXPERIMENT USING THE CATHENA THERMALHYDRAULICS CODE

N.K. Popov and B.N. Hanna
AECL Research, Whiteshell Laboratories,
Pinawa, Manitoba, R0E 1L0, Canada

J.W. DeVaal, C. Wong, L.W. Dickson, R.J. Dutton and M.G. Jonckheere
AECL Research, Chalk River Laboratories,
Chalk River, Ontario, K0J 1J0, Canada

ABSTRACT

The BTF-107 (Blowdown Test Facility) experiment involved subjecting a bundle of three fully-instrumented CANDU-type (CANada Deuterium Uranium, registered trademark of AECL) fuel elements to a coolant depressurization while coolant conditions, fuel and sheath temperatures, fuel-element internal gas pressures, and fission-product release were monitored. During the experiment, the BTF-107 fuel assembly experienced a series of different conditions, including periods of dryout, rewet, rapid fuel-temperature escalation, relocation of material from the bottom portion of the fuel assembly, and final reflooding of the fuel channel.

A series of simulations of the BTF-107 experiment was conducted with the CATHENA code (Canadian Algorithm for Thermalhydraulic Network Analysis) after the experiment was completed to assess the influence of the various parameters affecting the thermalhydraulic behaviour of the experiment.

This paper summarizes the major events and conditions of the BTF-107 experiment, describes the CATHENA idealization of the BTF-107 loop, and discusses the most important results obtained in these simulations.

INTRODUCTION

In Canada, a significant research program is in place for determining the behaviour of CANDU fuel under various postulated accident conditions. One vital aspect of this research program is performing integrated "all-effects" tests on CANDU-type fuel to generate data for verifying and assessing computer codes used in safety analyses and licensing of CANDU reactors. Since data generated from in-reactor experiments are useful both for licensing current CANDU stations and for designing advanced CANDU reactors, this program is funded by the CANDU Owners Group (COG), a cost-sharing partnership between Atomic

Energy of Canada Limited (AECL) and the Canadian electrical utilities that own and operate CANDU reactors.

The principal experimental tool in Canada for performing in-reactor fuel safety experiments is the Blowdown Test Facility (BTF) [Walsworth J.A. et al., 1989] located in the NRU reactor at AECL's Chalk River Laboratories. Following the completion of commissioning experiments in 1989, the first loss-of-coolant accident (LOCA) experiment, BTF-107, was performed in 1990 November [MacDonald R.D. et al., 1991].

The BTF-107 experiment involved subjecting three fully-instrumented CANDU-type fuel elements, each operating at about 45 kW/m, to a coolant depressurization while coolant conditions, fuel and sheath temperatures, fuel-element internal gas pressures, and fission-product release were monitored. Following blowdown, the BTF-107 fuel assembly experienced a series of different conditions, including periods of dryout, rewet, rapid fuel temperature escalation, relocation of material from the bottom portion of the fuel assembly, blockage of the bottom of the fuel channel by relocated fuel debris, and final reflooding of the fuel channel. Some of these aspects of the experiment were not predicted to occur before the experiment was performed. Therefore, it is important that we develop an understanding of these phenomena.

The CATHENA code [Richards D.J. et al., 1985] was developed by AECL at Whiteshell Laboratories primarily for the analysis of postulated LOCAs in CANDU reactors. CATHENA uses a full two-fluid representation of one-dimensional two-phase flow in piping networks, resulting in different pressures, velocities and temperatures for the liquid and vapour phases. Interphase mass, energy and momentum transfers are specified using flow-regime-dependent constitutive relations obtained either from the literature or developed from separate-effects tests. The code includes properties of light and heavy water, and noncondensable gases may be included in the vapour phase. The code uses a

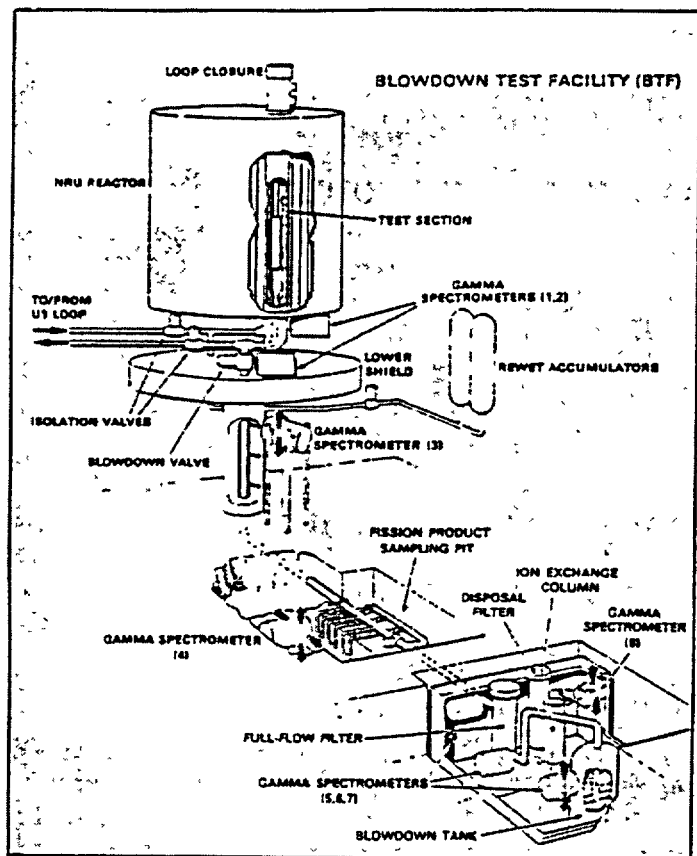


Figure 1: Schematic Representation of the Blowdown Test Facility

staggered-mesh, one-step, semi-implicit, finite-difference solution method, which is not transit-time limited. The mass/energy control volumes are called nodes and the momentum connections in an idealization are called links. The extensive wall heat-transfer package is general and allows the connection of multiple wall surfaces to a single thermalhydraulic node. CATHENA includes a variety of component models, such as pipes, pressurizers, tanks, pumps, valves, separators, etc.

A series of simulations of the BTF-107 experiment was conducted with CATHENA after the experiment was completed to assess the influence of the various parameters affecting the thermalhydraulics behaviour of the experiment [DeVaal J.W. et al., 1993]. These simulations were focused on the different phases of this very complex experiment, and were intended 1) to help us understand the thermalhydraulic phenomena that occurred in the test, and 2) to validate the code's capability to simulate these phenomena accurately.

DESCRIPTION OF THE BTF-107 EXPERIMENT

The BTF-107 experiment was designed to provide information on fuel and sheath behaviour and fission-product release from CANDU-type fuel elements operating at high sheath temperatures. The experiment was also intended to investigate the effects of cold water rewet on fuel behaviour and fission-product release.

Test Facility

Figure 1 shows a schematic drawing of the BTF, where the in-reactor test section is visible in the cutaway drawing of the NRU reactor [MacDonald R.D. et al., 1991]. The heart of this facility for performing severe-fuel-damage experiments is the vertical stainless-steel pressure tube in the reactor core, in which the experimental fuel stringers are located. During the pretransient steady-state irradiation, the fuel in the test section is cooled by flow from the U-1 loop, with pressurized water flowing over the fuel from top to bottom.

To initiate a transient, two isolation valves are closed to stagnate the coolant in the test section. The blowdown valve is then opened to depressurize the test section and allow the coolant to escape through the blowdown line into a sealed blowdown tank located in the basement of the reactor building. After depressurization, a low flow of superheated steam is established over the fuel to sweep fission products down the blowdown line past fission-product monitoring stations. Cold water from the rewet accumulators can be injected into the test section at any time during the accident sequence.

A schematic cross section through the fuel assembly portion of the BTF-107 fuel stringer is shown in Figure 2. The fuel assembly contained three CANDU-sized fuel elements positioned in a trefoil fuel carriage. All of the elements were fuelled with UO_2 pellets and were sheathed with Zircaloy-4. Two of the elements contained fresh fuel, whereas the third element had been previously irradiated to a burnup of 134 MWh/kg U. The carriage was constructed of Zircaloy-4 and had three empty sheath segments (dummy fuel elements) to space the fuel elements and reduce the coolant flow area.

The fuel carriage was located inside a thick-walled thermal shroud made up of a NILCRA (100% theoretical density ZrO_2) inner liner and a Zircaloy-4 clad ZIRCAR (21% density of ZrO_2) outer layer. This shroud was designed to protect the test-section pressure tube from high temperatures by limiting the radial heat transfer from the fuel.

Figure 3 shows a schematic of the BTF-107 fuel stringer. An important component of the fuel stringer was a debris retainer (or fuel catcher) located about 300 mm below the fuel carriage to catch large fragments that might fall from the fuel assembly during a test. This debris retainer was constructed entirely of NILCRA and consisted of a sieve plate containing a large number of small holes located at the bottom of a NILCRA-lined cavity. The deposition tube, shown downstream of the fuel catcher in Figure 3, was designed to collect cumulative aerosol deposits at various elevations.

Figure 3 shows the direction of fluid flow through the fuel stringer. The coolant flows upward inside the pressure tube, and enters the re-entry tube via the coolant ports. At this location, the flow turns downward and splits between the re-entry tube (30%) and the fuel channel (70%).

The stringer and fuel assembly were extensively instrumented for this test [MacDonald R.D. et al., 1991]. Temperatures of the element sheaths, the carriage, carriage ribs, shroud, coolant and pressure tube were measured during the experiment, as well as the coolant pressure and the internal pressures of the two fresh elements.

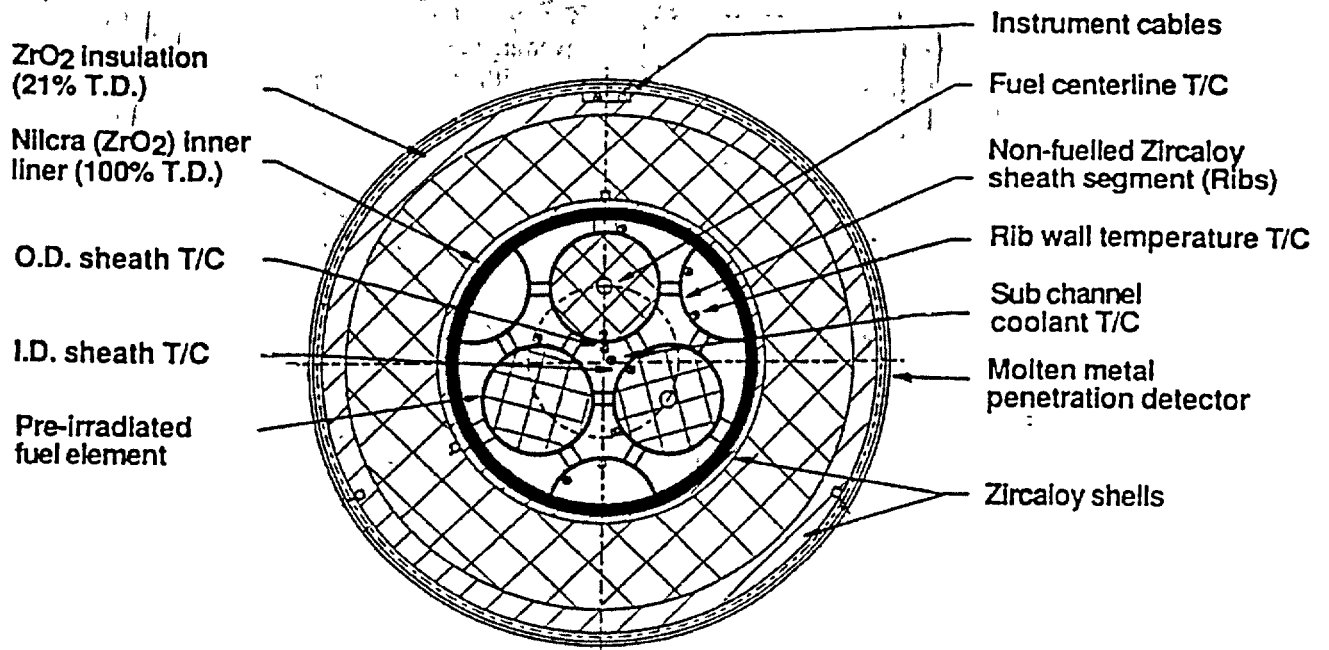


Figure 2: Schematic Cross Section Through the BTF-107 Fuel Stringer

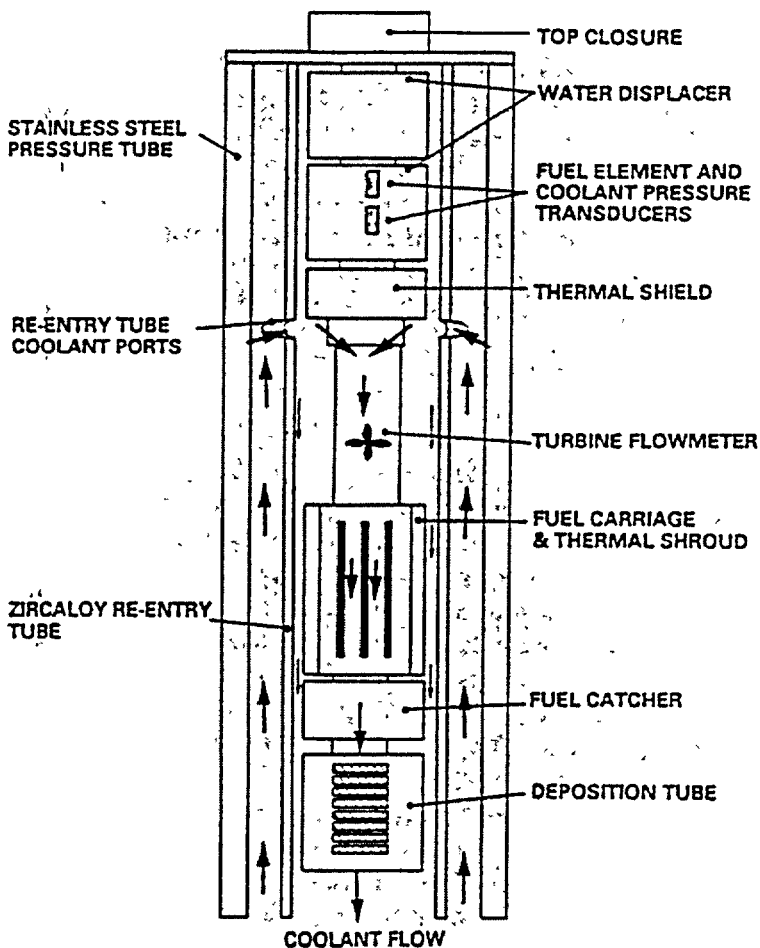


Figure 3: Schematic Drawing of the BTF-107 Fuel Stringer

Test Objectives

The BTF-107 experiment was designed to represent the behaviour of CANDU fuel located in a reactor fuel channel for the case of a rapid blowdown followed by a prolonged period of dryout at full reactor power, and terminated with a rewet by emergency core cooling [MacDonald R.D. et al., 1991]. Specific objectives of the experiment were to a) determine the amount and distribution of sheath strain in fuel elements operating at sheath temperatures between 1200 and 1400 °C, b) establish the timing and mechanisms of fuel element failure, c) measure the release of fission products from the damaged elements, d) characterize the behaviour of the fuel and sheath oxidation, and e) determine the effect of a cold water quench on fuel integrity.

The scenario planned for the experiment was a blowdown from pressurized water cooling conditions with fuel operating at a linear power of about 60 kW/m (full reactor power). This reactor power was to be maintained until any part of any sheath reached a temperature of 1350 °C. At this point, the reactor would be shut down and a cold water rewet would be initiated manually when sheath temperatures drop below 900 °C.

As a backup to the manual control of the experiment and as a safety feature, three sheath thermocouples, three inner shell shroud thermocouples and three pressure-tube thermocouples were wired into the reactor safety circuits. The sheath and shroud safety circuits were programmed to shut down the reactor and initiate rewet if two out of three of the thermocouples exceeded preset temperature limits. These limits were 1450 °C for sheath temperatures and 1250 °C for the shroud. If two out of three pressure-tube temperatures exceeded 417 °C, the reactor would also be shut down, but rewet would not be initiated.

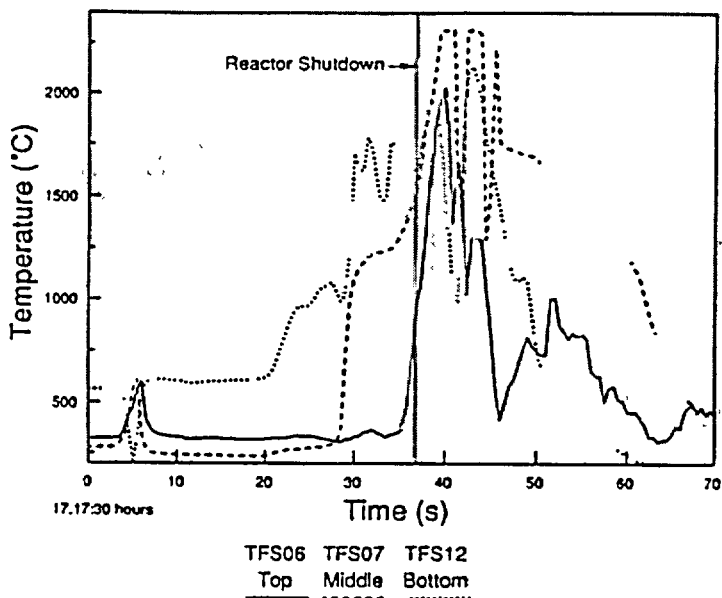


Figure 4: Sheath temperatures Measured at Top, Middle and Bottom Elevations During the BTF-107 Transient

Test Procedure and Observations

Prior to the blowdown, the fuel elements were operating at linear powers of about 41 kW/m (fresh fuel elements) and 43 kW/m (irradiated fuel element) in pressurized water at 9.6 MPa and 250°C. At the time of the transient, the fresh fuel elements contained small defects (likely from failed internal instrument penetrations), whereas the previously irradiated element was intact.

Figure 4 shows the measured behaviour of selected sheath thermocouples during the transient. Zero time in the figure corresponds with the time when the blowdown sequence was initiated. After 3 s, the BTF test section was fully isolated, and the coolant stagnated. Since the elements were operating at nominally full power, this stagnation caused a dryout of the fuel elements, with sheath temperatures quickly rising to about 600°C just before the blowdown. This is evident in the response of thermocouples TFS06 and TFS07 over the first 5 s in Figure 4; TFS12 is not representative over this period, likely because of water ingress at the measurement junction. The locations of the thermocouples TFS06, TFS07 and TFS12 were not in the same subchannel. A subchannel is defined as a portion of the flow area of the fuel channel bounded by the fuel sheaths and the spacer ribs (see Figure 2).

Once the blowdown was initiated (at 5 s in Figure 4), flow over the fuel rapidly increased as the test section depressurized. This increased flow caused the fuel to rewet and the elements then remained well cooled for the first 10 to 15 s of the blowdown.

As the test section inventory declined and the flow slowed, intermittent dryout was observed, as shown in Figure 4, beginning at the bottom of the fuel elements (at 20 s) and moving upward along the length of the elements over a period of about 15 s. The post-dryout behaviour at the bottom of the elements shows a sharp increase in temperature (noted by TFS12 at 28 s) as the middle of the elements pass into dryout (noted by TFS07), indicating that

the coolant temperature increased significantly as it passed over the fuel.

With the rapid increase in sheath temperatures at the bottom and middle of the elements, two events occurred in quick succession. The first was a sudden increase in the measured pressure drop across the test section at 36 s in the test (by about 2.2 MPa, indicating that a flow blockage had occurred in the test section). This was followed about a second later (at 37 s in the test) by an automatic reactor shutdown and the initiation of a cold-water rewet triggered by high sheath temperatures. Figure 4 shows a rapid increase of sheath temperatures at all elevations. The temperature increase continued after reactor shutdown, indicating a significant contribution to sheath heating from Zircaloy oxidation.

The rewet water reached the fuel assembly about 4 to 5 s after the reactor shutdown. The initial cooling of the fuel may have been by steam pushed ahead of the rewet front. All sheath temperatures decreased sharply as the rewet water arrived, but the effect was brief as it is believed that the injected water vaporized and formed a steam bubble above the fuel. Because the normal flow path through the carriage was now blocked, this expanding steam bubble momentarily backed up the inlet flow path, resulting in temperature spikes on upstream coolant thermocouples and disruption of the accumulator discharge. This rewet and evaporation cycle repeated several times with decreasing severity, with rewet eventually cooling the fuel over a period of about 25 s.

SIMULATIONS WITH CATHENA MOD-3.3

Simulations of the BTF-107 experiment with the CATHENA code were conducted to better understand the conditions that were observed in this experiment, and to validate the CATHENA code's capability to simulate complex thermalhydraulic and heat transfer phenomena.

In order to simulate these experiments we had to idealize the experimental loop, and to provide boundary and initial conditions.

Test Loop Idealization

Figure 5 shows the idealization of the BTF-107 loop used in these simulations. This idealization consists of two major groups of elements: the fuel stringer and the rewet line. CATHENA is a one-dimensional code that models various loop components, such as pipes, using a one-dimensional representation. Having available experimental measurements of pressure and flow at various points in the loop, we were able to idealize a portion of the BTF-107 loop (shown in Figure 1) by introducing boundary conditions at those locations.

The fuel stringer (schematically shown in Figure 3) consists of three vertically oriented and interconnected flow paths: the pressure tube, the re-entry tube and the fuel channel. These flow paths were modelled by a group of pipe components (shown as rectangles in Figure 5) and connected by appropriate links. Figure 5 indicates the portion of the fuel stringer located in the core.

The fuel stringer was connected to the main inlet and main outlet of the loop in the idealization by a group of horizontal pipes arranged to represent the loop inlet and loop

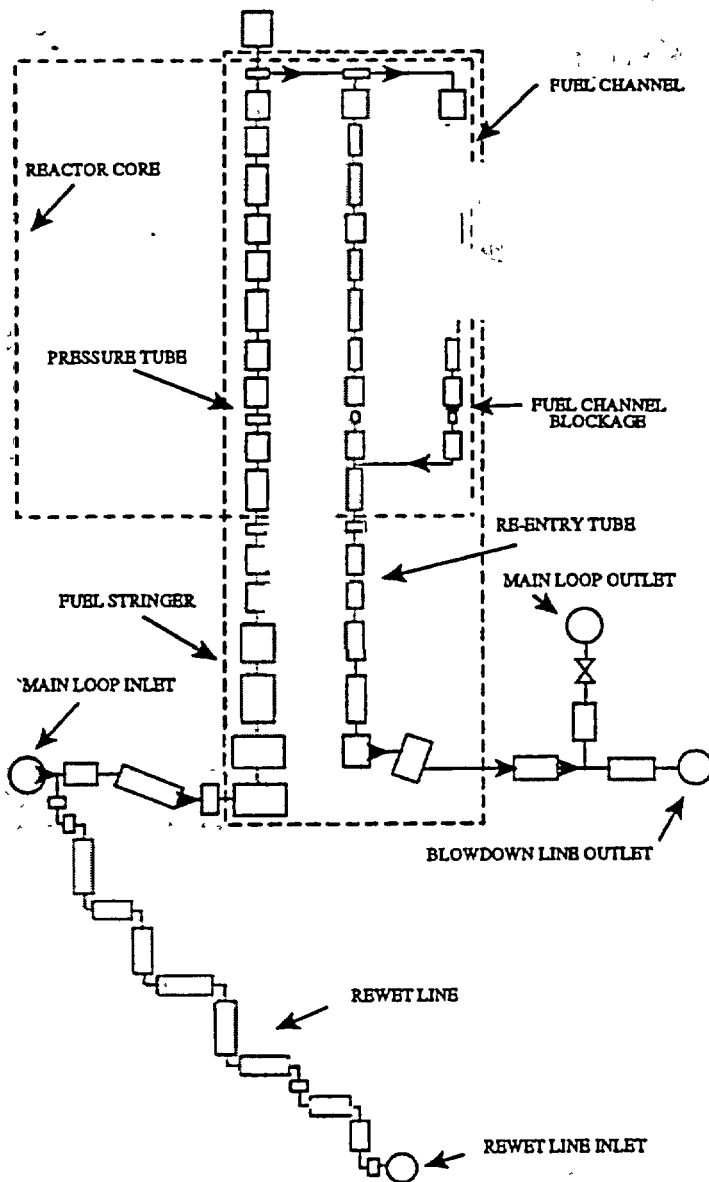


Figure 5: CATHENA Idealization of the BTF-107 Experimental Loop

outlet piping. Also, a horizontal group of pipes was used in the idealization to represent the entrance into the blowdown line. The rewet line was represented by a group of vertical and horizontal pipes. The axial length of every section of the loop piping in the idealization was selected to represent the portions of the flow paths that had approximately uniform cross-sectional area.

Experimentally derived boundary conditions (shown as circles in Figure 5) were applied at loop ends to represent the influence of non-modelled portions of the loop. These boundary conditions specified information about pressure or flow at the points of application.

Flow resistances were introduced at certain pipe locations in the idealization to produce the flow split of 30%/70% between the re-entry tube and the fuel channel observed during the steady-state operation.

In post-test examinations of the fuel stringer, a quantity of relocated material (likely a U/Zr/O₂ alloy) was observed blocking the fuel catcher sieve plate. During the experiment, a rapid increase of the pressure drop across the loop was

observed beginning at 34 s in the experiment. This pressure drop increase was attributed to the development of the flow blockage which reduced the fuel channel area, and increased the flow resistance. To model the development of this blockage in the simulation (while maintaining the same flow area of the fuel channel) a flow resistance was introduced in the fuel channel at the location of the fuel catcher (denoted in Figure 5 as "fuel channel blockage"). This flow resistance was adjusted to obtain a reasonable agreement between the measured and calculated pressure drop along the loop.

Two-dimensional wall heat-transfer models (in the radial and circumferential directions) were used to calculate heat transfer between the loop components. Within the reactor core, there was one wall heat-transfer model between the fuel channel and the re-entry tube (to account for the heat-transfer through the fuel shroud), one wall heat-transfer model between the re-entry tube and the pressure tube (to account for the heat-transfer through the re-entry tube wall) and one wall heat-transfer model at the outside of the pressure tube (to account for the heat-transfer through the pressure tube wall). A separate set of wall heat-transfer models was provided for the fuel elements and the fuel carriage of the fuel stringer located in the fuel channel.

Radiation heat transfer was modelled at every axial level between the fuel elements and the thermal shroud. This was necessary to account for the heat transfer by radiation when the fuel channel was voided and the fuel elements were hot.

Initial and Boundary Conditions

Boundary conditions were applied at certain points in the idealization (shown by circles in Figure 5) to specify the influence of the rest of the loop. At the loop main outlet and the blowdown line outlet locations, pressure boundary conditions were applied (using the measured pressure at these locations in the experimental loop). At the loop main inlet and the rewet line inlet, flow boundary conditions were applied using the measured mass flow rates.

A steady-state simulation was performed before running the transient simulation to obtain the initial conditions at all locations in the loop. The required initial conditions consisted of pressure, temperature, and void fraction for all nodes, and velocities for all links in the idealization.

DISCUSSION OF SIMULATION RESULTS

The analysis of the simulation results covers the observed behaviour during a) the initial blowdown phase of the experiment (flow stagnation and first dryout), b) the prolonged dryout and subsequent rapid fuel heatup (with material relocation), and c) the final rewet phase of the experiment. Figures 6 through 10 show a comparison of measured and simulated temperatures during the initial phase of dryout and subsequent fuel heatup. Figures 11 and 12 show a comparison of temperatures during the rewet phase of the experiment.

The initial period of blowdown started at 3 s in the transient, with isolation and stagnation of the loop; this was followed by first dryout and then rewet, lasting until about 23 s in the transient. The phase of prolonged dryout and rapid fuel heatup started at about 23 s in the transient and ended at about 29 s, when emergency coolant injection in the

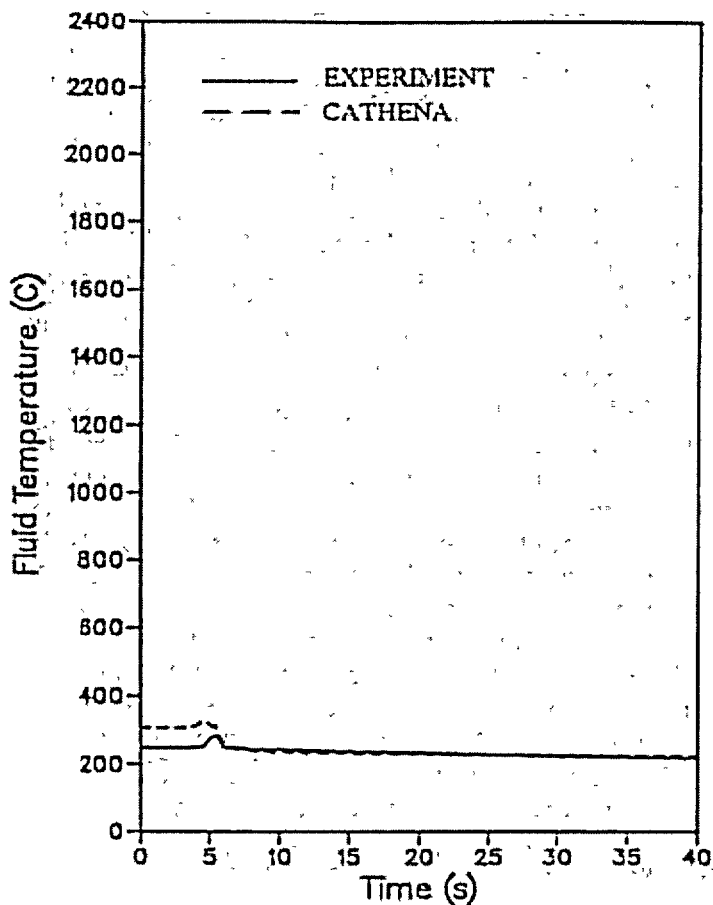


Figure 6: Fluid Temperature at the Top of the BTF-107 Fuel Channel

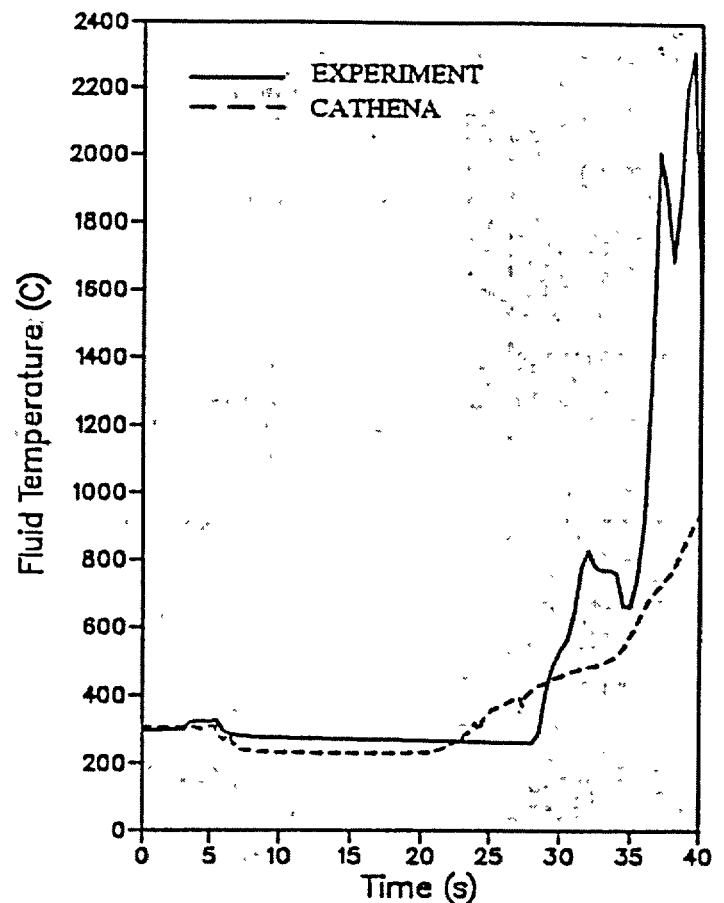


Figure 7: Fluid Temperature at the Bottom of the BTF-107 Fuel Channel

loop was initiated. The period of final rewet ended at about 70 s in the transient, when the fuel channel was completely rewetted.

All thermocouples located at the bottom elevation of the fuel assembly failed in the experiment, because of rapid heatup and material relocation. Therefore, these measurements are not used in this paper, and the calculated bottom sheath temperatures are not analyzed.

In the simulation presented in this paper, a flow blockage of 98% was applied after 34 s in the transient. This amount of flow blockage was determined as a result of a sensitivity study.

The Flow Stagnation and the Blowdown Phase

Fluid Temperatures. Figures 6 and 7 show a comparison of measured fluid temperatures and calculated steam temperatures at the top and bottom elevations of the fuel assembly. Note that the initial calculated steam temperature in Figure 6 (the first 5 s of the simulation) is higher than the measured fluid temperature because this was a period of single-phase liquid flow.

The temperature calculation at the top elevation agrees very well with the experiment, and indicates that there was no evidence of reverse flow during the transient (i.e., no heatup of the passing steam flow was calculated and none was observed in the experiment).

The temperature at the bottom elevation (Figure 7) was correctly calculated to rise slightly at about 5 s, during the period of flow stagnation. When the blowdown line opened and discharge flow was established, the calculated steam temperature decreased. The calculated steam temperature in this period was less than the measured temperature because the calculated discharge flow rate was larger and the calculated pressure at this location was lower than in the experiment.

Figure 7 shows that at about 22 s the code calculated the steam temperature to increase. This indicates that the code calculated the initiation of the phase of prolonged dryout earlier than it was observed in the experiment. The reason for this was the overestimation of the discharge mass flow rate, which resulted in earlier depletion of the loop. The calculated rate of the steam temperature rise in the period of prolonged dryout and rapid heatup was not as high as measured in the experiment. This disagreement was attributed to possible changes in the geometry of the fuel assembly and the overestimation of the heat transfer by radiation.

Sheath Temperatures. Figures 8, 9 and 10 show fresh fuel and irradiated fuel sheath temperatures during the initial phase of flow stagnation and the blowdown phase followed by a prolonged dryout.

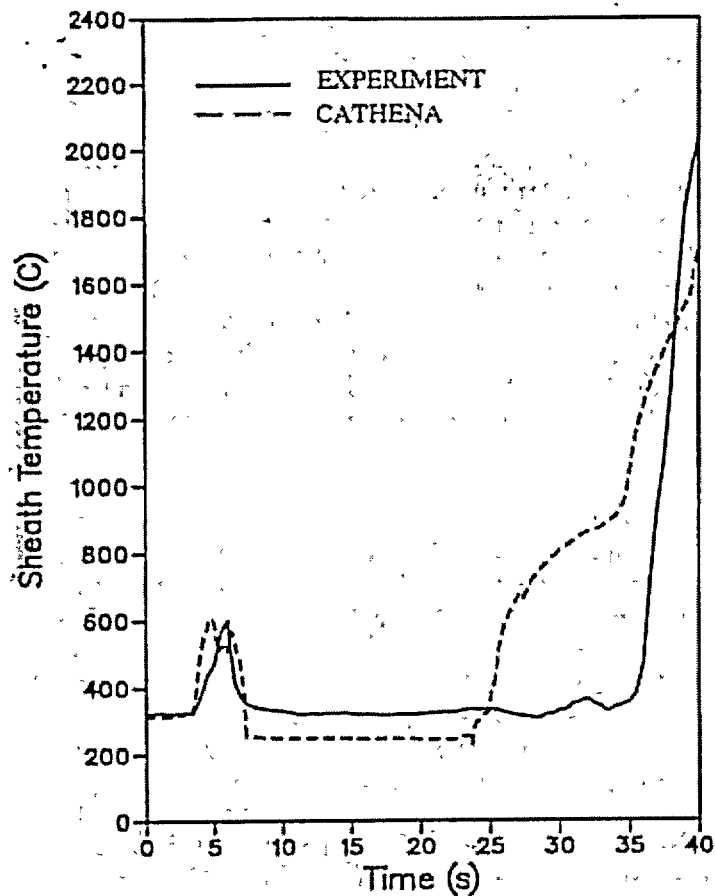


Figure 8: Sheath Temperature at the Top of the BTF-107 Fresh Fuel Element

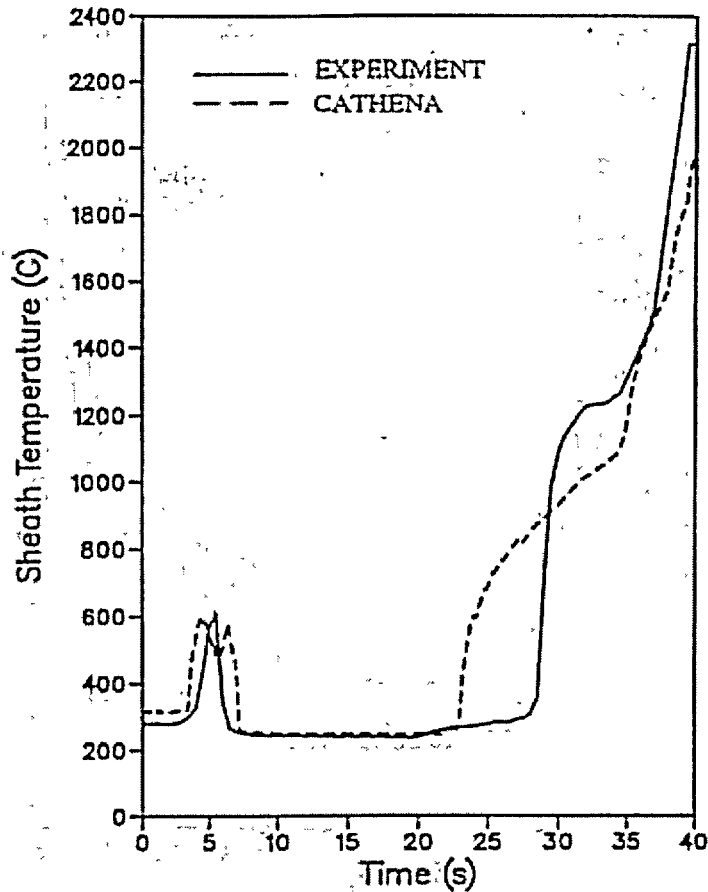


Figure 9: Sheath Temperature at the Middle of the BTF-107 Fresh Fuel Element

The calculated fuel (fresh and irradiated) sheath temperatures at the top elevation and middle elevation agreed very well with the measured temperatures during the period of flow stagnation. At about 3 s into the transient the sheath temperature increased to about 600°C as a result of loss of flow in the fuel channel and voiding. After the blowdown valve was opened (at about 5 s), the calculated sheath temperature decreased at 7 s into the transient as cooling resumed.

During the blowdown phase (from 7 s until 24 s in Figure 8) the calculated top sheath temperature of the fresh fuel was lower than the measured temperature. However, the calculated middle sheath temperature of the fresh fuel element (Figure 9) agreed very well with the measured temperature. The calculated sheath temperature at the middle elevation of the irradiated element (Figure 10) had a trend similar to that of the calculated temperatures of the fresh fuel elements. The measured sheath temperature at the middle elevation of the irradiated fuel element indicates that the measurement was in error during the flow stagnation phase and the blowdown phase, perhaps because of water ingress at the measurement junction.

The CATHENA results indicate a premature increase of sheath temperatures at all elevations during the phase of prolonged dryout at about 24 s in the transient (Figures 8, 9 and 10), whereas in the experiment this was not observed until 35 s. The reason for this discrepancy was the higher calculated discharge mass flow rate than was observed in the experiment, resulting in earlier depletion of the loop liquid inventory.

A comparison of Figures 8, 9 and 10 shows that the code calculated a sheath temperature increase during the period of prolonged dryout at approximately the same time for all elevations in the fuel channel (a delay of only 1 s was calculated), whereas a significant delay was observed in the experiment. The middle sheath temperature started to increase in the experiment at 28 s, whereas the top sheath temperature was delayed by about 7 s. Note that this delay observed in the experiment does not indicate the actual travelling time of the dryout front for two reasons. First, the measured temperatures were not in the same subchannel, and different fluid velocities can be expected in different subchannels (because of deformation of the fuel elements and the empty sheath segments). Second, it was observed in the experiment that some instrument junctions were slightly dislocated during the blowdown transient. Since these were not accounted for in the simulations, the code calculations of the dryout delay time between the bottom and the top of the fuel assembly would not be expected to agree with the experiment.

At the three locations shown in Figures 8, 9 and 10, after 34 s in the transient, the calculated sheath temperature rise during the phase of rapid fuel heatup increased because the flow blockage of 98% was activated during this period and because the rate of Zirconium-steam reaction increased as the sheath temperature increased.

Good agreement between the calculated and measured sheath temperatures was obtained at all three locations during the period of rapid heatup and flow blockage. The simulations performed without the fuel blockage resulted in

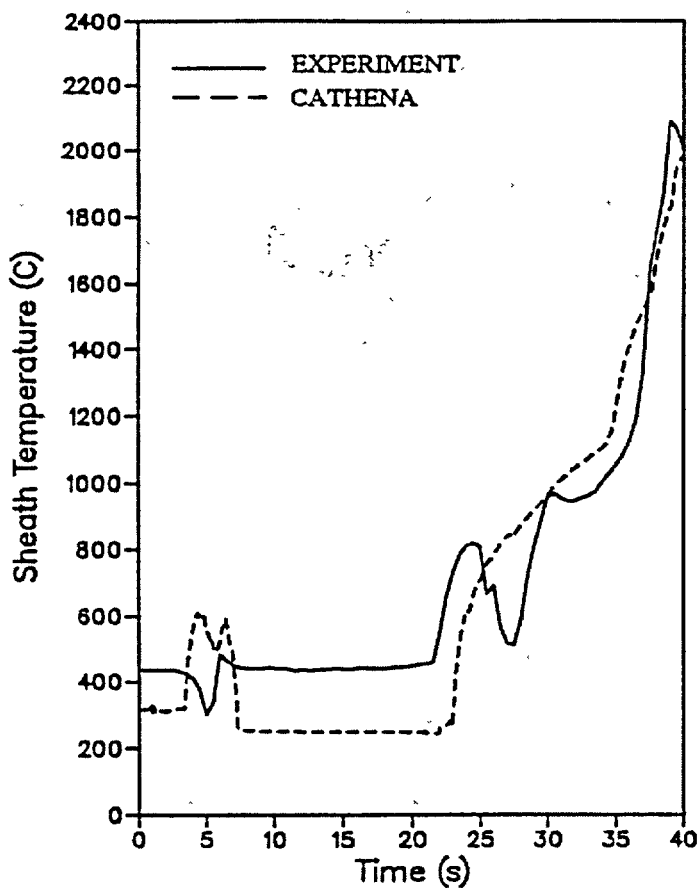


Figure 10: Sheath Temperature at the Middle of the BTF-107 Irradiated Fuel Element

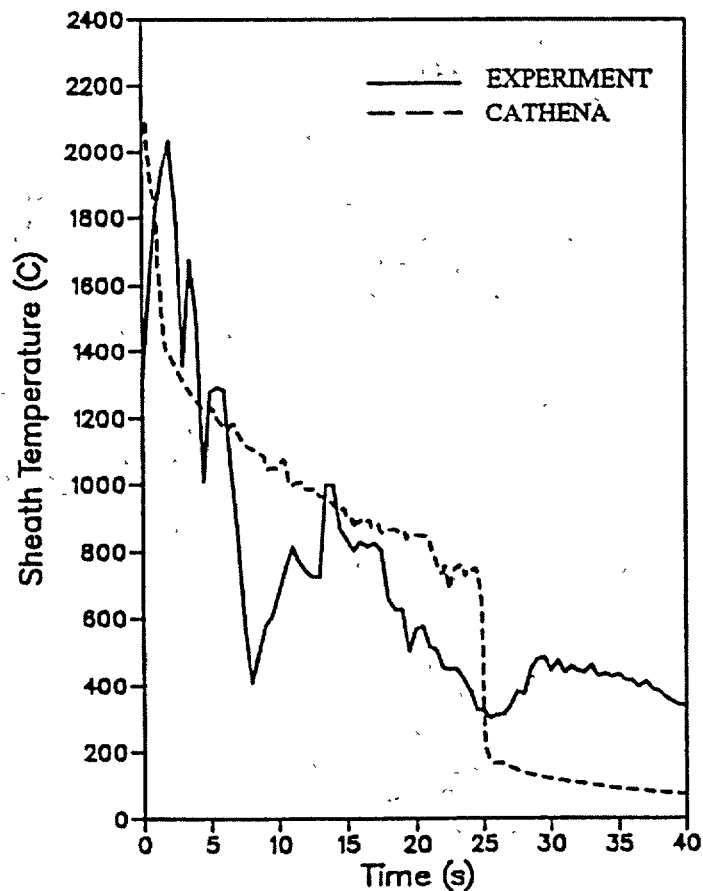


Figure 11: Sheath Temperature at the Top of the BTF-107 Fresh Fuel Element

a much lower rate of sheath temperature increase. This helped us to explain the observed behaviour in the test and to confirm the development of a flow blockage in the channel resulting from melted portions of fuel elements.

At the end of the blowdown (at 38 s in the experiment), which coincides with the reactor shutdown, the calculated sheath temperatures at all elevations were lower by about 300°C than the measured temperatures. This discrepancy was attributed to several factors, such as a low rate of Zirconium-steam reaction obtained from Urbanic and Heidrick correlation [Urbanic V.F. and Heidrick T.R., 1978], and the fact that heat transfer by radiation between the fuel elements and the empty sheath segments was neglected.

The Rewet Phase

Figures 11 and 12 show a comparison of calculated and measured temperatures at the top and middle elevation of the fresh fuel elements. The results presented in these figures were obtained from a separate simulation started at 38 s of the blowdown simulation (the time of reactor shutdown), which coincides with the zero time in Figures 11 and 12. These results were obtained with two assumptions; the initial sheath temperatures at the beginning of the rewet period were increased to approximately equal the measured sheath temperature at this time, and the flow blockage was 90% of the fuel channel area. This amount of flow blockage during the rewet phase was determined from a sensitivity study.

Figures 11 and 12 show good agreement between the calculations and the measurements. However, the code did not capture the oscillations of sheath temperatures during the

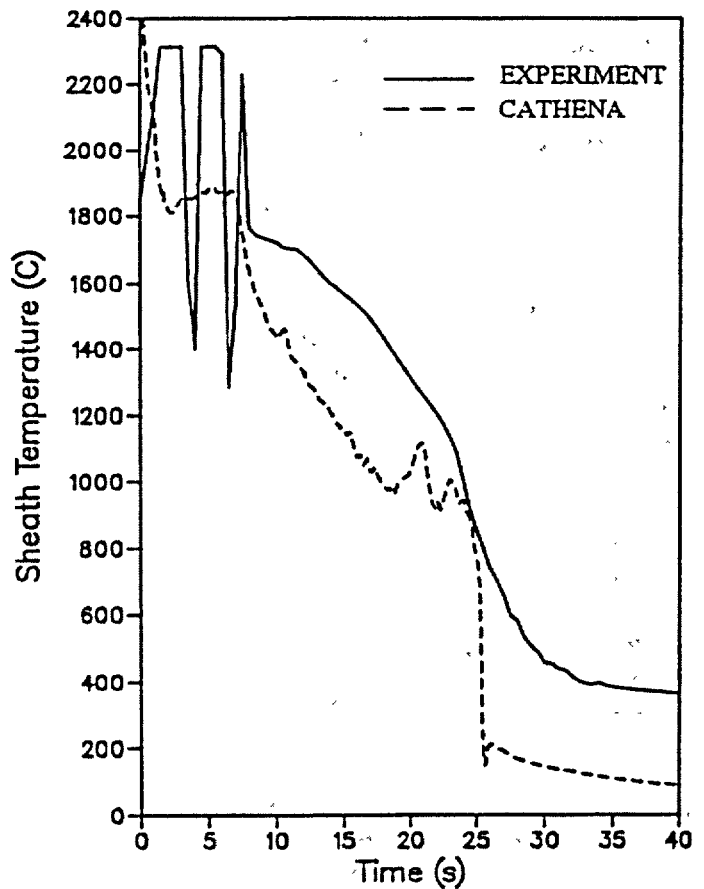


Figure 12: Sheath Temperature at the Middle of the BTF-107 Fresh Fuel Element

first 10 s of the rewet period of the transient. These oscillations were probably a result of rapid evaporation of the injected water in the channel and the pressure increase, combined with the flow blockage, temporarily halting injection. Instead, the code calculated a smooth decrease of sheath temperatures by about 500°C in the first 2 s of the transient before the rewet front reached the fuel channel. During this time, the channel was dry, thus indicating that the calculated rate of convective heat transfer to single-phase steam and the calculated rate of radiation heat transfer to the fuel shroud were overestimated.

The calculated timing of rewet completion and refilling of the channel agreed very well with the observed behaviour in the experiment.

CONCLUSIONS

This paper describes the BTF-107 experiment and presents selected CATHENA simulations of the thermalhydraulic behaviour observed in this complex severe-fuel-damage experiment.

The results of the analysis performed with the CATHENA code illustrate that CATHENA is capable of modelling the essential features of the experimentally observed thermalhydraulic behaviour. The calculations obtained with CATHENA generally agree well with the experimentally observed behaviours, thus demonstrating that CATHENA is able to model thermalhydraulic and heat transfer phenomena in experiments of this type.

Using the code calculations, it was possible to confirm the occurrence of a near-total flow blockage in the fuel channel during this experiment. This unexpected flow blockage significantly influenced the behaviour of the experiment and altered the planned test scenario.

The analysis presented in this paper helped to identify several areas in code performance where further improvements and refinements of the code would be useful. These areas included an improvement of the correlation for the Zirconium-steam reaction, an improvement in the modelling of the discharge flow rate in blowdown scenarios, the introduction of an option to change flow areas and fuel element geometry during a transient, and the introduction of an option for conductive heat transfer in the axial direction. Some of these improvements have been recently implemented in the code. Also, these simulations helped

determine the applicability of some heat transfer correlations in film boiling (such as the modified Berenson and Bromley correlation), and some critical heat flux correlations (such as the Biasi and Groeneveld correlation).

ACKNOWLEDGEMENTS

The authors acknowledge the financial support of the CANDU Owners Group (COG) consisting of the Canadian utilities (Ontario Hydro, Hydro-Québec and the New Brunswick Electric Power Commission) and AECL.

REFERENCES

DEVAAL J.W., POPOV N.K., MACDONALD R.D., DICKSON L.W., DUTTON R.J., COX D.S. and JONCKHEERE M.G., 1993 - "*Post-Test Simulations of BTF-107: An In-Reactor Loss-of-Coolant Test with Flow Blockage and Rewet*," AECL Report, AECL-10758.

MACDONALD R.D., DEVAAL J.W., COX D.S., DICKSON L.W., JONCKHEERE M.G., FERRIS C.E., KELLER N.A., and WADSWORTH S.L., 1991 - "*An In-Reactor Loss-of-Coolant Test with Flow Blockage and Rewet*," AECL Report, AECL-10464.

RICHARDS D.J., HANNA B.N., HOBSON N. and ARDRON K.H., 1985 - "*ATHENA: A Two-Fluid Code for CANDU LOCA Analysis*," Presented at the Third International Topical Meeting on Reactor Thermalhydraulics, Newport, RI, USA, 1985 October 15-18, pp. 7.E-1 - 7.E-14 (ATHENA was subsequently renamed CATHENA).

URBANIC V.F. and HEIDRICK T.R., 1978 - "*High-Temperature Oxidation of Zircaloy-2 and Zircaloy-4 in Steam*," AECL report, AECL-6149.

WADSWORTH J.A., ZANATTA R.J., DICKSON L.W., KELLER N.A., MACDONALD R.D., FEHRENBACH P.J., and WADSWORTH S.L., 1989 - "*The Canadian In-Reactor Blowdown Test Facility (BTF) Program in Support of Reactor Safety*," IAEA-SM-310/102, presented at the IAEA Symposium on Research Reactor Safety, Operations and Modifications, Chalk River, Ontario, 1989 October 23-27.

THE SOLUTION OF SPARSE MATRICES IN CATHENA

T.G. Beuthe and J.B. Hedley

Safety Thermalhydraulics Branch
Atomic Energy of Canada Limited
Whiteshell Laboratories
Pinawa, Manitoba, Canada R0E 1L0

ABSTRACT

CATHENA presently uses the Harwell MA28 routines to solve the sparse matrices generated by the thermalhydraulics numerical method. The objective of this paper is to present an overview of commonly used sparse matrix solution techniques, and to examine the potential benefits of using other solvers in CATHENA. Previous out-board tests have shown that the SMPAK, Y12M, and IMSL direct solvers and the PCGPAK3 iterative solver may be competitive with the MA28 solver. In the present investigation the performance of these solvers was tested in-situ in CATHENA using a wide variety of different simulations. The results indicate the SMPAK and Y12M direct solvers show the best performance and can increase the overall simulation speed by up to a factor of 8 for the largest CATHENA simulations tested.

1. INTRODUCTION

CATHENA (Canadian Algorithm for THERmalhydraulic Network Analysis) is a computer program designed for the analysis of two-phase flow and heat transfer in piping networks. The CATHENA thermalhydraulic code was developed by AECL, Whiteshell Laboratories, primarily for the analysis of postulated accident conditions in CANDU[®] reactors.

The thermalhydraulic model employed in CATHENA uses a one-dimensional, non-equilibrium two-fluid model consisting of six partial differential equations for mass, momentum and energy conservation; three for each phase. A first-order finite-difference representation is used to solve the differential equations, utilizing a semi-implicit one-step method in which the time step is not limited to the material Courant number [1]. At each time step the linearization of the differential conservation equations results in a sparse matrix which is written and solved. Currently the solution is provided using the Harwell MA28 sparse matrix solver which was developed in the early 1970s.

When relatively small network simulations are performed, for example when the order of the matrix to be solved n is less than 4000, less than 25% of the total simulation time is usually spent in the sparse solver. In general, the computational effort needed to assemble the CATHENA sparse matrix scales linearly with the order of the matrix as n . In contrast, the computational effort needed to solve a sparse matrix scales less than n^2 but is still far from linear with n , depending on the efficiency of the solver, the sparsity and the structure of the matrix [2]. As a result, the fraction of the total time spent solving the generated sparse matrices increases as the size of the simulation increases. Earlier studies have shown that as the order of the CATHENA matrix increases to greater than 17,000 more than 90% of the simulation can be spent in solving the sparse matrices. In these cases, the efficiency of the sparse solver can become a dominant factor in the computational efficiency of CATHENA [3].

CANDU[®] is a registered trademark of Atomic Energy of Canada Limited (AECL).

Although the CATHENA sparse matrices are non-symmetric, non-positive definite, and relatively stiff, the MA28 routines have proven themselves robust and reliable for more than 10 years. In the interim a number of potentially more efficient solvers have become available. A preliminary study where CATHENA generated sparse matrices were solved on a stand-alone basis, using 6 direct and 2 iterative sparse matrix solvers, showed that it may be possible to achieve significant savings in solution time through the use of alternative matrix solvers [3].

After presenting a review of the available sparse matrix solution techniques, the present study examines five (5) of the most promising matrix solvers (4 direct and 1 iterative) investigated in the preliminary study. These solvers were directly implemented in a test version of CATHENA MOD-3.5c/Rev 0 and were used to solve a wide range of thermalhydraulic simulations, from very small and simple to extremely large and complex. The solvers under examination were tested for both accuracy and speed. The results of this investigation indicate that two of the direct solver solvers are much faster than the MA28 routines and significantly enhance the overall performance of CATHENA for large simulations.

2. REVIEW OF SPARSE MATRIX SOLUTION TECHNIQUES

The solution of systems of linear equations is one of the most important areas of numerical mathematics. A large number of different descriptions of physical problems can be reduced to a linear system of the form:

$$Ax = b \tag{1}$$

where x represents a vector of variables to be solved for, A represents the matrix of coefficients of the linear system, and b represents a vector of constants.

The matrix A is often sparsely populated (less than 10% of the positions are occupied, often significantly less) and the problem can involve the simultaneous solution of a system involving millions of equations. Problems of such magnitude can seriously challenge the computational capabilities of any given machine. They can only be solved using numerical algorithms that take sparseness and structure into account, and use special storage and programming techniques.

Matrices to be solved may have real or complex elements, may be symmetric or unsymmetric (for real matrices) or Hermitian or non-Hermitian (for complex matrices). They may be positive definite, banded, have a block structure, or be diagonally dominant. Depending on which of these characteristics a given matrix displays, special algorithms have been developed to solve the system of equations to minimize storage and computation time.

2.1 Solution Methods

Solution methods for sparse matrices can be classified into one of three general categories:

1. **Direct Methods** that yield the required solution with a fixed number of arithmetic operations.
2. **Iterative Methods** that begin with a starting vector x^0 , and compute a sequence of iterands x^m for $m = 1, 2, 3, \dots$

$$x^0 \mapsto x^1 \mapsto x^2 \mapsto x^3 \mapsto \dots \mapsto x^{m-1} \mapsto x^m \mapsto x^{m+1} \mapsto \dots$$

where x^{m+1} is only dependent on x^m , and starting value x^0 is not part of the method.

3. **Parallel Solvers** that solve parts of the matrix simultaneously. These methods also often take advantage of available vector processing, and typically avail themselves of methods developed for direct and iterative solvers.

2.2 Direct Methods

At the heart of every direct method lies the Gaussian elimination process and the related triangular decomposition. To solve equation 1, a decomposition of matrix A into lower L and upper U triangular matrices is performed:

$$A = LU \quad (2)$$

and a forward and back-substitution is performed to find the solution vector x :

$$LUx = b \Leftrightarrow Ly = b \quad Ux = y \quad (3)$$

Variants of the basic direct method differ primarily in the way the matrix A is stored, the details of the elimination process, the precautions used to minimize rounding errors, and the methods of refining solutions.

Special direct methods exist for symmetric or positive definite matrices that need only about half the number of storage cells. A special direct method known as the **frontal technique** also exists. Although originally developed for finite element analysis, it is not restricted to that application [4, 5].

The numerical accuracy and stability of direct methods is normally assured by moving the largest elements into the diagonal through row and column exchanges, an operation called **pivoting**. **Partial pivoting** involves exchanging only rows and **full pivoting** involves exchanging both rows and columns. The usefulness of pivoting is not always guaranteed due to the time and effort it takes to perform the pivoting operations [6].

In the process of solving the matrix A , new non-zero elements, known as fill-ins, will be created. Direct solvers attempt to minimize the number of fill-ins wherever possible. Some of these new elements will be physically significant, whereas others could theoretically be dismissed as numerical roundoff. Some routines make provisions for dropping these insignificant values through a drop-tolerance parameter. Depending on the drop-tolerance used, it may be necessary to improve the accuracy of the final answer in a process known as residual refinement [2, 7].

Direct solution methods have received a significant amount of attention in the literature. Recent discussion on the use of direct methods in fluid mechanics problems can be found in articles by Onyejekwe et al [8] on fluid flow in pipe networks, and Habashi et al [9] on the use of direct methods well suited for use on supercomputers. The use of direct solvers in finite element problems is discussed by Leimbach and Zeller [10] (for the nuclear industry) and Peters [11].

If matrix A is not well conditioned, direct methods can sometimes succeed where iterative methods can fail. Young et al [12] discuss a case in which direct solvers were chosen over iterative solvers for intractable problems in the aerospace industry.

Due to their relative robustness, good track record, and ability to solve a matrix in a finite number of steps, direct solvers such as MA28 and Y12M [13, 14] have been in use for some time now, and are looked upon almost as an industry standard. As such, these routines are often used as baselines for comparisons between other routines. For example, Duff and Nowak compare the performance of NSPFAC and MA28 in the LARKIN program [15]. Good general discussions of direct methods for sparse matrices can be found in the books by Pissanetzky [4], Duff et al [2], and Zlatev [7]. The book by Duff represents a more general

introduction to direct methods. The book by Zlatev is a more extensive publication discussing a wide range of subject areas.

2.3 Iterative Methods

Some of the more commonly known iterative method include

- Jacobi, Gauss-Seidel, and Successive Overrelaxed (SOR) methods. These are sometimes referred to as classical methods.
- Conjugate-Gradient Methods. Although they are very popular, these algorithms unfortunately require positive definiteness in matrix A .
- Multi-Grid Methods. Unlike the previous routines which have at best a linear convergence, multi-grid methods have a convergence which is independent of step-size.
- Domain Decomposition.

In general, the \tilde{x}_{m+1} vector in iterative methods is only dependent on the x vector from the preceding step \tilde{x}_m , as well as matrix A and constant vector b :

$$\tilde{x}_{m+1} = \Phi(\tilde{x}_m) \quad \text{where} \quad \Phi = f(A, b) \quad (4)$$

Semi-iterative methods also exist. In this case, \tilde{x}_{m+1} is calculated using more than just \tilde{x}_m :

$$\tilde{x}_{m+1} = \Phi(\tilde{x}_m, \tilde{x}_{m-1}, \tilde{x}_{m-2} \dots) \quad (5)$$

An example of such a method is the Alternating-Direction Implicit or ADI method.

A preconditioner is often used to help speed up the convergence of the iterations. The term derives its name from the idea that an improvement in the condition number of matrix A helps the iteration proceed. An undesirable side effect of this process lies in the potentially large amount of time that can be spent in the preconditioning stage [16]. Nonetheless, iterative methods can be advantageous for sparse matrices since far fewer calculations are performed per iteration than are made during the solution when using direct methods. Additional advantages exist if a good approximation to x is already available to accelerate the convergence. Unfortunately, if a matrix is not positive definite, convergence is not guaranteed.

Comprehensive summaries of iterative techniques can be found in the books by Ilin [17] and Hackbusch [18]. The book by Hackbusch in particular stands out as a good and very up-to-date overview of iterative methods. A comparative summary of various iterative techniques can be found in the article by Dongarra and van der Vorst [19].

2.4 Parallel Solvers

Two general approaches are used to solve matrices in parallel:

1. Consider the inherent ability of the detailed coding to be performed in parallel, or by using vector processors. For example, row and column swapping might be done in parallel, or a section of the code might be rewritten to vectorize basic matrix operations.

2. Divide the matrix into sub-groups that can be separately calculated. Some commonly used techniques include partitioning, matrix modification, and tearing. These methods tend to perturb the matrix, but matrix perturbation techniques may also be used to better condition the matrix.

Parallel methods represent the forefront of development work in matrix solution. As new machines and hardware become available, new parallel methods are developed. Further details can be found in references [20, 21, 22, 23, 24]. The present investigation will only consider the use of direct or iterative techniques.

3. SOLVER TESTING

3.1 Solver Implementation and Choice of Test Cases

In an earlier investigation [3], a broad pallet of sparse matrix solvers was tested on a small number of CATHENA matrices. These tests were performed on an outboard basis and were benchmarked against the MA28 solver. The results indicated the direct solvers in the Y12M routines by Zlatev et al [13], the commercial IMSL routines, and the specialized SMPAK routines developed by Scientific Computing Associates (SCA) deserved further investigation. Of the iterative solvers tested, only the set of results from the PCGPAK3 routines offered by SCA warranted further investigation.

For the present investigation, these routines were integrated into a test version of CATHENA and used to run a wide range of test cases. As summarized in Table 1, the test cases ranged from the smallest cases such as TEST1 (16 equations and 34 non-zero terms) to some of the largest and most complex simulations being performed with CATHENA. The standard CATHENA acceptance test suite was used to ensure the solvers had been correctly integrated into the test version of CATHENA and were producing results consistent with MA28 results.

Wherever possible, the sparse solvers were implemented using the standard recommended preset values. The IMSL sparse solver was implemented in such a way that it could be utilized in row pivot, column pivot as well as row plus column pivot mode.

The iterative solver, PCGPAK3, which in fact represents a suite of iterative solution methods, was implemented using an incomplete LU preconditioner and a Generalized Minimal RESidual (GMRES) iteration method. This proved to be the most efficient and stable combination. Block solution was not used. The initial guess on the first step was given by the initial conditions provided by CATHENA. Initial guesses for subsequent steps were provided by the solution from the previous time step, thus fully utilizing this accelerative feature of iterative solvers.

Care was taken to ensure the test cases chosen in Table 1 represent a good cross section of the types of sparse matrices generated by CATHENA. As shown in Figures 1-4, the test cases chosen show a wide range of structure. The structure of the CATHENA-generated sparse matrices is largely dependent on the manner in which the network connections are assembled in the CATHENA input file by the user and thus tend to reflect both the structure of the physical facility and the approach used to idealize it. For example, the TEST20 matrix shown in Figure 4 represents an idealization of the RD-14M facility [25]. The square symmetric off-diagonal non-zero entries (as represented by the solid points in the figure) at the top left and the middle reflect the presence of the two sets of parallel heated sections in the facility. The clusters of off-diagonal non-zero entries at the bottom right represent the steam generators and the ECI system.

3.2 Test Results

The results of the tests are shown in Tables 2 and 3. Table 2 summarizes the average matrix solution time (in seconds) per CATHENA timestep, and Table 3 shows the performance of the solvers relative to the performance of MA28. As shown here, the SMPAK direct solver has the best overall performance relative to MA28 for both small and large cases. With the exception of the TEST17 case, the SMPAK routine is significantly faster than MA28. In one case (TEST25, one of the largest test cases) the SMPAK routines take only 2.3% of the time it takes MA28 to solve the CATHENA sparse matrices.

The next best performance was provided by the Y12M solver. Although it does not do as well with the small cases, it meets, and in one case (TEST24) even slightly exceeds the performance of SMPAK for the larger cases.

The IMSL sparse solver routine was tested in column, row, and row plus column pivot mode. For small cases, the IMSL routine performance was close to that of MA28, but in many cases it was slower. In general the choice of pivoting does not have a large effect on the performance of the routine when solving CATHENA matrices. Like the Y12M routine, the IMSL routine provided the best performance relative to the MA28 routine when solving large matrices. However, the overall performance was nowhere near that of the SMPAK and Y12M routines for CATHENA matrices.

On average, the iterative PCGPAK3 routine was about as fast as the MA28 solver. In some cases it was significantly slower (by a factor of up to 2.5). The PCGPAK3 routines were quite competitive with the MA28 solver for the larger matrices, but the performance for these cases was 2–4 times slower than the SMPAK or Y12M routines.

It should be noted that the PCGPAK3 routines make use of the Basic Linear Algebra Subroutines (BLAS). These routines are available as standard high-level language coded routines, as well as machine coded routines which are optimized for a particular machine hardware. Previous studies indicate savings of more than 20% in the run times can be achieved through the use of specially optimized BLAS routines [3]. This does not provide a large enough saving to make the PCGPAK3 routines competitive with direct solver routines like Y12M or SMPAK.

4. SUMMARY AND CONCLUSIONS

The MA28 solver is presently used as the standard sparse matrix solver in CATHENA. This solver is still competitive with newer routines when solving small to medium sized CATHENA matrices (order < 4000).

Recently, users have begun to create larger simulations. These typically model an entire CANDU reactor, including subsystems, with an increasing degree of detail. In these large simulations, a significant performance enhancement could be obtained through a simple replacement of the sparse matrix solver. The overall run times of the cases could be significantly reduced. For example, the TEST24 case spends more than 70% of its time in the MA28 sparse solver. A switch to the SMPAK solver would increase the overall performance of the code by a factor of more than 2.5. The TEST25 case, which spends 90% of its time in the MA28 solver, would run more than 8 times faster if the SMPAK solver was used instead.

The present study indicates the two routines which provide the best performance in comparison to the MA28 routine for solving CATHENA generated sparse matrices are the direct sparse matrix solvers: Y12M and SMPAK. Implementation of these routines is recommended as alternative sparse matrix solvers for future CATHENA versions.

ACKNOWLEDGEMENTS

The authors gratefully acknowledge the help and cooperation of D. Baxter at SCA for his help with the SMPAK and PCGPAK3 routines.

REFERENCES

1. B.N. Hanna, "CATHENA: A thermalhydraulic code for CANDU analysis", *Nuclear Engineering and Design*, 180 (1998) 113-131. 1
2. I.S. Duff, A.M. Erisman, and J.K. Reid, *Direct Methods for Sparse Matrices*, Oxford University Press, New York, 1986. 1, 2.2, 2.2
3. T.G. Beuthe and J.B. Hedley, "Preliminary Investigation of the Solution of Sparse Matrices in CATHENA", *Proceedings of the 20th Nuclear Simulation Symposium, Niagara-on-the-Lake, Ontario, 1997 September 7-9*. 1, 1, 3.1, 3.2
4. S. Pissanetzky, *Sparse Matrix Technology*, Academic Press, London, 1984. 2 2, 2.2
5. P. Hood, *Int. J. Num. Meth. Eng.*, 10(1976)379-399. 2.2
6. S. Thompson, *The Effect of Partial Pivoting in Sparse Ordinary Differential Equation Solvers*, *Comp. & Math. with Appl. Ser. A*, v. 12A, n. 12(Dec. 1986)1183-91. 2.2
7. Z. Zlatev, *Computational Methods for General Sparse Matrices*, Kluwer Academic, Boston, 1991. 2.2, 2.2
8. O.O. Onyejekwe, A. Okoromadu, and V. Onyema, *Advances in Engineering Software*, 17(1993)189-194. 2.2
9. W.G. Habashi, V.-N. Nguyen, M.V. Bhat, *Comp. Meth. Appl. Mech. & Eng.* 87(1991)253-265. 2.2
10. K.R. Leimbach, C. Zeller, *Advantages of Using a Node-Oriented Sparse-Matrix Solver in Nuclear Plant Dynamic Analyses*, *Nucl. Eng. & Des.* v. 70, n. 1(1982)85-100. 2.2
11. F.J. Peters, *Sparse Matrices and Substructures with a Novel Implementation of Finite Element Algorithms*, Amsterdam, Mathematisch Centrum, 1980. 2 2
12. D.P. Young, R.G. Melvin, F.T. Johnson, J.E. Bussoletti, L.B. Wigton, and S.S. Samant, *SIAM J. Sci. Stat. Comput.*, v. 10 n. 6(Nov. 1989)1186-1199. 2.2
13. Z. Zlatev, J. Wasniewski, K. Schaumburg, *Y12M solution of large and sparse systems of linear algebraic equations : documentation of subroutines*, Springer-Verlag, New York, 1981. 2.2, 3.1
14. O. Sterby, and Z. Zlatev, *Direct methods for sparse matrices*, Springer-Verlag, New York, 1983. 2 2
15. I.S. Duff, and U. Nowak, *IMA J. Num. Anal.* 7(1987)391-405. 2.2
16. G. Brussino, V. Sonnad, *Int. J. Num. Meth. Eng.* 28(1989)801-815. 2.3
17. V.P. Il'in, *Iterative Incomplete Factorization Methods*, World Scientific Pub. Co., River Edge, NJ, 1992. 2.3
18. W. Hackbusch, *Iterative Solution of Large Sparse Systems of Equations*, Springer-Verlag, New York, 1994. 2.3
19. J.J. Dongarra, and H.A. van der Vorst, *Supercomputer*, v. 9, n. 5(1992)17-30. 2.3
20. J.N. Shadid, and R.S. Tuminaro, *Concurrency: Practice and Experience*, v. 4, n. 6 (1992) 481-497. 2.4
21. U. Schendel, *Sparse Matrices: Numerical Aspects with Applications for Scientists and Engineers*, Halsted Press, John Wiley & Sons, New York, 1989. 2.4
22. D.J. Evans, *Sparsity and Its Applications*, University Press, New York, 1985. 2 4
23. X. Xu, N. Qin, and B.E. Richards, *Int. J. Num. Meth. Fluids* 15(1992)613-623. 2 4
24. J. Larsen, and T. Christensen, *A Parallel Sparse Matrix Solver*, *Proc. of the 1st & 2nd Nordic Transputer Seminars*, (1991)64-75. 2.4

25. P.J. Ingham, J.C. Luxat, A.J. Melnyk, T.V. Sanderson, Natural Circulation Experiments in an Integral CANDU Test Facility, IAEA Technical Committee Meeting on Experimental Tests and Qualification of Analytical Methods to Address Thermohydraulic Phenomena in Advanced Water Cooled Reactors, Paul Scherrer Institute, Villigen, Switzerland, 1998 September 14–17. 3.1

TABLE 1: Summary of test matrices.

Test	Order	#Non-Zero	% Sparsity
TEST1	16	34	13.28125
TEST2	39	205	13.47798
TEST3	94	586	6.63196
TEST4	130	447	2.64497
TEST5	142	805	3.99226
TEST6	142	918	4.55267
TEST7	194	680	1.80678
TEST8	202	1036	2.53897
TEST9	336	1191	1.05495
TEST10	368	1994	1.47241
TEST11	527	1842	0.66324
TEST12	754	2730	0.48020
TEST13	842	3602	0.50807
TEST14	884	3598	0.46042
TEST15	1368	5116	0.27337
TEST16	1654	6322	0.23109
TEST17	2292	10530	0.20045
TEST18	2390	9492	0.16617
TEST19	3008	18714	0.20683
TEST20	3168	15926	0.15869
TEST21	3846	13886	0.09388
TEST22	8009	32453	0.05059
TEST23	13391	45158	0.02518
TEST24	19470	88935	0.02346
TEST25	17733	91929	0.02923

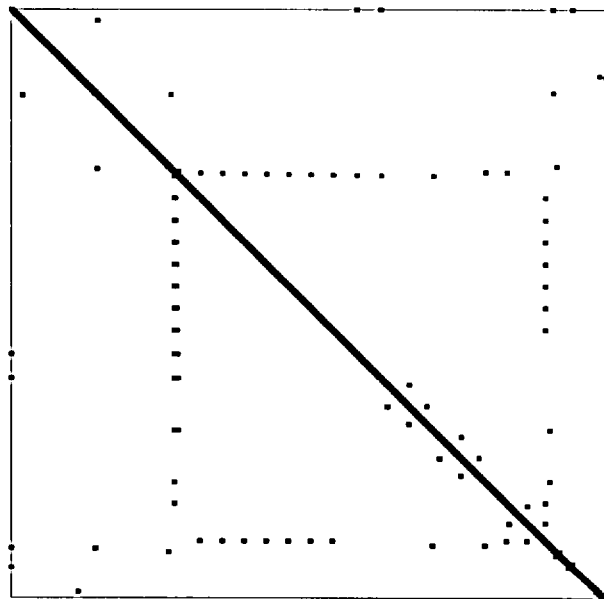


FIGURE 1: Structure of the TEST21 matrix.

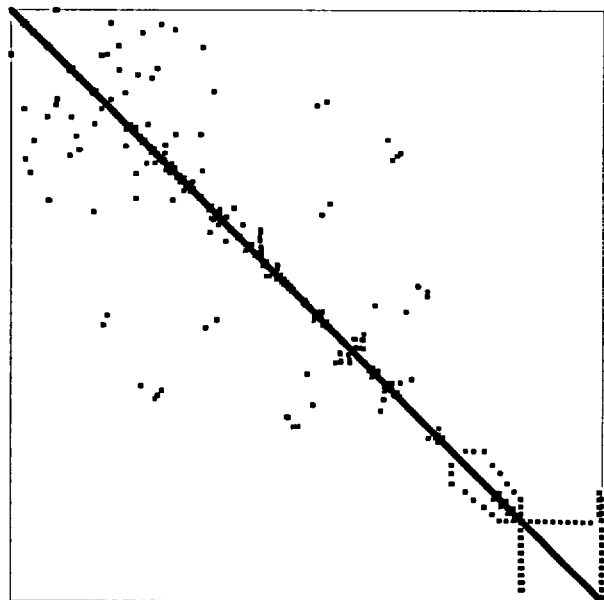


FIGURE 2: Structure of the TEST22 matrix.

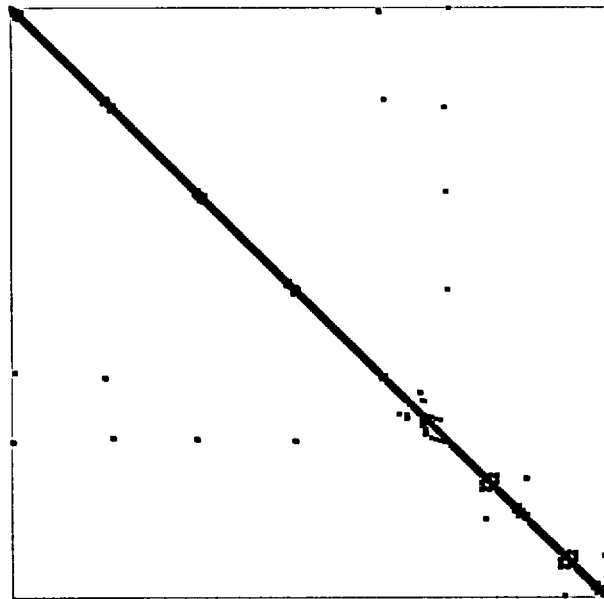


FIGURE 3: Structure of the TEST16 matrix.

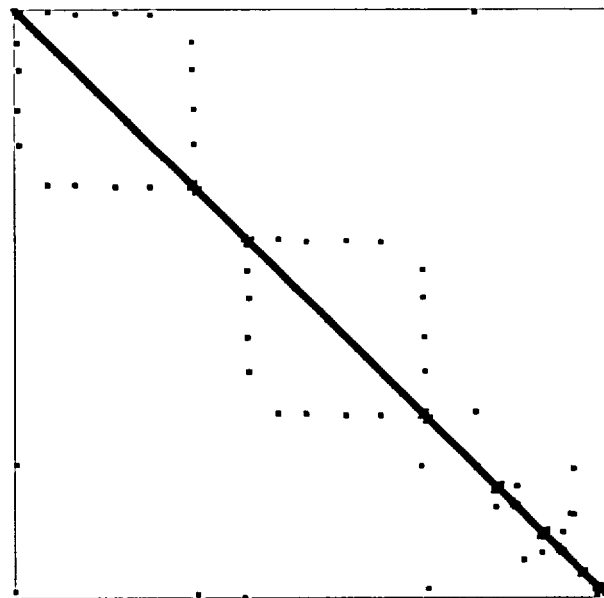


FIGURE 4: Structure of the TEST20 matrix.

TABLE 2: Average matrix solution times per CATHENA timestep in seconds.

Test	MA28	SMPAK	Y12M	IMSL ^C	IMSL ^R	IMSL ^{R+C}	PCGPAK3
TEST1	0.00164	0.00024	0.00136	0.00219	0.00239	0.00243	0.00216
TEST2	0.00625	0.00109	0.00603	0.00871	0.00832	0.00927	0.00601
TEST3	0.02034	0.00328	0.01445	0.02000	0.02020	0.02184	0.01328
TEST4	0.01048	0.00247	0.01034	0.01504	0.01556	0.01857	0.01314
TEST5	0.04117	0.00636	0.02586	0.03358	0.03268	0.03430	0.01799
TEST6	0.04488	0.00717	0.03047	0.05041	0.04429	0.04535	0.01911
TEST7	0.01578	0.00418	0.01549	0.02265	0.02194	0.02472	0.01907
TEST8	0.02802	0.00218	0.02273	0.03194	0.03514	0.03410	0.01865
TEST9	0.10086	0.02786	0.05912	0.08664	0.08045	0.08742	0.06338
TEST10	0.12494	0.01223	0.07180	0.08900	0.07415	0.07822	0.04422
TEST11	0.05196	0.01924	0.05009	0.06896	0.07863	0.07169	0.08833
TEST12	0.07402	0.01482	0.06661	0.09850	0.09681	0.09796	0.07532
TEST13	0.19925	0.03955	0.15844	0.18965	0.18889	0.18600	0.13238
TEST14	0.33869	0.04363	0.16969	0.22826	0.25000	0.25275	0.14462
TEST15	0.43649	0.12263	0.23328	0.29585	0.33152	0.31634	0.83258
TEST16	0.30557	0.09452	0.24626	0.30990	0.36084	0.34467	0.76422
TEST17	2.06144	6.34248	0.47990	0.72636	0.61338	0.68373	5.29129
TEST18	0.60114	0.14069	0.39721	0.52149	0.58179	0.56019	0.69512
TEST19	6.08560	0.32965	1.02191	1.31847	1.41485	1.33607	1.79781
TEST20	1.91507	0.30064	0.63099	0.94547	0.96651	0.86850	1.40442
TEST21	1.93109	0.66865	0.71353	0.95199	1.12711	0.98651	1.84000
TEST22	3.67701	2.08273	1.48422	2.06059	2.26208	2.11019	2.52024
TEST23	8.25507	2.17492	2.40791	3.49099	3.76920	3.42716	8.19024
TEST24	67.38019	8.89358	4.43000	7.55024	7.73181	6.84090	17.19706
TEST25	159.01497	3.64616	6.93148	7.64363	8.69818	8.84090	11.69482

C = columnwise pivot

R = rowwise pivot

R+C = row and columnwise pivot

TABLE 3: Relative performance of sparse solvers ($x/MA28$)

Test	SMPAK	Y12M	IMSL ^C	IMSL ^R	IMSL ^{R+C}	PCGPAK3
TEST1	0.150	0.830	1.334	1.459	1.479	1.317
TEST2	0.175	0.964	1.393	1.330	1.482	0.962
TEST3	0.162	0.710	0.983	0.993	1.074	0.653
TEST4	0.236	0.987	1.435	1.484	1.772	1.253
TEST5	0.154	0.628	0.816	0.794	0.833	0.437
TEST6	0.160	0.679	1.123	0.987	1.010	0.426
TEST7	0.265	0.982	1.435	1.391	1.567	1.209
TEST8	0.078	0.811	1.140	1.254	1.217	0.666
TEST9	0.276	0.586	0.859	0.798	0.867	0.628
TEST10	0.098	0.575	0.712	0.593	0.626	0.354
TEST11	0.370	0.964	1.327	1.513	1.380	1.700
TEST12	0.200	0.900	1.331	1.308	1.323	1.017
TEST13	0.199	0.795	0.952	0.948	0.934	0.664
TEST14	0.129	0.501	0.674	0.738	0.746	0.427
TEST15	0.281	0.534	0.678	0.760	0.725	1.907
TEST16	0.309	0.806	1.014	1.181	1.128	2.501
TEST17	3.077	0.233	0.352	0.298	0.332	2.567
TEST18	0.234	0.661	0.867	0.968	0.932	1.156
TEST19	0.054	0.168	0.217	0.232	0.220	0.295
TEST20	0.157	0.329	0.494	0.505	0.454	0.733
TEST21	0.346	0.369	0.493	0.584	0.511	0.953
TEST22	0.566	0.404	0.560	0.615	0.574	0.685
TEST23	0.263	0.292	0.423	0.457	0.415	0.992
TEST24	0.132	0.066	0.112	0.115	0.102	0.255
TEST25	0.023	0.044	0.048	0.055	0.056	0.074

C = columnwise pivot

R = rowwise pivot

R+C = row and columnwise pivot

REFINEMENT OF THE MASS CONSERVATION ALGORITHM USED IN CATHENA

T.G. Beuthe

Safety Thermalhydraulics Branch
Atomic Energy of Canada Limited
Whiteshell Laboratories
Pinawa, Manitoba, Canada R0E 1L0

ABSTRACT

The need to correct mass conservation errors is an integral part of the numerics underlying CATHENA. In the past, it was found necessary for stability reasons to neglect mass conservation errors when the code ran at the minimum time step or a re-do occurred. This could potentially lead to significant discrepancies in fluid inventory during some simulations. In CATHENA MOD-3.5b/Rev 0, a revised mass conservation strategy was implemented that addresses the weaknesses of the previous strategy. Mass is now conserved at all times, and a redistribution strategy has been implemented to ensure numerical stability when rapidly varying conditions could lead to node overfilling. This work outlines the refined algorithm, and illustrates its effectiveness.

1 INTRODUCTION

CATHENA (Canadian Algorithm for THERmalhydraulic Network Analysis) is a computer program designed for the analysis of two-phase flow and heat transfer in piping networks. The CATHENA thermalhydraulic code was developed by AECL, Whiteshell Laboratories, primarily for the analysis of postulated accident conditions in CANDU[®] reactors.

The thermalhydraulic model employed in CATHENA uses a one-dimensional, non-equilibrium two-fluid model consisting of six partial differential equations for mass, momentum and energy conservation; three for each phase. A first-order finite-difference representation is used to solve the differential equations, utilizing a semi-implicit one-step method in which the time step is not limited to the material Courant number. At each time step, the coupled linear finite-difference equations representing the thermalhydraulic network to be modelled form a sparse matrix which is written and solved. Details of the thermalhydraulic model employed in CATHENA and the numerical solution used to implement it can be found in reference [1].

2 MASS CONSERVATION ERROR CORRECTION ALGORITHM

One of the consequences of the linearized numerical algorithm employed in CATHENA to solve the thermalhydraulic conservation equations is need for a mass correction term. Since the density of the liquid and gas phases is not a linear function of pressure and phase enthalpy, a truncation error in

CANDU[®] is a registered trademark of Atomic Energy of Canada Limited (AECL).

mass and energy can develop over a time step. An additional error may also result during transitions between two-phase and single-phase conditions since the void fraction must be limited to values between zero and unity.

To prevent this truncation error from accumulating, a mass correction term is calculated at each time step for each phase for each thermalhydraulic node and is applied in the subsequent time step. The error correction ε term can be expressed as follows for both the gas and liquid terms:

$$\varepsilon_k^{n+1} = \left(\alpha_k^n \overline{\rho_k^{n+1}} - \alpha_k^{n+1} \rho_k^{n+1} \right) + \rho_k^n \left(\alpha_k^{n+1} - \overline{\alpha_k^{n+1}} \right) \quad (1)$$

where $k = f$ for liquid and $k = g$ for the gas phase, n represents the time step, ρ_k is phase density, and α_k is the void fraction. The $\alpha_k^n \overline{\rho_k^{n+1}}$ term in Equation (1) represents the mass in the system at time step $n + 1$ as calculated using the dependent variables and the linearized property routines. The $\alpha_k^{n+1} \rho_k^{n+1}$ term represents the actual phase mass in the system as calculated using the derived value for ρ_k . The difference between these two terms represents the mass error incurred as a result of the linearizing the property routines in CATHENA.

The $\rho_k^n (\alpha_k^{n+1} - \overline{\alpha_k^{n+1}})$ term in Equation (1) represents the phase mass error incurred due to truncation of the void fraction term. Here $\overline{\alpha_k^{n+1}}$ is the value of void fraction as obtained through the solution of the finite difference equations, and α_k^{n+1} is the “clipped” value of void fraction at one or zero which results if the calculated finite-difference solution result is outside these limits, as defined by:

$$\alpha_k^{n+1} = \min \left[\max \left[\overline{\alpha_k^{n+1}}, 0.0 \right], 1.0 \right] \quad (2)$$

The mass error ε_k is calculated at the end of the time step and is applied as a correction term in the new time step as shown schematically in Figure 1. The mass correction term is applied as a source term in the mass conservation equations in the next time step.

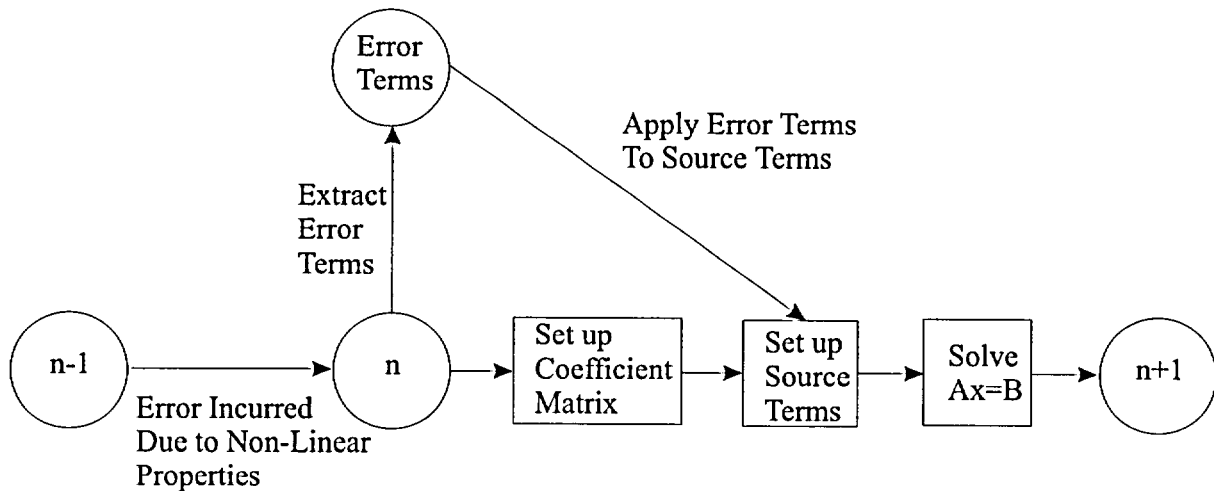


FIGURE 1: Overview of CATHENA Mass Error Correction Scheme.

It was found that the application of the mass error term could cause numerical instabilities under certain conditions. As shown in Figure 1, the mass truncation incurred from step $n - 1$ to n is applied

as part of the equations used to advance the code from step n to $n + 1$. However, if step $n - 1$ to n is much larger than step n to $n + 1$ problems may occur. For example, a rapid transient could decrease the time step and/or cause a `re-do` to occur. In this case, a potentially large error correction incurred from step $n - 1$ to n could be applied over a very small time step from step n to $n + 1$. This correction can cause instabilities in the solution by adding a large source term into the mass conservation relationships for the next time step.

An automatic timestep controller controls the size of time step CATHENA uses to advance the solution. The timestep controller monitors the change in critical state variables from one time step to another. If the change in these variables exceed pre-defined limits, the timestep controller decreases the subsequent solution timestep to minimize numerical errors in the solution. Conversely, if the change in these variables is smaller than pre-defined limits, the timestep controller can increase the subsequent solution timestep to minimize the computational time requirements. If the variable changes are bounded by the pre-defined limits, the timestep controller does not change the subsequent solution timestep.

In cases where the solution undergoes a particularly violent change, the timestep controller also has the ability to cause CATHENA to execute a `re-do`. In this case, the solution is rejected, and the step is "re-done" using 1/4 the previous time step. In particularly severe cases, several `re-dos` can occur in sequence, and the solution time step can be drastically reduced. This procedure can be repeated until the solution time step reaches the allowed minimum time step.

In versions of CATHENA prior to MOD-3.5b/Rev 0, a simple solution was chosen to avoid potential problems caused by the application of the mass correction term. Assuming numerical instabilities occurred primarily when the code was running at the minimum allowed timestep or performing a `re-do`, no mass conservation correction was performed under these conditions. However, this technique can cause undesirable mass discrepancies in the system under investigation if a significant number of `re-dos` or solutions steps at minimum timesteps are encountered.

3 REVISED MASS CONSERVATION ERROR CORRECTION ALGORITHM

For CATHENA MOD-3.5b/Rev 0, a revised mass conservation error algorithm was implemented. Since CATHENA is a two-phase code, both the liquid and vapour mass conservation equations have mass error correction terms. For the vapour phase, it was assumed that the relatively high vapour compressibility will accommodate a correction term of any size without causing numerical difficulties. As a result, the vapour mass error is always added back into the node from which it originated.

Figure 2 shows a flow chart of the revised mass correction algorithm for the liquid phase. First, each node is checked to see if the addition of the mass error correction term will overfill the node.

3.1 Overfilling Calculation

A node is considered overfull if the addition of the mass error correction term might cause the pressure or void fraction to change enough to reduce the subsequent time step.

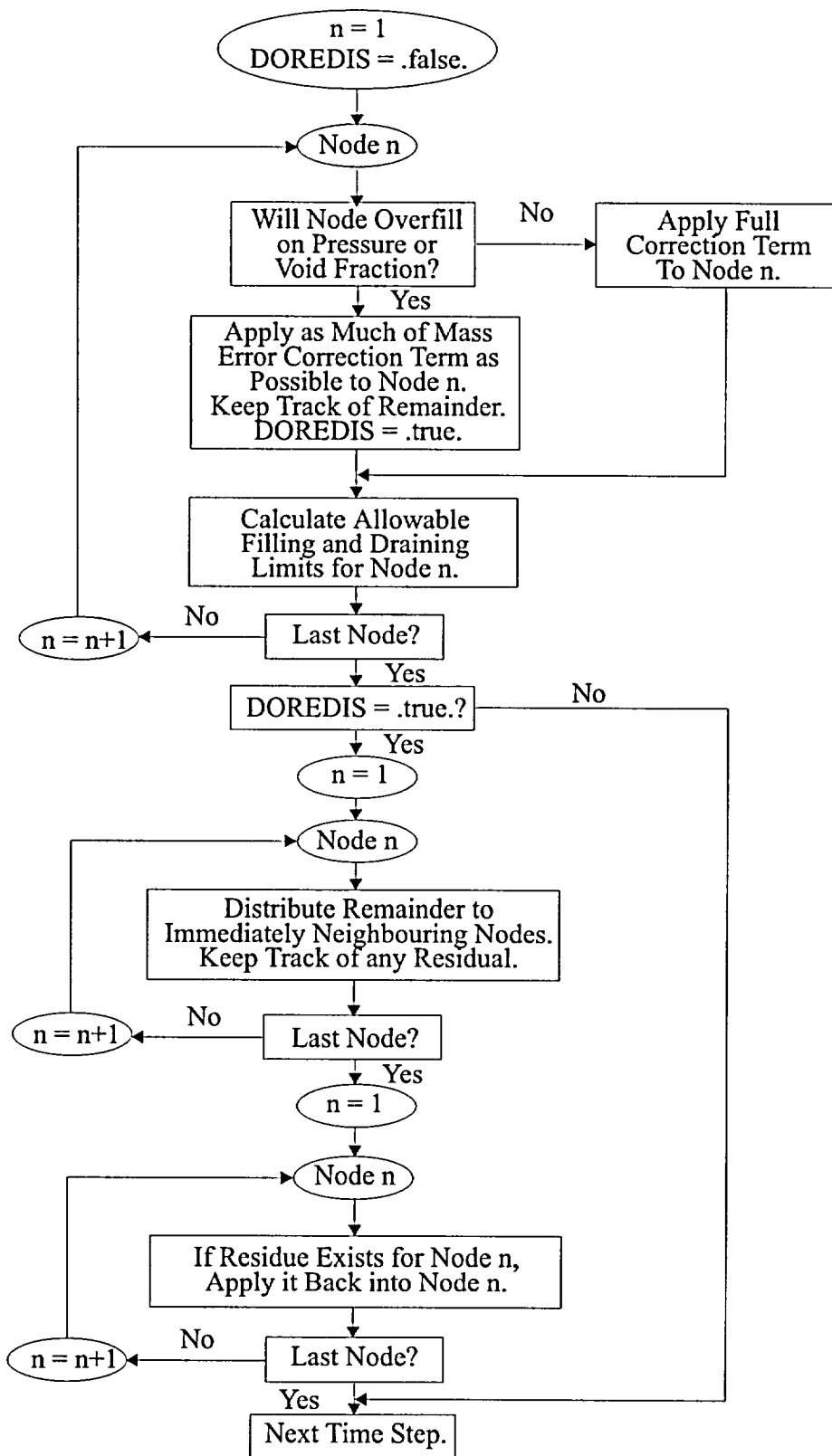


FIGURE 2: Detailed Schematic of CATHENA Liquid Mass Conservation Error Correction Algorithm.

If the node is filled with a single-phase liquid, the change in pressure of the node (ΔP_{node}) in response to the addition of the mass error correction term can be estimated as follows:

$$\Delta P_{node} \simeq \frac{\Delta \rho_f}{\left. \frac{\partial \rho_f}{\partial P_f} \right|_h} \quad (3)$$

where the change in mass is represented as a change in node liquid density $\Delta \rho_f$. The liquid isenthalpic compressibility $\left. \frac{\partial \rho_f}{\partial P_f} \right|_h$ is an available quantity in the CATHENA steam property tables.

If the node is in two-phase flow, the vapour phase can be displaced by the liquid, and the change in the node void fraction ($\Delta \alpha_{node}$) in response to the addition of mass from the error correction term can be estimated using the following expression:

$$\Delta \alpha_{node} \simeq \frac{\Delta \rho_f}{\rho_f} (1 - \alpha_g) \quad (4)$$

where α_g is the void fraction, and ρ_f is the density of the liquid.

Keeping in mind that the error correction term could be positive or negative, the largest allowed pressure perturbation as a result of a mass error correction is:

$$|\Delta P_f| \leq |x_P \Delta P_{TSC}| \quad (5)$$

where ΔP_f is the maximum pressure change allowed by adding the mass error correction term, ΔP_{TSC} is the maximum change in pressure allowed without causing the time step controller to decrease the time step, and x_P is the pressure time controller factor (constant, range: 0 \rightarrow 1).

Similarly, the largest allowed void fraction perturbation as a result of a mass error correction is:

$$\Delta \alpha_g \leq \max[x_\alpha \Delta \alpha_{TSC}, \Delta \alpha_g(\text{fill})] \quad (6)$$

if the node is being filled, and

$$-\Delta \alpha_g \geq \min[-x_\alpha \Delta \alpha_{TSC}, -\Delta \alpha_g(\text{empty})] \quad (7)$$

if the node is being emptied, where $\Delta \alpha_g$ is the maximum void fraction change allowed on adding the mass error correction term, $\Delta \alpha_{TSC}$ is the maximum change in void fraction allowed without causing the time step controller to decrease the time step, x_α is the void fraction time controller factor (constant, range: 0 \rightarrow 1), and $\Delta \alpha_g(\text{fill/empty})$ is the change in void fraction needed to fill or empty the node respectively.

The constant factors x_P and x_α are both set to 0.5. In other words, the values of ΔP_f and $\Delta \alpha_g$ are allowed to come to within a factor of 0.5 of reducing time step through changes in pressure and void fraction respectively, as estimated by equations (3) and (4).

The algorithm implemented in CATHENA also accounts for combinations of Equations (5) and (6) or (7). For example, the addition of the mass conservation error term could fill the node by displacing the last bit of void within the limits allowed by Equation (6), and then continue to overpressurize it within the limits allowed by Equation (5).

3.2 Application of Mass Error Correction Term

If the node will not overflow, the entire mass error correction term for the thermalhydraulic node being examined is applied back into the node. If the node might overflow, as much of the mass error correction term as possible is applied to the node. Any liquid mass that cannot be added back into the present node within the limits allowed by Equations (5) through (7) is saved for possible later re-distribution.

3.3 Fill and Drain Limits

As shown in Figure 2, after the mass correction error term has been applied to the maximum extent possible in the present node, a calculation is made using Equations (3) through (7) to determine how much more could be filled or drained from this node without disturbing the time step controller. These upper and lower limits are saved for use by the redistribution algorithm.

3.4 Mass Redistribution

Once an attempt has been made to apply the mass error correction term to all nodes, a check is made to determine if mass redistribution is required. If it was not possible to add the full mass error correction term back into any one of the original nodes without anticipating a pressure excursion, an attempt is made to redistribute this mass into neighbouring nodes.

The algorithm only allows mass to be redistributed into immediately adjacent nodes. In cases where two or more nodes are attached to a node, preference is given to nodes that have two-phase. If a neighbouring node is a boundary condition, all of the remaining mass is assumed to be redistributed to this node. A check is also made to ensure none of the links attaching neighbouring nodes are closed due to the presence of large resistances (k 's) or closed valves. All redistributions are subject to the fill and drain limits previously calculated to avoid potential perturbation of the timestep controller.

3.5 Residual Mass Error Correction Term

Finally, as shown in Figure 2, a mass error correction term may still remain which cannot be distributed to the immediately adjacent nodes. This residue is placed back in the originating node, regardless of the limits established by Equations (3) through (7).

4 TEST OF MASS CONSERVATION ALGORITHM

To test the revised mass conservation algorithm, a test problem was needed that involved potentially violent phenomena. A simulation of such a test problem may spend a significant fraction of its time at the minimum time step, and result in a large number of re-dos. Using the previous mass conservation strategy, a potentially significant mass error could be accumulated as the mass error correction terms are neglected at the minimum time steps and during re-do. The revised mass conservation algorithm should correct this mass error.

A test problem that fits these requirements is a hot horizontal tube refill experiment [2]. Figure 3 shows a schematic of the experimental facility. A horizontal pipe was electrically heated, and subsequently cooled through the introduction of highly subcooled liquid from one end of the pipe. A CATHENA model of this experiment was constructed. The condensation and subcooled boiling phenomena experienced in the experiment tend to frequently drive the simulation down to the minimum time step, and rapid changes in void fraction, pressure, and phase enthalpies cause frequent re-dos to occur. CATHENA calculate models were used to determine the relative mass imbalance incurred by CATHENA as the simulation proceeds. The relative mass imbalance, RMI, is expressed as:

$$RMI = \frac{\Delta M_{CMI}}{M_{TOT}} \quad (8)$$

where ΔM_{CMI} is the cumulative mass imbalance and M_{TOT} is the total mass in the system.

As shown by the solid line in Figure 4, a significant relative mass imbalance was incurred before the implementation of the present mass error correction algorithm. After implementation of the mass error correction algorithm outlined in Section 3, the RMI is reduced by several orders of magnitude. Small momentary residual mass imbalances still occur at isolated points in the simulation as shown by the spikes in the broken line in Figure 4, but they do not accumulate as before. These small residual spikes may be the result of momentary rounding errors in the finite-difference matrix solution or the calculate models used to calculate the actual mass in the system.

5 SUMMARY AND CONCLUSIONS

Prior to CATHENA MOD-3.5b/Rev 0, mass was not strictly conserved during re-do and at minimum timestep size, potentially leading to errors in fluid inventory during a simulation. A revised mass conservation error correction algorithm has been successfully implemented in CATHENA. Mass is now conserved at all times, and a redistribution strategy to nearest neighbouring nodes has been implemented to ensure numerical stability during simulations containing rapidly varying conditions. As shown by the test results, the major source of mass conservation error has been corrected. Some residual mass error remains, possibly as a result of numerical rounding errors in the matrix solution or the calculate models. These residual errors are negligible however, and do not accumulate.

ACKNOWLEDGEMENTS

The author gratefully acknowledges the advice of B.N. Hanna in the preparation of this mass conservation algorithm, and to T. MacDonald for the preparation of the original test case.

REFERENCES

1. B.N. Hanna, "CATHENA: A thermalhydraulic code for CANDU analysis", Nuclear Engineering and Design, 180 (1998) 113-131. 1
2. A. Abdul-Razzak, A.M.C. Chan, and M. Shoukri, "Rewetting of Hot Horizontal Tubes", Nuclear Engineering and Design, 138 (1992) 375-388. 7

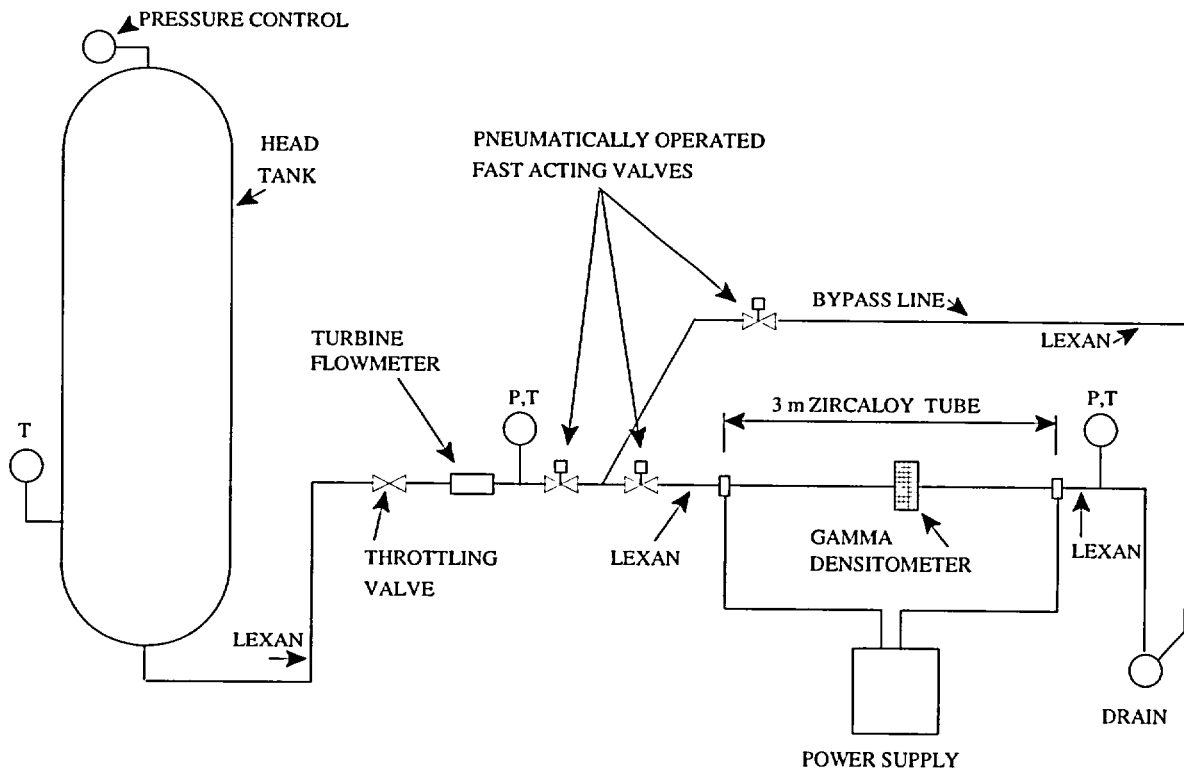


FIGURE 3: Schematic of Refill Test Loop.

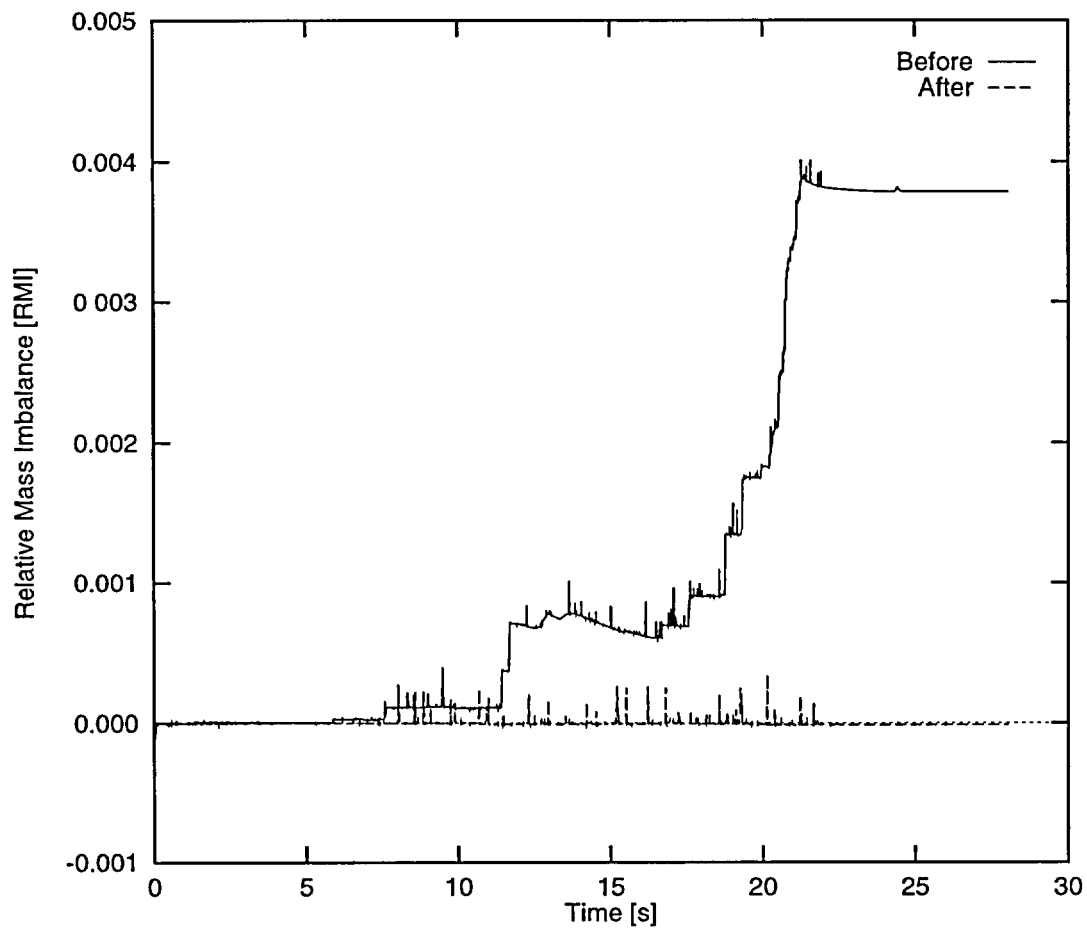


FIGURE 4: Mass Imbalance, Before and After Implementation of New Mass Conservation Error Correction Algorithm.

VALIDATION OF CATHENA MOD-3.5c/Rev0 FOR VOID-COLLAPSE WATER HAMMER

T.G. Beuthe and J.W. Gu

Atomic Energy of Canada Limited
Chalk River Laboratories
Safety Thermalhydraulics Branch
Chalk River, Ontario
Canada K0J 1J0

ABSTRACT

This paper summarizes the work performed to validate CATHENA MOD3.5c/Rev 0 for two-phase water hammer involving the generation and collapse of void. The work is part of the effort to validate CATHENA for the water hammer phenomenon, which in turn is part of a larger effort to qualify CATHENA MOD-3.5c/Rev 0 for reactor safety analysis. Simulations were chosen from fast-closing valve tests, vertical void collapse tests, and horizontal void collapse tests, performed at the Seven Sisters Water Hammer Facility, located in the Seven Sisters Generating Station of Manitoba Hydro. The results indicate the shape, timing, and peak of the leading edge of the initial water hammer pressure pulses were accurately predicted. The CATHENA results also accurately predict the detailed features of the overall pressure pulses. The predicted pressures were typically within the experimental error band, although they tended to be slightly higher than the experimentally measured pressures. This may have occurred because the effect of energy dissipation due to fluid/structure interactions is not currently included in the MOD-3.5c/Rev 0 version.

1 INTRODUCTION

CATHENA is a system thermalhydraulics code developed by Atomic Energy of Canada Limited (AECL) primarily for analysis of postulated Loss Of Coolant Accident (LOCA) events in CANDU[®] reactors [1]. One of the phenomena CATHENA will be used to analyze is water hammer. Water hammer can occur in nuclear power plants under normal as well as shutdown conditions. Some water hammer events can be averted by making design modifications or by changing operating procedures. However, under certain circumstances it may not be possible to avoid conditions that lead to water hammer. For example, water hammer may be unavoidable during emergency core cooling of a reactor. In such cases, the potential for water hammer and its impact can be assessed through numerical simulation. Thus, it is important to have a validated tool available to perform these simulations.

CANDU[®] is a registered trademark of Atomic Energy of Canada Limited (AECL).

This paper summarizes the validation conducted to assess the ability of CATHENA MOD3.5c/Rev 0 to simulate two-phase water hammer involving the generation and collapse of void. In this work, CATHENA simulation results are compared with experimental data obtained from the Seven Sisters Water Hammer Facility. These results provide a basis on which validation of condensation-induced water hammer can be conducted.

2 WATER HAMMER WITH GENERATION AND COLLAPSE OF VOID

Water hammer is defined as the change in pressure that occurs in a fluid system as a result of a change in the fluid velocity. This pressure change is a result of the conversion of kinetic into potential energy, that creates compression waves, or the conversion of potential into kinetic energy, that creates rarefaction waves. Water hammer can be strong enough to cause mechanical failure of systems in nuclear power plants.

Vapour pockets can form in a pipeline if the local pressure drops below the saturation pressure of the liquid. If a vapour pocket is formed dynamically, the phenomenon is termed cavitation. In this case, the presence of the vapour pocket does not persist and it collapses in a relatively short time after it forms. This can cause water hammer. Cavitation can occur on the upstream side of a closed valve during a water hammer event if the initial water flow rate in the system is high enough before the valve is closed. If a vapour pocket is formed under static conditions, it is termed column separation. Vapour pockets can be created in quiescent systems where the difference in elevation between the highest and lowest points in the system is large enough to cause column separation. Such a vapour pocket will remain in place for as long as the water in the pipe is not flowing. When flow is re-established in the system the vapour pocket can collapse and cause water hammer. Water hammer involving both cavitation and column separation are considered in this report.

3 THE CATHENA CODE

The acronym CATHENA stands for Canadian Algorithm for THERmalhydraulic Network Analysis. The CATHENA MOD-3.5c/Rev 0 code was developed by AECL at Whiteshell Laboratories in Pinawa, Manitoba [1]. It was developed primarily for analysis of postulated LOCA events in CANDU reactors, although it has been applied to a wide range of thermalhydraulic problems. CATHENA uses a transient, one-dimensional two-fluid representation of two-phase flow in piping networks. In the thermalhydraulic model, the liquid and vapour phases may have different pressures, velocities, and temperatures. The thermalhydraulic model consists of solving six partial differential equations for the conservation of mass, momentum, and energy for each phase. Interface mass, energy, and momentum transfer between the liquid and vapour phases are specified using constitutive relations obtained either from the literature or developed from separate-effect experiments. The code uses a staggered-mesh, one-step, semi-implicit, finite-difference solution method, that is not transit time limited. The extensive wall heat transfer package includes radial and circumferential conduction, solid-solid contact, thermal radiation, pressure tube deformation, and the zirconium-steam reaction. The heat transfer package

is general and allows the connection of multiple wall surfaces to a single thermalhydraulic node. The code also includes component models required to complete loop simulations, such as pumps, valves, tanks, break discharge, separators and an extensive control system modelling capability.

4 CATHENA SIMULATION RESULTS OF SEVEN SISTERS WATER HAMMER TESTS

All experiments cited in this paper were performed at the Seven Sisters Water Hammer Facility, located in the Seven Sisters Generating Station of Manitoba Hydro. This facility was built to provide water hammer data for code validation.

Results from three Seven Sisters test series are shown in this paper. They include:

1. Fast-Closing valve tests, or FC-series tests,
2. Vertical void collapse tests, or T-series tests, and
3. Horizontal void collapse test, or H-series tests.

In all, simulations of ten experiments were performed to validate CATHENA for water hammer involving the generation and collapse of void. A representative sample of these simulations was chosen for illustration in this paper. These simulations were performed using CATHENA MOD-3.5c/Rev 0 on cu2 HP-UX 9000/889 with PA 8000 CPUs. The maximum time step was set to 1.0×10^{-5} sec, the minimum time step to 1.0×10^{-7} sec, and the maximum length per node was 1 m.

4.1 Fast-Closing Valve Tests

The Seven Sisters facility configuration used for the fast-closing water hammer tests is shown in Figure 1. It includes a large reservoir tank at the bottom of the facility labelled TK1, various horizontal and vertical branches, three full port control valves, MV13, MV2, and MV1 as well as various pressure (P) and temperature (T) monitoring locations. For the Fast-Closing valve tests, the MV1 valve was located at the top of the system just upstream of the turbine flow meter, as shown in Figure 1.

Valve MV13 was open, and valve MV2 was closed for the duration of the experiment. Valve MV1 was initially open. After establishing a desired flow and pressure in the system, MV1 was rapidly closed, initially creating a single-phase water hammer. The initial system pressure and flow conditions were set such that subsequent to this initial water hammer pressure excursion, cavitation void pockets were created and collapsed on the upstream side of the MV1 valve at location 8P in Figure 1.

The CATHENA idealization used to simulate the fast valve closure test is shown in Figure 2. This idealization used 125 nodes and 124 links. Valves MV13 and MV2 were not modelled in the simulation. Valve MV13 was a full bore valve, and was open at all times during the experiment

and therefore was no different from the pipe it was attached to. Valve MV2 was closed at all times, and was therefore modelled as a blind end.

Measured and predicted pressure transients at valve MV1 are shown in Figures 3 and 4 for this experiment. Figure 3 shows the overall experiment, and Figure 4 shows a detailed view of the first, and most important, water hammer pressure excursion. The error bars shown on the experimental results indicate the uncertainty in the measured values of pressure according to the manufacturer's quoted instrument accuracy.

Generally, the salient features of the experimental pressure excursions caused by the water hammer were reflected in the CATHENA simulations. The first two water hammer pressure excursions were examined in more detail in this study, as they are considered representative samples of the overall water hammer scenario. The first pressure excursion is created as a direct result of the closing of valve MV1. The second (and all subsequent) water hammer pressure excursions result from the collapse of a cavitation void created on the upstream face of valve MV1. As a result, the initial pressure excursion tends to have a more gentle initial increase in pressure reflecting the valve closure curve and a single, distinct peak. However, the second and subsequent pressure excursions exhibit a much sharper initial pressure increase, reflecting the more forceful collapse of the cavitation void. These pressure excursions also each exhibit an initial pressure rise created as a result of the void collapse, as well as a series of further oscillations with peaks typically greater than the initial pressure rise.

The CATHENA simulation predicted the timing of the pressure increase in the system resulting from the initial closing of the valve to within 0.002 s for this test as shown in Figure 4. This figure also shows that CATHENA overestimates the initial pressure excursion by 0.8 MPa (10%) for this experiment. The predicted pressures were higher than the experimental ones and fell outside of the experimental error band. This may in part result because energy dissipation due to fluid/structure interaction is not currently accounted for in CATHENA.

The overall decay of the predicted water hammer pressure excursions was significantly slower than the experimentally measured decay as illustrated in Figure 3. Also, the predicted period of pressure excursions (time between pressure excursions as measured from the first to the second pressure excursion) was significantly greater than the experimentally measured period. This may be a result of the limited inclusion of energy dissipation mechanisms such as wall friction under accelerated flow conditions in CATHENA [2].

A sensitivity analysis was also conducted to examine the effect of uncertainties in the measured initial steady state flow and system temperature. The results showed that both of these uncertainties had a negligible effect on the outcome of the simulations.

4.2 Vertical Void Collapse Tests

In the vertical void collapse tests, valve MV1 was located in the horizontal pipe just downstream of tank TK1, and an additional system isolation valve MV4 was added as shown in Figure 5. In

vertical void collapse tests, column separation void pockets were created and collapsed at valve MV4, and subsequent cavitation void pockets also occurred at this location.

In the vertical pipe void collapse tests, the entire piping system was initially filled with water and measures were taken to ensure that all air was purged from the system. Valve MV2 was then opened and a measured amount of water was drained to create a void with a known volume immediately below valve MV4. Valve MV2 was then closed and the pressure within the established void was subsequently reduced to the required sub-atmospheric level using a vacuum pump attached to the system.

When the desired void volume and pressure were achieved and the system was in equilibrium, the data acquisition system was started. The experimental transient was initiated by opening valve MV1. This action pressurized the system and collapsed the void, thus creating a water hammer.

The CATHENA idealization used to simulate the vertical void collapse test is shown in Figure 6. This idealization used 127 nodes and 126 links. The void located at the top of the experimental rig was accounted for by adjusting the appropriate initial conditions for void fraction and pressure. Since there was no flow in the system, the temperature of the fluid was also set using the initial conditions. For the same reasons as explained in the fast closing valve test, valves MV13 and MV2 were not modelled in the simulation.

Measured and predicted pressure transients at location 8P are shown in Figures 7 and 8 for this experiment. The error bars shown on the experimental results indicate the uncertainty in the measured values when both the manufacturer's quoted instrument accuracy and the experimental repeatability are taken into consideration.

The CATHENA simulation results were adjusted to make the timing of the initial pressure rise of the first pressure excursion agree with the experimental results because the exact timing of the opening of the MV1 valve was not recorded in vertical void collapse experiments.

Generally, the salient features of the experimental pressure excursions caused by the water hammer were reflected in the CATHENA simulations. All of the water hammer pressure excursions shown in Figures 7 and 8 are created as a result of the collapse of a void in a vertical pipe. The first pressure excursion is created as a result the collapse of a column separation void and the second (and all subsequent) water hammer pressure excursions result from collapse of a cavitation void located below valve MV4. As a result, all pressure excursions shown in these tests exhibit sharp initial rises in pressure as well as a series of further oscillations with the peak typically greater than the initial pressure rise. It should be noted that when analyzing void collapse generated water hammer pressure excursions, both the simulated initial water hammer pressure rise and the simulated maximum peak pressure are compared to their experimental counterparts. The maximum peak pressure oscillation is defined as the maximum peak exhibited by the experimental results.

The results in Figure 8 show that CATHENA overestimates the initial peak pressure by 0.3 MPa (5%) and the maximum peak pressure by 1.4 MPa (23%) in the void collapse experiment. All predicted pressure spikes were greater than the experimental values and typically fell inside the

experimental error band. Energy dissipation due to fluid/structure interaction is not currently modelled by CATHENA, and this might account for part of the difference in pressure values.

The overall decay of the predicted water hammer pressure excursions was significantly slower than the experimentally measured decay in the experiment as shown in Figure 7. Also, the predicted period of pressure excursions (time between pressure excursions as measured from the first to the second pressure excursion) was significantly greater than the experimentally measured period. This may be due to the fact that energy dissipation mechanisms such as wall friction may not be accurately accounted for in CATHENA under accelerated flow conditions.

A sensitivity analysis was conducted to examine the effect of measurement errors on predicted pressures at 8P. These measurements include tank pressure, initial void pressure, initial void volume, MV1 valve opening time, and water temperature.

Uncertainties in initial void pressure and water temperature were found to have no significant impact on the predicted water hammer behaviour. An uncertainty in the valve opening time was found to have a slight effect on the onset of the water hammer pressure excursions, but no significant effect on the peak pressures. Uncertainties in the tank pressure and initial void volume were found to lead to slight changes in water hammer peak pressure and onset time. The maximum simulated pressure was altered by at most 0.14 MPa (2%) and the onset of pressure excursions was altered by up to 0.02 s

An analysis was also conducted to assess the effect of code uncertainties on predicted results. The selected CATHENA variables include uncertainties in the mixed flow regime transition factors, the single and two-phase friction factors, and the Colebrook-White friction factor correlation. Uncertainties in the mixed flow regime factors and the single and two-phase friction factors did not have a significant effect on the predicted pressures. Uncertainties in the Colebrook-White friction factor had a significant effect on both the onset time and size of the pressure excursions. The peak pressure was altered by ± 0.2 MPa (3%) and the onset of the first pressure spike by ± 0.002 s.

4.3 Horizontal Void Collapse Tests

In the horizontal void collapse tests, valve MV1 was located in the horizontal pipe just downstream of tank TK1, and an additional system isolation valve MV4 was added as shown in Figure 9. In horizontal void collapse tests, column separation void pockets were created and collapsed at the dead end at location beside valve MV4 as shown in Figure 9. Subsequently, cavitation void pockets were created and collapsed at this location.

Initially, the entire system was filled with water to ensure that no air was left in the system. As in the vertical void collapse tests, valve MV2 was then opened and a measured amount of water was drained to create a void with a known volume immediately next to valve MV4. Valve MV2 was then closed and the pressure within the established void was subsequently reduced to the required sub-atmospheric level using a vacuum pump attached to the system.

When the desired void volumes and pressure were achieved and the system was in equilibrium, the data acquisition system was started. The experimental transient was initiated by opening valve MV1. This action pressurized the system and collapsed the voids, thus creating a water hammer.

The CATHENA idealization used to simulate the horizontal void collapse test is shown in Figure 10. This idealization used 131 nodes and 130 links. The void located at the top of the experimental rig was accounted for by adjusting the appropriate initial conditions for void fraction and pressure. Since there was no flow in the system, the temperature of the fluid was also set using the initial conditions. For the same reasons as explained in the fast closing valve test, valves MV13 and MV2 were not modelled in the simulation.

Measured and predicted pressure transients at location 8P are shown in Figures 11 and 12. As with the vertical void collapse test results, the error bars shown on the experimental results indicate the uncertainty in the measured values when both the manufacturer's quoted instrument accuracy as well as experimental repeatability are taken into consideration. Also, the CATHENA simulation results were adjusted to make the timing of the initial pressure rise of the first pressure excursion agree with the experimental results because the exact timing of the opening of the MV1 valve was not experimentally recorded in these experiments.

Generally, the salient features of the experimental pressure excursions caused by the water hammer were reflected in the CATHENA simulations. The pressure excursions are created as a result of void collapse in a single horizontal branch. The first pressure excursion is caused by the collapse of a column separation void and the second (and all subsequent) pressure excursions result from the collapse of a cavitation void located next to valve MV4. As a result, all water hammer pressure excursions shown in these tests exhibit a sharp initial rise in pressure.

The results in Figure 12 show that CATHENA overestimates the initial peak pressure by 0.2 MPa (4%) and the maximum peak pressure by 0.1 MPa (2%). All predicted pressure spikes were greater than the experimental values and typically fell inside the experimental error band. As energy dissipation due to fluid/structure interaction is not currently modelled by CATHENA, this might account for part of the difference in pressure values.

The overall decay of the predicted water hammer pressure excursions was significantly slower than the experimentally measured decay shown in Figure 11. Also, the predicted period of pressure excursions (time between pressure excursions as measured from the first to the second pressure excursion) was greater than the experimentally measured period. This may be due to the fact that energy dissipation mechanisms such as wall friction may not be accurately accounted for in CATHENA under accelerated flow conditions.

5 SUMMARY AND CONCLUSIONS

CATHENA MOD-3.5c/Rev 0 was used to perform simulations of Seven Sisters fast closing valve tests, as well as vertical and horizontal void tests. CATHENA was shown to capture the salient features of the experimental pressure excursions.

In the fast-closing valve water hammer test modelled, the maximum pressure was simulated to within 10% and the timing of the valve closure was simulated to within 0.002 s. In the vertical void collapse test, the initial pressure rise was simulated to within 5% and the maximum peak pressure to within 23%. In the horizontal void collapse water hammer test, the initial pressure rise was simulated to within 4%, and the maximum peak pressure to within 2%.

The CATHENA simulated results exhibited larger initial pressure excursions than were measured in the experiments and the decay of all subsequent water hammer pressure excursions was significantly slower than the experimentally measured decay. Also, the simulated period of the pressure excursions was significantly greater than the experimentally measured period. This may in part result because energy dissipation due to fluid/structure interaction is not currently accounted for in CATHENA. It may also be due in part to the fact that energy dissipation mechanisms such as wall friction may not be accurately accounted for in CATHENA under accelerated flow conditions.

A sensitivity analysis of the vertical void collapse test showed that modelled results were not sensitive to measurement uncertainties in the initial void pressure and water temperature. The maximum simulated pressure was altered by at most 2% and the onset of pressure excursions was altered by up to 0.02 s by uncertainties in the measured tank pressure, initial void volume, and valve opening time.

An uncertainty analysis showed that the uncertainties in the Colebrook-White friction factor correlation altered the peak pressure by $\pm 3\%$ and the onset of the first pressure spike by ± 0.002 s. Uncertainties in the two-phase friction factor and mixed flow regime transition factors had no significant impact on modelled results.

6 ACKNOWLEDGEMENTS

Thanks go out to Randall Swartz and Tracy Sanderson for their help and cooperation with the experimental data.

REFERENCES

1. B.N. Hanna, "CATHENA: A thermalhydraulic code for CANDU analysis", Nuclear Engineering and Design, 180 (1998) 113-131.
2. T.G. Beuthe, "CATHENA Study of Two-Phase Water Hammer Inter-Peak Timing", Proceedings of the 20th Nuclear Simulation Symposium, 1997, Niagara-on-the-Lake, Ontario.

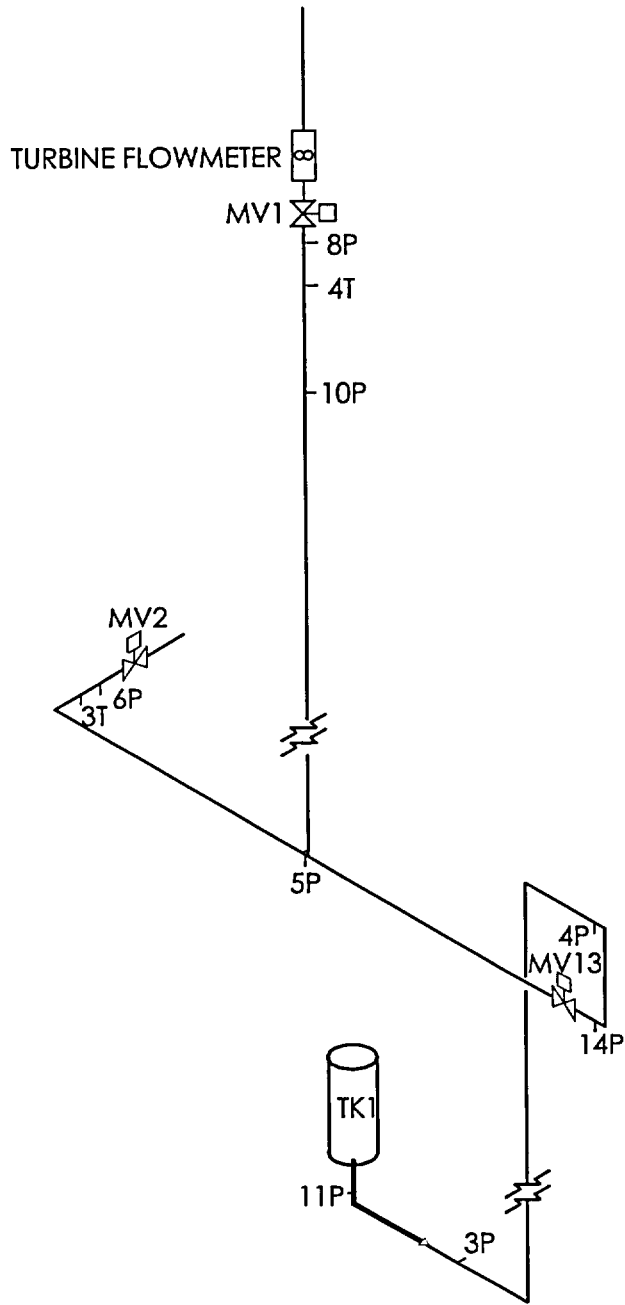


FIGURE 1: Schematic of the Seven Sisters Water Hammer Facility for the Fast-Closing valve tests.

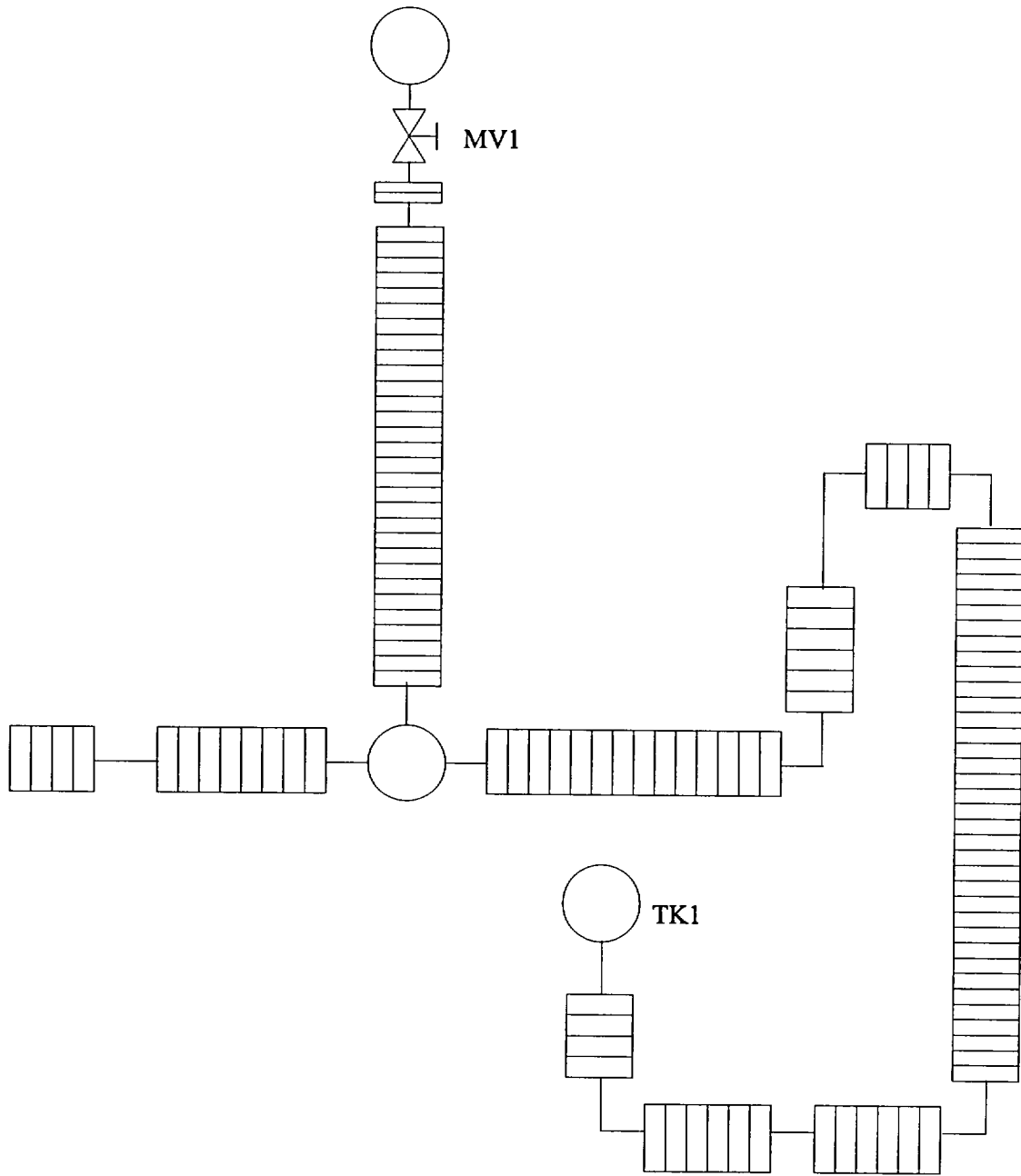


FIGURE 2: CATHENA idealization of the Seven Sisters Water Hammer Facility for the Fast Closing valve test.

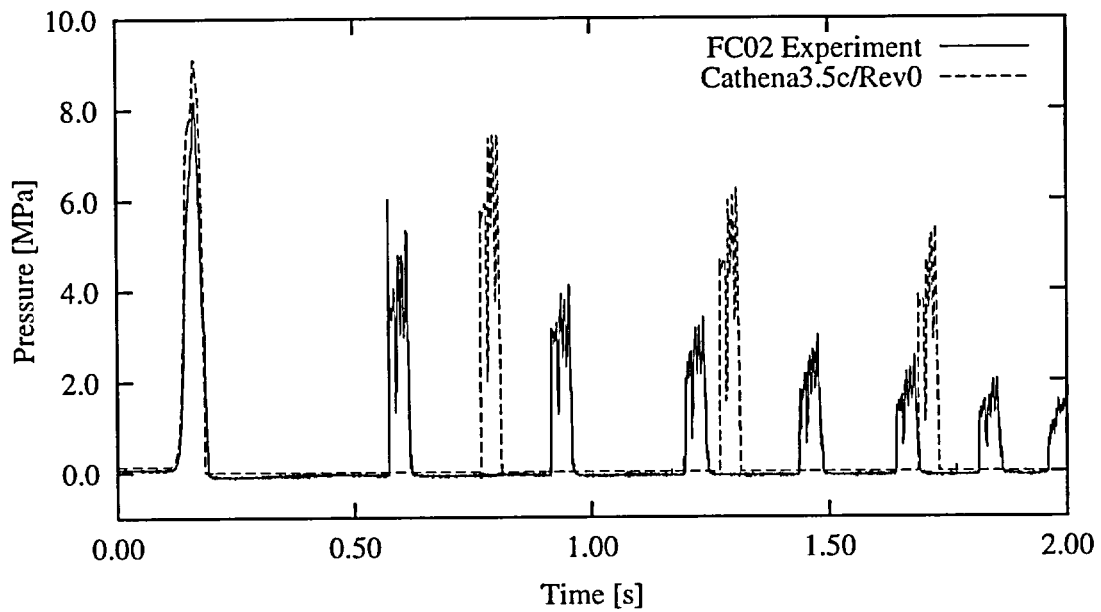


FIGURE 3: Experimental and CATHENA predicted system pressure at valve MV1 for the Fast Closing valve test.

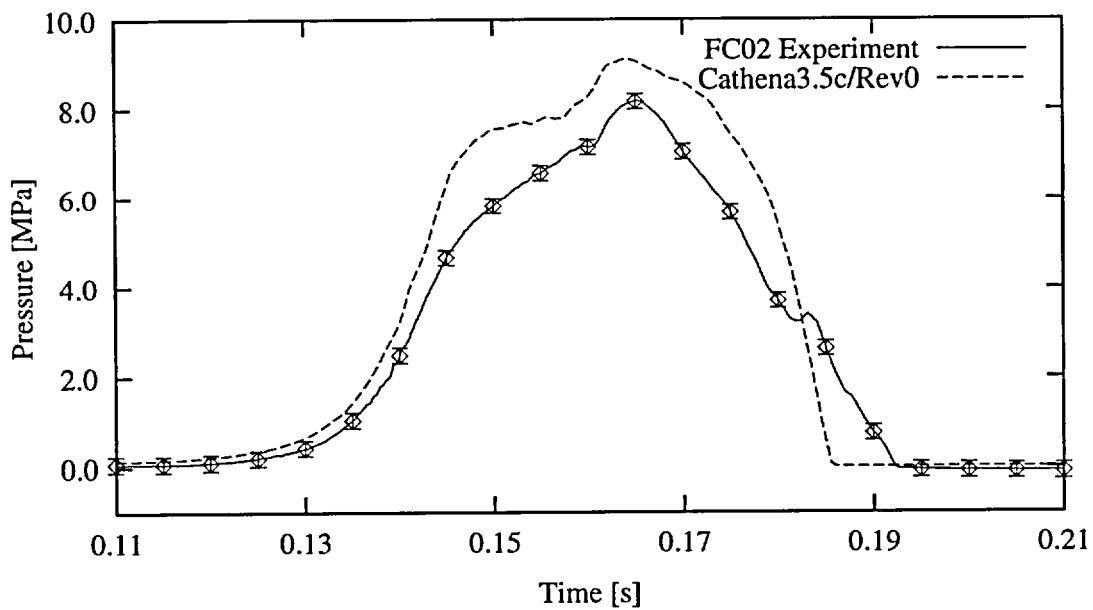


FIGURE 4: Experimental and CATHENA predicted system pressure at valve MV1 for the Fast Closing valve test, first water hammer pressure excursion.

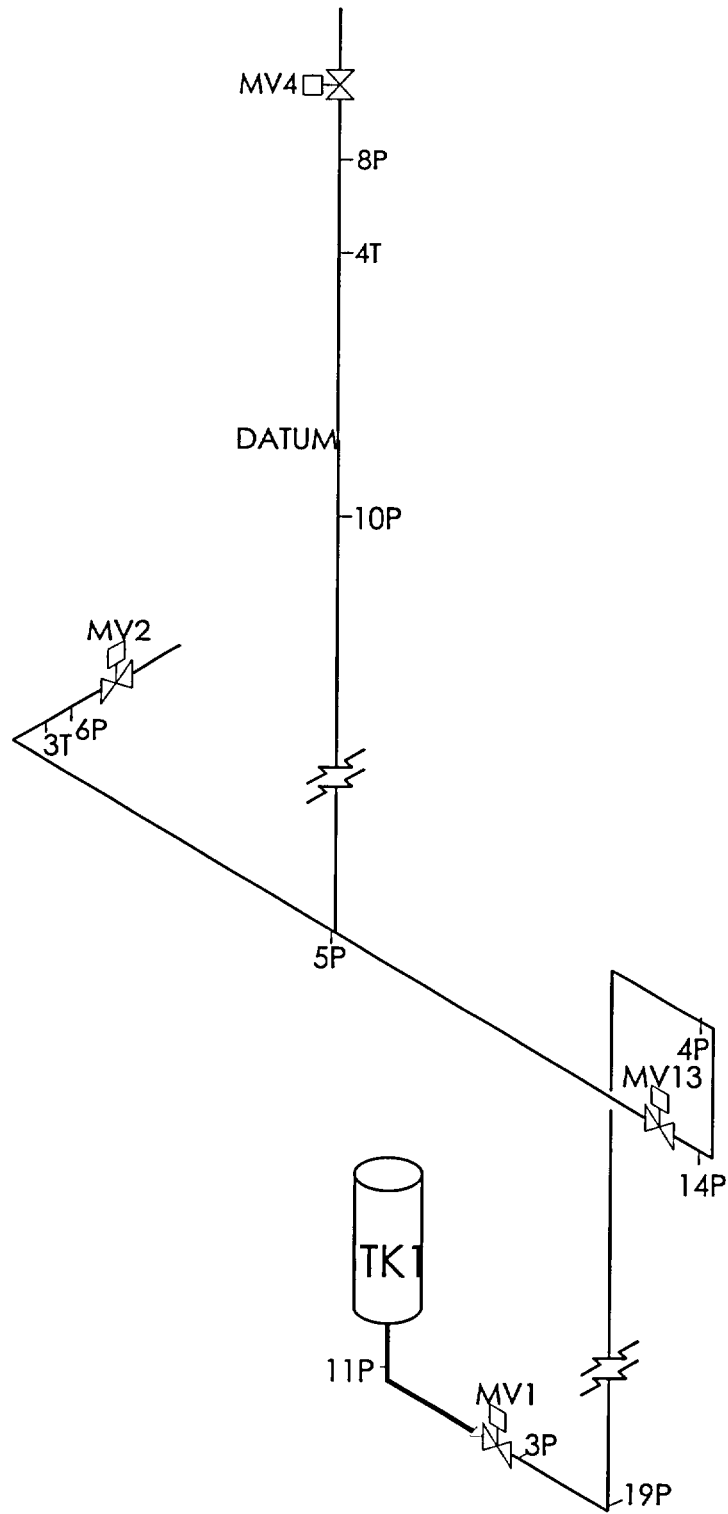


FIGURE 5: Schematic of the Seven Sisters Water Hammer Facility for the vertical void collapse tests.

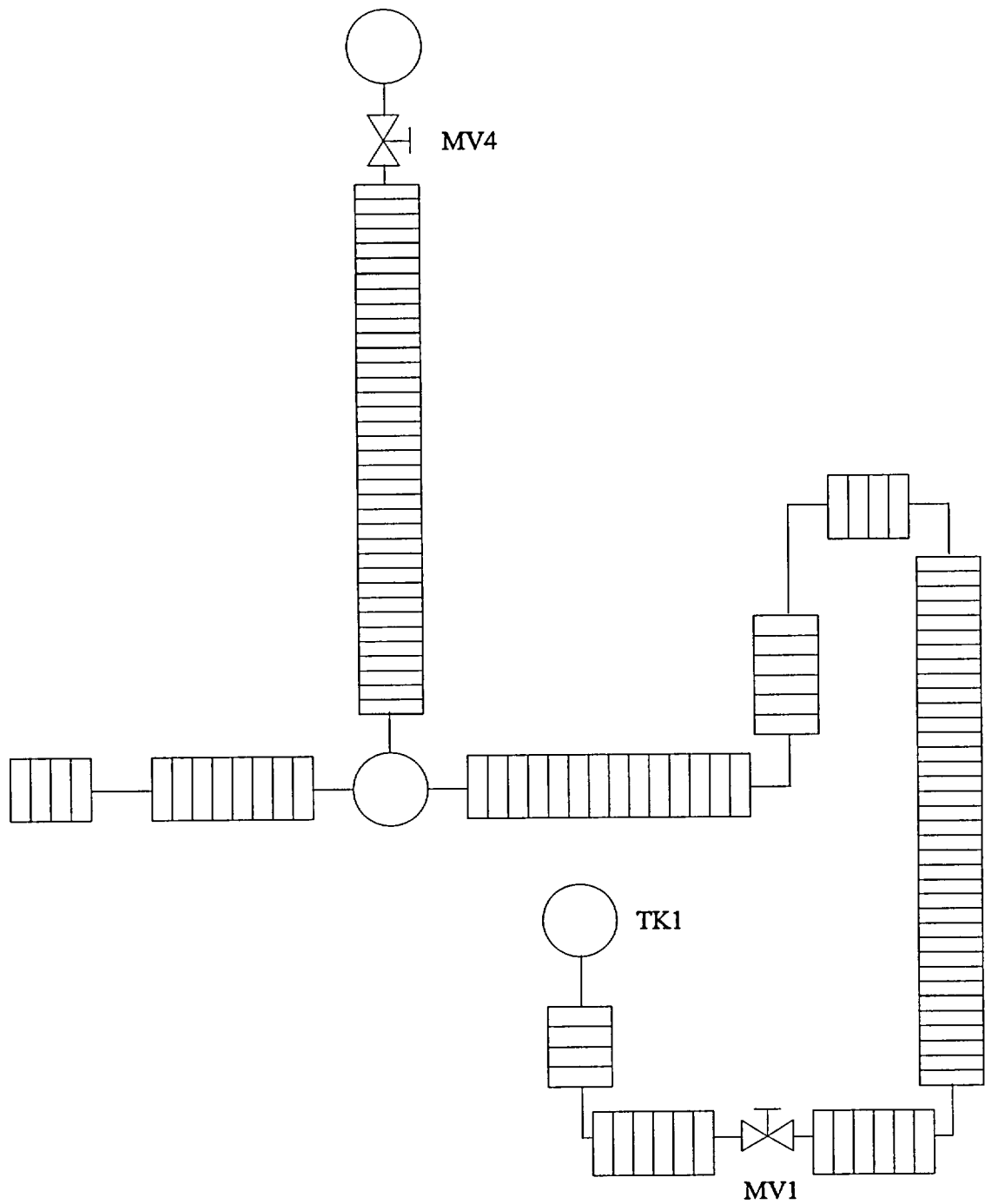


FIGURE 6: CATHENA Idealization of the Seven Sisters Water Hammer Facility for the vertical void collapse test.

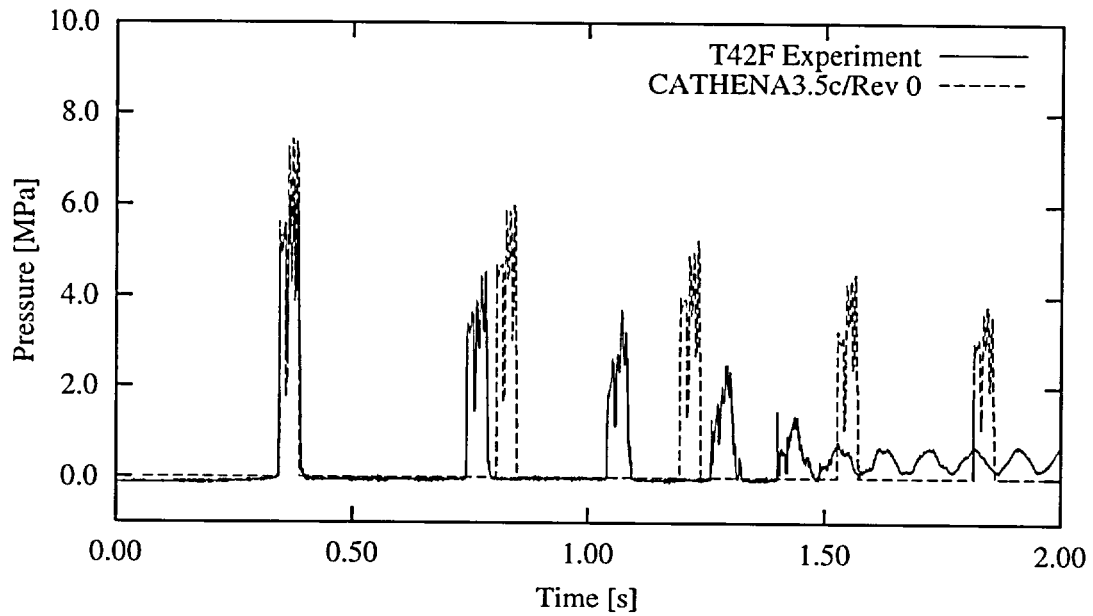


FIGURE 7: Experimental and CATHENA predicted system pressure at 8P (vertical void location) for the vertical void collapse test.

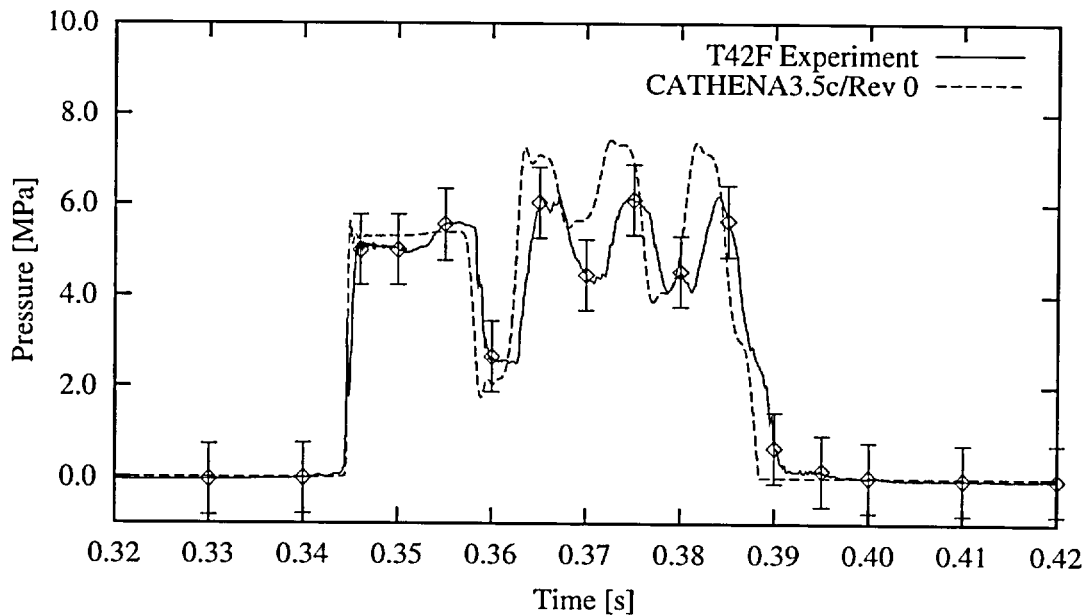
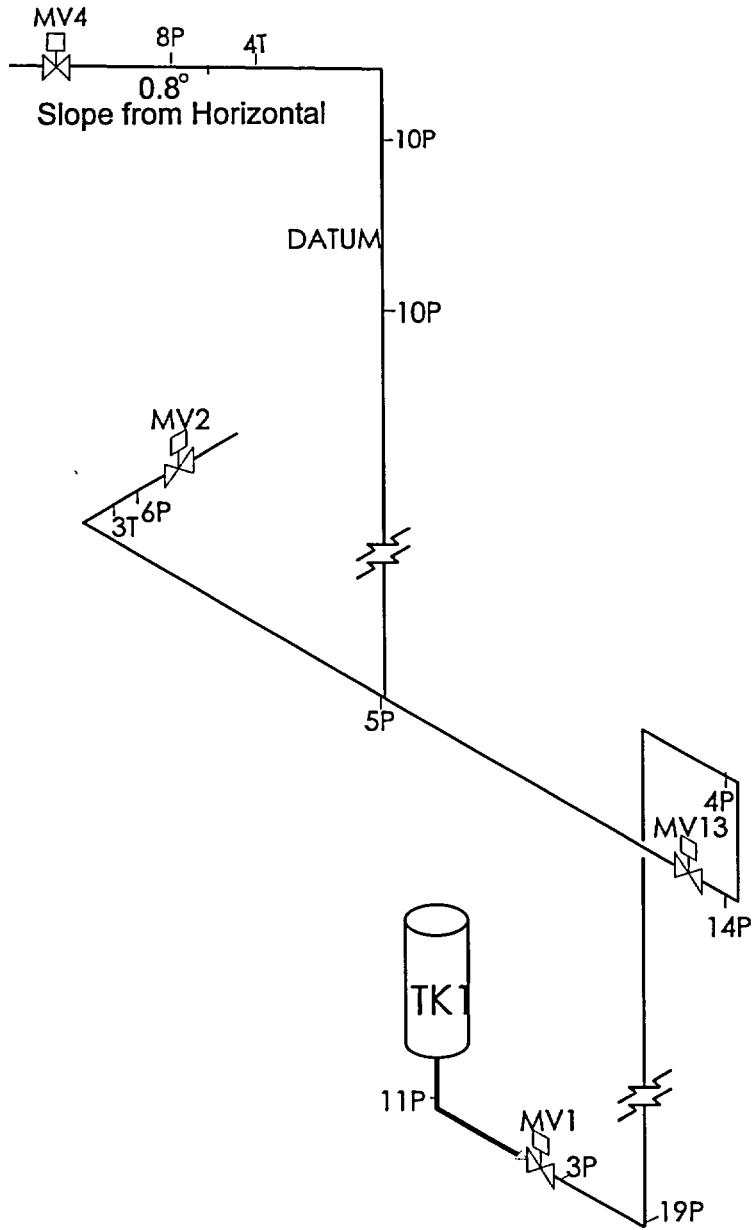


FIGURE 8: Experimental and CATHENA predicted system pressure at 8P (vertical void location) for the vertical void collapse test, first water hammer pressure excursion.



gufigure6 cdr

FIGURE 9: Schematic of the Seven Sisters Water Hammer Facility for the horizontal void collapse tests, single horizontal branch.

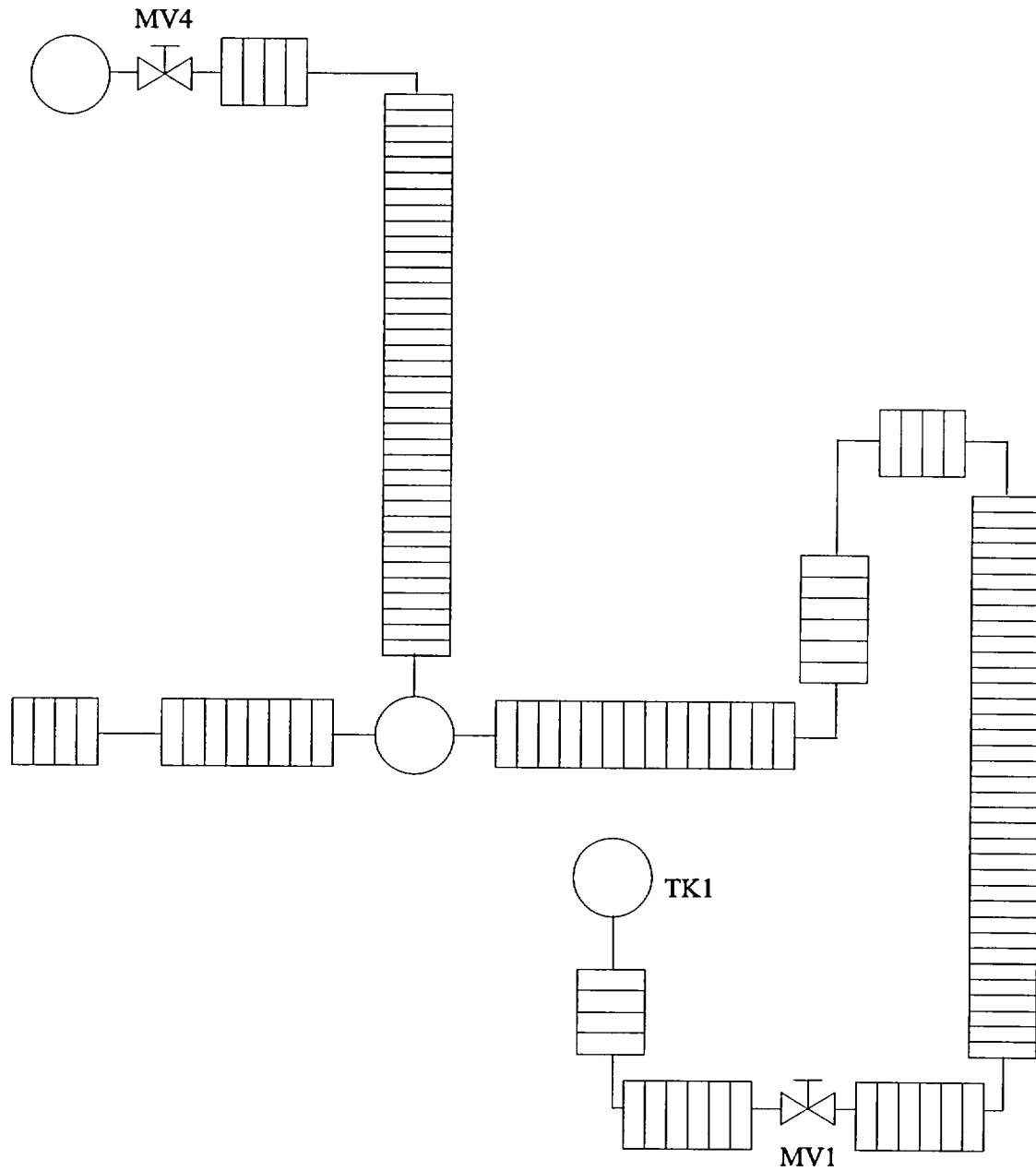


FIGURE 10: CATHENA Idealization of the Seven Sisters Water Hammer Facility for the single horizontal branch void collapse test.

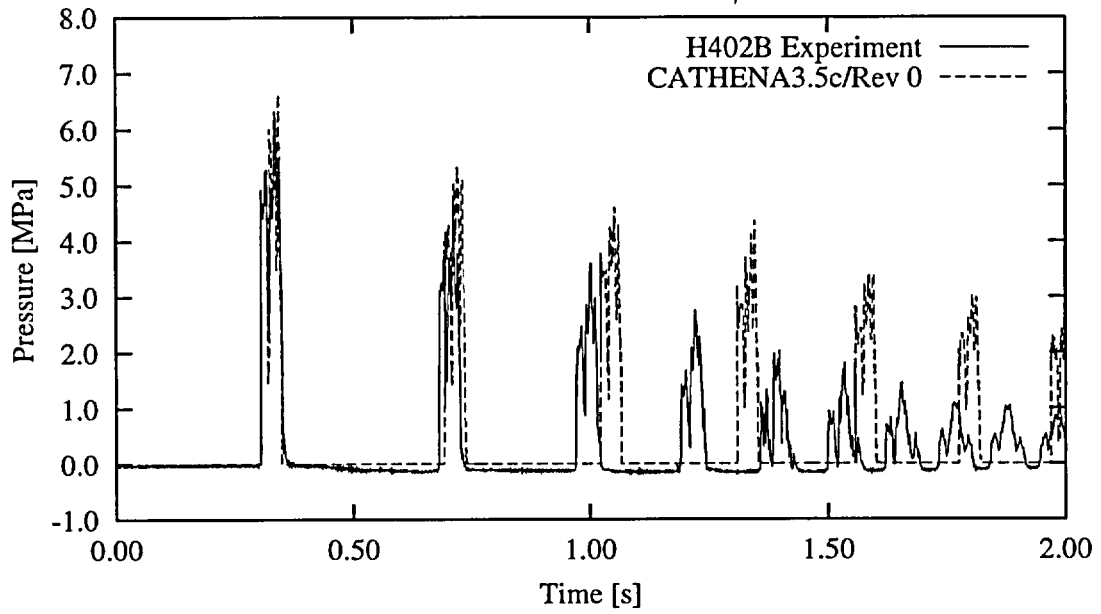


FIGURE 11: Experimental and CATHENA predicted system pressure at 8P (horizontal void location) for the horizontal void collapse test.

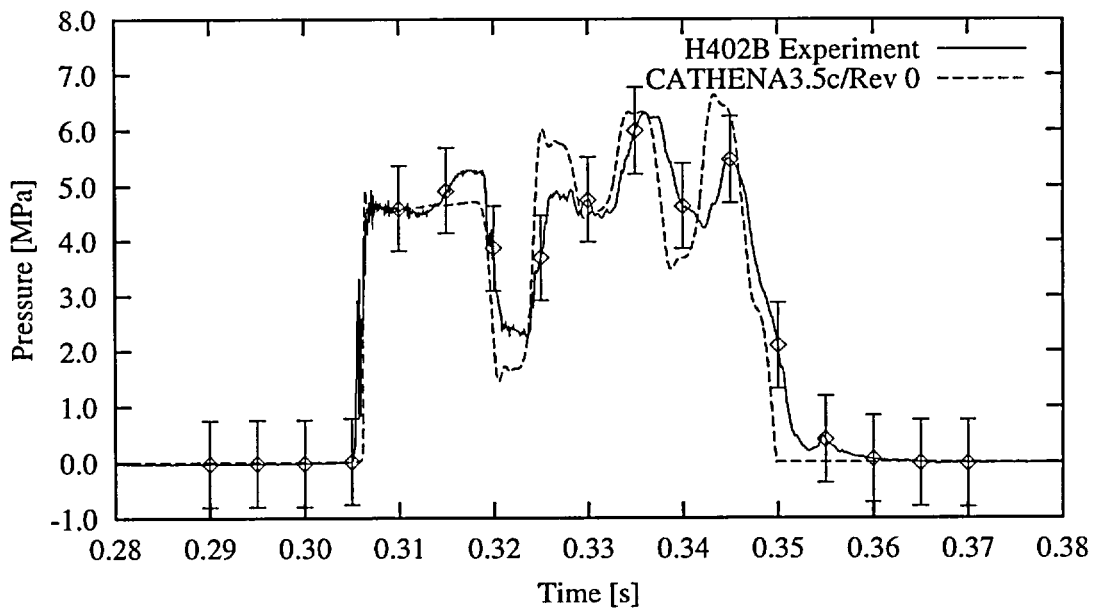


FIGURE 12: Experimental and CATHENA predicted system pressure at 8P (horizontal void location) for the horizontal void collapse test, first water hammer pressure excursion.